

**ONR GRANT N00014-95-1-0539**

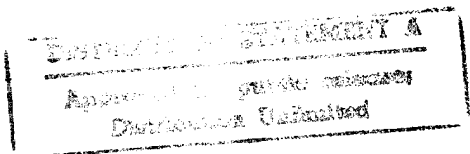
*A DoD Multidisciplinary Research Program  
of the University Research Initiative (M-URI)*

**ANNUAL REPORT**

---

# **INTEGRATED DIAGNOSTICS**

*March 1, 1995 - February 29, 1996*



FOR

**Office of Naval Research**  
800 N. Quincy Street  
Arlington, VA 22217-5660

PREPARED BY

Richard S. Cowan, Interim Program Manager

Ward O. Winer, Principal Investigator

**Georgia Institute of Technology**

MULTIUNIVERSITY CENTER FOR INTEGRATED DIAGNOSTICS

Woodruff School of Mechanical Engineering

Atlanta, GA 30332-0405

Ph: 404-894-3200

SUBGRANTEES

**Northwestern University**

Jan D. Achenbach, Director

Center for Quality Engineering and Failure Prevention

Ph: 847-491-5527

**University of Minnesota**

Dennis Polla, Professor

Department of Electrical Engineering

Ph: 612-624-0256

S. Ramalingam, Professor

Department of Mechanical Engineering

Ph: 612-625-4017

19960603 018

DTIC QUALITY INSPECTED 1

# REPORT DOCUMENTATION PAGE

FORM APPROVED  
OMB No. 0704-0188

Public reporting burden for this collection of information is estimated to average 1 hour per response, including the time for reviewing instructions, searching existing data sources, gathering and maintaining the data needed and completing and reviewing the collection of information. Send comments regarding this burden estimate or any other aspect of the collection of information, including suggestions for reducing the burden to Washington Headquarters Services, Directorate for Information Operations and Reports, 1215 Jefferson Davis Highway, Suite 1204, Arlington, VA 22202-4302 and to the Office of Management and Budget, Paperwork Reduction Project (0704-0188), Washington, DC 20503.

1. AGENCY USE ONLY (Leave blank)	2. REPORT DATE	3. REPORT TYPE AND DATES COVERED	
	29 February, 1996	Year 1 Performance: Mar. 1, 1995-Feb. 29, 1996	
4. TITLE AND SUBTITLE OF REPORT		5. FUNDING NUMBERS	
Integrated Diagnostics		G N00014-95-1-0539	
6. AUTHOR(S)			
Richard S. Cowan and Ward O. Winer (eds.)			
7. PERFORMING ORGANIZATION NAME(S) AND ADDRESS(ES)		8. PERFORMING ORGANIZATION REPORT NUMBER:	
Georgia Institute of Technology MULTIUNIVERSITY CENTER FOR INTEGRATED DIAGNOSTICS G. W. Woodruff School of Mechanical Engineering 801 Ferst Drive Atlanta, GA 30332-0405		19960603 018	
9. SPONSORING/MONITORING AGENCY NAME(S) AND ADDRESS(ES)		10. SPONSORING/MONITORING AGENCY	
Office of Naval Research 800 N. Quincy Street Arlington, VA 22217-5660			
11. SUPPLEMENTARY NOTES:  The information conveyed in this report does not necessarily reflect the position or the policy of the Government, and no official endorsement should be inferred.			
12a. DISTRIBUTION AVAILABILITY STATEMENT		12b. DISTRIBUTION CODE	
UNLIMITED			
13. ABSTRACT (Maximum 200 words)  This document summarizes performance activity regarding basic research being conducted in the area of <i>Integrated Diagnostics</i> , a term associated with the technologies and methodologies used to determine how mechanical failures occur, and how they can be detected, predicted, and diagnosed in real-time. Objectives, set forth through the Department of Defense Multidisciplinary Research Program of the University Research Initiative (M-URI), are being addressed by faculty and staff from the Georgia Institute of Technology, Northwestern University, and the University of Minnesota. This activity is funded through the Office of Naval Research for a basic period of three years, with a potential for two additional years. First-year accomplishments, future plans, and technology transfer actions achieved to date are reported upon.  During this reporting period, critical components have been identified, from which the mechanisms of failure are to be better understood through the development of failure models. These models can serve as a guide in the selection and development of sensors to detect faults and pending failures. Effort has been placed on micro-sensor development, and achieving the means to analyze and correlate reliable sensor output for operator use. Organizationally, this activity is being accomplished through (15) projects, categorized by three thrust areas.			
14. SUBJECT TERMS			15. NUMBER OF PAGES: 223
Integrated Diagnostics; Condition-based Maintenance Failure Detection; Failure Prediction; Sensors; Direct Sensing			16. PRICE CODE
17. SECURITY CLASSIFICATION OF REPORT: Unclassified		18. SECURITY CLASSIFICATION OF THIS PAGE: Unclassified	19. SECURITY CLASSIFICATION OF ABSTRACT: Unclassified
20. LIMITATION OF ABSTRACT: SAR			

**ONR GRANT N00014-95-1-0539**

*A DoD Multidisciplinary Research Program  
of the University Research Initiative (M-URI)*

**ANNUAL REPORT**

---

# **INTEGRATED DIAGNOSTICS**

*March 1, 1995 - February 29, 1996*

FOR

**Office of Naval Research**  
800 N. Quincy Street  
Arlington, VA 22217-5660

PREPARED BY

Richard S. Cowan, Interim Program Manager

Ward O. Winer, Principal Investigator

**Georgia Institute of Technology**

MULTIUNIVERSITY CENTER FOR INTEGRATED DIAGNOSTICS

Woodruff School of Mechanical Engineering

Atlanta, GA 30332-0405

Ph: 404-894-3200

SUBGRANTEES

**Northwestern University**

Jan D. Achenbach, Director

Center for Quality Engineering and Failure Prevention

Ph: 847-491-5527

**University of Minnesota**

Dennis Polla, Professor

Department of Electrical Engineering

Ph: 612-624-0256

S. Ramalingam, Professor

Department of Mechanical Engineering

Ph: 612-625-4017

## TABLE OF CONTENTS

---

Title Page .....	i
Table of Contents .....	iii
List of Tables .....	v
List of Figures .....	vii
<b>EXECUTIVE SUMMARY</b> .....	1
<b>1. INTRODUCTION</b> .....	3
1.1 Mission.....	3
1.2 Organization.....	4
<b>2. RESEARCH ACCOMPLISHMENTS and PLANS</b> .....	9
2.1 Failure Detection and Identification .....	13
2.1.1 Study of Acoustic Emission and Transmission from Incipient Fatigue Failure ..	13
2.1.2 Crack Detection in Annular Structures by Ultrasonic Guided Waves.....	20
2.1.3 Flaw Detection and Characterization .....	34
2.1.4 Detection of Mechanical Seal Failure in Turbomachinery .....	44
2.2 Failure Prediction Methodology .....	47
2.2.1 Structural Fatigue Investigation .....	47
2.2.1.1 Stress Analysis and Stress Intensity Factor Solutions for Cracks.....	49
2.2.1.2 Characterization of Fatigue Behavior and Mechanisms .....	59
2.2.1.3 Remaining Life Estimation Methodology .....	73
2.2.2 Failure Prediction Methodology using First-Order Reliability Method .....	80
2.3 Direct Sensing, Analysis, and Real-time Diagnosis.....	86
2.3.1 Integrated Microsensors for Aircraft Fatigue and Failure Warning.....	86
2.3.1.1 Microsensor Development .....	86
2.3.1.2 Signal Processing .....	112
2.3.2 Eddy Current Microsensors for Integrated Diagnostics.....	130
2.3.3 Magnetic-Electrical-Impedance Tomography.....	150
2.3.4 Acoustic Emission Modeling for Integrated Diagnostics .....	163
2.3.5 Monitoring of Harmonic Oscillations in Rotating Machine Elements .....	187
2.3.6 Dynamic Metrology as a Wear Diagnostic .....	194
2.4 References.....	201
<b>3. TECHNOLOGY TRANSFER ACHIEVEMENTS</b> .....	205
3.1 Publications.....	205
3.2 Presentations .....	207
3.3 Education .....	208
3.4 Partnerships.....	208
<b>APPENDIX A. Program Participants</b> .....	A-1

## **LIST OF TABLES**

---

1. Tests on 304 SS and 1045 Steel .....	62
2. Phase II Test Matrix (each material) .....	64
3. Summary of PZT Thin-Film Electrical and Mechanical Material Properties.....	89
4. Voltage and Charge Readout Modes for Piezoelectric Microsensors.....	94
5. Literature Summary of Sensor Type/Sensitivity for Wear and Defect Monitoring.....	196
6. Primary Failure Modes of Bearings .....	197

## LIST OF FIGURES

---

1. Program Organization Diagram, General.....	5
2. Allocation of M-URI Funding, Participating Institutes.....	7
3. Allocation of M-URI Funding, Research Focus .....	7
4. Program Organization Diagram, Topical .....	11
5. Schematic of Bending Beam Fatigue Tester .....	14
6. Non-rotating Test Specimen.....	15
7. Fatigue Tester Head Assembly.....	16
8. Optical Fibre Receiving Array .....	19
9. Two Concepts for Ultrasonic Inspection of Annular Structures.....	21
10. Methodology for Mode Selection and Control with Ultrasonic Guided Wave Inspection.....	23
11. Experimental Facility .....	25
12. Waveforms Inside/Outside the Ring (no wedge) at $f = 0.5$ MHz.....	26
13. Effect of the Source/Receiver Wedge Angles on the Waveforms .....	27
14. Waveforms with Tone Burst Generator .....	28
15. Wavelet Transform.....	29
16. Dispersion Curves .....	30
17. Amplified Profile within the Structure from Inner Surface to Outer Surface.....	32
18. Guided Waves and Creeping Waves in a Partially Annular Structure.....	33
19. Schematic Illustration of the Optical Fiber Array Laser Generation System .....	35
20. Plots of Ultrasonic Waveforms Detected by 5 Mhz Surface Wave Transducer .....	36
21. Plots of Power Spectra of Generated Waveforms.....	37
22. Theoretically Predicted (a) Waveform and (b) Power Spectrum for Ultrasonic Signal Generated by an Array of ten $230 \mu\text{m}$ dia. Fibers, Separated by $880 \mu\text{m}$ .....	38
23. Unaveraged and Unamplified Piezoelectrically Detected Waveforms for Fiber-optic Array Laser Generated Surface Waves .....	39
24. Power Spectra of Waveforms of Figure 22 Averaged 100 Times .....	40
25. Power Spectra of Figure 24 Normalized by the Single Fiber Spectrum to Remove the Effects of Transducer Response.....	41
26. Weiner Filtered Versions of the Waveforms of Figure 22.....	42

27. Mechanical Seal Test Apparatus.....	44
28. Seal Test System .....	45
29. Solid Model of the Rotor Hub.....	51
30. Typical Finite Element Mesh.....	53
31. Von Mises Stress Distribution .....	55
32. Location of the Maximum Mises Stress.....	57
33. Thin-walled Tubular Specimen Design.....	63
34. Flat Panel Specimen, Design A.....	69
35. Flat Panel Specimen, Design B .....	70
36. Flat Panel Specimen, Design C .....	71
37. H-46 Helicopter Connecting Link.....	75
38. H-46 Helicopter Connecting Link.....	77
39. Mapping of Crack Size Distribution on the Final Crack Line .....	82
40. Change of Crack Size Distribution with the Number of Fatigue Cycles .....	82
41. Shape of Failure Probability Density Function ( $p_f$ ) With and Without Inspection.....	83
42. Change in Probability of Failure (CDF) Curve after Inspection.....	83
43. CDF versus N for an Edge Crack in a Plate under Tension.....	84
44. Concept of an Inexpensive, Small, and Light-weight Aircraft Condition Monitoring Coupon.....	87
45. Abbreviated Schematic of Process Steps Used to Fabricate an Accelerometer.....	90
46. Chemical Processing Route Leading to the Preparation of Piezoelectric Thin Films for Sol-gel Dispensing on Silicon Wafers .....	91
47. X-ray Diffraction Spectrum Obtained for a $0.35\text{ }\mu\text{m}$ -thick PZT Thin Film on a Platinum-coated Silicon Substrate .....	92
48. Acoustic Emission Microsensor Approach showing a Piezoelectric Thin Film Acoustically-coupled to an Aircraft Component .....	95
49. Optical Photograph of an AE Piezoelectric Microsensor with Active Area of $2.0 \times 10^{-3}\text{ cm}^2$ .....	96
50. Voltage Responsivity for an AE Microsensor to the Breakage of Pencil Lead.....	96
51. Cross-section of a Piezoelectric Microsensor Fabricated on a Silicon Nitride Microbridge .....	98
52. Scanning Electron Micrograph of a Cantilever Beam Piezoelectric Vibration Monitoring Device.	99
53. Vibration Monitoring Method for Real-time and Maintenance-based Fatigue Cycle Monitoring ...	100
54. Experimental Setup for Monitoring of Acoustic Emission during Nanoindentation.....	102
55. Nanoindentation Sample Penetration versus Load Characteristic .....	103
56. (a) Nanoindentation Sample Penetration vs. Load Characteristic for a Nitride/Al/Sapphire (b)-(e) AE Signals from Indentation .....	106

57. (a) Nanoindentation into Tantalum Nitride/Al/Sapphire Sample with Higher Loading (b) AE Signals from Both Load Drops Offset for Clarity .....	108
58. Scanning Electron Micrograph of a Crack Generated using Nanoindentation Technique .....	109
59. (a) Load-depth Indentation in Fe-Si (b) Acoustic Emission Output Obtained from Nanoindentation .....	110
60. (a) Maximum Amplitude as a Function of Load at First Loading Discontinuity (b) Rise Time as a Function of Load at First Loading Discontinuity.....	111
61. Illustration of Microcrack AE and Associated Signal Processing Block Diagram.....	113
62. Tantalum Nitride on Sapphire Microcrack AE Signal.....	117
63. Iron on Silicon Microcrack AE Signal.....	118
64. Tungsten Microcrack AE Signal .....	119
65. (a) Two Channel Engine with Rotor Noise Acquired with A3 Sensors (b) Power Spectrum Estimates for Two Channel Engine with Rotor Noise .....	120
66. Principal Component Frequency vs. Time Plot for a Prony Fit to the Engine with Rotor Noise ....	124
67. Singular Values of 8000 Samples of Engine with Rotor Noise .....	124
68. Noise Power Spectrum at 15-th order LP Filter Output.....	125
69. Noise Power Spectrum at 80-th order LP Filter Output.....	125
70. Tantalum Nitride AE Signal Superimposed on Engine with Rotor Noise .....	126
71. Linear Prediction Filter Output for Figure 70 Signal Output .....	126
72. Block Diagram of the Processor for Generating -th Decision Statistic.....	127
73. Decision Statistic Sequence Generated by Figure 72 Processor with Figure 71 Input.....	127
74. Bifrequency Spectrum Magnitude Plots.....	128
75. Magnitude of the Wigner Distribution of the AE Signal in Additive Engine with Rotor Noise after LP Filtering .....	129
76. Time-Frequency Plot Resulting from Optimum Smoothing.....	129
77. Single Element Micro-sensor for Eddy Current Sensing and Imaging of Micro-flaws .....	132
78. Schematic of Conventional Eddy Current Sensing System for Flaw Detection .....	132
79. Test Samples Built to Evaluate Resolution Characteristics of Experimental Sensors .....	133
80. A Flux-focusing Eddy Current Sensor for Flaw Detection .....	134
81. Calculated Vector Potential Distribution in a Ferromagnetic Test Sample, Sensor, and Associated Near-space; Axisymmetric Model with non-Ferromagnetic Pole Piece; AC Excitation at 25 KHz .....	137
82. Calculated Eddy Current Density Distribution in a Ferromagnetic Test Sample, Sensor and the Associated Near-space; Axisymmetric Model with non-Ferromagnetic Pole Piece; AC Excitation at Indicated Frequencies.....	138

83. Calculated Vector Potential Distribution in a Ferromagnetic Test Sample, Sensor, and the Associated Near-space; Axisymmetric Model with Ferromagnetic Pole Piece; AC Excitation at 25 kHz .....	139
84. Calculated Vector Potential Distribution in a Ferromagnetic Test Sample, Sensor, and the Associated Near-space; Axisymmetric Model with Ferromagnetic Pole Piece; AC Excitation at 100 kHz .....	140
85. Calculated Eddy Current Density Distribution in a Ferromagnetic Test Sample, Sensor, and the Associated Near-space; Axisymmetric Model with Ferromagnetic Pole Piece; AC Excitation at Indicated Frequencies. ....	141
86. (a) Flaw Map Constructed by Scanning a Through-the-Thickness Flaw (0.250 inch Dia., Drilled Hole) in a Steel Plate with Flux-focusing Sensor of Figure 80 (b) Flaw Map Constructed by Scanning a Through-the-Thickness Flaw (0.080 inch Dia., Drilled Hole, Connected to 0.008 inch Slot, 0.5 inch in Length) in a Steel Plate with Flux-focusing Sensor of Figure 80.....	144
87. (a) Flaw Map Constructed by Scanning a Through-the-Thickness Flaw (1/8 inch Dia., Drilled Hole) in a Steel Plate with Flux-focusing Sensor Having a 0.125 inch Dia. Pole-Piece (b) Flaw Map Constructed by Scanning a Through-the-Thickness Flaw (0.080 inch Dia., Drilled Hole, Connected to 0.008 inch Slot, 0.5 inch in Length) in a Steel Plate with Flux-focusing Sensor Having a 0.125 inch Dia. Pole-Piece .....	145
88. Mask Geometry for Fabrication of Single-element and Multi-element Sensor Arrays.....	146
89. Schematic Illustration of Redesigned, Eddy Current Micro-sensor Arrays .....	147
90. Schematic of the Excitation Coil Pole Piece for First Evaluation of the 3-Mask, Flux Focusing, Single-Element Eddy-current Micro-sensor .....	148
91. Schematic Illustration of a Flux Focusing Micro-sensor based on GMR .....	149
92. Current Flow between Two Electrodes on a Device under Test with and without a Flaw .....	151
93. Schematic Diagram of the Experimental Test Bed .....	152
94. Drawings of Constructed C- and D-type Focusing Probes .....	154
95. Response of the Differential Pair of D-type Probes as a Function of Frequency .....	155
96. Diagram Indicating Geometry Used to Scan the Probe across the Device under Test .....	157
97. Magnitude and Phase of the Response of the D-type Probe as a Function of Position for Scans A and B; Flaw is a 2.54 mm Slit, f = 1kHz.....	158
98. Magnitude and Phase of the Response of the D-type Probe as a Function of Position for Scans A and B; Flaw is a 0.34 mm dia. Hole, f = 1kHz.....	159
99. Magnitude and Phase of the Difference between Responses for Scans A and B as a Function of Position for the D-type Probe; Flaw is a 2.54mm Slit, f = 1kHz.....	160
100. Magnitude and Phase of the Difference between Responses for Scans A and B as a Function of Position for the D-type Probe; Flaw is a 0.34 mm dia. Hole, f = 1kHz.....	161
101. Example of Spatial Filtering for Noise Suppression.....	164

102. Acoustic Emission and Stress vs. Strain for a 7075-T6 Aluminum Specimen under Monotonic Tension .....	166
103. Acoustic Emission and Stress vs. Strain for Incoloy 901 under Montonic Tension.....	167
104. Cumulative Number of AE Counts vs. Stress Intensity Factor for Notched Specimens .....	168
105. Edge-notch Tensile Fatigue Specimen .....	170
106. Compact Tension Specimen (ASTM 399) .....	171
107. Stages of Fatigue Life and Characteristic AE Output.....	173
108. AE Events and Crack Extension vs. Normalized Fatigue Cycles (2024-T3 Aluminum).....	174
109. Crack Extension Rate as a Function of Stress Intensity Range.....	177
110. Rate of AE Counts as a Function of Stress Intensity Range .....	178
111. Crack Extension and AE Count Rate vs. Stress Intensity Factor Range for Two Materials .....	179
112. Histogram of AE Events as a Function of Stress, Stage I.....	180
113. Histogram of AE Events as a Function of Stress, Stage II.....	181
114. Histogram of AE Events as a Function of Stress, Stage III.....	182
115. Development of Phase Distributions of Cumulative Counts for LCF Test, Aluminum .....	183
116. Development of Phase Distributions of Cumulative Counts for LCF Test, Aluminum .....	184
117. Development of Phase Distributions of Cumulative Counts for LCF Test, Aluminum .....	185
118. Fatigue Testing for Investigation of Effects of Stress Amplitude and Stress Ratio.....	186
119. Photograph of FMR Mechanical Face Seal Test Rig.....	188
120. Schematic of FMR Mechanical Seal Test Rig .....	189
121. Pressurized Air and Water System Connections.....	191
122. Schematic of HHO Research Effort .....	193
123. Schematic Diagram of the $\beta$ -Test Stand .....	197
124. Schematic Diagram and Sensitivity Measurements for Contact Potential Difference Probe .....	198

## **EXECUTIVE SUMMARY**

---

**F**aculty and staff from the Georgia Institute of Technology, Northwestern University, and the University of Minnesota are pleased to submit this document, summarizing first year activities of Office of Naval Research (ONR) Grant N00014-95-1-0539, *Integrated Diagnostics*. Supported through the Department of Defense (DoD) Multidisciplinary Research Program of the University Research Initiative (M-URI), this program was initiated to promote basic research in the technologies and methodologies used in determining how mechanical failures occur, and how they can be detected, predicted, and diagnosed in real-time.

To accomplish the objectives set forth by the M-URI program, the MULTIUNIVERSITY CENTER FOR INTEGRATED DIAGNOSTICS was formed. Under the direction of Principal Investigator Ward Winer, Regents' Professor and Chair of the Woodruff School of Mechanical Engineering at Georgia Tech, research is being conducted by seventeen (17) faculty associated with four schools from the Georgia Tech College of Engineering, four (4) faculty from Northwestern University, and eleven (11) from the University of Minnesota. Dr. Dennis Polla and Dr. S. Ramalingam of the University of Minnesota, and Dr. Jan Achenbach of Northwestern University serve as Subgrant Principal Investigators for their respective schools.

During this reporting period, critical components have been identified, from which the mechanisms of failure are to be better understood through the development of failure models. These models can serve as a guide in the selection and development of sensors to detect faults and pending failures. Effort has been placed on micro-sensor development, and achieving the means to analyze and correlate reliable sensor output for operator use. Organizationally, this activity has been accomplished through fifteen (15) projects, categorized by three (3) thrust areas:

- Failure Detection and Identification
- Failure Prediction Methodology (Failure Mechanisms, Life Estimation)
- Direct Sensing, Analysis, and Diagnosis (Sensor Development, Real-time Diagnosis)

The broad range of cross-disciplinary research topics addressed by the Integrated Diagnostics program has necessitated an effective communication network encompassing both the faculties and sponsors. A number of activities have been engaged to facilitate the flow of information during this reporting period including traditional publication channels, meeting presentations, monthly updates, partnerships, and electronic reporting (<http://www.me.gatech.edu/Diagnostics/>). Of course, the primary mode of transfer is through students, who upon entering an engineering profession, will be trained in an aspect of integrated diagnostics. To date, this program has accommodated six (6) post-doctoral researchers, twenty-four (24) graduate students, and six (6) advanced undergraduate students.

# 1. INTRODUCTION

---

Office of Naval Research (ONR) Grant N00014-95-1-0539, *Integrated Diagnostics*, was initiated on March 1, 1995, following approval of a research proposal submitted to the Department of Defense Multidisciplinary Research Program of the University Research Initiative (M-URI). To accomplish the objectives set forth by the M-URI program, the MULTIUNIVERSITY CENTER FOR INTEGRATED DIAGNOSTICS was formed, supported by faculty and staff from the Georgia Institute of Technology, University of Minnesota, and Northwestern University. Funded for a basic period of three years, with a potential for two additional years, this document reports on the Center's first year of activity.

## 1.1 Mission

America's military machines (e.g., ships, aircraft, and land vehicles) are growing old. Many of the systems that are confidently relied upon today were designed and built twenty and thirty years ago. Given the present economic climate, replacement with next generation equipment can no longer be taken for granted. As a result, an expectation of keeping aging machines in service well into the next century has emerged, which has elevated concern that poor performance, inadequate safety, and increasingly expensive maintenance will result.

To respond to this technological challenge, pending failures must be identified before disastrous consequences occur. Incipient failures, however, are hard to locate, and current maintenance systems have limited capabilities to do so. Today's systems rely mainly on time-based inspection, which requires that parts be inspected at specified intervals, and be replaced when deemed unfit for service. A more effective and efficient alternative to time-based inspection is to continuously monitor critical components. This necessitates an understanding of *Integrated Diagnostics*, a term associated with the technologies and methodologies used to determine how mechanical failures occur, and how they can be detected, predicted, and diagnosed in real-time.

Researchers, representing a variety of engineering disciplines at the Georgia Institute of Technology, Northwestern University, and the University of Minnesota, have been assembled to perform studies associated with three major Integrated Diagnostic needs: the need to detect and identify incipient failures, the need to reliably predict the occurrence of failures, and the need to monitor the condition of a component or system in real-time. Organizationally, this has led to the formation of three research thrust areas, the missions of which are defined below.

- I. **Failure Detection and Identification:** perform studies pertaining to deterioration mechanisms and techniques for detecting the initiation of fractures or other failures.
- II. **Failure Prediction Methodology:** perform studies pertaining to the methodology for failure prediction in real-time, including modeling fault initiation and failure signatures, and observing the propagation and fracture phases of fatigue-based failure.
- III. **Direct Sensing, Analysis and Real-time Diagnosis:** perform studies with respect to the responses of signals early in fault inception, including research on sensors that can be placed at critical sites on mechanical systems for responses to change in variables of state or vibration.

## **1.2 Organization**

To provide an overview of what is needed for developing the new technologies associated with integrated diagnostics, Figure 1 is offered. This "delivery system" begins through the understanding of Department of Defense (*DoD*) *needs* and is ultimately cultivated to produce payoffs in *decision technology*. The MultiUniversity Center for Integrated Diagnostics has focused attention on *sensor development*, the results of which are of use in accomplishing the Center's mission in furthering the understanding of *failure mechanisms* and the ability to reliably address *failure detection*. It is anticipated that such knowledge will further the development of the two major components needed for the advancement of diagnostic/prognostic technologies: *life estimation* and *real-time diagnosis*.

A technical organization built on effective management and efficient communication has been formed to facilitate and combine the various disciplines required to develop the needed scientific and engineering foundation outlined above. The participating faculty and staff, representing the Georgia Institute of Technology, Northwestern University, and the University of Minnesota, are recognized for their significant contributions with respect to structural fatigue, fracture, nondestructive testing, acoustics, ultrasonics, sensors, and signal processing. Identified in Appendix A, Integrated Diagnostic research is being carried out by seventeen (17) faculty associated with four schools from the Georgia Tech College of Engineering, four (4) faculty from Northwestern University, and eleven (11) from the University of Minnesota. In addition, the program has accommodated six (6) post-doctoral researchers, twenty-four (24) graduate assistants, and six (6) advanced undergraduate students.

Through M-URI support, studies have been initiated with respect to understanding the mechanisms of failure (through detection, identification, and prediction) and the means to analyze them (through sensors/hardware, signal processing/software and real-time diagnosis). Figures 2 and 3 provide an indication has to how these moneys have been distributed to the participating institutions and prioritized with respect to research area. Sections 2 and 3 of this annual report summarize the first-year accomplishments obtained by this financial commitment.

## Program Organization Diagram

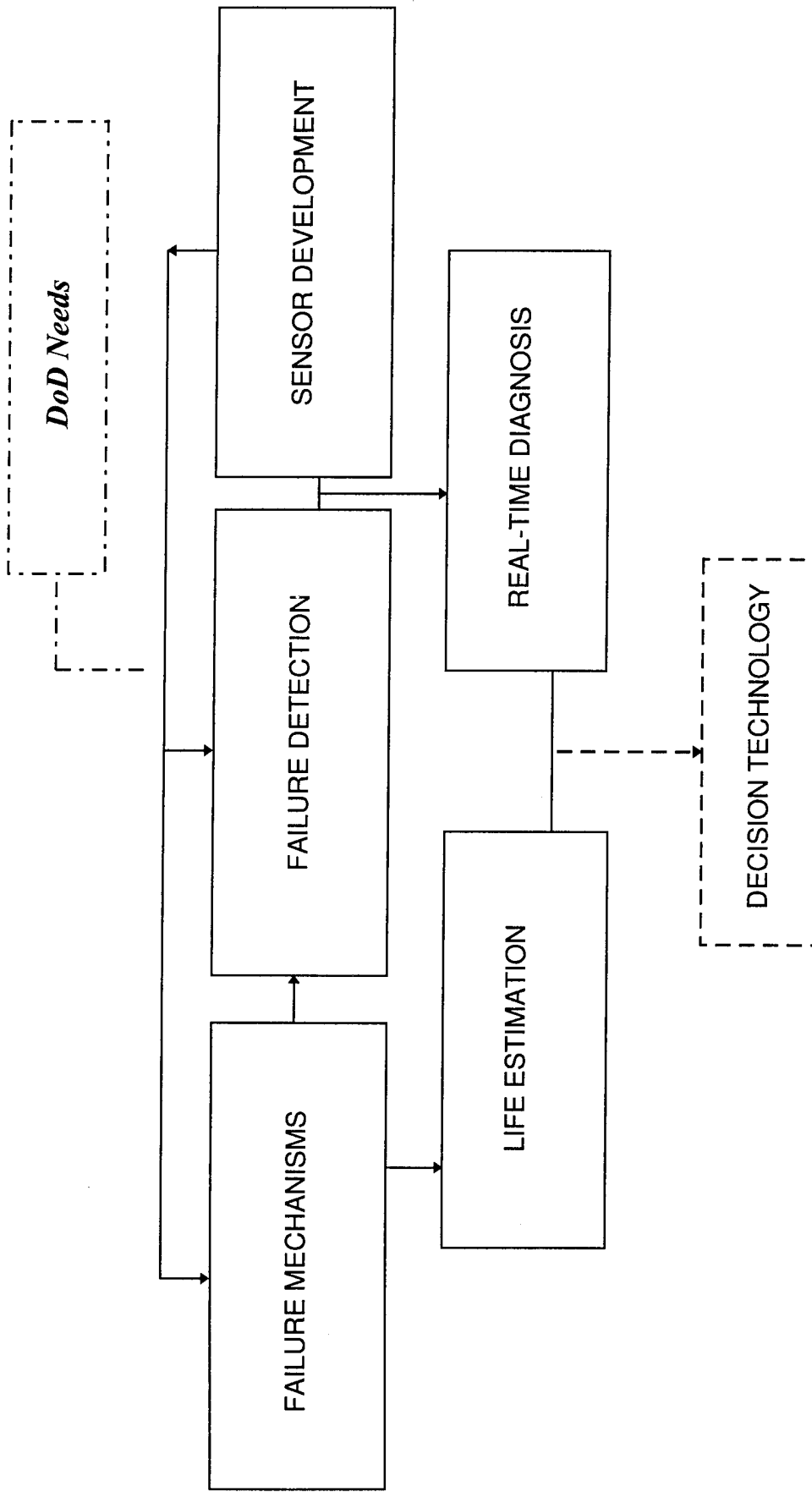


**Figure 1**

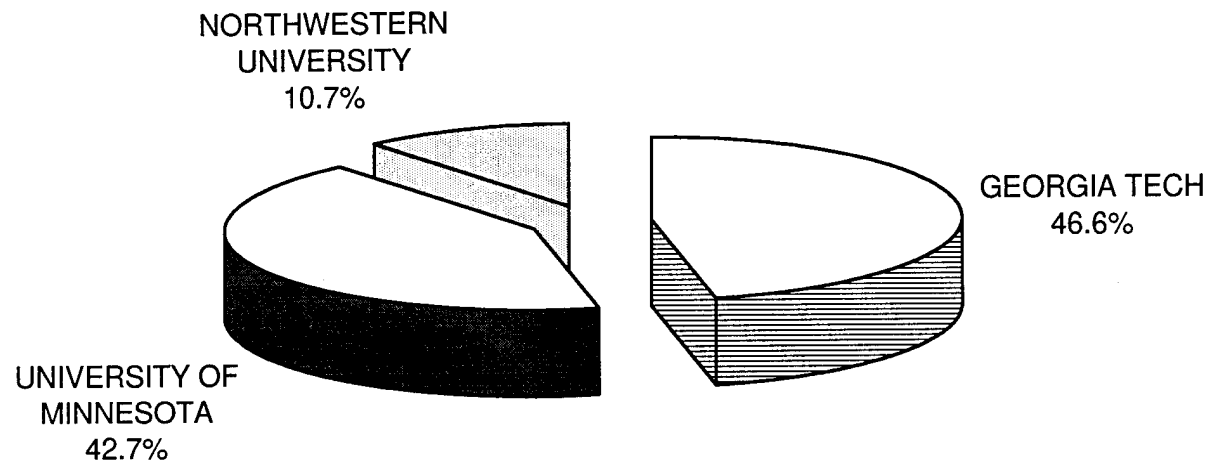


**Figure 2** Allocation of M-URI Year 1 Funding (Participating Institutes)

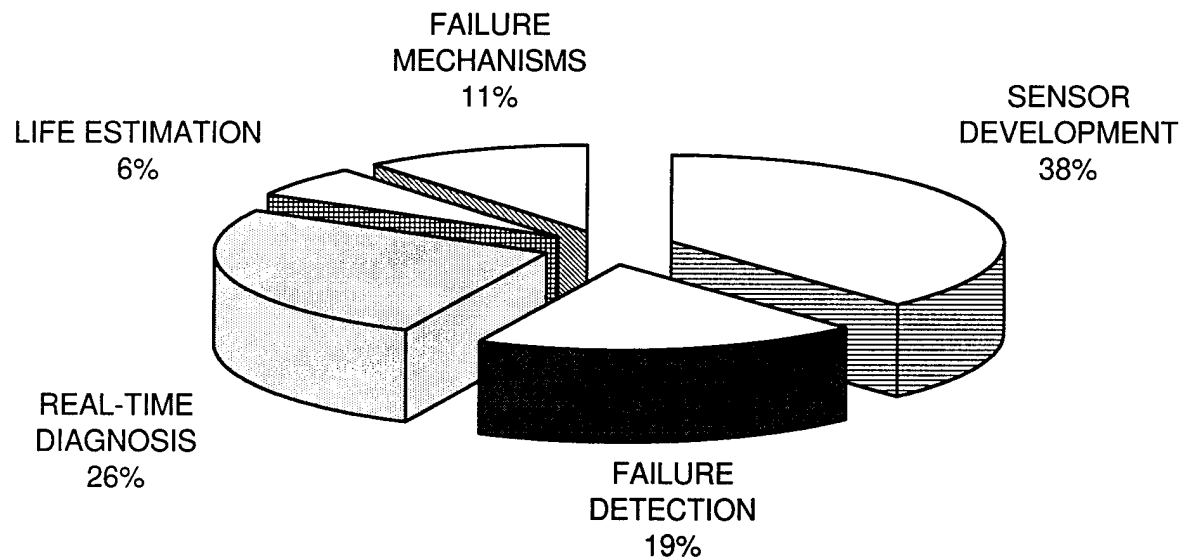


**Figure 3** Allocation of M-URI Year 1 Funding (Research Focus)

## **2. RESEARCH ACCOMPLISHMENTS and PLANS**

---

The MultiUniversity Center for Integrated Diagnostics is focused on providing a meaningful program of research for use in minimizing the impact and or occurrence of *critical failures* in mechanical systems, including vehicle platforms and machinery. In the Predictive Maintenance community, a failure is identified as critical when it results in serious injury, loss of life, or significant financial burden.

As discussed in Section 1, a multidisciplined team has been formed to address an assortment of research projects, organized according to thrust areas that overlap in responsibility. This enables the faculty and staff to focus on a particular integrated diagnostic need, while maintaining an awareness of the progress achieved through the overall program.

During this reporting period, critical components have been identified, from which the mechanism of failure is to be better understood through the development of failure models. These models can serve as a guide in the selection and development of sensors to detect faults and pending failures. Effort has been placed on micro-sensor development, and achieving the means to analyze and correlate reliable sensor output for operator use.

The following pages summarize the accomplishments and future plans for the integrated diagnostic research pursued during this reporting period. Project titles, associated with a particular thrust area, are listed below, and are identified with their respective coordinators in the organization diagram of Figure 4.

### **I. Failure Detection and Identification**

1. Study of Acoustic Emission and Transmission from Incipient Fatigue Failure
2. Crack Detection in Annular Structures by Ultrasonic Guided Waves
3. Flaw Detection and Characterization (Ultrasonics)
4. Detection of Mechanical Seal Failure in Turbomachinery

### **II. Failure Prediction Methodology**

1. Structural Fatigue Investigation
  - Stress Analysis and Stress Intensity Factor Solutions for Cracks
  - Characterization of Fatigue Behavior and Mechanisms
  - Remaining Life Estimation Methodology
2. Failure Prediction Methodology using First-Order Reliability Method (FORM)

### **III. Direct Sensing, Analysis, and Real-time Diagnosis**

1. Integrated Microsensors for Aircraft Fatigue and Failure Warning
  - Microsensors
  - Signal Processing
2. Eddy Current Microsensors for Integrated Diagnostics
3. Magnetic-Electrical-Impedance Tomography
4. Acoustic Emission Modeling for Integrated Diagnostics
5. Monitoring of Sub or Higher Harmonic Oscillations in Rotating Machine Elements
6. Dynamic Metrology as a Wear Diagnostic

## Program Organization Diagram

*Coordinators identified in parentheses*

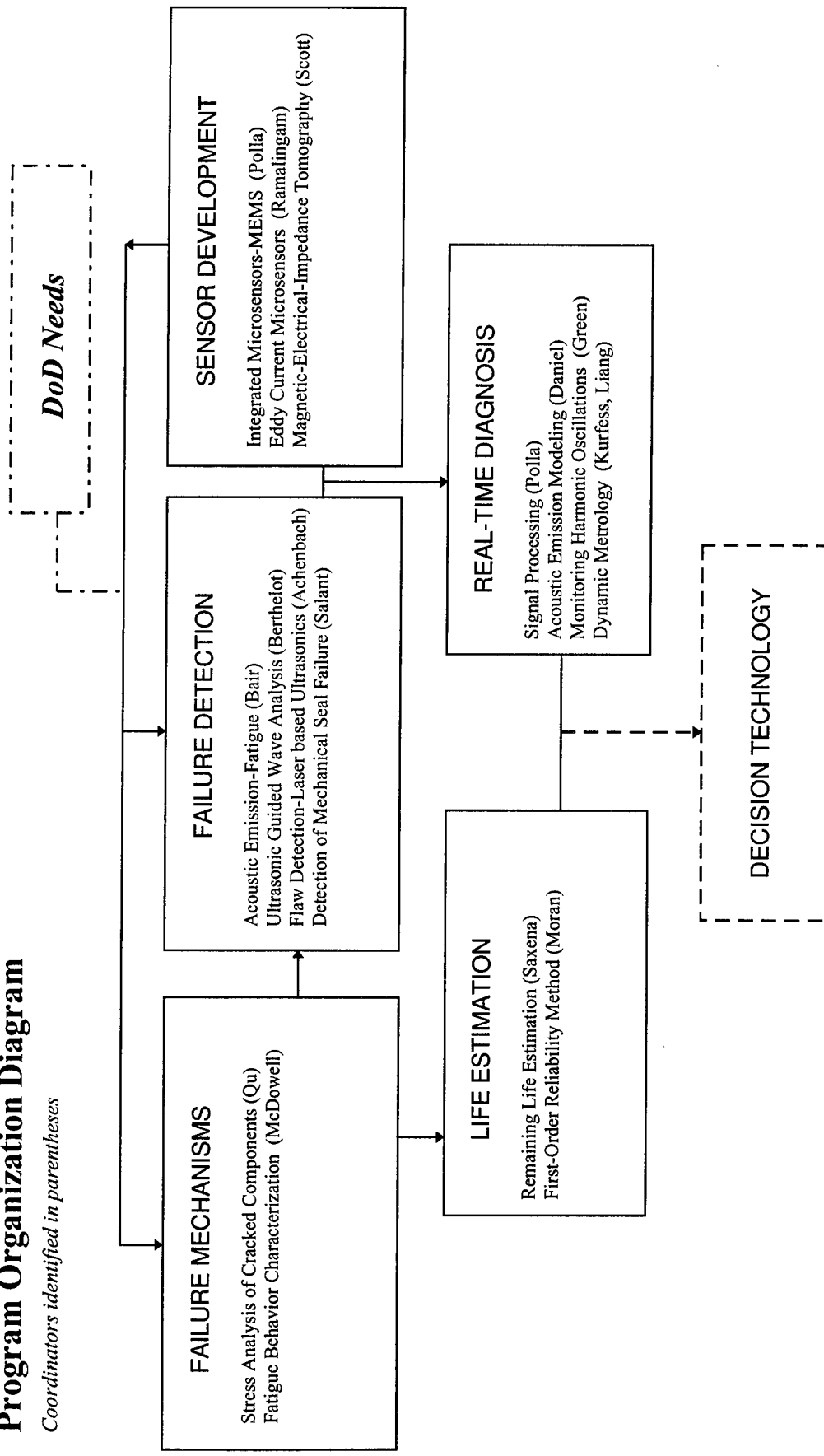


Figure 4

### **2.1.1 STUDY OF ACOUSTIC EMISSION AND ACOUSTIC TRANSMISSION FROM INCIPIENT FATIGUE FAILURE**

Co-investigators: Scott Bair, Jacek Jarzynski, Laurence Jacobs (Georgia Tech)

#### **Overview**

The objective of this project is to develop both active (ultrasonic transmission) and passive (acoustic emission detection) techniques to determine incipient failure in vehicle platform and machinery components. During the first year, this research focused on acoustic emission methods; these techniques offer a distinct advantage over other methodologies because they allow for the real-time monitoring of in-service components. However, to be effective, acoustic emission methods must be able to identify an emission source and characterize the severity of the damage associated with that source. One of the primary difficulties in the application of acoustic emission techniques is in interpreting and categorizing the large quantity of data and in removing erroneous information. As a step in that direction, this research effort is focused on developing both experimental (including a variety of test specimen geometries, materials and loading platforms) and theoretical procedures to quantify acoustic emission sources.

This first year of the integrated diagnostic acoustic emission and transmission program has resulted in the acquisition of a new laboratory, with an adjoining machine shop, devoted to Integrated Diagnostics, as well as the purchase of a complete data acquisition system. A lathe was purchased to serve as a power source and test bed for an improved Non-Rotating Bending Beam Tester. This tester along with the data acquisition system was utilized to design, test, and perfect new sensors for detecting acoustic emission and software for capturing and recording bursts of acoustic emission. A delay rod was constructed to evaluate the response of novel sensors to well-controlled stimulus.

A broad-band polymer film ( $\text{PVF}_2$ ) sensor was found to be most promising as far as sensitivity and rejection of RF pick-up. A miniature (<1mm), high gauge-factor semiconductor strain gauge was evaluated for use both as a static strain sensor and acoustic detector. Its frequency response was observed to 50 kHz.

Specimens were prepared for the Non-Rotating Bending Beam Tester in alloy steel, stainless steel and aluminum. Cycles to failure were found to be repeatable. Acoustic emission bursts were always obtained after one-half to two-thirds life and can be discriminated from noise. Acoustic emission bursts are stored on hard-drive and will be forwarded to the Minnesota Signal Processing Group (see Section 2.3.1.2).

#### **Accomplishments**

##### *Equipment*

A new Non-Rotating Bending Beam Tester was designed and constructed. This device applies a cyclic strain to a cylindrical specimen so that acoustic sensors may be evaluated and wave capturing techniques can be developed. These sensors will be utilized later on well controlled fatigue tests where the progress of defect growth is known. The new tester is shown schematically in Figure 5. This device is useful in that a large number of large strain amplitude cycles can be accumulated in a short time. The specimen shown in Figure 6 does not rotate so that electrical connection to the sensor is simple. This tester was improved by the addition of a spherical bearing to the rotating head as shown in Figure 5 and in greater detail in Figure 7. This spherical bearing reduces the moment applied at the rotating head and allows for variable strain amplitude.

A delay rod was constructed for sensor evaluation. A PZT driver launches a burst form one end in of the rod. The spacial separation of the driver from the test sensor allows for temporal separation of the sensor acoustic signal from electromagnetic pick-up from the driver.

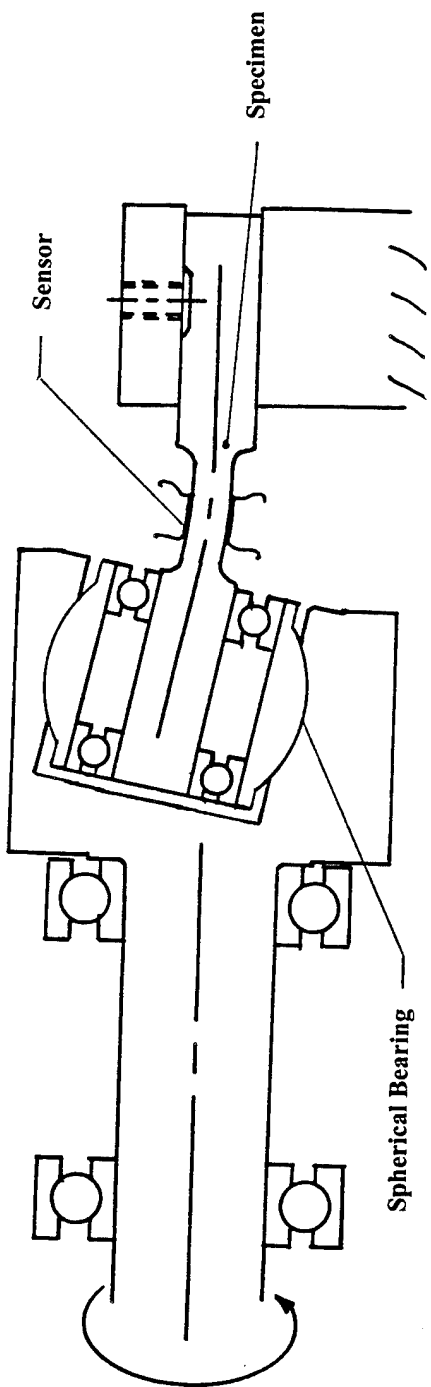
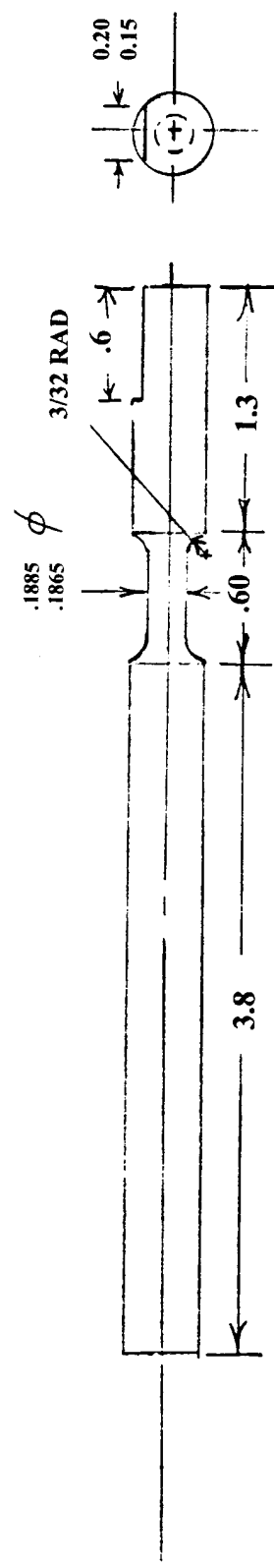
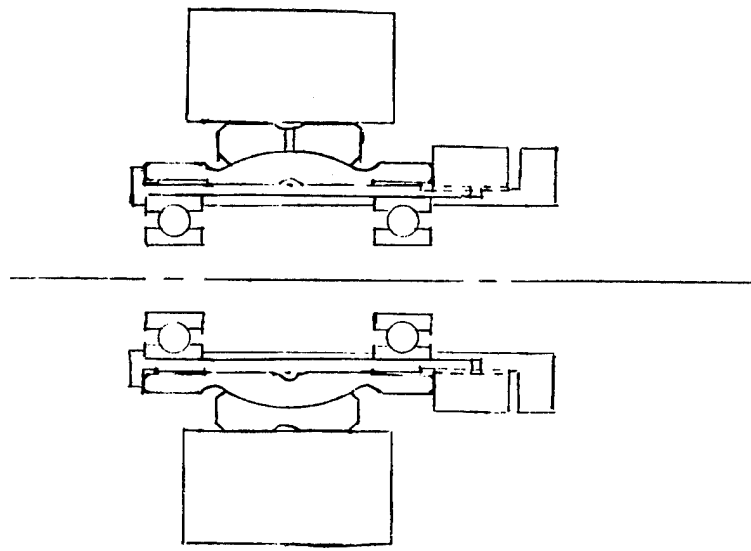


Figure 5 Schematic of Bending Beam Fatigue Tester



**Figure 6** Non-rotating Test Specimen  
(Dimensions in inches)



**Figure 7** Fatigue Tester Head Assembly

A digital storage oscilloscope (Tektronix TDS 420A) with a sample rate of 100 Ms/s and four channels of 128ks each was obtained. The scope was interfaced with a 486 PC running Lab View software. A program was written to capture and record waveforms from a sensor when the scope was triggered.

#### *Sensor Design And Evaluation*

The long term objective of this effort is to develop sensors and sensor arrays which can measure acoustic emission and acoustic transmission in structures of arbitrary shape, for example, structures with curved surfaces. Sensor arrays will be needed to focus on components which are known to be subjected to high levels of strain or stress and which, therefore, are more likely to fail.

During FY 95 one of the main requirements was the need for sensors on samples used in the bending beam fatigue tester. These samples are metal rods, and the region where fatigue failure occurs, and where transducers are attached, has a small diameter (high curvature) of 0.187 inches. The transducers developed for this application use thin, piezoactive plastic film elements (PVF<sub>2</sub> - polyvinylidene chloride). The PVF<sub>2</sub> film can be cut to any shape, and can be bent to conform to curved surfaces. Rectangular strips (6 x 3mm) of PVF<sub>2</sub> were used, with a backing lead mass to increase sensitivity. The transducers were attached to the metal samples with a viscous compound (shear wave couplant). Good performance was obtained with the above transducers. One advantage of the PVF<sub>2</sub> transducers is the broad bandwidth - from dc to above 10 Mhz. However, the capacitance of the PVF<sub>2</sub> elements is low and it is necessary to place a preamplifier close to the element to drive the transmission line which carries the signal to the data acquisition system.

The piezoactive plastic transducers are limited in the temperature range over which they can operate - the Curie temperature of PVF<sub>2</sub> is ~ 90 °C. This is not a limitation in the laboratory, where the measurements are made at room temperature. However, it may be a limitation for field applications. Therefore, piezoelectric ceramic (PZT) elements were also studied, as an alternative to PVF<sub>2</sub>. PZT ceramic is the standard sensor material used in transducers for ultrasonic nondestructive testing. It has high sensitivity to stress signals and a Curie temperature of ~ 300 °C. However, this material is hard, brittle, and cannot directly conform to a curved surface. PZT elements were thin (resonance frequency ~ 12Mhz), rectangular (2 x 6mm), and they were mechanically coupled to the fatigue test sample with the viscous shear wave couplant. Strong signals were received with the PZT transducers but they were more sensitive, than the PVF<sub>2</sub>, to external noise, particularly electromagnetic pickup. Work is continuing to improve the transducer design to reduce pickup.

Another type of sensor which was evaluated in FY95 was a high gauge-factor semiconductor strain gauge. The advantage of this sensor is that it is inexpensive, it is small, thin and can be attached to curved surfaces. Another important advantage is that this type of sensor can be used to simultaneously monitor both static strains and acoustic emission (AE) in a structure. The strain gauge sensors were tested using the setup shown in Figure 5 and described in the previous section (*Equipment*). The initial tests covered a frequency range up to 50 kHz, and it was found that the strain gauge could detect acoustic signals in this frequency range. However, the sensitivity (output voltage) of the strain gauge was significantly lower than the sensitivity of a PZT transducer. The evaluation of the strain gauge sensor is continuing with tests over a wider frequency range and direct AE measurements with the gauge sensor attached to a fatigue test sample.

## **Plans**

### *Interface With Structural Fatigue Group*

The Structural Fatigue Task Group (see Section 2.2.1) has developed a test specimen to address elements of structural fatigue and remaining life estimation. We intend to collaborate with this group as a means of identifying and tracking acoustic emission signals from fatigue cracks. The fatigue specimen geometry has been determined, so the current effort is in determining an experimental Green's function that removes the influence of this specimen geometry from a measured acoustic emission waveform. This transfer function is being developed from waveforms created by a repeatable point source (either a pencil lead break or laser pulse), measured at different locations.

### *Interface with Signal Processing*

The Signal Processing Group (see Section 2.3.1.2) requires realistic waveforms for the development of signal processing algorithms. We will begin to transfer our captured waveforms this month.

### *Source Model*

A measured acoustic emission signal depends upon three factors: its source; wave propagation from the source to the receiver (component geometry); and receiving sensor and instrumentation. Each of these three elements must be understood in order to effectively identify and characterize measured acoustic emission waveforms. The source of an acoustic emission waveform determines its initial shape and frequency content; acoustic emission waveforms are transient and broad band in nature. In this project, the integral equation method is being used to develop an acoustic emission source model created from a fatigue crack.

### *Evaluation of New Sensors*

Several promising new types of sensors have been identified and will be evaluated in FY96. One new sensor is the optical fiber array sensor shown in Figure 8. The potential advantages are freedom from electromagnetic pickup and high sensitivity. The fiber array consists of short lengths of fiber bonded to a thin plastic base which is coupled mechanically to the test sample. Strains due to acoustic waves are transferred to the fiber and change the phase of the light through the fiber. This phase change is detected by intersecting the signal light beam with a second reference beam. The optical fiber array is a narrowband sensor with peak response at the frequency at which the bonded length of fiber is equal to one half of the trace wavelength (along the sample surface) of the acoustic wave in the sample. The fiber array is also directional, with peak response in the direction for which the trace wavelength of the acoustic wave matches the spacing between adjacent bonded lengths of fiber.

The loops of fiber between the bonded lengths provide stress relief to ensure that the optical phase shift due, for example, to an instantaneous extension of the bonded length of fiber is not canceled by an opposite phase shift due to compression of adjacent fiber. In addition to frequency and direction, the sensitivity of the optical fiber array is proportional to the number of bonded fiber segments. Initial estimates show that with six bonded segments the minimum detectable displacement in the test sample is  $\sim 5 \times 10^{-14}$  meters.

Another new type of sensor which will be evaluated is the thin film aluminum nitride (AlN) sensor. This study will be done in collaboration with the research group of Dr. S. Ramalingam at the University of Minnesota (see Section 2.3.2). They have developed techniques for assembly of these sensors. The AlN sensor is potential replacement for PVF<sub>2</sub> in field applications. The advantages of the AlN sensors are low cost and the ease of fabrication of both single sensors and arrays of sensors.

Also, new developments in the area of PZT sensors will be investigated. There have been major developments recently in the fabrication of plastic - PZT composite sensors. These sensors retain the very high sensitivity of PZT but do not have the disadvantage of being hard or brittle. They can be easily fabricated to conform to curved surfaces. Also, sensors arrays can be easily fabricated.

### *Failure Detection and Identification*

**Responds to strains in the plane of the sample surface. Maximum response at the frequency for which the trace wavelength of the incident sound matches the periodicity of the fiber elements bonded to the surface.**

**Advantages:**

**High sensitivity**

**Immunity to electromagnetic noise**

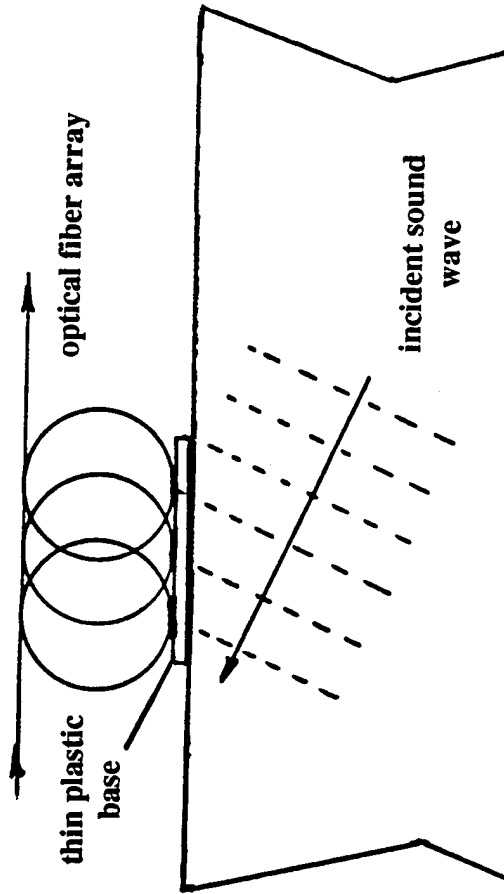


**Figure 8 Optical Fiber Receiving Array**

## 2.1.2 CRACK DETECTION IN ANNULAR STRUCTURES BY ULTRASONIC GUIDED WAVES

Co-investigators: Yves Berthelot, Jianmin Qu, Laurence Jacobs (Georgia Tech)

### Overview

The objective of this research effort is to develop an ultrasonic technique that is particularly well adapted to the detection of cracks in annular structures. Crack-induced failure often occurs in annular structures (such as those present in the rotor hub, connecting link, and pitch shaft of the H-46 helicopter) and they often occur at places that are inaccessible to transducers for conventional ultrasonic inspection. Since conventional ultrasonic methods can detect only cracks in the immediate vicinity of the transducer, limited access to the part means that, in general, conventional methods are ineffective in detecting cracks in annular structures.

Instead, "ultrasonic guided waves" are being used to inspect an annular structure. The main advantage of this technique over the conventional transmission technique is that (i) one can detect cracks that are far from the transducer (and therefore partial access to the part is perfectly adequate), and (ii) it is much faster because one inspects the entire structure, or a large portion of it, at once. The main disadvantage of the technique is that ultrasonic signals are much more difficult to interpret than those obtained with the conventional technique.

The basic idea behind ultrasonic inspection by guided waves is extremely simple. If a transducer generates a signal at point A in a waveguide (see Figure 9), and another transducer receives that signal at point B further down the waveguide, the received signal will contain information about the path along which it traveled. Hence, the presence of a crack in the waveguide should definitely affect the received signal. The main challenge is that there is not a unique path between A and B. Many paths are possible, depending on frequency of the source, the thickness of the waveguide, and also its curvature. Therefore, the received signals are in general of a very complicated nature. It is however crucial to fully understand the complexity of these signals if one is to extract information about the presence of cracks along the path between A and B. The complexity of this information is embedded in what are called the "dispersion curves" of the structure. The main challenge of the proposed research is to somehow put most of the ultrasonic energy in a path (~ a mode) that is particularly appropriate for crack detection.

### Strategy

As indicated below, the project is divided into three partially overlapping phases.

- Phase I (June 95-Dec. 96): Basic research

Ideal annular structure:

Establish the feasibility of using guided wave techniques in thick annular structures. i.e., develop theory, experimental facility, and signal processing capability to verify the concept: controlling the generation and detection of a (few) ultrasonic mode(s) that are particularly appropriate for crack detection.

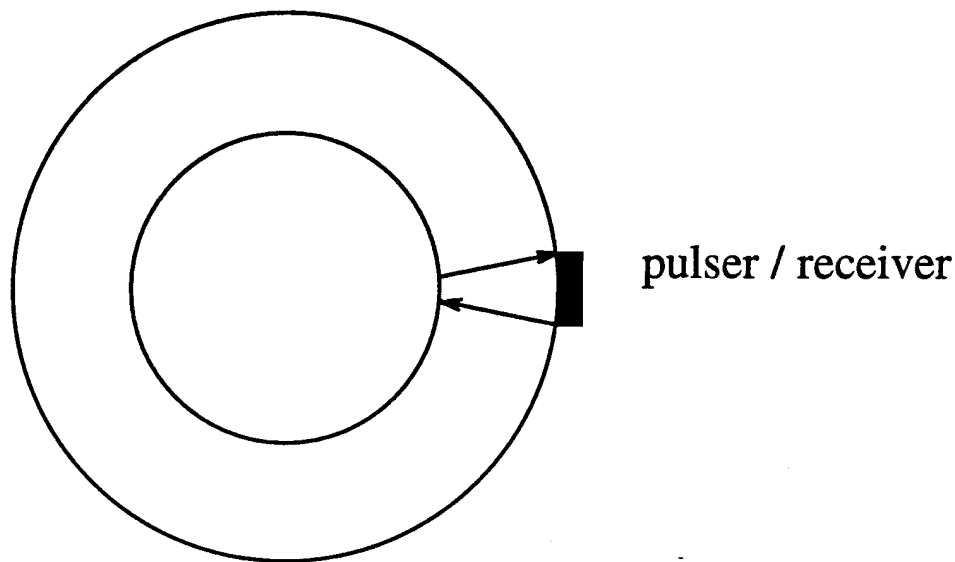
- Phase II (June 96-June 97): Semi-basic research

Crack detection - effect of inner shaft - partially annular structures:

Detection of simulated cracks; effects of crack size, location, etc. Scattering of ultrasound by cracks in annular structure. Finite element modeling. Effect of inner shaft and lubricant. Applicability of the method with partially annular structures.

### Failure Detection and Identification

(a) Conventional ultrasonics



(b) Ultrasonic guided waves

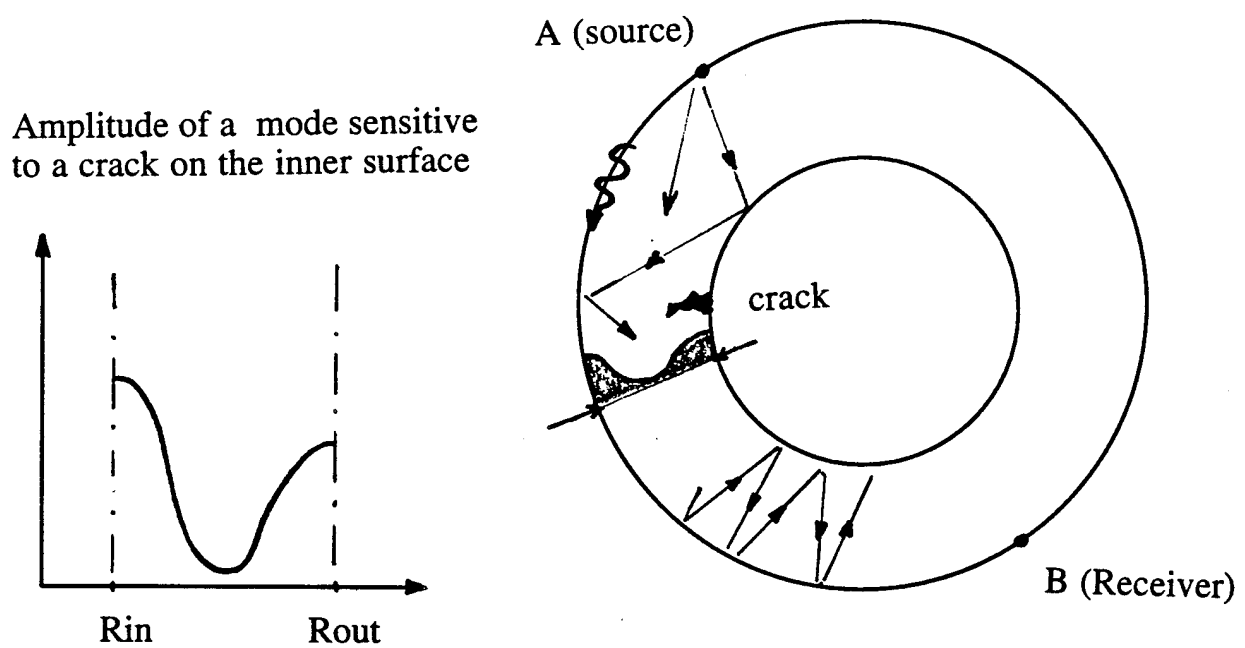


**Figure 9** : Two concepts for ultrasonic inspection of annular structures: (a) transmission / reflection; (b) guided waves with various propagation modes between A (source) and B (receiver)

- Phase III (March 97-March 98): Applied research  
Application to some real parts:

Crack detection by ultrasonic guided wave techniques in some real parts. Fine-tune the methodology. Determine system limitations. Toward a laser-based system for onboard real-time monitoring.

## **Accomplishments**

The “proof-of-concept” for using ultrasonic guided waves in annular structures has been demonstrated in a series of experiments with a simple structure. In particular, we have validated on a simple annular ring the premise that the modal content of the ultrasonic signals can be controlled by using variable angular wedges at the source and the receiver and that it can be somewhat optimized for crack detection.

A methodology has been designed and successfully implemented to determine and control the modal nature of ultrasonic signals in the simple structure. The methodology integrates both experimental data and signal processing techniques with theoretical and numerical predictions.

The methodology is shown in Figure 10. It consists in four basic steps: Step 1 is the experimental data collection; Step 2 is the experimental mode determination (number and group velocities); Step 3 is the actual mode determination by comparison with the dispersion curves; and Step 4 is the calculation of the amplitude distribution within the structure to assess its effectiveness in crack detection. The methodology and the results are discussed in more detail below.

### *Methodology*

Experimental waveforms are recorded with the ultrasonic pulser/receiver system which sends a short pulse whose frequency content is broad but peaks around 0.5 MHz. By changing the wedge angles of either the source or the receiver, one can control the complexity of the signal, i.e., one can visually reduce the number of modes present in the received signal. To determine and control precisely the modal nature of the signal, a wavelet transform is first applied to the signal to obtain a time-frequency representation of the signal. Then, the arrival times of various modes are determined, at a given frequency, so that one can determine the number of modes present in the signal and measure their corresponding group velocities, (and therefore determine also their phase velocities). To identify which modes are present in the signal, it is necessary to compare with theoretical predictions from the dispersion curves analysis. Because of the importance of this step, a large effort has been devoted to deriving the appropriate dispersion relation for thick annular structures, and taking limiting two cases: (I) the case of a thin annulus, which reduces the dispersion relation to the known case of the Donnell thin shell theory; and (ii) the infinitely large radius of curvature, which reduces the dispersion relation to the known case of plate theory. After validation of the dispersion relation for thick annular structures, it is possible to compute the predicted group (or phase) velocities of each mode at a given frequency and compare these velocities with the values measured experimentally. The last step of the method consists in evaluating whether the modes present in the signal are sensitive to the presence of a crack. To do so, it is necessary to determine the amplitude profile of the ultrasonic waves within the structure and determine whether it contains sufficient amplitudes near the inner surface (where crack are expected to form) and near the outer surface (where the receiving transducer is located). This is achieved by the method of normal mode decomposition for transients, a computationally intensive but powerful technique.

## **experiment**

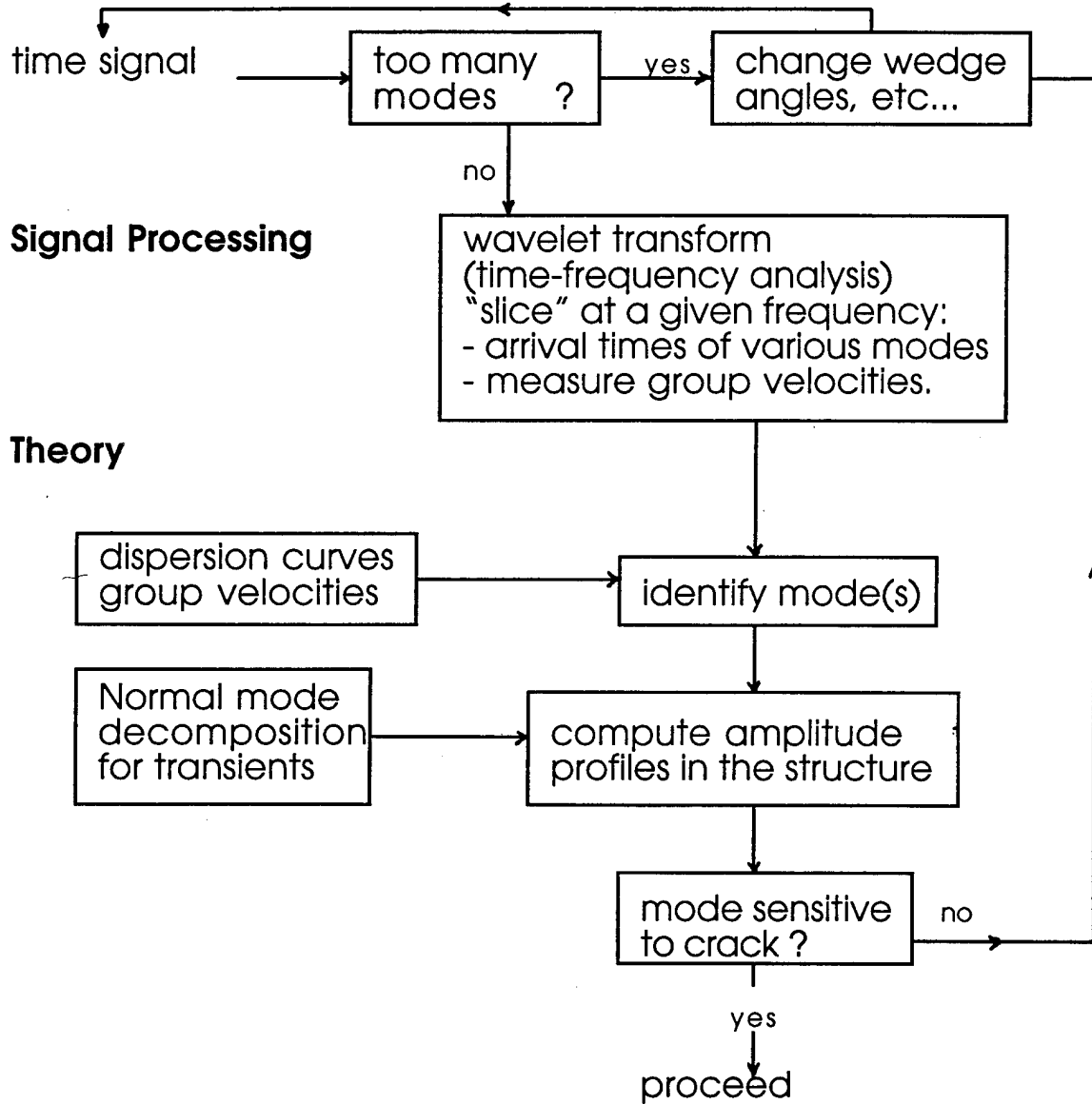


**Figure 10** Methodology for mode selection and control with ultrasonic guided wave inspection

### *Experimental Facility*

The experimental setup is shown in Figure 11. A pulser/receiver (Panametrics 500 PR) is used to send and receive ultrasonic signals in a simple annular structure made of stainless steel. A variety of piezoelectric transducers can be used for generation and detection: standard angle beam transducers (0.5, 1.0, and 2.25 MHz), variable angle wedges (0° to 50°), and also shear wave transducers (1.0 MHz). For non-single pulse excitation, one can use a tone-burst generator instead of the pulser/receiver. The data is then preamplified, filtered and acquired on an oscilloscope (TDS 420). It is interfaced via a GPIB to a computer for data analysis and processing.

Also available in the same laboratory, under a different ONR contract, is a laser interferometric system capable of detecting both in-plane and out-of-plane displacements. At present the system is configured for low-frequency detection (kHz range) but it could easily be modified for ultrasonic inspection (MHz range). Such a non-invasive point measurement receiver would prove very useful in the present project, and the proposal modification is planned for Year 2.

### *Experimental Data Base*

A large data base of ultrasonic waveforms has been collected for (i) various source/receiver geometries (inside/outside surfaces at various positions), (ii) for various wedge angles of either or both the source and the receiver, and (iii) with various curvature matching pieces between the curved structure and the flat transducer. So far, almost all experiments have been conducted with the 0.5 MHz transducers because at higher frequencies the number of modes becomes quickly very large. Some experiments were also conducted with the tone burst generator instead of the pulser/receiver. Examples of a few waveforms, showing the modal complexity of the waveforms, are shown in Figure 12-14.

### *Wavelet Transform Analysis*

The wavelet transform (Morlet wavelet) was implemented and an example is shown in Figure 15. The top part is a contour plot of the time-frequency event, and the bottom part is a cut at about 0.5 MHz to identify clearly the two major modes present in the signal and determine their corresponding group velocities.

### *Dispersion Curve Analysis*

The dispersion equation for guided circumferential waves in an annulus of arbitrary wall thickness were derived from first principles. Analytical expressions of the dispersion equation for both in-plane and anti-plane wave motions are presented in the paper "Dispersion of Guided Waves in a Concentric Annulus." A numerical example of the dispersion curves are shown in Fig. 16. The parameters used in the calculation are  $C_L=5,600$  m/s,  $C_T=3120$  m/s,  $a=5.08$  cm, and  $b=6.28$  cm. The non-dimensional circular frequency,  $\varpi$ , and non-dimensional wavenumber,  $k^*$ , in the figure are defined as  $\varpi=\omega h/C_T$ ,  $k^*=kh$ , where  $h=b-a$ , and  $\eta=a/b$ .

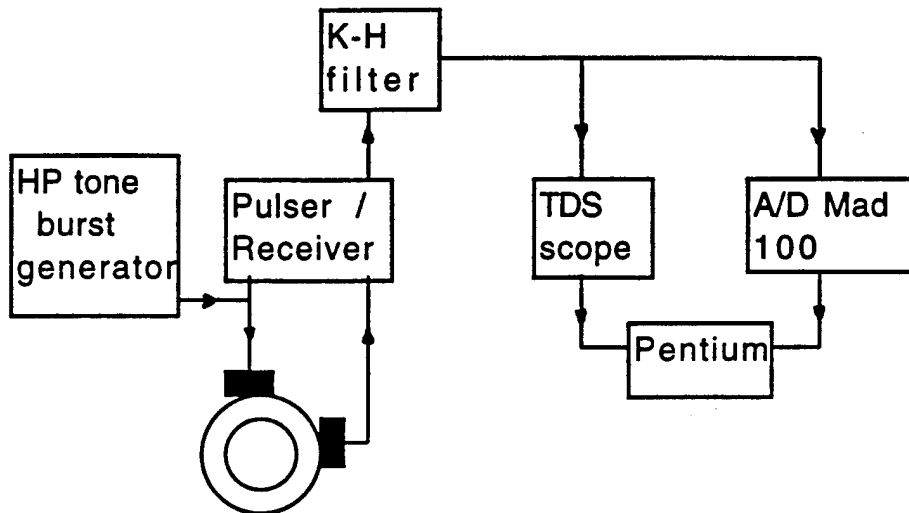
Asymptotic Limits: Two limiting cases were considered:

- (i)  $b \rightarrow \infty$  while keeping  $b-a=h$  (finite)
- (ii)  $a \rightarrow b$

It is conceivable that the dispersion equation should be reduced to that of a plate of thickness  $h$  for case (i), and that of a thin shell for case (ii). This has been confirmed for the anti-plane wave motion. Work is in progress to prove this for the in-plane wave motion.

### *Failure Detection and Identification*

## Experimental arrangement



Transducers: standard angle beam Xducers (0.5" x 1") -  
frequency: 0.5, 1.0, and 2.25 MHz



Variable angle beam wedges (0° to 50°)

normal incidence shear wave Xducers. (1MHz)

Mounting Pieces:

*also available: laser interferometric measurement of surface velocity*

Figure 11: Experimental Facility

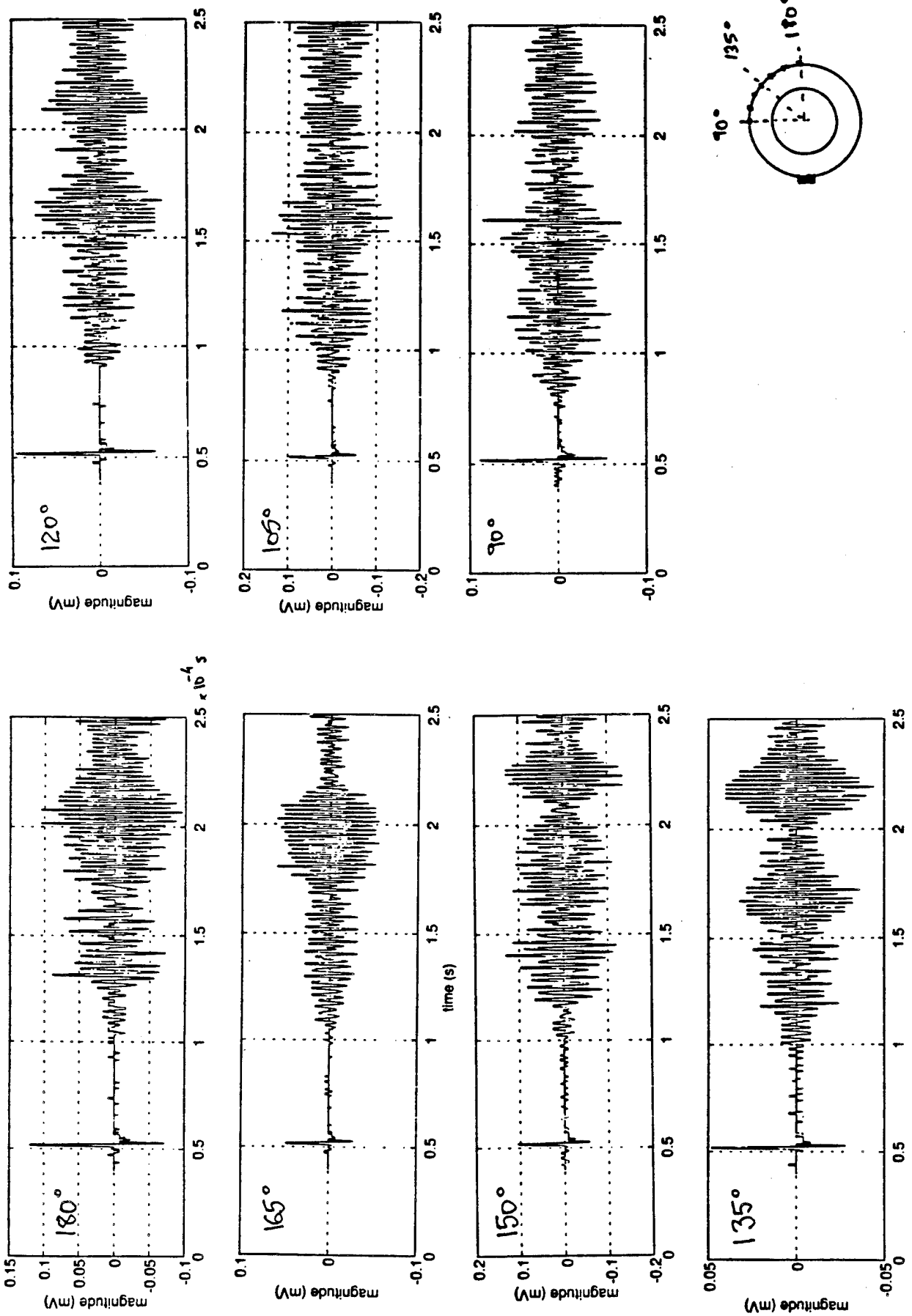
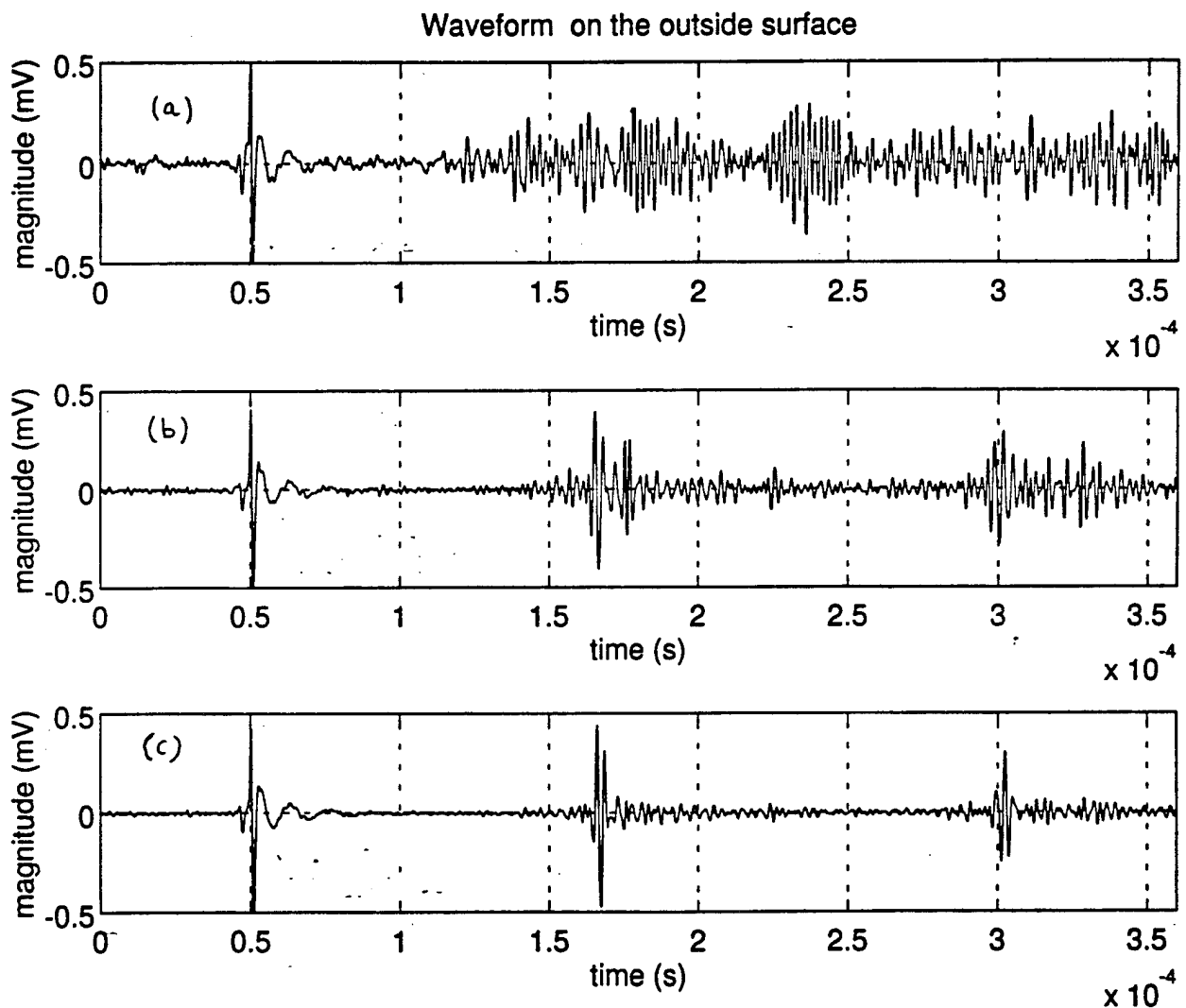


Figure 12 : Waveforms inside/outside the ring (no wedge) at  $f=0.5$  MHz



**Figure 13 :** Effect of the source/receiver wedge angles on the waveforms.  
 (a): no wedges; (b) source and receiver wedge angles =  $30^\circ$ ; (c) source wedge angle =  $30^\circ$ , receiver wedge angle =  $60^\circ$ .

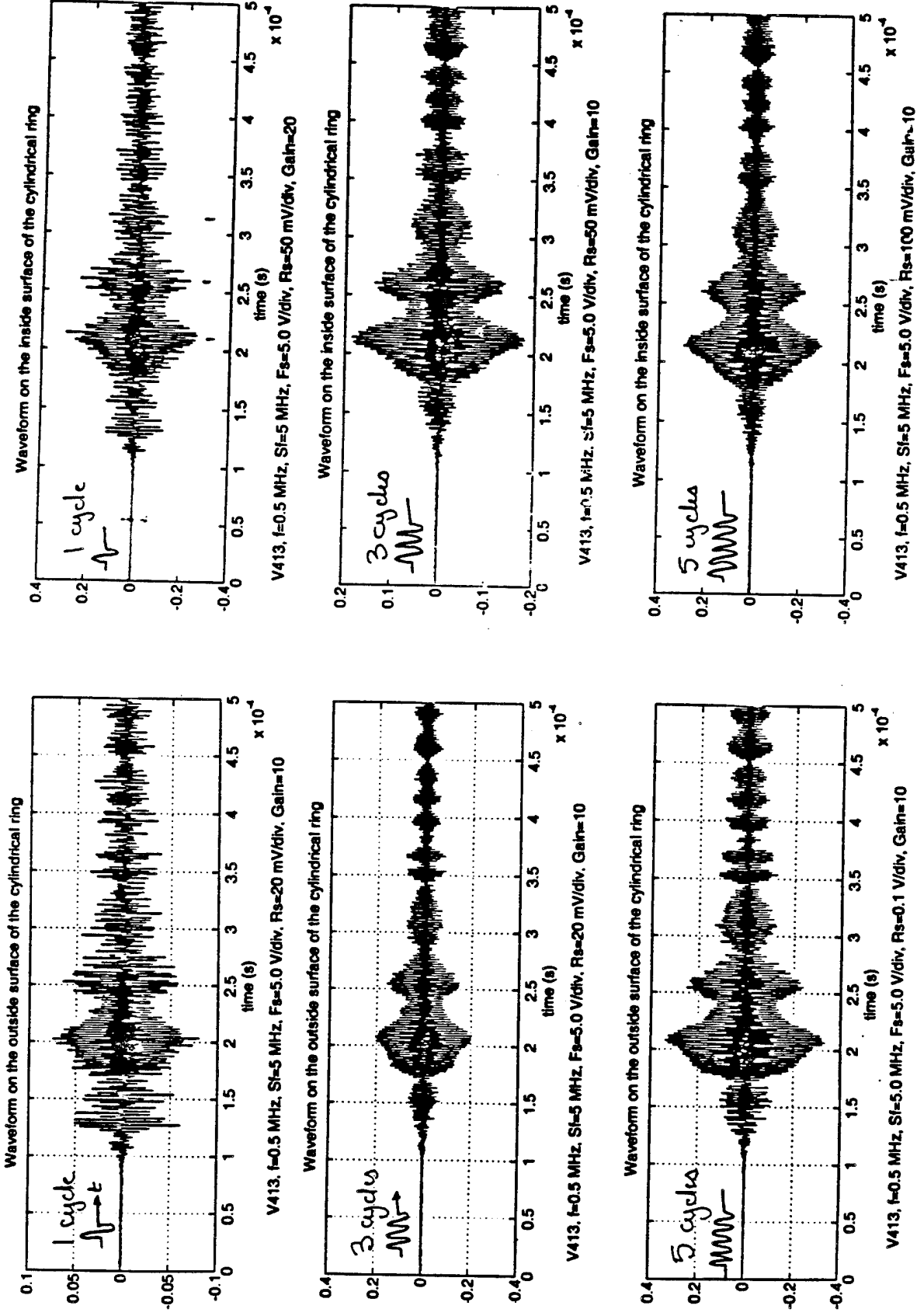
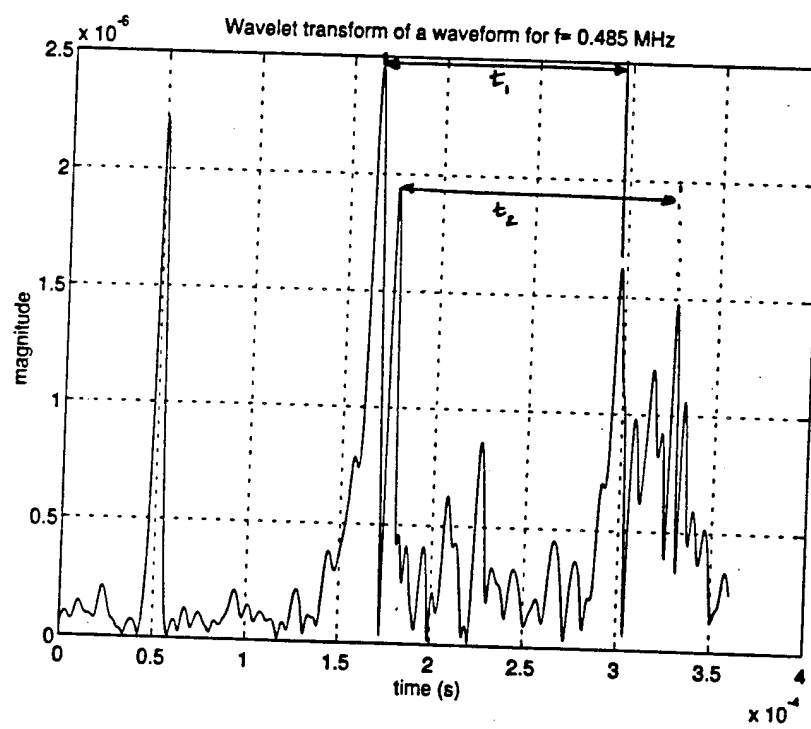
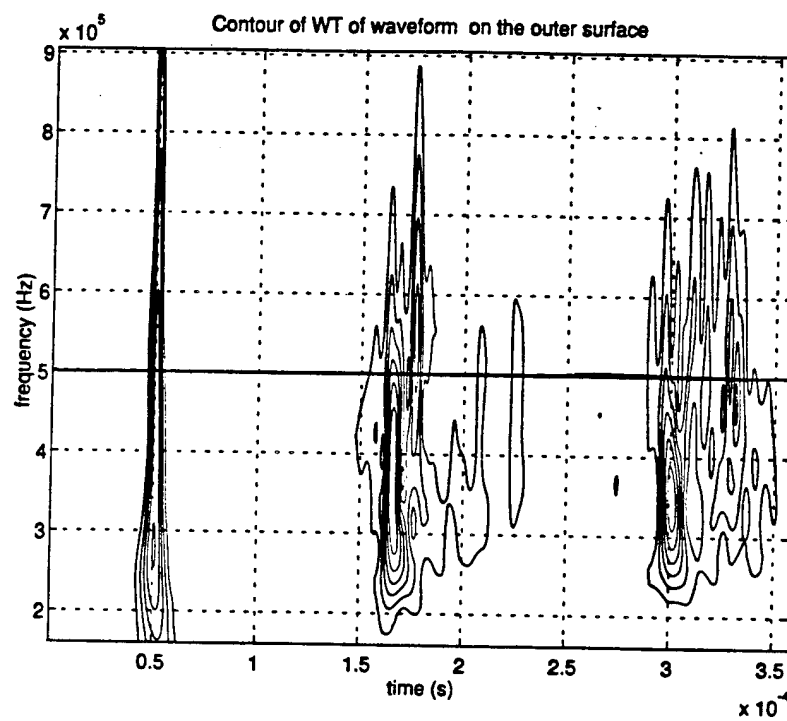


Figure 14: Waveforms with Tone burst generator. Up: 1 cycle; Middle: 3 cycles; Bottom: 5 cycles. Left waveforms measured on the outer surface. Right waveforms measured on inner surface. No wedges. Waveforms measured directly opposite to the source ( $180^\circ$ ).



**Figure 15 :** Wavelet transform. (a) top: contour plot; (b) Bottom: cut of contour plot at  $f \sim 0.5 \text{ MHz}$ .

$$\eta = 0.8089172$$
$$v = 0.2817$$

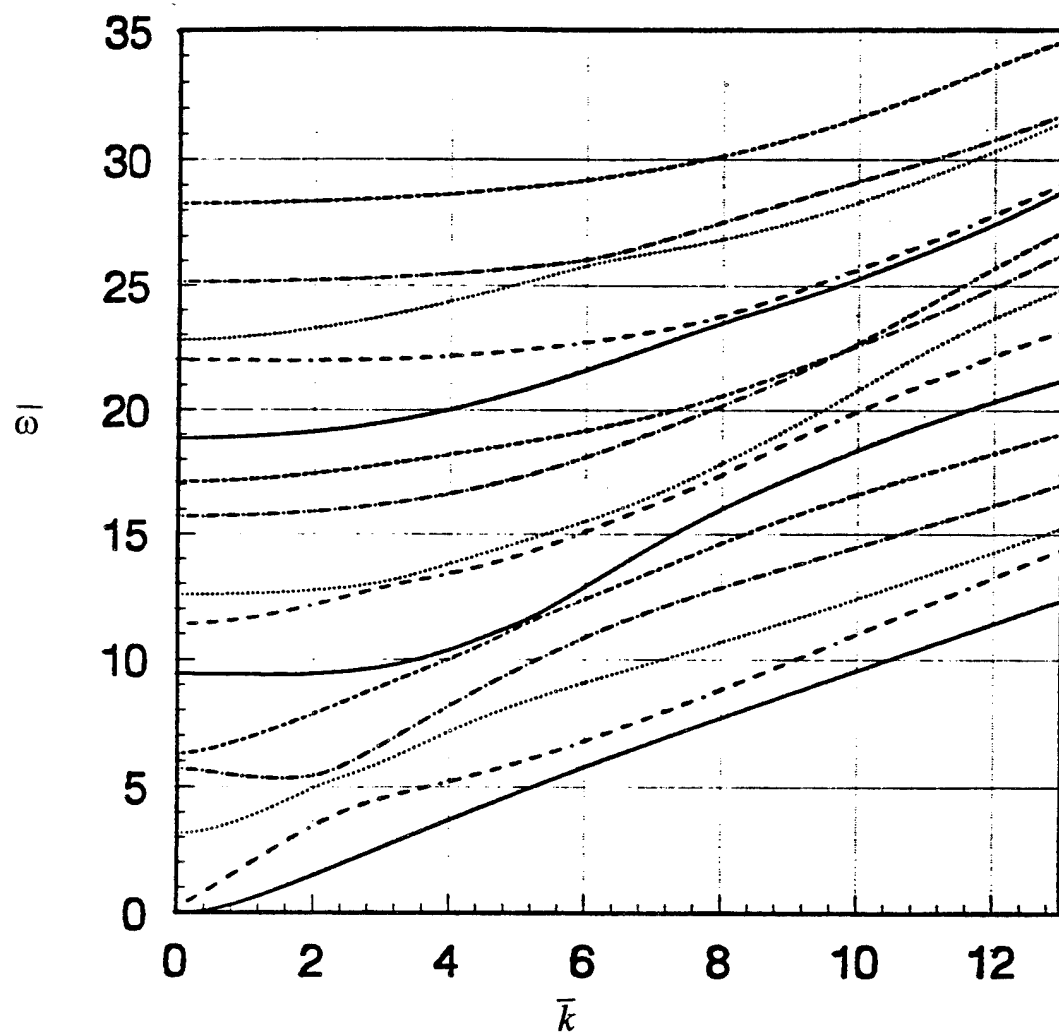


Figure 16 : Dispersion curves

### *Normal Mode Decomposition for Transients*

The displacement profile for each propagating mode was obtained. Using the parameters mentioned above, the displacement distribution of the first several modes were computed. At 0.5 MHz frequency ( $\omega=1208$ ), the amplitude distribution across the wall thickness is presented in Figure 17. It is noted that at this frequency, seven propagating modes are possible. Although the relative displacement magnitude between different modes are not meaningful, the distribution across the thickness provides us with clear idea of which mode should be generated in order to detect internal radial cracks. For example, the first mode (Fig. 17a) is not suitable for it has almost zero amplitude near the inner wall, which will not be able to interact with the internal radial cracks. The second mode (Fig. 17b) has higher amplitude at the inner wall, but its amplitude is very low at the outer wall. This may not be acceptable either because the signal needs to be detected on the outer wall.

## **Plans**

### *Uncracked Annulus*

- Complete data analysis for efficient mode selection and control.
- Develop computational algorithm for the evaluation of time-dependent (transient) guided circumferential waves in the annulus.
- Compare numerical predictions with measurements.
- Identify range of modes and provide guidance on how to generate them.
- Repeat experiments in light of theoretical/numerical predictions.
- Develop the laser interferometric capability for ultrasonic detection (in-plane and out-of-plane surface motion on inside and outside surfaces); if available, also develop capability for laser generation of ultrasound.

### *Partial Annulus*

- Perform experiments to assess the feasibility of the method with structures that are partially annular. (See Figure 18).

### *Cracked Annulus*

- Develop a boundary integral equation method to study the scattering of guided circumferential waves by an internal radial crack.
- Identify wave modes that are most sensitive to the presence of cracks.
- Identify the transducer locations for optimal crack detection.
- Identify the minimum detectable crack size.
- Perform experiments on crack detection in the simple annular ring, with simulated cracks (various sizes, positions, and shapes).

### *Annulus with a Shaft Insert*

- Derive the dispersion equation.
- Calculate the displacement profiles in the radial direction.
- Study the effects of lubricants between the shaft and the bearing.
- Perform experiments to determine the feasibility of using guided-waves ultrasonic inspection in annular structures with a shaft insert.

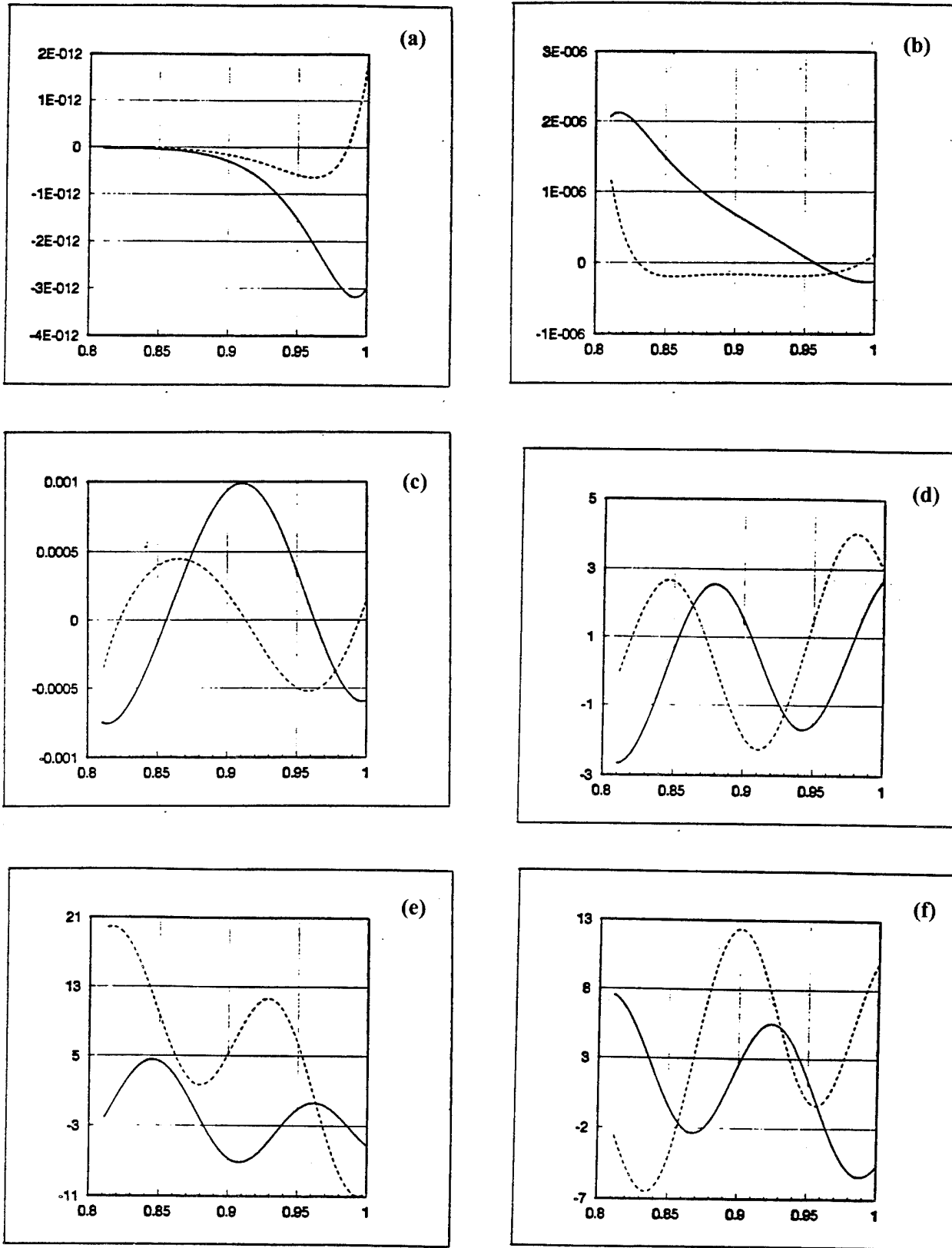


Figure 17: Amplitude profile within the structure from inner surface to outer surface.

First 6 of 7 Mode Shapes. ( $f=0.5$  MHz)

(Tangential Component ----- ; Radial Component ——)

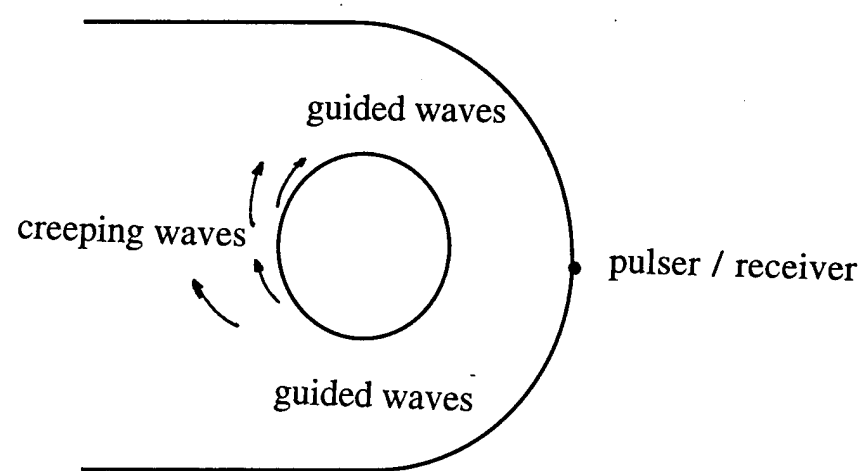


Figure 18 : Guided waves and creeping waves in a partially annular structure

### 2.1.3 FLAW DETECTION AND CHARACTERIZATION

Co-investigators: Jan D. Achenbach and J. Scott Steckenrider (Northwestern)

#### Overview

Surface acoustic waves are commonly used to nondestructively investigate the near-surface region of a solid component for cracks (and other defects). One particularly attractive method of generating and detecting such ultrasonic signals is the use of laser based techniques. By directing a high-energy pulse of light at the surface of interest, ultrasound is generated through the rapid thermal expansion of the surface material. Conversely, a propagating ultrasonic disturbance (whether actively or passively generated) can be detected and measured using laser interferometry. Conventional laser based ultrasonics (LBU) methods provide a number of advantages over conventional ultrasonic systems (e.g., point generation/detection, non-contact, high bandwidth, scanning ease, etc.). Although LBU has acceptable high-bandwidth sensitivity, further enhancement of that sensitivity is possible by narrowing the detection bandwidth, as the signal-to-noise ratio for such a shot-noise limited laser detection system is given by

$$SNR \propto \delta^2 \frac{P}{B} \quad (1)$$

where  $\delta$  is the ultrasonic displacement amplitude,  $P$  is optical detection power and  $B$  is the detection bandwidth. To maximize the gain achieved by bandwidth reduction, the generation bandwidth should be narrowed to match the detection bandwidth as closely as possible. (Narrowband generation and detection is also a particularly desirable alternative when inspecting for particular resonance modes or guided waves.) However, the most attractive feature of LBU for the current study (i.e., use in real-world applications) is its ability to use fiber optics for system miniaturization. This would allow access to even internal components, requiring only enough access to allow the passage of optical fibers to the surface of interest (i.e., only a few millimeters). Furthermore, the surface need not be polished, but need only to reflect light and be free of oil and debris (though this requirement is primarily critical only for the detection of ultrasound).

#### Approach

The objective of this research is to develop an ultrasonic technique for the in-situ detection and characterization of flaws in components of complicated structures without disassembling or physically touching the component. Other researchers [1,2] have used fiber optic systems to enhance signal strength and directivity for both bulk and surface waves. However, these systems use a "star-coupler" device in which a single pulse of light is focused into a single fiber, which is then distributed to a series of fibers, and are therefore limited by the amount of light which can be focused into a single fiber. The approach undertaken for the effort reported here employs a binary diffraction grating to separate the single laser pulse into ten equal but spatially separated laser pulses which can then be focused into ten individual fibers. Because the detection signal-to-noise ratio is proportional to the square of surface displacement, which is in turn directly proportional to optical generation power (within limits), this fiber optic method will improve detectability by two orders of magnitude. The resulting system will act both as a sensor in support of guided wave based defect detection and as an independent defect detection system.

## Accomplishments

The focus of effort for this first year has been the implementation of a fiber-optic narrowband ultrasound laser generation system. A Q-switched Nd:YAG laser operating at a 1064 nm wavelength with a pulse duration of approximately 10 ns and pulse energies of up to 300 mJ was used as the laser source. Initial experiments used a single large-core multi-mode optical fiber to determine the optical transmission efficiency through the fiber, as well as the ultrasonic generation efficiency at the output end, for a range of fiber diameters. Although the critical parameter for ultrasonic generation efficiency (light energy per unit illuminated area) is the same for all fiber diameters, input coupling efficiency falls off appreciably with smaller and smaller fibers. Thus, the smallest possible fiber diameter (which would have the greatest flexibility for internal component inspection and the lowest cost) that provided efficient input coupling was desired. It was determined that a 200  $\mu\text{m}$  core diameter fiber, while not able to transmit the full 10 mJ of energy for which it was designed (primarily due to spatial non-uniformity of the input laser pulse), was able to transmit sufficient energy to allow three types of ultrasonic generation: 1) maximum point source thermoelastic ultrasonic generation (in which the surface is undamaged), 2) maximum line source (5 mm long perpendicular to the desired direction of propagation/measurement) thermoelastic ultrasonic generation, or 3) ablative ultrasonic generation (in which the ultrasound is substantially stronger than that generated thermoelastically but the surface is slightly burnished). This would appear to be sufficient for the present work, and thus all results presented herein were obtained using 200  $\mu\text{m}$  core fiber. However, if longer line source geometries prove necessary, the 400  $\mu\text{m}$  fiber seems preferable to maximize generation efficiency.

A schematic illustration of the experimental arrangement for the 10-fiber system is shown in Figure 19. In this case, a binary diffraction grating is used to separate the input laser pulse into ten spatially separated (by 5.5 mrad) but equal energy pulses. (Note that because of higher order diffraction losses, each of the 10 pulses contains only 7% of the total input energy.) By placing a positive lens before the diffraction grating, these 10 pulses are focused into 10 fibers which are rigidly mounted on 1 mm spacings.

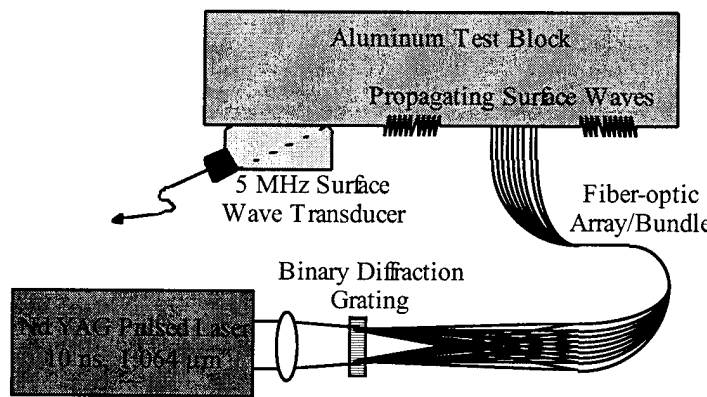


**Figure 19.** Schematic illustration of the optical fiber array laser generation system.

At the output end of the fiber array, one of two methods is used to generate surface waves, depending on the center frequency of the generation band desired. For a linear generation array, the frequency of generation parallel to that line is determined by the source spacing by the simple relationship

$$f = \frac{c_R}{d} \quad (2)$$

where  $d$  is the source spacing and  $c_R$  is the Rayleigh velocity in the material. For a material with a Rayleigh velocity of 2900 m/s, a spacing of 0.58 mm would be needed for generation at 5 MHz. Thus, if the material to be inspected and the desired narrowband center frequency are known, then the fibers at the output side can simply be spaced accordingly, and surface waves can be generated by placing the output array very near the surface (as shown in the figure).

Alternatively, if a range of frequencies are desired (or if the Rayleigh velocity of the inspected material is unknown) or if a non-point generation source is preferred, a series of lenses may be used at the output end of the fiber array (though this does require some additional space). In this case the center frequency is continuously tunable through a range of frequencies (limited by the relative numerical apertures of the fibers and lenses). Furthermore, line sources may be generated using cylindrical lens(es) to increase surface wave amplitude without causing surface damage. For the results presented below, the latter option was used to provide maximum flexibility.

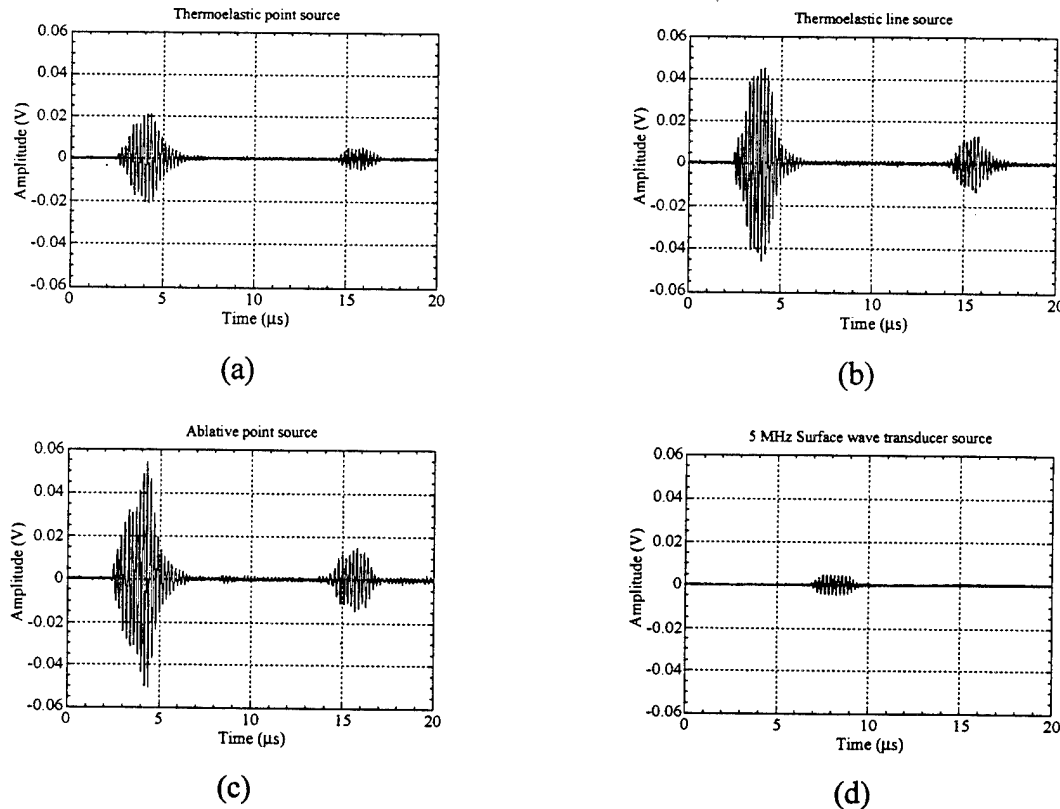


**Figure 20.** Plots of ultrasonic waveforms detected by 5 MHz surface wave transducer and generated by (a) thermoelastic point source, (b) thermoelastic line source, (c) ablative point source, and (d) second 5 MHz surface wave transducer.

Examples of the three source geometries (thermoelastic point source, thermoelastic line source, and ablative point source), optimized for a center frequency of 5 MHz and detected by an unamplified 5 MHz piezoelectric surface wave transducer, are shown in Figure 20. (The 10 pulses are not of exactly equal energy owing to a slight misalignment of individual fibers in the fixture at the input end.) Also shown is the waveform generated by a second 5 MHz piezoelectric surface wave transducer which was pulsed with a 10 cycle tone-burst. Figure 21 plots the power spectra from these waveforms, indicating the difference in ultrasonic generation efficiency. Clearly, all three laser generated sources provide a larger signal at 5 MHz than did the piezoelectric source. Interestingly, the ablative source and the thermoelastic line source provided approximately the same generation efficiency. However, this is likely because the detecting transducer was slightly wider than the line source length, and therefore was able to integrate the total surface wave energy generated (where a laser interferometric detection scheme would only detect at a point).

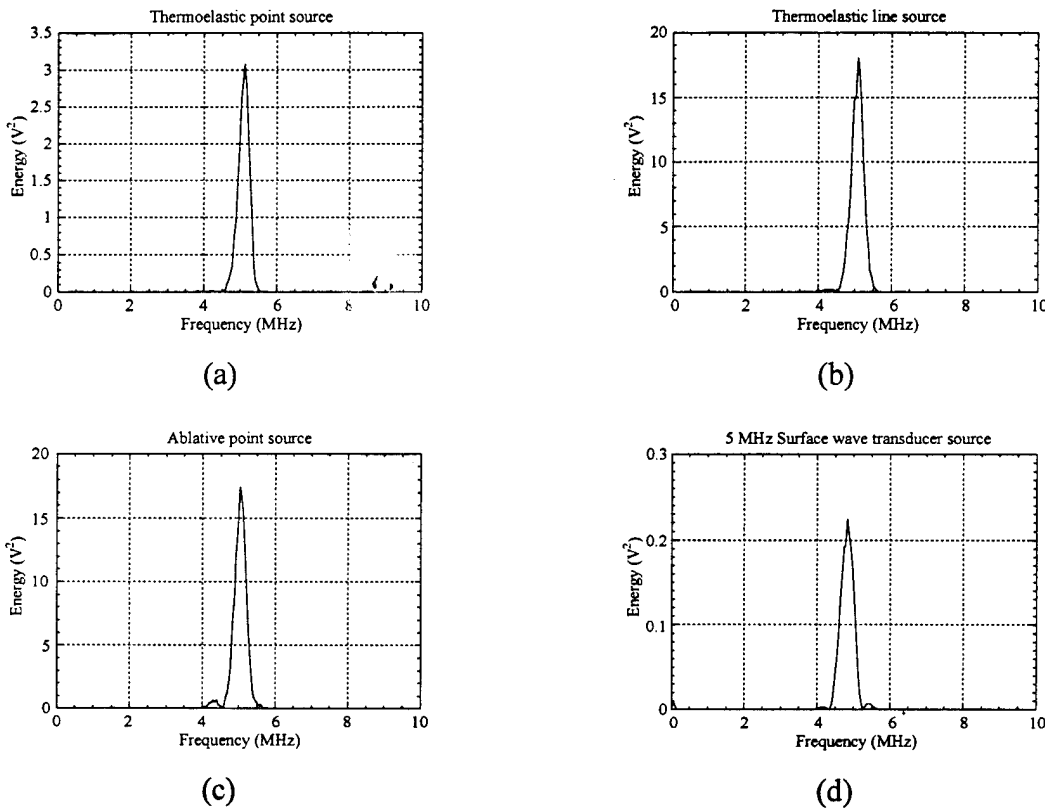


**Figure 21.** Plots of power spectra of the waveforms shown in Fig. 20 as generated by (a) thermoelastic point source, (b) thermoelastic line source, (c) ablative point source, and (d) second 5 MHz surface wave transducer.

To assess the tunability of the system, waveforms were recorded at a series of source spacings (and corresponding frequencies). Theoretically, the frequency content of the waveform should be controllable within the overall frequency envelope of a single laser generated surface wave, as presented in Figure 22. Experimentally, the thermoelastic line source geometry was used, but with less than the maximum possible transmitted energy. The 6 frequencies tested were 7.7, 6.5, 5.5, 4.7, 3.3, and 2.7 MHz, and the resulting unaveraged waveforms (along with the single-fiber waveform) are shown in Figure 23. Here the large first arriving tone-burst corresponds to the directly transmitted wave, while the smaller second arrival corresponds to the reflection off the back edge of the block (to the right in Fig. 19)

of the counterpropagating wave. Figure 24 then shows the power spectra of the corresponding averaged waveforms, with the spectrum of Fig. 24a (the single-fiber waveform spectrum) giving a general indication of the detecting transducer's frequency response. Although the highest and lowest center frequencies appear to be well outside the transducer's response, they are still detectable owing to the presence of subsidiary and harmonic peaks in the narrowband generation spectrum (shown theoretically in Fig. 22) which do fall within the transducer's response. These frequencies are more clearly seen by normalizing the power spectra by the transducer response from the single fiber waveform, as shown in Fig. 25. However, those frequencies which do fall well within the transducer's response (5.5 MHz, 4.7 MHz, and the first harmonic of 2.7 MHz) are very easily detected and shown a significant reduction in bandwidth.

To emphasize the benefit of narrowband generation, Weiner (optimal) filtering was performed on the unaveraged waveforms. To determine the correct frequency concentration for each of the 6 narrowbands, an averaged waveform ( $n = 100$ ) was acquired on a reference block of the material. The power spectrum of this averaged waveform was then used to represent the desired frequencies for the Weiner filter. Each of the waveforms of Fig. 22 were filtered accordingly and the filtered waveforms are presented in Fig. 26. While the signal-to-noise ratio of the 4.7 and 5.5 MHz waveforms were fairly high to begin with, so that the effect of filtration is not as noticeable, there is a marked improvement in signal-to-noise ratio in the highest frequency waveform to the extent that the previously undetectable second arrival is now clearly evident. One advantage to Weiner filtering is that the envelop of the tone-burst is significantly less distorted than would be the case for a simple narrow-band filter, and in fact the fidelity of the 3.3 MHz waveform appears to actually be improved somewhat, in that individual arrivals are visible in the filtered waveform. (Note that this improvement is not seen in the 2.7 MHz waveform because the first harmonic is in the center of the detection response and therefore dominates over the fundamental.)

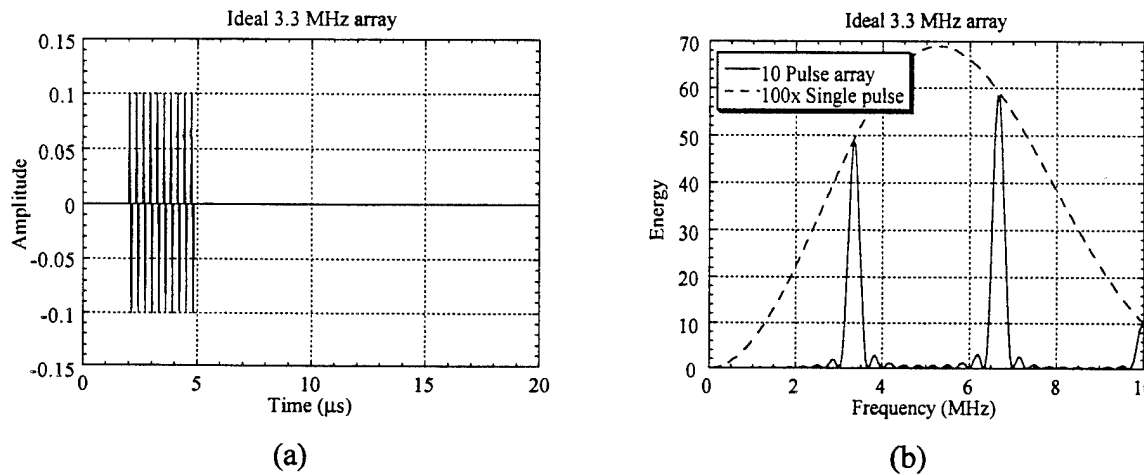


**Figure 22.** Theoretically predicted (a) waveform and (b) power spectrum for the ultrasonic signal generated by an array of ten 230  $\mu\text{m}$  diam. fibers separated by 880  $\mu\text{m}$  (corresponding to 3.3 MHz in aluminum) and detected by a broadband displacement sensor.

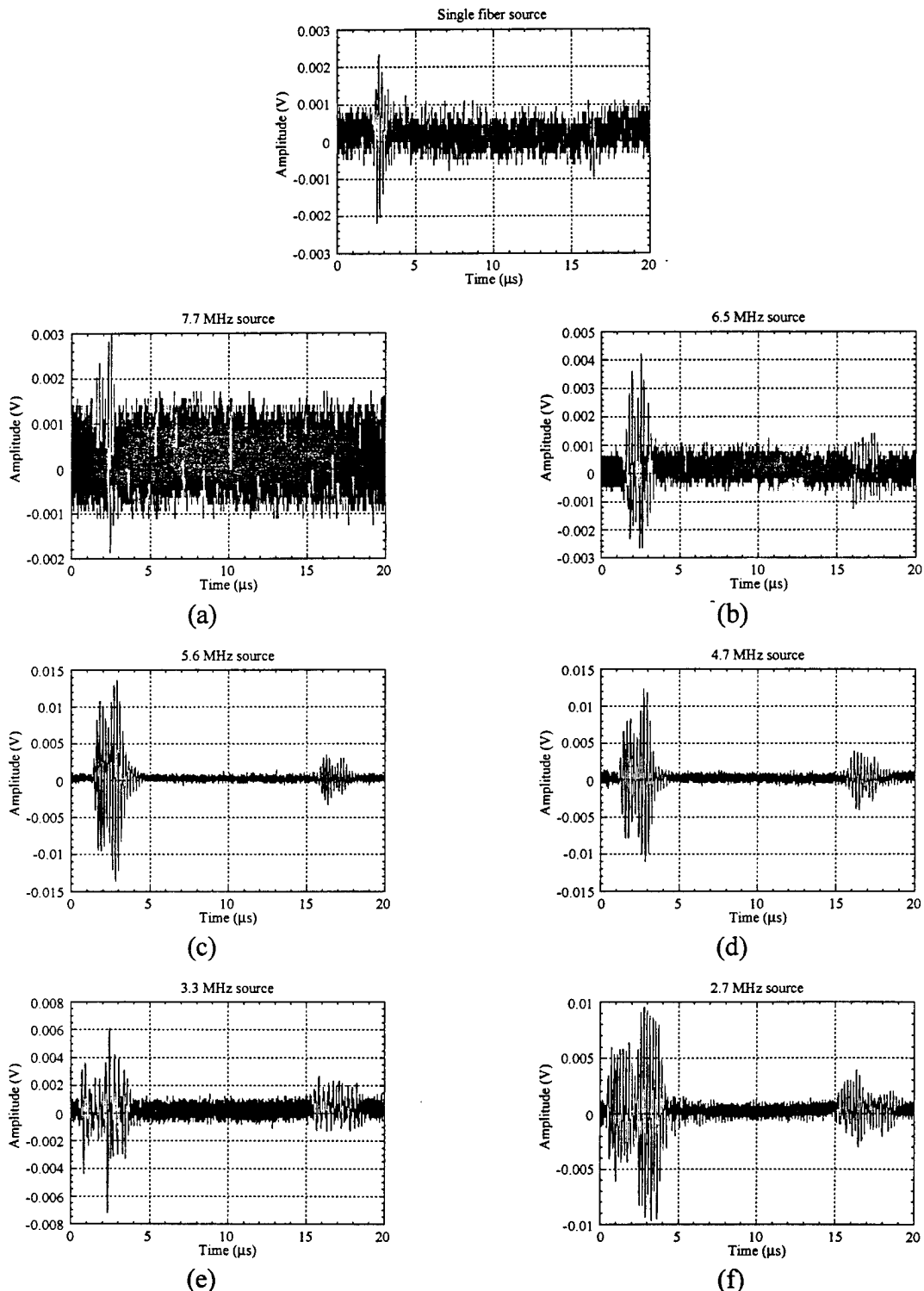


**Figure 23.** Unaveraged and unamplified piezoelectrically detected waveforms for fiber-optic array laser generated surface waves centered at frequencies of (a) 7.7 MHz, (b) 6.5 MHz, (c) 5.5 MHz, (d) 4.7 MHz, (e) 3.3 MHz, and (f) 2.7 MHz. Also shown at the top is the waveform generated by a single fiber source.

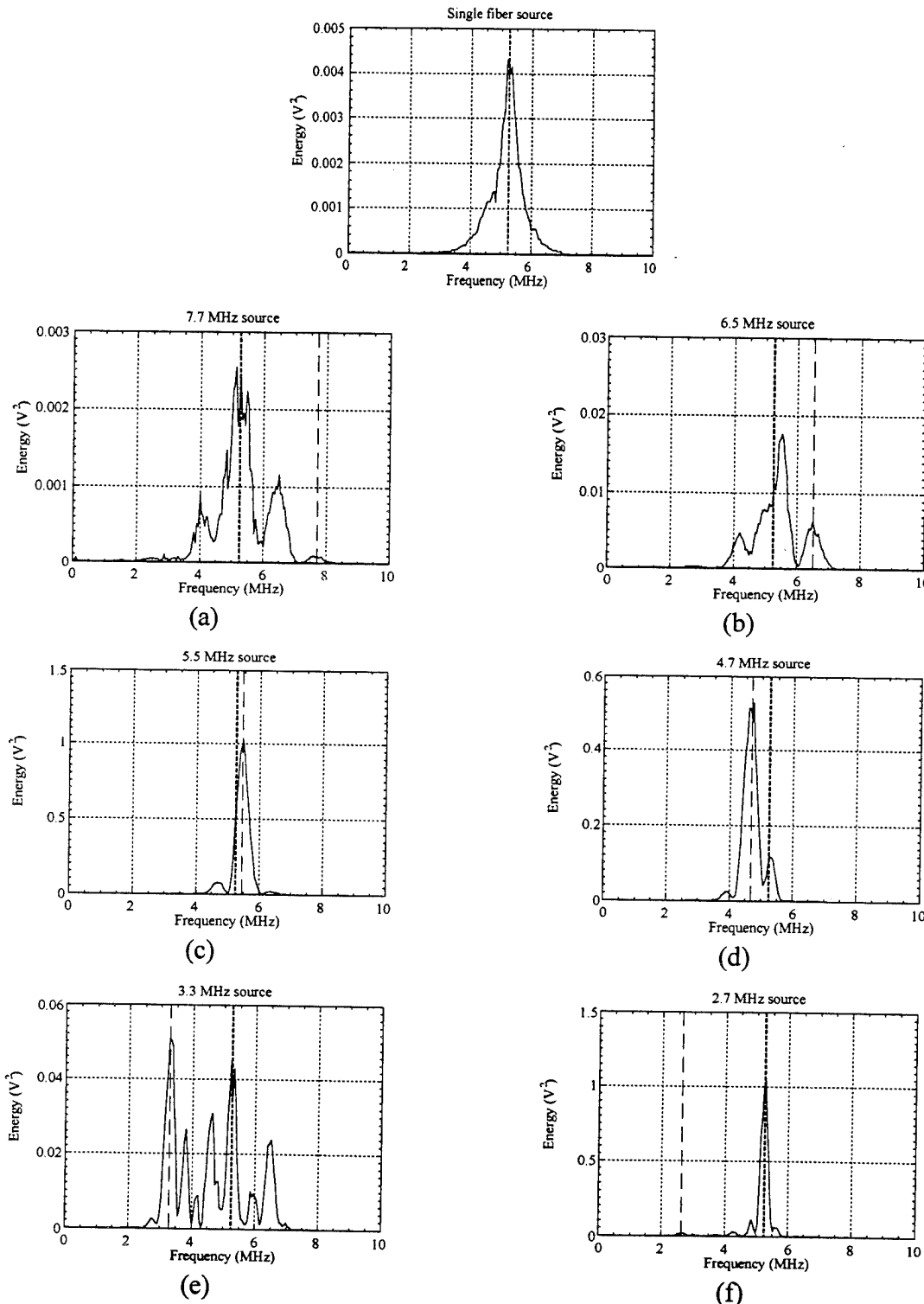


**Figure 24.** Power spectra of the waveforms of Fig. 22 averaged 100 times, with center frequencies of (a) 7.7 MHz, (b) 6.5 MHz, (c) 5.5 MHz, (d) 4.7 MHz, (e) 3.3 MHz, and (f) 2.7 MHz. Also shown at the top is the single fiber source power spectrum.

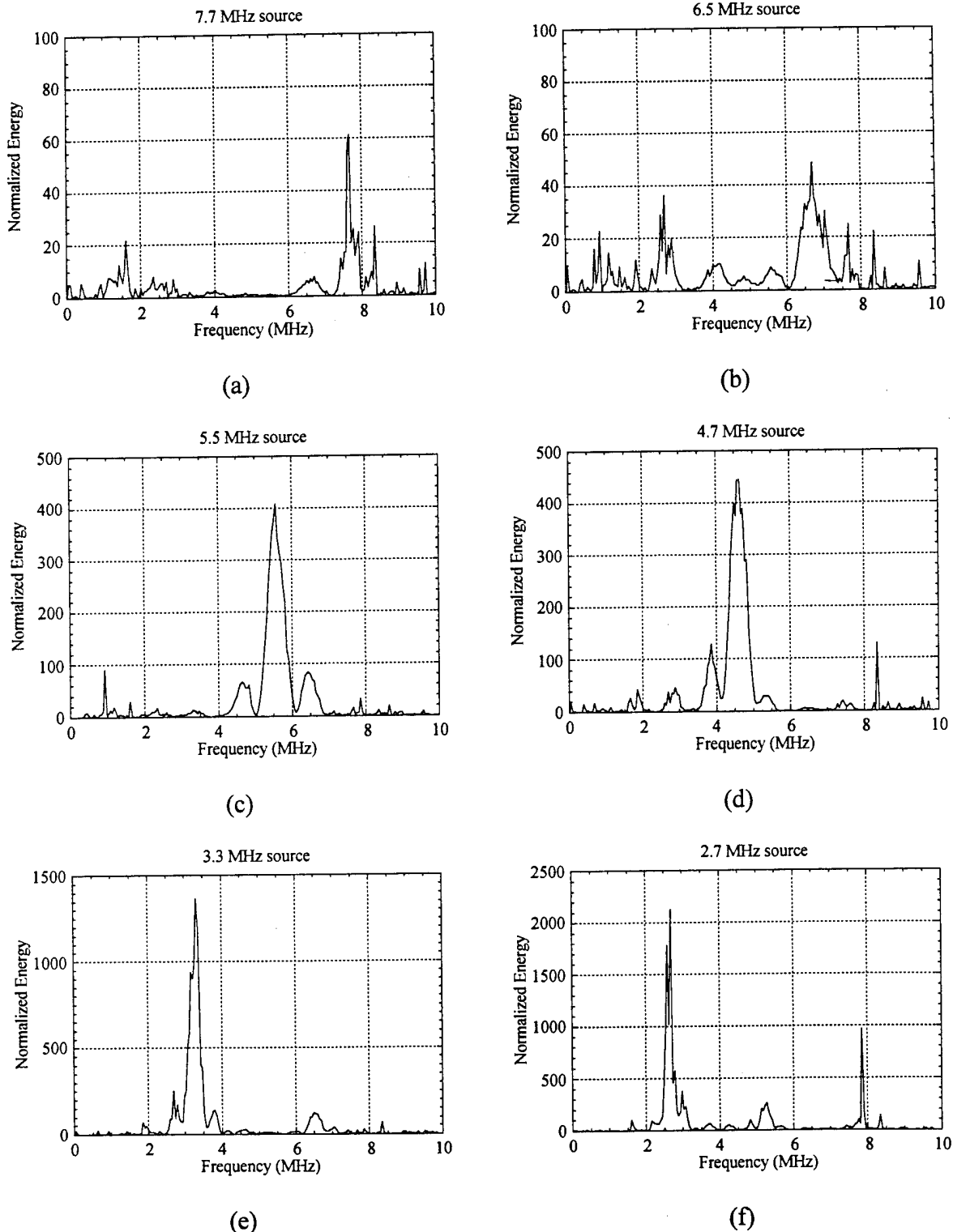


**Figure 25.** Power spectra of Fig. 24 normalized by the single fiber spectrum to remove the effects of transducer response, showing center frequencies of (a) 7.7 MHz, (b) 6.5 MHz, (c) 5.5 MHz, (d) 4.7 MHz, (e) 3.3 MHz, and (f) 2.7 MHz.

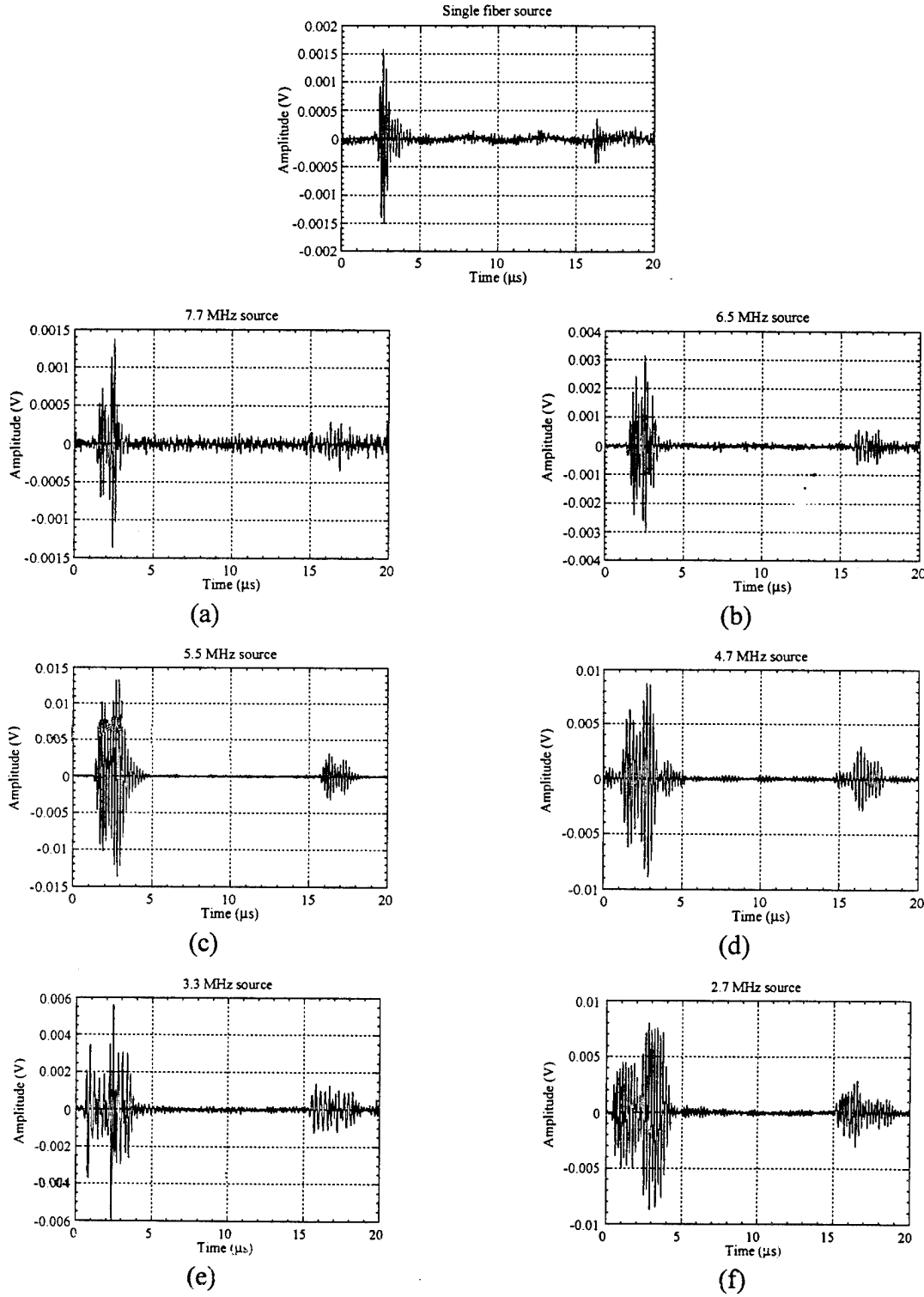


**Figure 26.** Weiner filtered versions of the waveforms of Fig. 22, with center frequencies of (a) 7.7 MHz, (b) 6.5 MHz, (c) 5.5 MHz, (d) 4.7 MHz, (e) 3.3 MHz, and (f) 2.7 MHz. Also shown is the Weiner filtered single fiber source waveform.

## Plans

A fiber-optic based laser ultrasonic system has been developed for the generation of narrowband surface waves. The system has been demonstrated at a range of frequencies from 2.7 to 7.7 MHz, with noticeable signal-to-noise improvements attained through additional narrow-band filtering. Signals were detected piezoelectrically using a 5 MHz surface wave transducer with a relatively narrow frequency response. However, field implementation of such a system will likely not permit the use of piezoelectric detection. Therefore, the second year's effort will be to develop alternative non-contact (e.g., fiber-optic laser interferometric) detection systems, as well as continued refinement of the fiber-optic laser generation system. Effort will focus on a technique which maximizes sensitivity on rough surfaces while minimizing the increased noise associate with remote sensing. In order to take full advantage of the bandwidth reduction, the detection system's frequency response should be as closely matched to that of the generation system as possible. While active filtering of a broad-band detected signal is possible, detection systems which are inherently narrowband would provide greater speed and simplicity, and will thus be emphasized.

## 2.1.4 DETECTION OF MECHANICAL SEAL FAILURE IN TURBOMACHINERY

Co-investigators: Richard F. Salant and Jacek Jarzynski (Georgia Tech)

### Overview

Mechanical (face) seal failure is one of the principal causes of breakdown in such turbomachines as centrifugal pumps, compressors, turbines, turbopumps, propeller shaft assemblies, and gas turbine engines. In this project, a real-time monitoring system for detection of the precursor to seal failure is being developed. Such a system will allow preventive action to be taken to avoid failure.

Mechanical seals generally fail as the result of the collapse of the lubricating film between the two seal faces. The goal of this project is to develop a system to detect the collapse of the film before mechanical and thermal damage is sustained. The approach involves placing a piezoelectric transducer behind the nonrotating seal face and monitoring (and processing) the output of the transducer in real time. When the lubricating film collapses, the relative motion of contacting asperities will generate ultrasonic waves in the face, which will be detected by the transducer. The primary challenge is to correlate the detector signal characteristics with the degree of contact between the mating seal faces. This will be done through experiments utilizing a seal tester in which the degree of contact between the seal faces can be varied. The results of the experiments will identify the signal features that characterize the collapse of the lubricating film, which is the precursor to seal failure.

The primary test apparatus consists of a double mechanical seal contained within a housing. It is shown schematically in Figure 27. A single tungsten carbide rotating face is fixed to the shaft. Two non-rotating controllable face assemblies float in the axial direction. Each of the latter assemblies consists of a carbon graphite face bonded to a PZT-5H piezoelectric actuator (in the form of a ring), a piezoelectric detector, a boron nitride holder, O-ring secondary seals, and coil springs, as shown. The actuator crystal is poled in the radial direction, so that when a voltage is applied across the crystal (in the axial direction), the crystal undergoes shear deformation and causes the carbon face to cone. The larger the applied voltage, the larger the coning. The interface between the carbon and the tungsten carbide faces consists of a fluid film. It can be shown that the larger the coning, the higher the average fluid pressure in the film (for a fixed film thickness), and therefore the thicker the film. As the applied voltage and the coning is reduced, the film thickness will be reduced, until there is partial (asperity) contact between the faces. As the applied voltage is further reduced, the degree of contact increases. Thus, by adjusting the applied voltage, one can control the degree of contact.

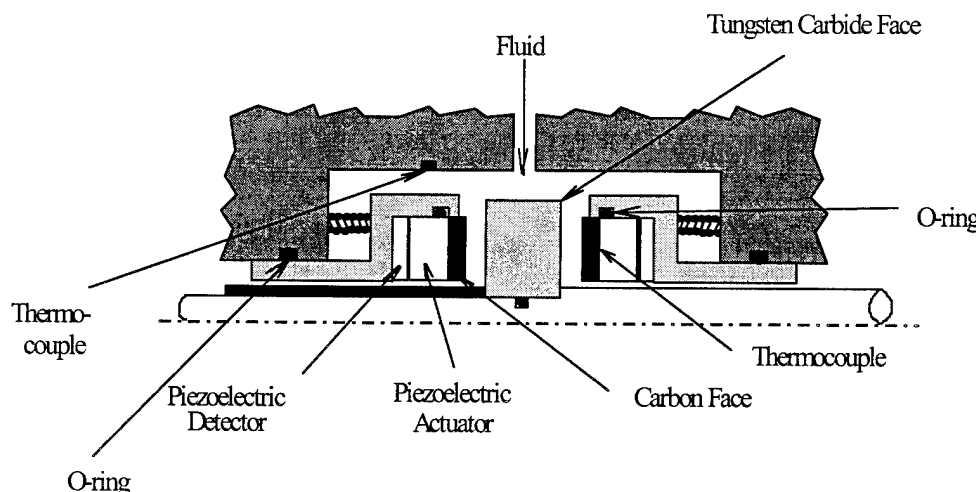
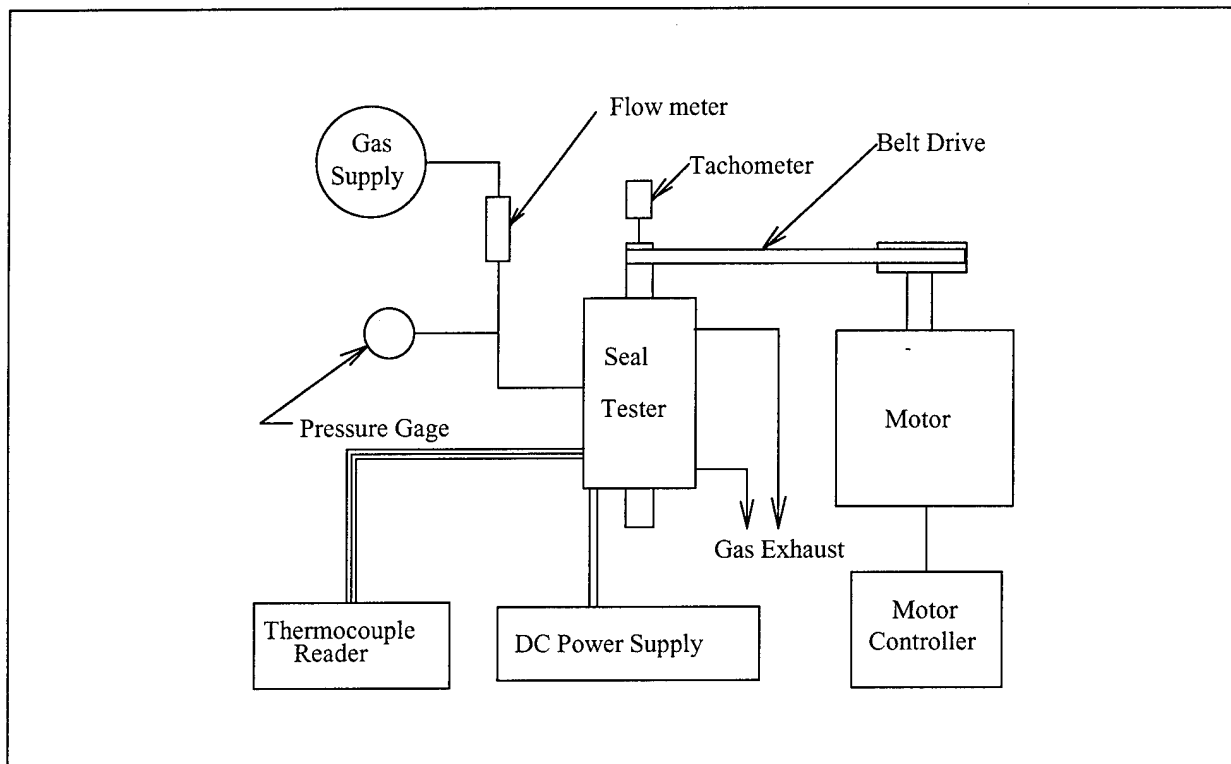


Figure 27 Mechanical Seal Test Apparatus

When partial contact occurs, the relative motion between contacting asperities generates ultrasonic waves within the carbon face. These waves will be detected by the ultrasonic detector, located behind the actuator and the carbon face. The actuator itself will also be used as a detector for the lower frequencies; however, its design has been optimized for control of the degree of contact while the detector is optimized for sensing the generated ultrasonic waves. Once the waves are detected, the signals will be processed to distinguish them from the surrounding noise, and relate them to the degree of face contact.

The seal tester is driven by a motor, through a belt drive, as shown in Figure 28. Figure 28 also shows some of the auxiliary equipment required for tester operation.



**Figure 28** Seal Test System

## **Accomplishments**

The principal activities planned for this project over a three year period are:

1. rebuilding and modification of existing seal tester, with air as the sealed medium;
2. mathematical modeling of wave generation and detection;
3. design, analysis and construction of piezoelectric detector;
4. development of signal processing methods;
5. shakedown tests of system;
6. steady state tests with varying degree of face contact;
7. transient tests;
8. destructive tests to failure.

During the first year effort was devoted to tasks 1 and 3. In task 1, an existing seal tester that was previously used for tests of an electronically controlled seal has been modified and completely rebuilt. This has involved the following:

- complete disassembly of existing tester.
- design of deformable face assembly actuator, and procurement of necessary PZT material.
- design and procurement of carbon face material.
- fabrication of several deformable face assemblies without ultrasonic detectors.
- deformation tests on deformable face elements.
- tests of high voltage power supply for actuators.
- tests and calibration of pressure transducers, flow rate transducers, thermocouples.
- tests of motor.
- procurement and installation of new tachometer.
- design and fabrication of new belt drive system.
- procurement of digital storage scope, variable filter/preamplifier, signal processing software.
- leak testing and leak elimination - in process.

In task 3, a literature search was performed and yielded several studies of acoustic emission from sliding systems. This allowed determination of the most likely frequency range of interest in the present study. The piezoelectric ultrasonic detectors were then designed and procured.

## **Plans**

At the beginning of M-URI year 2, the deformable face assemblies will be fabricated with the piezoelectric ultrasonic detectors installed and tested, and the entire tester system reassembled. This will complete task 3. Effort will then be directed to tasks 5 (shakedown tests of system), 4 (development of signal processing methods), and task 6 (steady state tests with varying degree of contact). It is anticipated that year 3 will comprise completion of task 6, task 2 (mathematical modeling of wave generation and detection, task 7 (transient tests) and task 8 (destructive tests to failure).

### 2.2.1 STRUCTURAL FATIGUE INVESTIGATION

Co-investigators: David McDowell, W. S. Johnson, R. C. Neu, J. Qu, A. Saxena (Georgia Tech)

#### Overview

The objective of condition based maintenance relies on the integration of appropriate diagnostics technology directly into rotorcraft components. Maintenance and retirement decisions are ultimately based on the conditions as assessed by an algorithm which interprets the outputs of various diagnostic sensors. Accordingly, understanding the fatigue behavior of rotorcraft materials is foundational. There are several important aspects of fatigue crack development that are not yet sufficiently developed to perform remaining life assessment, including:

- propagation of microstructurally and physically small cracks, including transition to mechanically small conditions and growth from notches.
- mixed mode growth.
- load interaction effects under variable loading.
- three-dimensional crack effects.
- algorithms for multi-site/multi-scale fatigue damage to interface with transducer/sensor outputs.

The first four items form the gist of the work for the initial three years of the program, while the last topic will integrate these issues into system diagnostics issues and extrapolation procedures in the final two years.

One of the key issues in current procedures for maintainance of platforms and machinery is the ability to accurately estimate the remaining life and to set safe inspection intervals for the critical structural parts of complex systems such as helicopters. A successful strategy should employ a design which is damage tolerant so that detectable fatigue cracks form in critical parts prior to catastrophic failure. This requirement is typically met in aircraft components which are designed to damage tolerant specifications. However, it is often not possible to avoid cases where cracks grow rapidly after reaching some relatively small length beyond detection. A maintenance strategy depends on periodic inspection during service for continued safe operation as well for avoiding costly unscheduled outages. The inspection interval, the choice of inspection technique(s) and the inspection criterion must be specified as part of an overall strategy which provides the basis for making decisions such as continuation of operation, retirement, replacement at present or replacement at a future date (possibly during a scheduled maintenance outage). Such a periodic inspection covers the risk due to the uncertainties in the predicted component life related to:

- detection of small cracks,
- propagation of small cracks in fatigue, and
- service loading conditions.

The estimation of remaining life of in-service components based on such an inspection methodology is an important component of fleet maintenance for either military or commercial transportation vehicles. Remaining life estimates of components subjected to spectrum fatigue loading has traditionally been coupled with a non-destructive inspection scheme to ensure that no flaws should grow to critical dimensions between inspection intervals. This philosophy has formed the basis of the so-called damage tolerant methodology currently employed by military aircraft maintenance procedures. Such inspections are relatively effort intensive, requiring a substantial investment in inspection facilities and manpower.

Various components in rotary aircraft, for example, can sustain different allowable degrees of cracking prior to compromise of overall structural integrity and performance of the vehicle. In some cases, the cracks are easily visible well in advance of catastrophic consequences. In other cases,

however, the cracks may be essentially undetectable by optical methods, due either to length or lack of accessibility, until after the crack has reached critical dimensions. This is particularly true of metallic components subjected to high frequency, relatively low amplitude fatigue loading such as rotor and drive components of helicopters. Under such conditions, fatigue cracks may remain very small (e.g. < 0.5 mm) for over 90% of the life, propagating to catastrophic dimensions only near the very end of life. In components, the determination of whether or not a crack is on the verge of catastrophic propagation depends on the rate of change of the driving force for crack growth as a function of crack length (e.g.,  $dK/da$ ). Consequently, the operator may be faced with the relatively rapid in-flight onset of deleterious structural performance, include loss of control, landing capabilities, etc.

Addressing such rapidly developing failures in more thorough fashion requires modification of the inspection scheme outlined earlier to provide for a higher frequency of feedback in the loop between "inspection" and estimation of remaining life. In the limit, something close to real-time sampling and assessment of remaining life may be necessary for certain components. For example, the helicopter pilot must make very quick decisions concerning landing a helicopter in which the rotor drive-train or guidance components have sustained damage which compromises performance. Passive and active on-board sensors which can detect the presence and growth of crack-like defects offer a means to achieve nearly continuous feedback. In turn, this information must be provided to an on-board computational device for assessment of remaining life based on material fatigue mechanisms under spectrum loading and stress analysis of cracks in critical components from which the signals emanate. In the proposed work, we address the elements of structural fatigue and remaining life estimation essential to a successful integrated diagnostics system based on the concept of *Condition Based Maintenance*. Specifically, the assessment of material fatigue behavior, cracked component stress analyses, and algorithms for fatigue damage under spectrum loading will be undertaken. Close cooperation will be maintained with the component level testing and sensor development efforts of the program to ensure an integrated system capability.

It is recognized in general that a number of mechanisms may additionally contribute to fatigue of a given in-service component, including wear, corrosion, failure of joints and impact damage.

#### *Organization of Sub-tasks*

For implementing Condition Based Maintenance as described above for dynamically loaded airframe and drive-train components, the STRUCTURAL FATIGUE INVESTIGATION is decomposed into three different areas:

- I. Stress analysis and stress intensity factor solutions for cracks in notched components and specimens (Qu)  
OBJECTIVES: Perform stress analyses to provide necessary component level stress and stress-intensity factor information to enable the application of fatigue crack growth laws for remaining life estimation (years 1-2); 3-D aspects of crack analysis (years 2-3).
- II. Experimental characterization and models for correlating the growth of microstructurally small and mechanically small fatigue cracks (McDowell, Johnson, Neu)  
OBJECTIVES: Assess material fatigue mechanisms, developing fatigue crack growth models which employ state-of-the-art technology and address those technology deficiencies noted in the Introduction, starting with simple specimens (years 1-2) with some component verification involving on-board sensors (year 3)
- III. Development of remaining life estimation methodology for components (Saxena, McDowell)  
OBJECTIVES: Develop methodologies to incorporate fatigue crack initiation/growth models to assess remaining life, including small crack growth effects and crack growth under variable loading. Developing appropriate algorithms for remaining life to interface with the NDE output, providing a rapid evaluation of the impending criticality of flaws.

#### *Failure Prediction Methodology*

The efforts of individual faculty are dedicated as follows across these sub-tasks:

*W.S. Johnson* - fatigue crack growth modeling; loading spectrum and interaction effects.

*D.L. McDowell* - growth laws for small fatigue cracks under multiaxial stress states; remaining life algorithms for multi-site/multi-scale damage; TASK coordination.

*R.W. Neu* - experimental study of fatigue crack growth mechanisms and modeling; notch effects.

*J. Qu* - analysis of cracked components

*A. Saxena* - remaining life algorithms for fatigue of components; quantification of fatigue damage in components.

Component level fatigue testing which makes use of appropriate sensor technology to measure the extent of fatigue damage is one part of developing a viable system for condition based maintenance. It is particularly useful for (i) determining "hot-spots" in the structure which favor fatigue crack initiation/propagation and (ii) establishing correlations between signals from various sensors and fatigue damage in specific components.

It is important to point out, however, that fatigue life exhibits considerable scatter for the same loading conditions, particularly at long lives. Accordingly, remaining life estimates invariably have some associated confidence level. Establishing this confidence level generally requires insight into the mechanisms of fatigue failure, which in turn depend on material and loading conditions. The local approach to fatigue crack initiation and fracture mechanics have both progressed substantially over the past two decades. Any robust technology for condition based maintenance of in-service components must integrate such assessment tools, along with structural characteristics and material properties, into the scheme for assessment of remaining life. In particular, cumulative damage concepts (e.g. crack growth) for small cracks must be addressed in the algorithm.

#### **2.2.1.1 *Stress Analysis and Stress Intensity Factor Solutions for Cracks in Notched Components***

*J. Qu*

The objectives of this sub-task are to:

- i. Calculate the "driving" force (SIF) for crack growth in rotor and drive system components in the H-46 helicopter (Connecting Link, Pitch Shaft, and Rotor Hub); 3-D finite element calculations are being performed to obtain the stress intensity factors for these cracks.
- ii. Study the effects of crack-tip mode mixity on 3-D crack growth (3-D fracture criterion), and develop fracture criteria for 3-D crack growth that accounts for non-self similar crack front advances due to mode mixity and crack front curvature.
- iii. 3-D crack growth simulation and visualization. By combining crack initiation, small crack growth, and large crack growth models together with fatigue properties, a computer simulation program is being developed to visually illustrate fatigue crack growth in a selected component under various loading conditions. The simulation program Data Explorer will be used for this purpose.

#### **Accomplishments**

A graduate student, Brian Gardner, was recruited in June, 1995 to work on this project. A dedicated IBM RISC/6000 workstation was purchased in July, 1995 and delivered in January, 1996. Work is underway to set the system up for numerical calculations. Meanwhile, the Office of Information Technology at Georgia Tech was contacted for the possibility of using their SP-2 system for numerical intensive calculations. To leverage the funding for computational equipment, we participated in the IBM

Strategic University Research Grant proposal for an 8-processor SP-2 system and a local access station. We have established a working relationship with the Graphic and Visualization Laboratory at Georgia Tech as well. This state-of-the-art facility is interested in the interaction and is willing to assist in development of the visualization tools for this program.

Dr. Jeff Schoess of Honeywell was contacted for possible collaboration in identification of realistic loading conditions. Dr. Schoess has been very cooperative and has provided information regarding the loading history on the rotor hub.

Our collaborator Brian Moran of Northwestern University (see Section 2.2.2) visited Georgia Tech in October to coordinate his activities in probabilistic fracture and 3-D stress analysis of cracked bodies.

After careful considerations, we chose the Rotor Hub (P/N A02R2550) as the first component for the numerical analysis. A solid model of the Rotor Hub is shown in Fig. 29, which was generated using IDEAS. A finite element model for the Rotor Hub is developed using 4-node tetrahedron elements. A typical mesh (1/3) is shown in Fig. 30. For convenience, material constants used in the calculation are  $E = 3 \times 10^3$  ksi,  $\nu = 0.25$ .

To study the convergence of the finite element mesh, three models consisting of 9,200, 13,384 and 18,937 elements, respectively, were considered. The strain energy density and stress values at selected locations were compared. It was found that the model with 13,384 elements is able to provide numerical results with relative error less than a few percent.

Considering the drive system geometry and the machine mechanism, the load on the rotor hub can be decomposed into two torques plus two forces. The dominant force is the lifting force in the z-direction. Under the lifting force, the stress distribution is calculated. The Mises effective stress distribution is shown in Fig. 31. To reveal the stresses inside the Hub, Fig. 32 shows only the elements that have the Mises stress higher than a certain value. It is seen that the maximum stress occur at the back of the ring-shape part. This is in agreement with the crack locations recorded at Cherry Point.

Clearly, to better understand the 3-D stress distribution, a more sophisticated visualization scheme must be developed to represent the field quantities. To this end, we have elected a program called Data Explorer. Work is in progress to use this program for the presentation of stress distribution in any cross-section of the Hub.

## Plans

- Develop a "Test Matrix" for various loading conditions to carry out the parametric studies of both uncracked and cracked components.
- Use *Data Explorer* to develop a multimedia visualization method for presenting the FEM results.
- Brian Gardner should finish his M.S. thesis and begin his Ph.D. program
- Initiate work on modeling of 3-D Crack Growth. Effects of crack-tip mode mixity on 3-D crack growth will be studied. Proper fracture criteria for 3-D crack growth will be developed that take into account the non-self-similar crack front advances due to mode mixity and crack front curvature.
- Compare FEM results with experiments conducted by other team members

## Failure Prediction Methodology

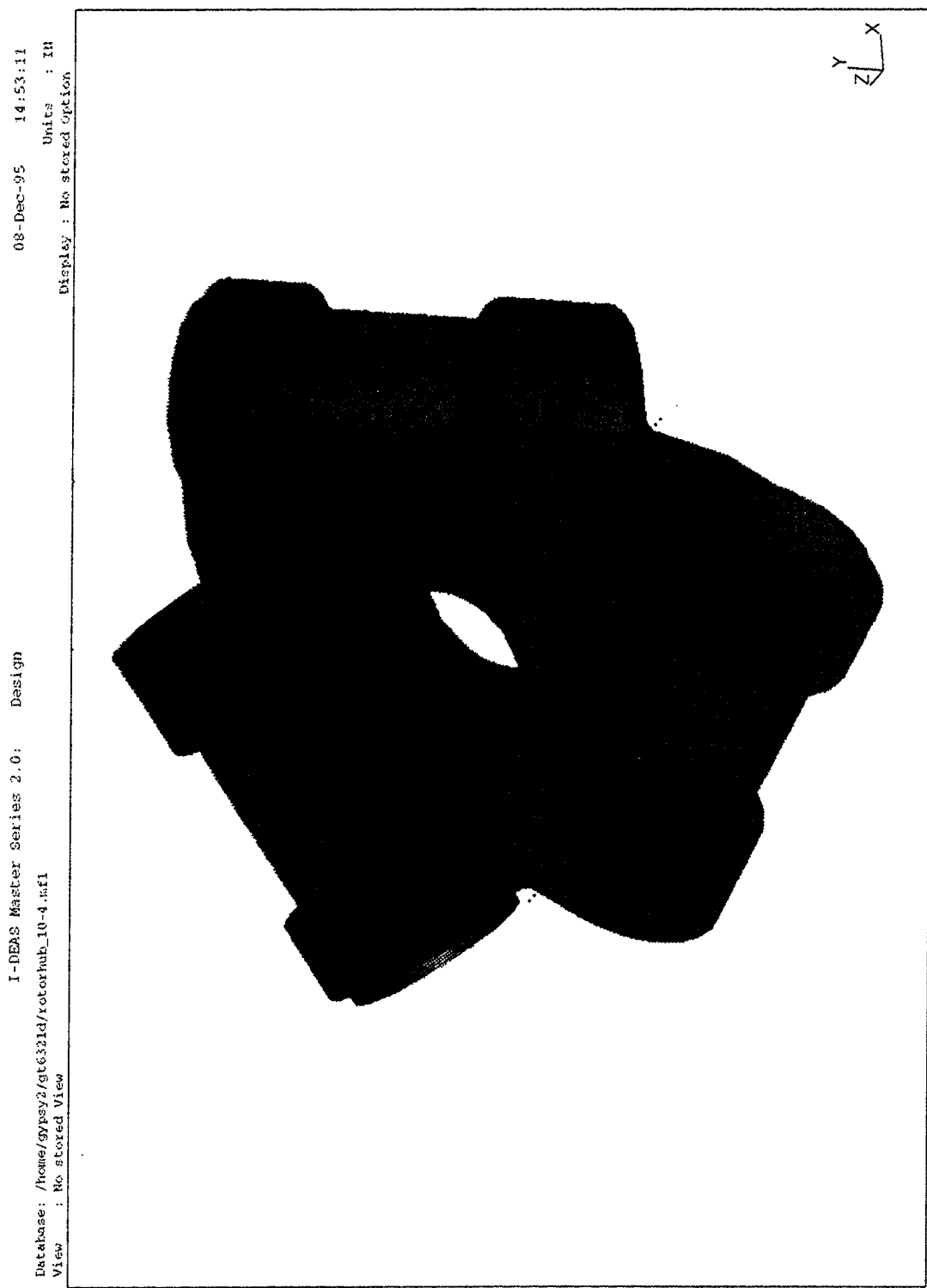


Fig. 29 Solid model of the Rotor Hub

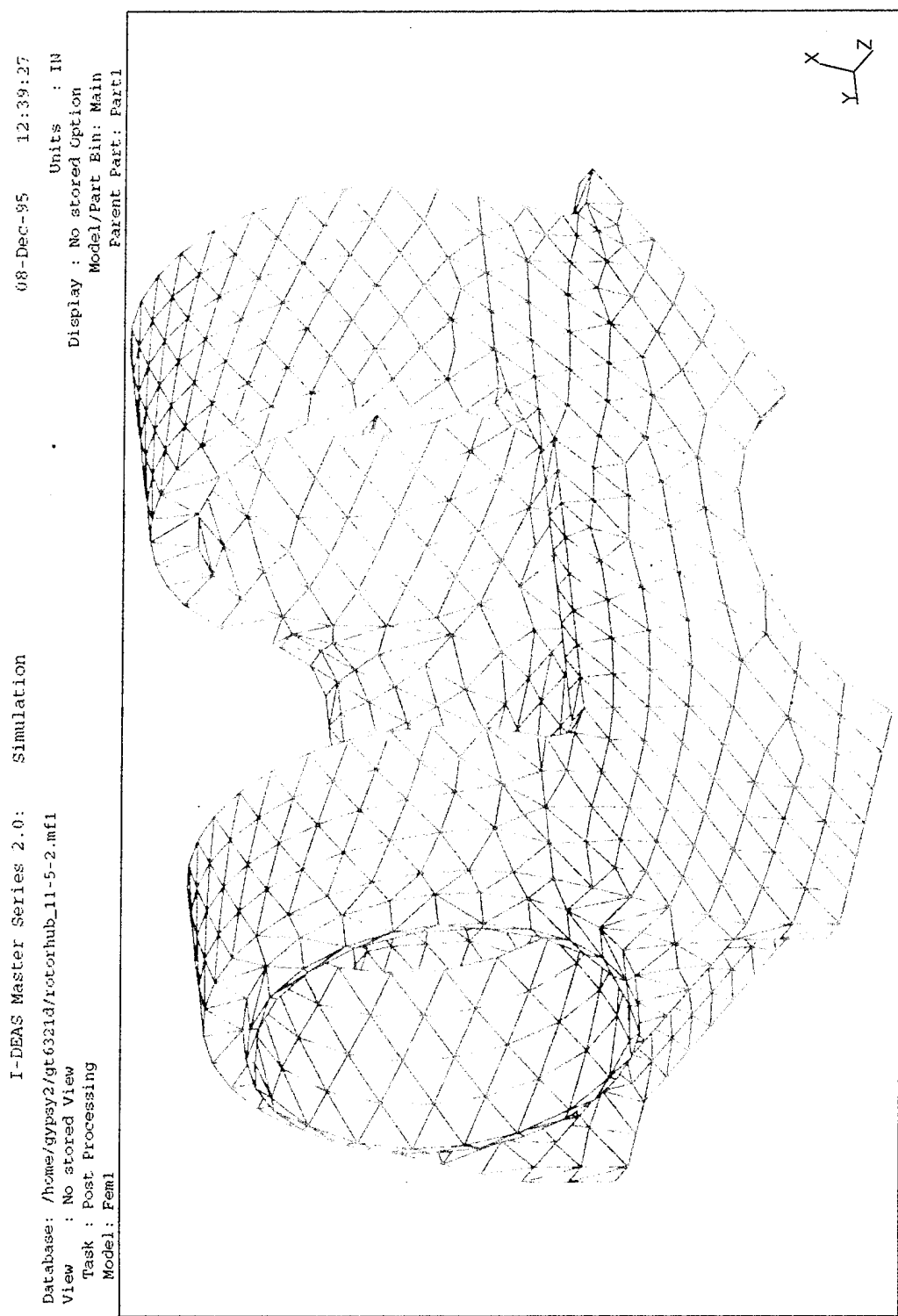


Fig. 30 Typical finite element mesh (1/3)

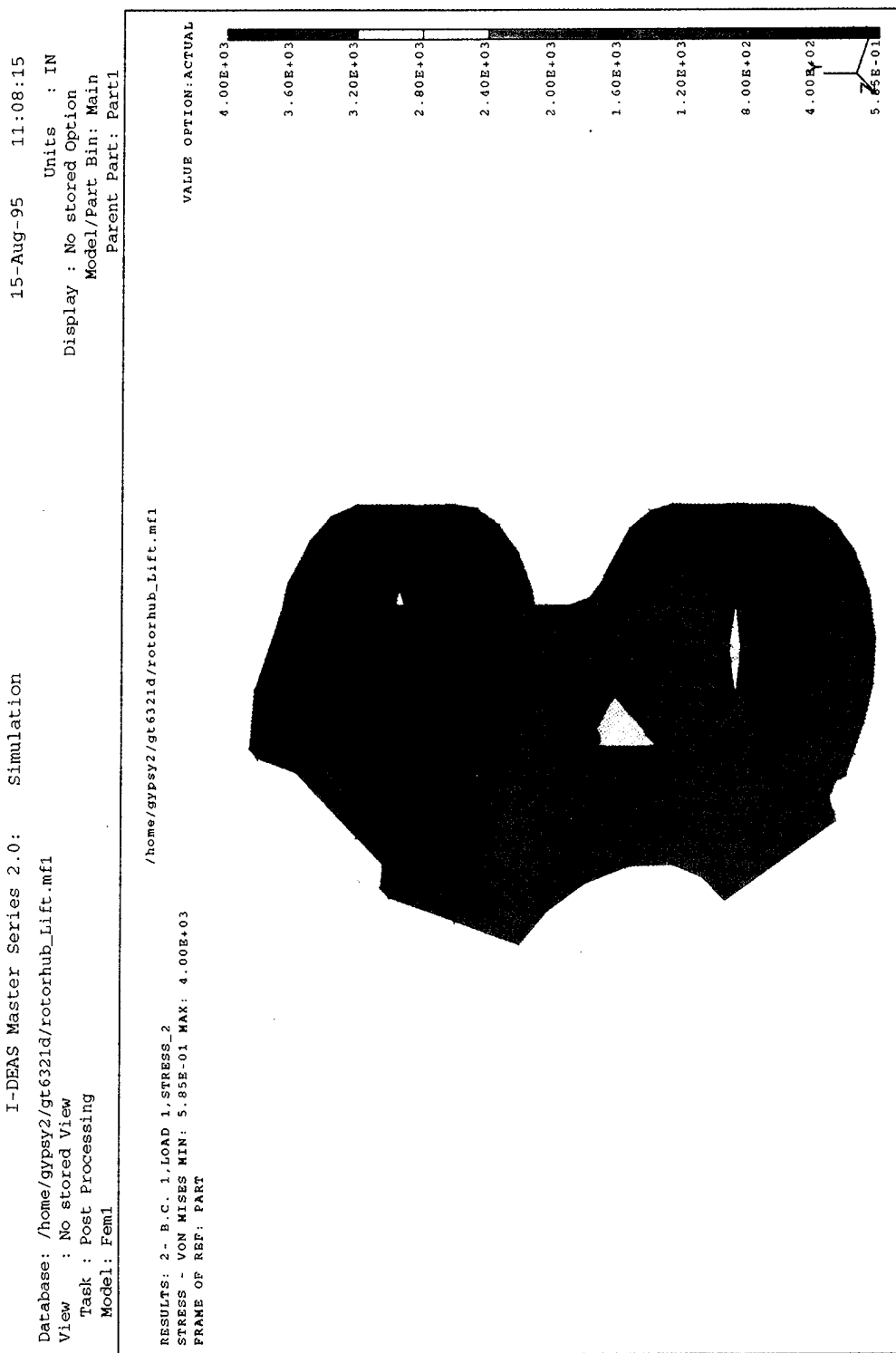


Fig. 31 Von Mises stress distribution

15-Aug-95 11:09:30

I-DEAS Master Series 2.0: Simulation

Database: /home/gypsy2/gt6321d/rotorhub\_Lift.mf1

View : No stored View

Task : Post Processing

Model: Fem1

RESULTS: 2 - B.C. 1, LOAD 1, STRESS\_2

STRESS - VON MISES MIN: 4.72E-01 MAX: 5.51E+03

FRAME OF REF. PART

CRITERION: ABOVE : 5.51E+02

/home/gypsy2/gt6321d/rotorhub\_Lift.mf1

VALUE OPTION: ACTUAL

5.51E+03

4.96E+03

4.41E+03

3.96E+03

3.31E+03

2.75E+03

2.20E+03

1.65E+03

1.10E+03

5.51E+02

5.51E+02

4.72E+01

Fig. 3.2 Location of the maximum Mises stress

### **2.2.1.2 Characterization of Fatigue Behavior and Mechanisms**

*D. L. McDowell, W. S. Johnson, R. Neu*

To conduct remaining life assessments based on fatigue crack growth and fracture, associated material properties must be known. We expect to make use of existing data (from ONR, other DoD agencies, industrial vendors, etc.) regarding the fracture and fatigue properties of the appropriate materials, as well as data to be generated in this task. First, the conditions of criticality of cracks must be well understood for each component; this requires appropriate stress analysis as well as fracture toughness information. Depending on the length of cracks that must be detected prior to criticality, several fatigue methodologies must be considered. For small cracks (i.e. < 1 mm), it is generally observed that the rate of propagation exceeds that of longer cracks based on correlation with the cyclic stress intensity factor,  $\Delta K$ . This correlation for growth of small cracks, including effects of biaxial stress fields, is an important consideration. For cracks growing from notches, there may be additional crack growth rate deceleration effects associated with the reduction of crack driving force. For longer cracks which are suitably treated with linear elastic fracture mechanics principles, there is still the issue of propagation which depends upon the mean stress (R-ratio) and biaxiality of the stress fields (i.e. mixed mode loading). Load interaction effects will be investigated for microstructurally small and mechanically small cracks to aid in developing appropriate crack growth methodology for a variable loading spectrum. It is important to note that the numerous crack growth models which have been developed for long cracks do not necessarily apply to small/short cracks. Crack growth models for the latter are not mature, and considerable attention must be devoted to such models, particularly under high cycle fatigue conditions or sequences of low and high cycle fatigue amplitudes.

Fatigue crack growth experiments will be carried out on smooth and standard fracture mechanics specimens in the Mechanical Properties Research Laboratory (MPRL) to the extent necessary to supplement already existing data in support of component lifetime estimation (Task III). One or two metallic materials will be considered, as appropriate. These procedures will be verified by conducting selected component fatigue testing and interfacing with the NDE/NDT effort, using the stress analysis results from Task I. As necessary, material degradation effects of various types which influence fatigue life will be considered.

In addition to the component materials, another concern is the degradation of the sensors with fatigue loading. It will be necessary to support sensor development and stability studies with selected fatigue testing of isolated and in-situ sensors. Degradation of signal due to sensor fatigue processes must be quantified and considered. This effort will interface with the sensor development task(s).

#### **A. ACTIVITY OF D.L. McDOWELL**

##### **Accomplishments**

A suitably general engineering model for the growth of cracks from a length on the order of a grain size to detectable dimensions (perhaps 200 to 1000  $\mu\text{m}$ ) does not presently exist, particularly under multiaxial loading conditions. Such a model will provide a fundamental advance relative to the current cyclic stress- and strain-based crack initiation approaches. The model must facilitate a consistent treatment of the growth of fatigue cracks ranging in length from microstructurally small to mechanically long cracks; the latter can be correlated using traditional LEFM or EPFM fracture mechanics principles. This model will facilitate practical algorithms for remaining life assessment for areas where small cracks dominate life estimation. This approach will lead to innovative advances in fatigue design/analysis methodology by introducing a hybrid form which seeks to unify the currently distinct methodologies of fatigue crack "initiation" and "propagation."

We are extending the multiaxial fatigue microcrack propagation approach of McDowell & Berard [3,4] to span regimes of microcrack growth ranging from microstructurally short cracks to physically short cracks to cracks governed by standard fracture mechanics correlations. The first regime represents strongly microstructurally-influenced crack propagation, typically applicable to cracks of length on the order of several grain diameters. The second regime reflects a diminished role of microstructure. The identification of the Stage I-Stage II transition may be associated with the transition between these two regimes of crack growth, pending further study.

In view of the strong amplitude and stress state dependence of crack growth in the first regime, the nonlinearity of crack length dependence in the growth law depends both on the strain range and the degree of biaxiality. The microcrack propagation law to be developed here is consistent with critical plane concepts for multiaxial stress states as demonstrated previously by McDowell & Berard [3,4] as well as observations of fatigue crack growth behavior for short cracks [5-12]. This is of practical significance since effective stress and strain concepts do not accurately correlate fatigue life, in general, over a wide range of stress states. The present approach offers treatment of nonlinear cumulative damage and sequence effects, similar to that of damage curve [13] and related continuum damage mechanics [14] approaches.

The primary goal of this research is to address many of the outstanding issues which hinder development of a satisfactory theory for fatigue growth of small/short cracks in structures, including:

- (i) establishing a framework for correlation/prediction of fatigue crack growth of small fatigue cracks consistent with concepts of elastic-plastic fracture mechanics and critical plane theories of multiaxial fatigue [15], focusing on growth of microstructurally short cracks and physically short cracks;
- (ii) developing crack length-, amplitude- and stress state-dependent criteria for the transition from one regime to the next to denote limits of applicability of certain correlative forms;
- (iii) understanding the propagation behavior of microcracks as a function of stress state and amplitude and developing appropriate modeling concepts; and
- (iv) introducing threshold conditions for cyclic microplasticity and nonpropagating cracks (i.e., fatigue limit) into the framework of a multiaxial HCF fatigue theory;

The modeling component is the present focus of the program and accounts for the efforts of the doctoral student supported by the program. It employs state-of-the-art crystal plasticity theory to conduct detailed solutions for cyclic deformation within a set of grains in the vicinity of the free surface, with and without cracks. Experiments will focus on smooth and selected notched specimens subjected to uniaxial, torsional and axial-torsional loading. Socie and colleagues at the University of Illinois (cf. [15,16], etc.) have conducted a series of investigations concerning the evolution of microcrack distributions under constant amplitude and stress state loading conditions for several different ductile alloys; these studies have yielded tremendous insight into the dependence of the fatigue process (for cracks on the order of a grain size to 1 mm) on both amplitude and stress state from LCF to HCF conditions. It was found that some materials (e.g. IN 718 and 1045 steel) exhibit pronounced Stage I propagation independent of stress state, while others (e.g. 304 stainless steel) exhibit an early transition to Stage II growth, particularly under HCF conditions. The former materials were considered as "shear-dominated," while the latter was labelled as normal stress-dominated. The observations for these materials are extensive and small cracks in materials of interest to the Navy will likely adhere to one of these two types of behaviors; hence, the second year of this study will include some additional stress state and sequence experiments on these materials, not considered in the University of Illinois studies, in order to verify certain model features. Moreover, considerable data already exist in the HCF region for these materials that might be used in developing models for nonpropagating cracks.

An AASERT proposal was submitted in November 1995 to support an additional student to conduct the second phase of the experimental study, to begin in 1996, which will involve development of a multiaxial fatigue database (axial-torsional loading of thin-walled tubular specimens), including

#### ***Failure Prediction Methodology***

replicate information on formation and growth of microcracks for lives ranging from  $10^4$  to  $10^7$  cycles for 4340 steel and perhaps an Al alloy or 13-8 PH stainless steel, projected for use in future rotor hub applications. These data will be used to characterize constants for the microcrack propagation model, as well as to verify prediction of sequence effects, stress state and mean stress effects.

The modeling effort is being conducted in parallel with the experimental program for the duration of the program. Modeling concepts developed here will be made available to other tasks, and likewise will consider small/short crack experiments developed in other tasks that focus on mean stress and surface effects, crack growth from notch root fields, and load sequence effects. Ultimately, the model will be cast in a form analogous to that of LEFM for use in a remaining life estimation algorithm which appropriately couples with LEFM algorithms for mechanically long cracks.

#### A.1 Experimental Effort:

##### Amplitude and Stress State Sequence Effects

###### Phase I: Sequence and Mean Stress Effects of Well-Characterized Model Alloys

The completely reversed small crack growth behavior of type 304 stainless steel and 1045 steel have been previously extensively studied and documented by Socie et al. [15,16] under conditions of both proportional and nonproportional loading. Moreover, these two materials are somewhat similar in nature to the 4340 steel and 13-8 PH stainless steel materials to be investigated in Phase II. Interestingly, these two materials display enormous differences in the transition crack length from Stage I to Stage II growth. Phase I of this study will employ the baseline results to make use of this extensive database and further examine amplitude, mean stress and stress state sequence effects on the propagation of microcracks in smooth specimens subjected to combined axial-torsional loading. Such studies are critically important to development of realistic microcrack propagation laws which aspire to capture the nonlinearity of damage evolution; tracking of microcrack development in such experiments has not been previously undertaken. With this strategy, it will be possible to study and verify certain modeling features rather fully at an intermediate stage of the M-URI program by making use of unique existing data, whereas it would likely take two years to develop the equivalent baseline database for new materials. Hence, this will facilitate model development in the current program, while permitting a parallel experimental effort in Phase II which addresses baseline data development for rotorcraft materials such as 708PH stainless steel and 4340 steel.

The Phase I fatigue tests are designed to offer a critical evaluation of certain model features:

- (i) Limited baseline constant amplitude, proportional loading experiments to certify accordance with previously reported behavior for these materials [15,16] regarding microcrack propagation behavior over a systematic variation of fatigue lives ranging from  $10^3$  to  $10^6$  cycles.
- (ii) High-low and low-high amplitude sequence tests under proportional loading to establish sequence effects for the same crack systems.
- (iii) Stress state sequence tests involving sequences of torsion followed by tension and vice versa to establish sequence effects for stress states with the same target fatigue life (cf. [17,18]).

For the amplitude sequence effects, target lives of the high and low amplitude levels will be  $10^3$  and  $10^6$  cycles, respectively. Stress state sequence loading levels will be selected for target fatigue lives of  $10^3$  and  $10^6$  cycles, with either applying to both loading conditions in each experiment. Cycle fractions for the first loading level for all sequence experiments will be 0.25 and 0.75, permitting characterization of interaction effects over a range of cycle fraction. These experiments will be completely reversed. Selected experiments with mean axial and torsional stresses will also be conducted to clarify modeling concepts more fully.

The test matrix appears in Table 1; in this Table, the strain ratio is defined by  $\lambda = \Delta\gamma/(\sqrt{3}\Delta\varepsilon)$ . Fatigue life will be defined as the relating to the occurrence of the first 1 mm surface crack, consistent with the data of Socie et al. [15,16]. A nominal thin-walled tubular specimen design appears in Fig. 33,

although the wall thickness of the gage section varies from material to material. Phase I experiments are underway in connection with the thesis of Valerie Bennett, assisted by an undergraduate research assistant.

Fatigue tests will be periodically interrupted to apply cellulose acetate tape to obtain replicas of surface cracking, a technique which has proven highly successful in tracking the process of orientation and growth of microcracks and crack systems from a sub-grain length scale on the order of 5-10 microns [10,15,16]. All fatigue tests will be conducted at room temperature and in laboratory air.

Although replicate experiments will be conducted, characterization of scatter is not of primary interest. Rather, the focus is on the nature of microcrack system development and interaction associated with sequences of loading.

**Table 1** Tests on 304 SS and 1045

---

Baseline:

	Target $N_f$	
	$10^3$	$10^6$
$\lambda$		
0	X	X
$\infty$	X	X

Amplitude Sequence:

	$n_i/(N_f)_i$	
	0.25	0.75
0	X	X
1	X	X
$\infty$	X	X

Stress State Sequence:

	$n_i/(N_f)_i$	
	0.25	0.75
$0 \rightarrow \infty$	X	X
$\infty \rightarrow 0$	X	X

Note: Also selected mean stress experiments to supplement literature results

Note: 1 replicate of each test

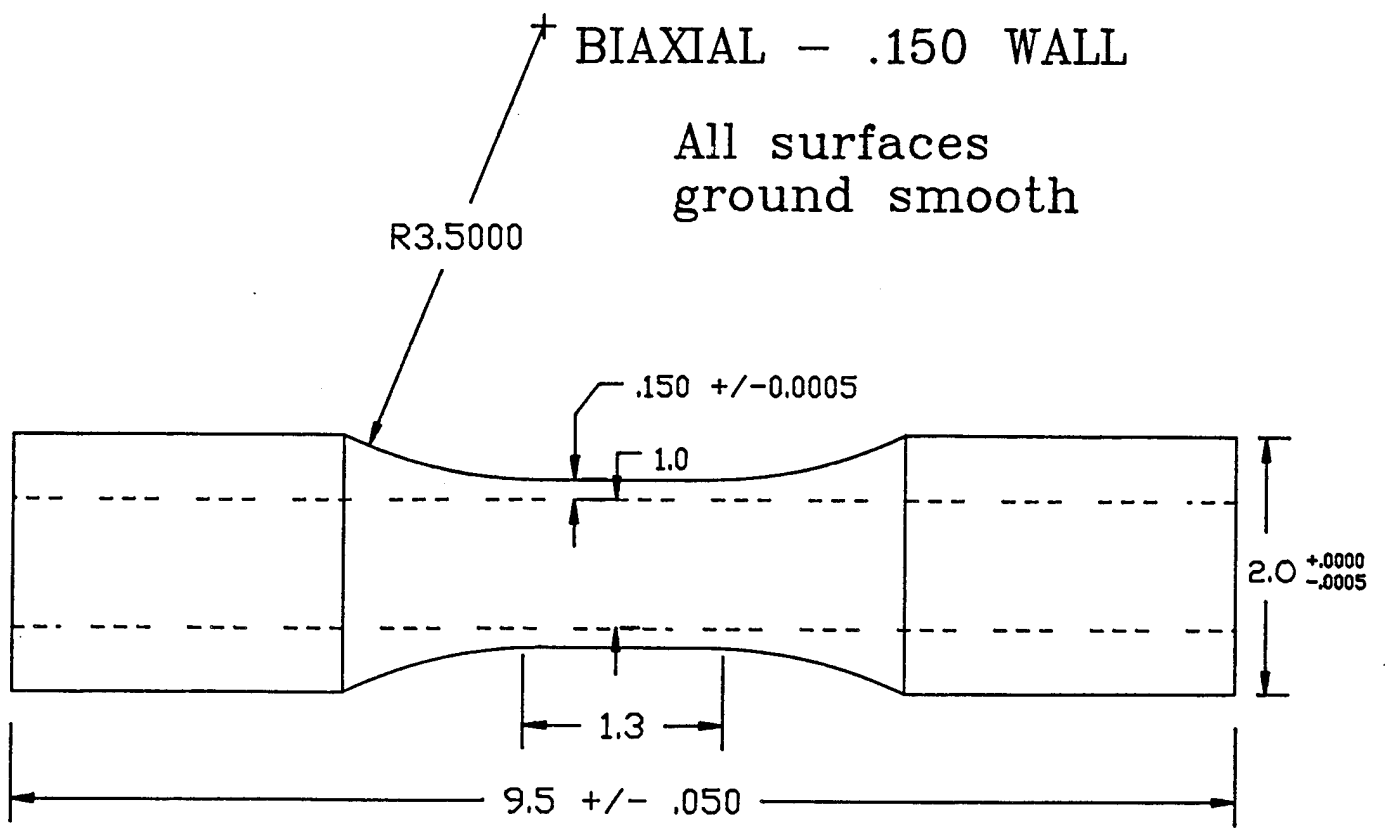


Figure 33 Thin-walled Tubular Specimen Design

## Phase II: Baseline Characterization of Multiaxial Behavior of Rotorcraft Alloys

Baseline completely reversed axial-torsional loading experiments will also be conducted on a 4340 alloy presently used in rotor hub applications to characterize their small crack formation and propagation behavior, as shown in Table 2. Following this program, selected amplitude and stress state sequence experiments will be conducted, along with some mean stress experiments, as shown in Table 2. This Phase will commence later in 1996 and carry through the third year of the M-URI. An AASERT proposal "Multiaxial Fatigue Small Crack Growth in Helicopter Component Alloys" was submitted by D.L. McDowell in November 1995 to support an additional student to conduct the Phase II program. If supported in the next budget cycle, testing will commence in summer 1996. Otherwise, this phase will be delayed until January 1997 and will be conducted by the next doctoral student supported by the parent grant. Specimen machining for Phase II will commence in early 1996.

The experimental program will be carried out in Georgia Tech's Mechanical Properties Research Laboratory (MPRL). The MPRL is equipped with two computer-controlled servohydraulic axial-torsional load frames for testing tubular specimens. One machine presently employs well-aligned hydraulic collet grips. A biaxial extensometer is available for measurement of axial and shear strains in cyclic tension-compression-torsion tests.

**Table 2** Phase II Test Matrix (Each Material)

Baseline:

	Target N <sub>f</sub>	
	10 <sup>4</sup>	10 <sup>7</sup>
$\lambda$		
0	X	X
1	X	X
$\infty$	X	X

Amplitude Sequence:

	n <sub>1</sub> /(N <sub>f</sub> ) <sub>1</sub>	
	0.25	0.75
0	X	X
1	X	X
$\infty$	X	X

Stress State Sequence:

	n <sub>1</sub> /(N <sub>f</sub> ) <sub>1</sub>	
	0.25	0.75
0-> $\infty$	X	X
$\infty$ ->0	X	X

Mean Stress:

	10 <sup>4</sup>		10 <sup>7</sup>
0	X		X (mean shear)
$\infty$	X		X (mean tension)

Note: 1 replicate of each test.

## A.2 Modeling Effort:

The modeling effort is well-underway and is aimed at providing a physically consistent format for propagation of microcracks as influenced by microstructural barriers, amplitude and stress state. The modeling effort relies heavily on computational micromechanics calculations based on crystal plasticity along with experimental observations both from this study and from the literature. Key subjects include:

1. The grain-to-grain variation of the amplitude and orientation of cyclic slip is expected to play an increasingly strong role in the distribution and growth rate of microcracks with decreasing stress amplitude. Under HCF conditions, a much less uniform field of microcracks is typically observed compared to LCF conditions. Accordingly, we are implementing continuum slip crystal plasticity theory to relate the macroscopic stress state and amplitude to a distribution of driving forces among grains. Such effects are expected to play a more significant role for cracks on the order of several grain sizes and below; as cracks lengthen in fatigue, they begin to significantly influence the local driving forces for propagation, with diminishing influence of microstructure. Calculations will be performed using a planar double slip idealization of crystal plasticity [19,20] for a random, initially isotropic ensemble of grains subject to a range of constant amplitude stress states to understand the nature of the distribution of cyclic slip and normal stress to slip planes as a function of amplitude and stress state. Combined kinematic-isotropic hardening cyclic plasticity laws will be assumed at the slip system level (cf. [21]) to match the observed cyclic stress-strain response for the aggregate of grains. Moreover, the contribution of misorientation to blockage of fatigue crack growth under HCF conditions must be taken into account.
2. Using two dimensional finite element solutions based on planar double slip as an approximation of three-dimensional crystal plasticity, the cyclic stress and strain distribution in the vicinity of the crack tip will be determined for cracks with length ranging from sub-grain dimension to up to 10 grains in an equiaxed microstructure. It will be assumed that growth occurs in the orientation of one of the two slip systems in each grain (i.e. Stage I growth). Each grain will have one overall orientation of slip systems initially; to capture gradient effects of deformation within grains, it will be necessary to subdivide the grain into compatible elements with the same initial orientation which experience different degrees of slip.

The resulting information will be used to develop an approach for propagation of small cracks in the presence of microstructure interactions, including amplitude and stress state effects. Furthermore, since the grain size appears explicitly in the calculations, it may be possible for the first time to quantify the elusive conditions for transition from Stage I to Stage II in terms of the ratio of crack length to grain size, including possible additional effects of stress state and amplitude. These calculations should also shed additional insight into mechanisms of arrest for sub-grain size cracks and the occurrence of a fatigue limit as a function of stress state. Furthermore, the basis for transition from nonlinear, perhaps oscillatory, crack length dependence to approximately linear crack length dependence observed for crack lengths in excess of 3-5 grain diameters might be understood from these calculations. By considering the cyclic crack tip opening and sliding displacements as a function of crack length, amplitude and stress state, these calculations might also serve to improve on the isotropic continuum finite element calculations (cf. [22]) which presently serve as a basis for accounting for plasticity-induced crack closure effects.

Every attempt will be made to relate the microcrack propagation approach developed to standard strain-life fatigue theory. Accordingly, material constants determined for existing strain-life theories will be employed, along with additional parameters necessary for the description of stages of fatigue crack growth, multiaxiality effects, etc. Furthermore, asymptotic consistency with long crack fracture mechanics approaches for fatigue crack growth is an attractive feature of this framework, depending on the nature of the damage distribution.

In terms of human resource development, this project currently involves a doctoral student, Valerie Bennett, and one undergraduate research student, Jose Martinez. Model development activities

continue in earnest. Ms. Bennett is in the final stages of preparation of her PhD thesis proposal, and has nearly completed work on 2-D and 3-D finite element codes for crystal plasticity which will be used to assess unique attributes of small crack behavior, fatigue limits, etc.

## Plans

February 1996: Commence machining of 4340 steel test specimens; complete machining of 1045 steel and 304 stainless steel baseline specimens.

March 1996: PhD thesis proposal presentation of Valerie Bennett

September 1996: Interact with NDI faculty (Bair, Jarzynski, Polla) to instrument/monitor some specimens using in biaxial testing.

November 1996: Complete sequence experiments on 1045 and 304 stainless steel specimens

December 1996: Complete numerical modeling of small crack behavior; advance modeling concepts

The companion AASERT program would commence with a student in summer 1996.

## B. ACTIVITY OF W. S. JOHNSON

### Accomplishments

- Traveled to Cherry Point, North Carolina, in June 1995 to assess the potential fatigue problems, helicopters and materials that could be addressed as a part of this program. Numerous contacts were made and possible problems were identified. We decided to work on 4340 steel for the CH-46 and 7075-T73 aluminum for the H-53D. Dr. John Cammett of Cherry Point agreed to supply materials for the program. In July and August, contacted Georgia Tech and Northwestern participants about material requirements and sent information to Dr. Cammett at Cherry Point. Material from Cherry Point Dr. Cammett at Cherry Point was received in January 1996, and specimen machining will commence at once.
- In June, attended the National Symposium on Fatigue and Fracture held in Williamsburg, Virginia, to monitor the latest technology in small cracks.
- Made contacts at Boeing Helicopter and Sikorski. Both companies were very interested in our effort and would be interested in giving guidance and support in term of technical help and possibly materials.
- A Questar Long Focal Length Microscope was ordered on matching funds for equipment to allow optical viewing of cracks of length 30 microns and longer. The microscope system includes a VCR and digital frame grabber. This digital capability permits crack tip opening and crack tip opening angle to be measured accurately.
- Received the FASTRAN crack growth prediction program developed by Dr. Jim Newman of NASA Langley Research Center in January 1996. This program has been used in numerous studies to predict the behavior of small cracks. Collected a large number of papers on small cracks including several AGARD documents. Baseline data for the materials of interest have been collected. A complete set of MIL-HB-5 and the Damage Tolerance Handbook has been obtained.
- Conducting literature review on the Newman approach for predicting small crack behavior, including small crack growth arrest. A parametric study will be conducted in the near future to assess the parameters that most influence small cracks. Specimen geometries are being finalized and standardized between participants.
- Attended the ASTM E-8 on Fatigue and Fracture Fall Committee meeting to participate in small crack activities, and agreed to conduct a survey of small crack activities underway in the U.S., Europe and Japan. This information will help focus and highlight our ONR activity.

### Failure Prediction Methodology

## Plans

- Specimen machining will take place in March. The specimens will be made of 7075-T73 aluminum and contain a semi-circular edge notch on both sides of the specimen to serve as a fatigue crack initiation site.
- Constant amplitude fatigue initiation and growth data will be developed to serve as a baseline for subsequent tests to determine load interaction effects on the growth of small cracks. Electron beam "holes" will be created to serve as initiation points. It is anticipated that cracks as small as 20 microns can be detected and monitored using Questar Long Focal Length Microscopes. Testing will begin as soon as specimens are back from machining. The baseline testing should be completed by September.
- A systematic testing program to study the effect of load sequencing on the growth of small cracks will start at the completion of the baseline testing. This testing will identify any differences in crack growth behavior in the small crack compared to the well understood long crack behavior. Any observed differences will be assessed and modelled.
- Current prediction methodology for small cracks is currently being evaluated. One of the most promising was developed at NASA Langley Research Center by Dr. Jim Newman. His model has been obtained and is being implemented. A parametric study will be conducted to assess the sensitivity of the Newman plasticity induced crack closure approach to mechanisms known to control growth of small cracks. This study will be completed in June.

## C. ACTIVITY OF R. W. NEU

### Accomplishments

Two primary goals have been identified: (1) Develop a small crack growth prediction model that will be consistent with long crack growth models and is able to account for cracks growing through nonuniform stress fields as well as for variable amplitude loadings. (2) Establish the sensitivity of sensor technology for locating cracks, detecting their size or growth rate, and detecting impending failure under well-controlled crack growth conditions.

This effort will focus on 4340 steel and 13-8 PH stainless steel. Plans for the experimental work have been refined during year 1.

A common material used in helicopter rotor components, 4340 steel is a high strength low alloy steel typically used in the quenched and tempered condition. In this condition, the microstructure consists of small prior austenite grains (around 10  $\mu\text{m}$ ) that contain an even more finely divided structure of tempered martensite. These fine microstructural length scales result in a small crack traversing several martensite lathes, and consequently this steel has shown less pronounced anomaly in short crack growth behavior compared to other materials that contain relatively larger microstructural length scales. 4340 steel can be heat treated to different hardness levels. Even though much baseline data exists on quenched and tempered 4340 steel, strengths can range from a high of 1700 MPa for a 225 C temper to 850 MPa for a 650 C temper. A round robin of constant amplitude small crack growth tests have been conducted on this steel in the quenched and tempered condition (tempered at 440 C to 45 Rc and yield strength of 1413 MPa) in an earlier study. Inclusions, such as calcium-aluminate and manganese-sulfide particles (ranging from 5 - 40  $\mu\text{m}$  in diameter), typically serve as crack nucleation sites. The material for present investigation will be supplied by the Cherry Point Naval Depot and will be in the quenched and tempered state (yield strength between 1034 - 1172 MPa (150-170 ksi)), which is typical for the helicopter rotor components on the CH-46.

Small crack growth investigations of 4340 steel under constant amplitude loading have been conducted by other investigators. When  $R = 0$ , the crack growth behavior for small and long cracks can be correlated with  $\Delta K$  and no short crack effect is observed. For higher stress ratios ( $R = 0.5$ ), short cracks grow at a slightly lower rate than that of long cracks compared at the same stress intensity range, which may be attributed to some notch plasticity in these tests. For lower stress ratios ( $R = -1$ ), some short crack effect is observed, meaning that cracks grow at a  $\Delta K$  below the long crack threshold. The short crack effect becomes greater as  $R$  becomes more negative, though the effect in 4340 steel is not as pronounced as in aluminum alloys.

Relative to 4340 steel, little work on the fatigue behavior has been reported on 13Cr-8Ni PH stainless steel. This steel is used as a replacement for 4340 steel in rotor components of the CH-46 and is reported to have better performance properties. Compared to 4340 steel, this steel has a slightly higher yield strength 1172-1310 MPa (170-190 ksi). In salt environments, small cracks tend to grow faster (up to 2 orders) in 4340 steel and stress corrosion cracking is also a concern especially when quenched and tempered to higher strengths. This stainless steel is reported to have better resistance when exposed to a salt atmosphere.

The test specimens will be suitable for investigating both primary goals: (1) investigating the small crack growth behavior so that small crack growth prediction models can be developed and (2) correlating well-characterized long crack growth behavior with sensor output. For the small crack growth behavior (cracks generally less than 1 mm in size), crack growth through nonuniform stress fields from notches and peening and the influence of overloads and underloads will be studied. Crack length will be measured along the bore of the notch using acetate replicas as well as a Questar long-focal distance optical microscope, purchased through matching funds from Georgia Tech. As the crack grows larger, various sensors will be attached to the specimen through teaming arrangements with other groups within the ONR project. The crack tip conditions will be determined from the loading profile along with the crack size, which will also be automatically monitored by the switching DC electropotential method.

Three different flat panel specimens have been designed (Figs. 34-36). The first specimen is designed with a smaller gage length to allow fully-reversed loads without the need for buckling guides and will easily deform at loads well below the capacity of the fatigue testing machine. Either an EDM starter notch in the center of the panel or a center hole or edge notch will serve as crack nucleation sites. This specimen is the best design for studying small crack growth in a uniform stress field using a small EDM starter notch in the center of the panel. The two larger specimens (Figs. 35-36) will allow more flexibility in placement of sensors, but will require buckling guides, currently being designed, if compressive loads are applied. The dog-bone specimen in Fig. 35 is similar to the specimen that was used in a round robin investigating constant amplitude small crack growth in 4340 steel. An alternative straight-sided specimen (Fig. 36) can have a single edge notch or multiple notches as shown. A similar design has been used with lower strength materials (i.e., aluminum). However, the capacity of grips and fatigue machine are approached when testing high strength steel specimens.

Most specimens will have a single damage nucleation site, either a notch (e.g., Fig. 35) or EDM starter notch. Since nucleation of small cracks is dependent on inclusions or holes left by inclusions, crack nucleation is very probabilistic. Some specimens with multiple notches (e.g., Fig. 36) will be tested to increase the probability of capturing the small crack growth, by monitoring crack growth in each notch. Also, sensor detection in the presence of controlled multi-site damage can be studied with multiple notches.

Small crack growth in the presence of nonuniform residual stress fields will be studied. A gradual stress gradient will be studied by applying a single overload or underload sufficient to cause local plastic deformation around the notch where upon unloading, a nonuniform residual stress field remains. In addition, a decreasing elastic stress field from the notch will arise during application of the external load. Steep stress gradients will be examined by growing a crack in specimen surfaces that have

#### **Failure Prediction Methodology**

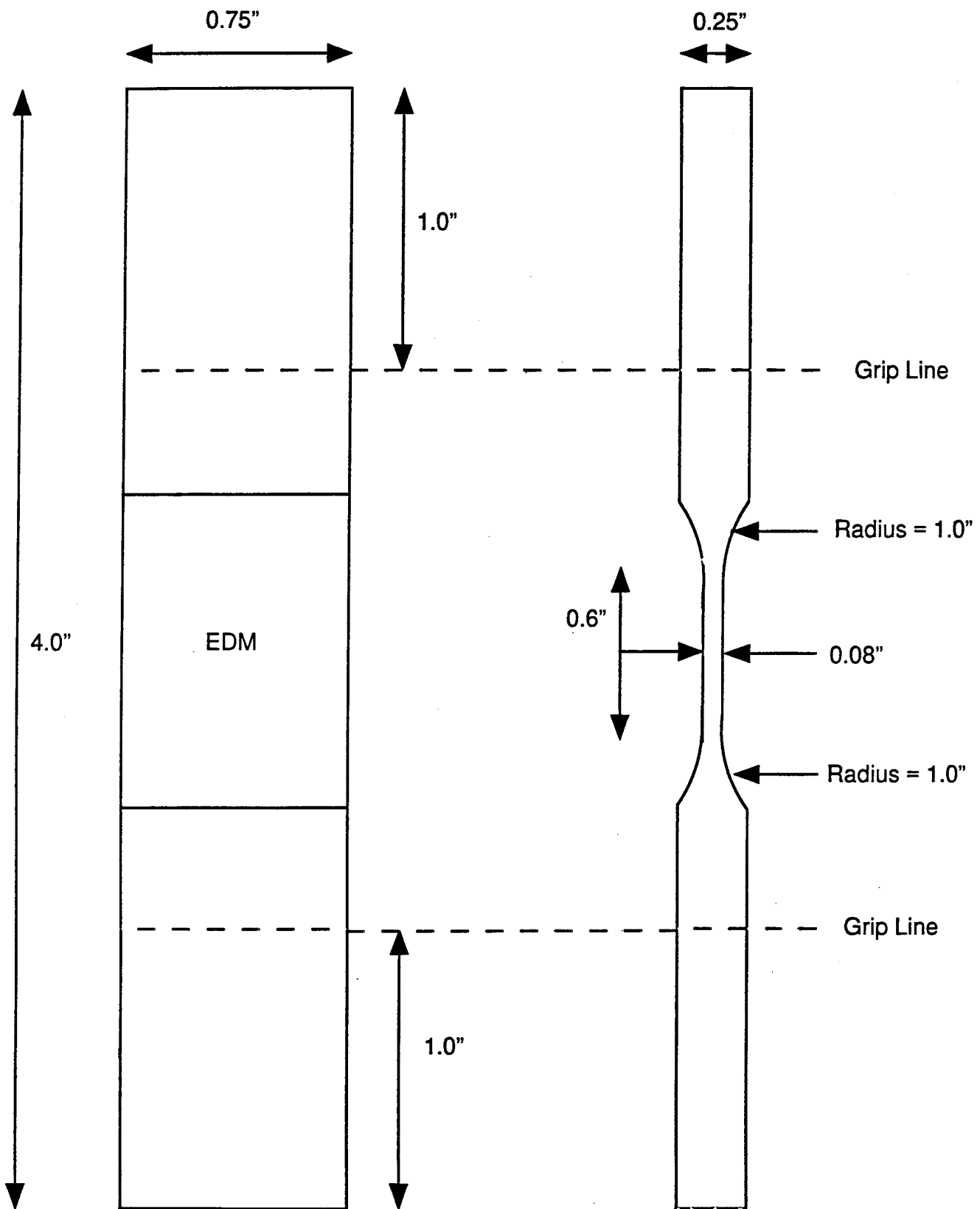
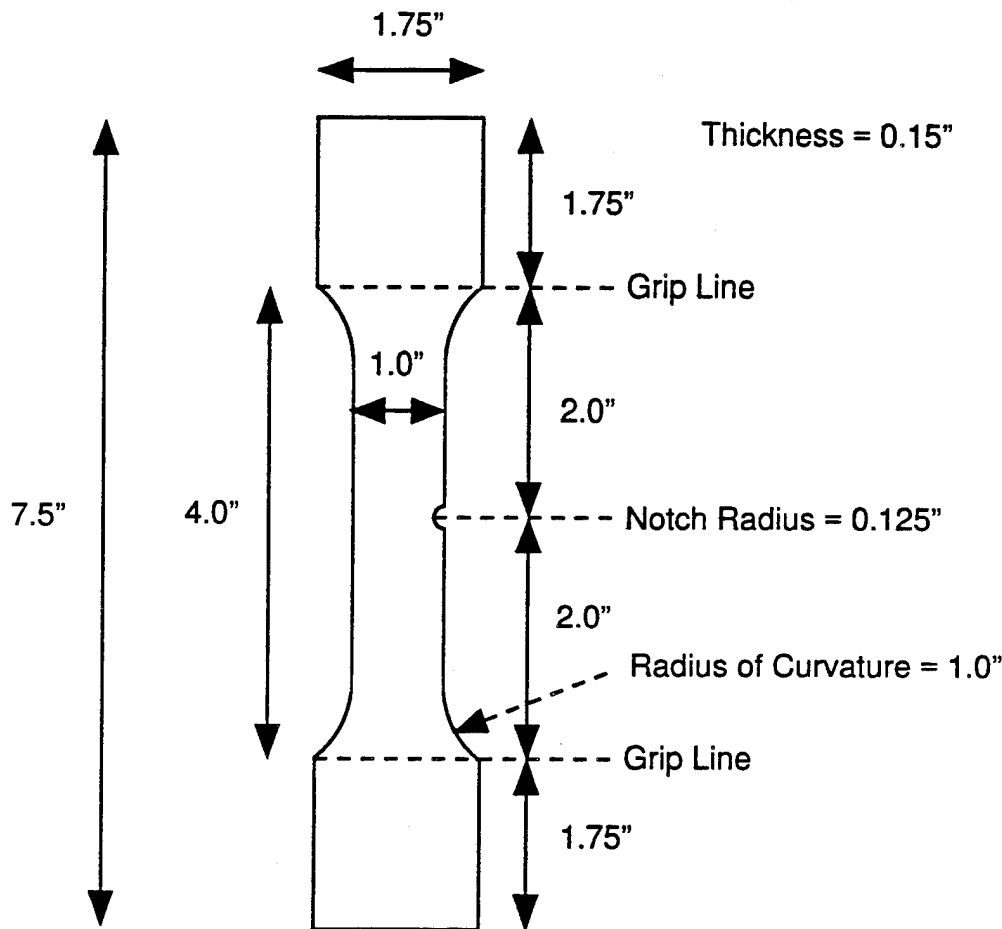


Figure 34 Flat Panel Specimen, Design A



**Figure 35** Flat Panel Specimen, Design B

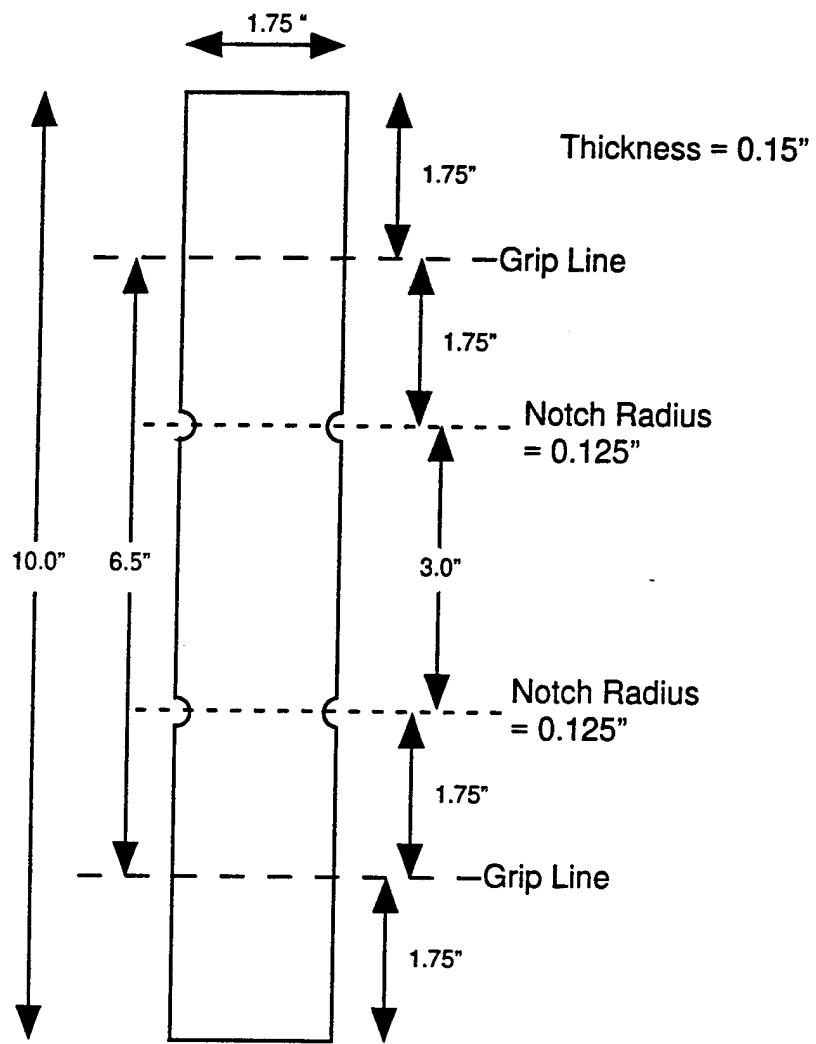


Figure 36 Flat Panel Specimen, Design C

undergone different levels of shot peening. As a baseline, crack growth in a uniform stress field (no notch) by small EDM starter mini-notch is also planned.

The final specimen design(s) will be chosen to minimize any constraints attaching various sensors. Potential specimen designs were taken to Profs. Jarzynski and Jacobs (see Section 2.1.1) to discuss constraints with regard to the specimen design and the interfacing of sensors. It appears that the size and geometry of the current specimen designs (especially the larger specimens) will allow the placement of acoustic emission (AE) transducers, which are about 2 mm in diameter. Their group plans to monitor acoustic emission under some of our well-defined crack growth conditions when the crack has transitioned to the long crack growth behavior. The correlation of crack growth parameters, such as the stress intensity factor and relative plastic zone size, with the sensor output will be further studied by applying a single overload (or underload) that retards (or enhances) the crack growth rate. Sensors will be monitored to specimen failure (separation). This will enable the determination of how AE signal changes when catastrophic failure approaches and has a potential for leading to algorithms for detecting impending failure in sufficient time.

Initially, tests will be conducted at  $R = 0.5$ , 0, and -1, since the small crack growth behavior is very dependent on  $R$ . The applied levels for tests will be guided by baseline long crack growth tests, low cycle fatigue tests, and past work on these steels.

A Master's candidate, Akshay Patel, who came to Georgia Tech, began to work on this project in October 1995. During the summer and fall of 1995, Dan Scott, conducted some preliminary work, primarily focusing on the initial stages of the current literature review. John Pape, who is a Master's candidate funded by Georgia Tech, will also conduct research associated with this project.

## Plans

March 1996: The first batch of specimens made from 4340 steel will be machined.

May 1996: Preliminary testing will begin. Measurement of small crack growth in the presence of various nonuniform residual stress fields will be the first task. Stress intensity factors for small cracks growing through nonuniform residual stress fields as well as the appropriate solutions for long crack growth behavior will be located or developed as needed. Profs. Jarzynski and Jacobs (see Section 2.1.1) will determine the ambient noise in our test apparatus.

June 1996: The switching DC electropotential system to automatically measure crack growth will be installed. In addition, an in-house capability to measure residual stress using X-ray diffraction is tentatively planned.

September 1996: Profs. Jarzynski and Jacobs (see Section 2.1.1) will attach acoustic emission sensors to some of our specimens with well characterized crack growth rates (i.e., longer cracks).

September 1996: Once the preliminary tests have been conducted, additional specimens will be machined from 13-8 PH stainless steel. A study to compare the small crack growth behavior of these two steels will commence.

Throughout the year, relationships with other sensor groups will be established aiding in identifying other opportunities for interaction.

Potential work that may be initiated in year 2 includes improving small crack growth prediction models, conducting a finite element analysis of the specimen to better establish the nonuniform residual stress fields, and investigating the influence of a salt atmosphere on the small crack growth rate behavior of the two steels.

## Failure Prediction Methodology

### **2.2.1.3 Characterization of Fatigue Behavior and Mechanisms**

*A. Saxena and D. McDowell*

One of the key issues in maintaining platforms and machinery based on condition assessment is the ability to accurately predict the remaining life and safe inspection intervals for the critical structural parts of complex systems such as helicopters. A successful strategy for avoiding failure must consist of first and foremost a design which is damage tolerant so that detectable fatigue cracks form in critical parts prior to failure. Since most aircraft components are designed to damage tolerant specifications, this requirement is expected to be met by the components in question. Secondly, the strategy must include periodic inspection during service for continued safe operation as well for avoiding costly unscheduled outages. The inspection interval, the choice of inspection techniques and the inspection criterion must be specified as part of the overall strategy which provides the basis for making decisions such as continue running, retire, replace or replace at a future date (possibly during a scheduled maintenance outage). The periodic inspection covers the risk due to the uncertainties in the predicted component life caused by (i) uncertainty in detectable flaw size; (ii) lack of representative material properties and how they degrade during service; (iii) uncertainties about the magnitudes of service loading; and (iv) lack of accurate models for predicting crack initiation and growth behavior particularly for small flaws under conditions of spectrum loading and for multiple cracks in the same damage location.

One of the main objectives of this task is to provide a methodology for estimation of remaining life or impending criticality of cracks which can be integrated with the information regarding detected crack size from the NDE task. NDE specialists must be made aware of the nature of information required to estimate remaining life, and fatigue analysts should be equally aware of the nature of information feasibly obtained. This will be accomplished by working collaboratively with the NDE group to develop condition monitoring approaches which are consistent with the remaining life prediction methodology.

If the inspection interval is very short, say as small as 10 - 15 seconds, which is the time needed to take evasive action, there should be a premium on integrating sensor inputs into a remaining life assessment algorithm which is nearly real time in nature. The rate of change of sensor signal with progression of loading history must be interpreted in terms of the rate of growth of damage, with damage itself also related to signal. Empirical component level testing can provide calibrations of signal to progression of fatigue failure. However, from a practical standpoint it may be difficult to resolve the rate of change of signal over a relatively short number of cycles until very late (perhaps too late) in life. In this case, the signature of a certain degree of damage, coupled with intelligent algorithms which employ fatigue life prediction algorithms, may provide a practical tool. Hence, one can conceive of systems which range from an indication of required maintenance to an indication of impending failure within some relatively brief time interval, depending largely on the degree to which the sensor signals can actually resolve damage. This is one of the most significant, basic, relatively uncertain aspects of the research in view of the potentially small scale of damage and the noise of actual applications which must be sorted out from sensor signals.

Accordingly, the overall objectives of this task are to:

1. Understand the damage modes, crack growth mechanisms and crack locations of selected helicopter parts.
2. Integrate fatigue crack growth models developed in other tasks into a comprehensive methodology for predicting (i) remaining life; (ii) inspection interval and criteria determination and; (iii) catastrophic failure prevention strategy.
3. Collaborate with groups working on on-board sensors for detecting cracks and develop algorithms which can be used to develop warning systems to evade catastrophic failures.

The methodology developed in this task will be verified both on smooth specimens and on notched specimens and/or a component. The fatigue loading of aircraft structures is potentially complex. Due to the variable amplitude and frequency loading conditions, it is necessary to employ the necessary tools available for variable amplitude fatigue loading in addition to realistic models for growth of small, short and long cracks.

## **Accomplishments**

### *Goals*

The goals for the first project year were to:

- (i) procure retired helicopter component(s) for a laboratory analysis to characterize the damage model and the causes for retirement from service;
- (ii) procure test materials, machine specimens and formulate a test plan; and
- (iii) initiate discussion with team-members on the NDE techniques being evaluated and developed as part of the M-URI effort.

### *Status*

A graduate student, Ms. Fan Yang was recruited to work on this program. Ms. Yang is expected to finish her Ph.D. degree in the Winter Quarter of 1996 and then stay on as a Post-doctoral Fellow for one year on this program.

A retired H-46 connecting link (Fig. 37) from AISI 4340 steel was received on 11/28/95. The surfaces of the pin holes were examined under a light microscope to characterize damage or cracking behavior. A network of what appears to be fretting fatigue cracks was found on the surface of the pin holes. Typical pictures of fatigue damage are presented in Fig. 38. This part was displayed for two days for examination by the other Georgia Tech participants. There are no obvious cracks in the part. The service history of this component is being requested and the search for other components with more advanced stages of damage are being sought. This component will now be sectioned to further characterize the nature of damage, microstructure, residual stresses etc. On the basis of these results, recommendations will be made on the types of damage accumulation and/or crack growth models needed for accurately predicting remaining life of these components. We expect to complete the investigation of this part by the end of March 1996.

Other accomplishments and activities of Prof. Saxena related to this project include the following:

- Invited to give a Keynote Lecture in "Fatigue '96 - International Conference" Berlin, Germany, May 6 - 10, 1996
- Attended ASTM Workshop on Fatigue Crack Closure Measurement and Modeling, Norfolk, VA, Nov. 1995
- Invited presentation at the ASTM Workshop on Application of Fracture Mechanics in Remaining Life Prediction, Norfolk, Va, Nov. 1995
- Elected Vice-Chairman of ASTM Committee E-08 on Fatigue and Fracture
- Attended the 27th National ASTM Symposium on Fatigue and Fracture in Williamsburg, Va in June 1995 and chaired two sessions. Ms. Fan Yang made a presentation at the symposium from her Ph.D. research.

**Figure 37** H-46 Helicopter Connecting Link  
(AISI 4340 Steel)

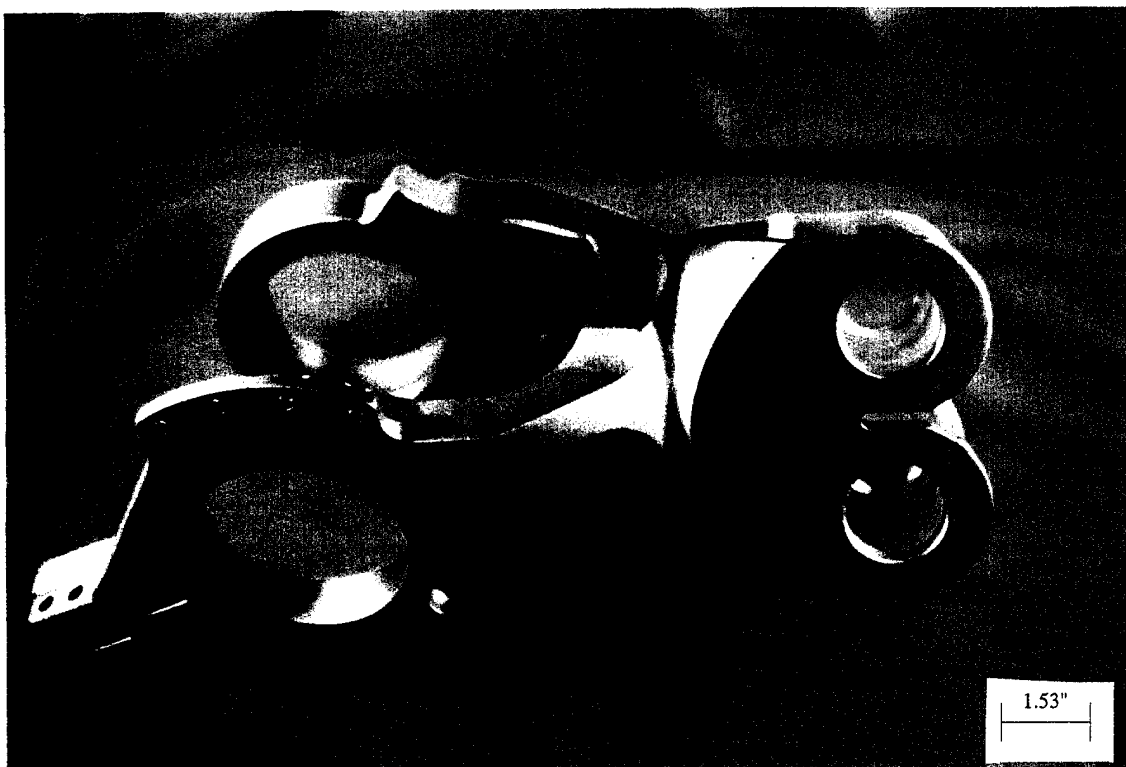
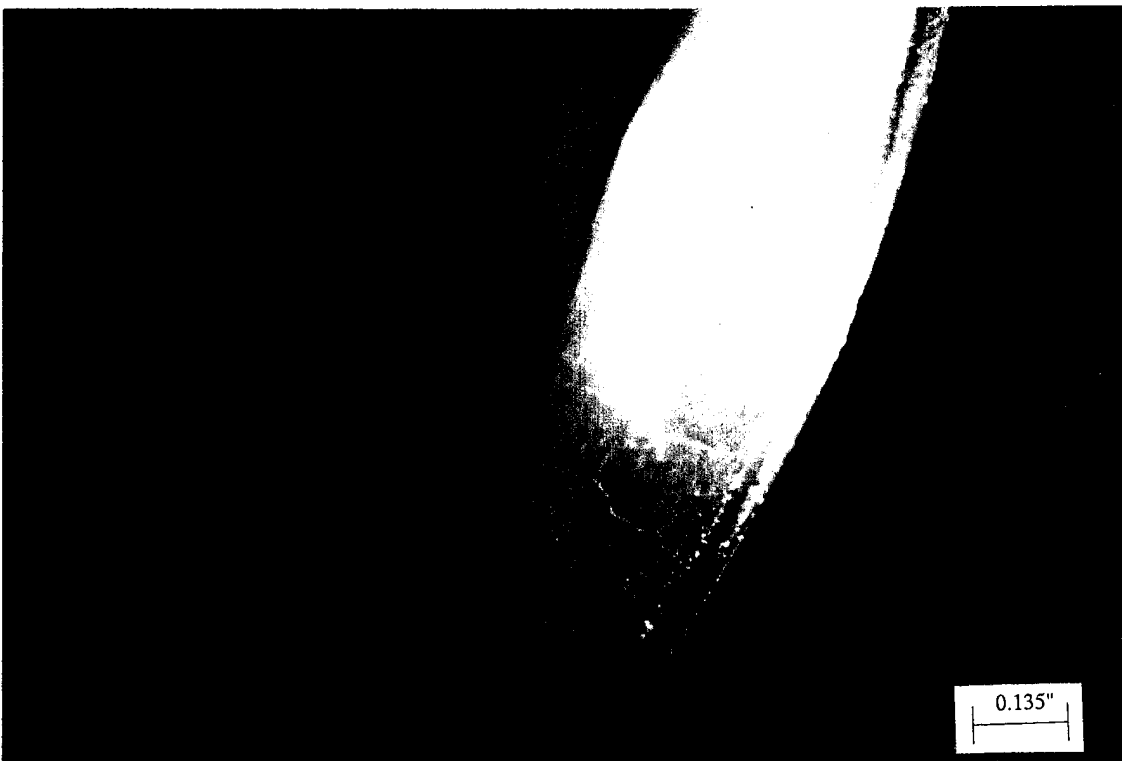


**Figure 38** H-46 Helicopter Connecting Link  
(AISI 4340 Steel)



## **Plans**

### *Second Year Goals:*

- Procure and analyze a second cracked component
- Write a report detailing the size, shapes and locations of cracks, damage modes and service loading in selected helicopter components
- Develop long crack fatigue crack growth rate data from near threshold to high crack growth rates at load ratios of 0.1, 0.5 and -1
- Characterize fracture toughness of the material
- Characterize residual stresses on critical surfaces of the cracked components
- Survey and collect all available fatigue and fracture data on 4340 steel
- Attempt a preliminary fatigue crack initiation and crack growth analysis of the H-46 connecting link using models developed by McDowell, Neu and Johnson and the component analysis of Qu
- Develop a test plan for the verification of the remaining life prediction methodology.

### *Third Year Goals:*

- Conduct model verification testing
- Refine remaining life prediction model
- Explore feasibility of developing user-friendly software for performing remaining life analysis.

## 2.2.2 FAILURE PREDICTION METHODOLOGY USING FIRST-ORDER RELIABILITY METHOD

Co-investigator: Brian Moran (Northwestern)

### Overview

The objective of this project is to develop a methodology for fatigue reliability and lifetime prediction of metallic structural components within the framework of condition based maintenance, and apply the method to failure-critical components and systems in military and civilian machinery.

The computation of fatigue life expectancy is an integral part of the condition based maintenance of structural components which experience cyclic loading [23,24]. Due to the statistical variability in such quantities as material properties and initial flaw sizes, for example, a probabilistic approach is required. Probabilistic fatigue methods can profitably be applied in a setting where critical structural components are monitored by non-destructive techniques so that cracked components can be identified and then repaired or replaced. Such monitoring can significantly reduce the probability of fatigue failure of a structure and increase its useful service life. Quantitative measures of reliability (provided by probabilistic methods) can be used to maximize the effects of inspections through optimization of the inspection schedule and techniques. The First Order Reliability Method (FORM) [25,26] is a relatively simple and straightforward technique for the evaluation of failure probabilities. The method is particularly useful in a fatigue reliability setting where each random trial or realization requires the integration of a crack growth relation to determine fatigue life. In such situations, Monte Carlo methods may prove unwieldy especially where extreme reliabilities such as those required in the aircraft industry are concerned.

In research carried out at Northwestern University, a First Order Reliability Method (FORM) has been developed which can account for in-service monitoring [26]. Statistical variations in material properties and associated fatigue crack propagation relations are determined in a companion materials thrust. Traditionally, the first order reliability method is applied to one inspection interval at a time which requires characterization of the crack size distribution (i.e., crack size probability density function) at the beginning of each inspection interval, which is costly and difficult. We have extended the traditional FORM to account for the effects of the inspections so that the crack size distribution need only be characterized at an initial state. As in the standard FORM, the probability of failure is evaluated through an integral over the failure set in a standardized Gaussian space, however a novel integration procedure is developed to account for the effects of inspections at discrete times. Numerical results show excellent agreement between the present method and Monte Carlo simulations (where Monte Carlo techniques are feasible and a comparison is possible). The present method also permits the analysis of complex components (involving 3D crack growth) for which the use of Monte Carlo methods at extreme reliabilities is impractical.

In addition to the FORM, Direct Integration methods provide an efficient and robust framework for the determination of fatigue reliability. A Direct Integration scheme will be developed and implemented for fatigue reliability to complement the FORM methodology and comparisons of the Direct Integration method, FORM, and Monte Carlo simulation will be carried out.

The fatigue reliability methodology for condition-based maintenance will be applied to failure critical components and systems identified by the PI in consultation with program monitors and industrial and military personnel. Candidate structural components include gears, drive shafts and rotor hub components in military helicopters, as well as similar hardware in civilian aircraft and in industrial machinery.

## Accomplishments

During M-URI year 1, some initial refinements of the First Order Reliability Method were carried out, particularly with respect to representation of failure probability in the case of multiple inspections. A Direct Integration scheme was then developed and coded. The method uses several techniques to enhance efficiency:

- i) A combination of Rao's method and Rosenblatt transformations has been used to map the given probability distributions for the random variables to a unit hypercube. By carrying out discretization (for integration of the probability of failure integral) on the unit hypercube, integration accuracy can be controlled.
- ii) By taking advantage of the conservation of probability mass, the effects of inspections can be separated out from the integration procedure. This is rigorously true for problems involving a single random variable. For more than one random variable(which is generally the case) the method is accurate to within the accuracy of the integration. More importantly, the method results in considerable savings in computer time over alternative methods which require application of the effects of inspection together with the integration. Consequently, the direct integration method, as implemented, is not limited by the number of random variables or the number of (NDE) inspections to be carried out - the effects of inspections enter through the so-called POD (probability of detection) curve.

The method was benchmarked against other methods to assess solution accuracy and was shown to be accurate, robust and efficient. In Figure 39, a schematic representation of the direct integration method is given. The initial crack size distribution is mapped (through the fatigue crack propagation relation) into the probability of failure distribution (i.e., the probability that the critical crack size  $a_f$  is exceeded).

Figure 40 shows how the initial crack size distribution evolves with load cycles  $N$ . The total probability of failure at cycle  $N$  is given by the integral of the probability of failure distribution in Figure 39. The effects of NDE inspections (which enter through application of a probability of detection (POD) curve) are illustrated in Figures 41 and 42. After an inspection at time  $N$ , only the shaded area in Figure 41, contributes to the probability of failure. This results in a reduction of the total probability of failure (CDF) below that obtained without inspections, as shown in Figure 42. A typical example is shown in Figure 43. The problem considered is that of an edge crack under cyclic (fatigue) loading. The probability of failure as a function of load cycles is shown and the effects of inspections at 3 times (150,000, 250,000 and 350,000 cycles) is evident. In Figure 43, a comparison of the results for the Direct Integration method and Monte Carlo simulation (MCS) shows excellent agreement between the two methods.

The direct integration scheme is currently being implemented for cracks in 3D components and comparisons of the method with FORM will be made for 3D problems.

A limitation of the FORM is that it can become inaccurate when the curvature of the failure hypersurface becomes large. (The failure surface is a surface which, at the load cycle in question, divides the space of random variables into safe and failure regions.) A method is being implemented to use piecewise linear (or hyperplanar) representations of the surface for increased accuracy.

Graduate student, Ali Zulfiqar, also familiarized himself with the working of *ProE* for purposes of generating solid models and meshes of safety critical components in future applications of the fatigue reliability methodology.

Brian Moran visited Cherry Point in January 1996 and was briefed on various fracture related issues pertaining to rotary components in helicopters. Potential areas for application of the fatigue reliability methodology were identified. The applications of the methodology in the context of both safe-life and damage tolerance analyses were also discussed. Contacts at Cherry Point include Wilbur Batten, John Cammett, Gary Smith, Tom Osiecki and Rob Atencio.

### Probability Mass Conservation

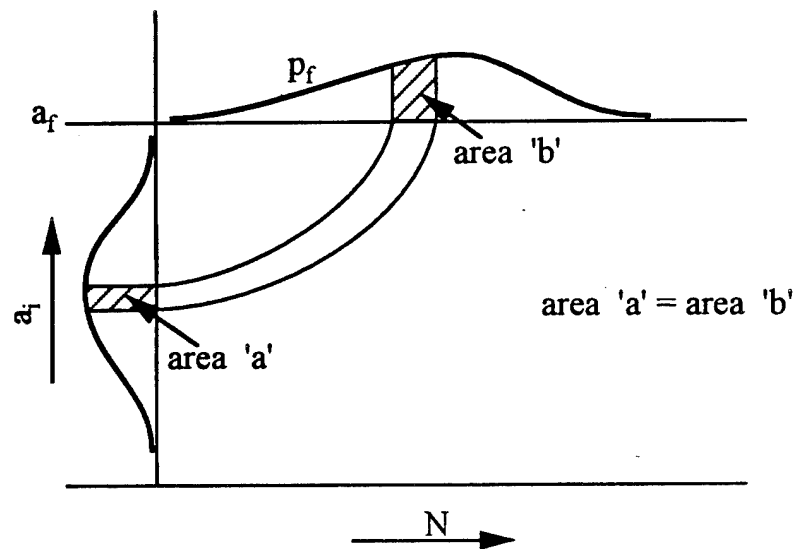


Figure 39 . Mapping of crack size distribution on the final crack line

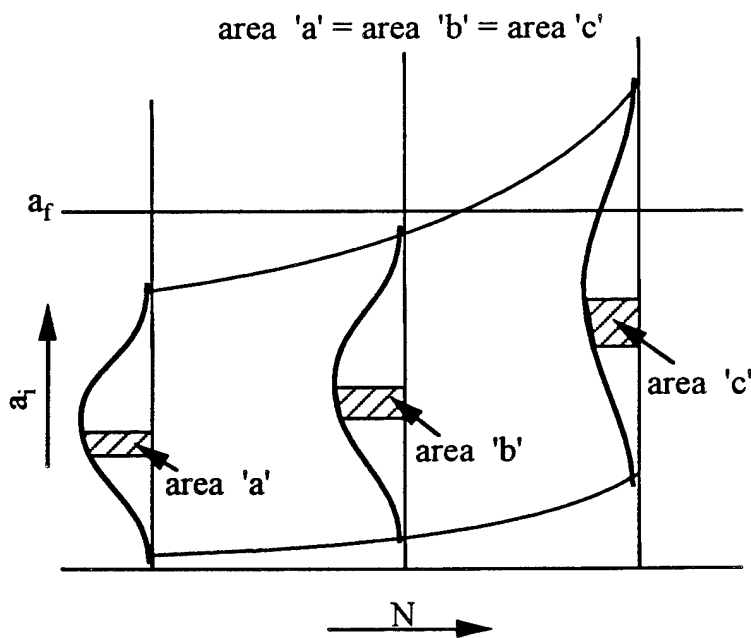
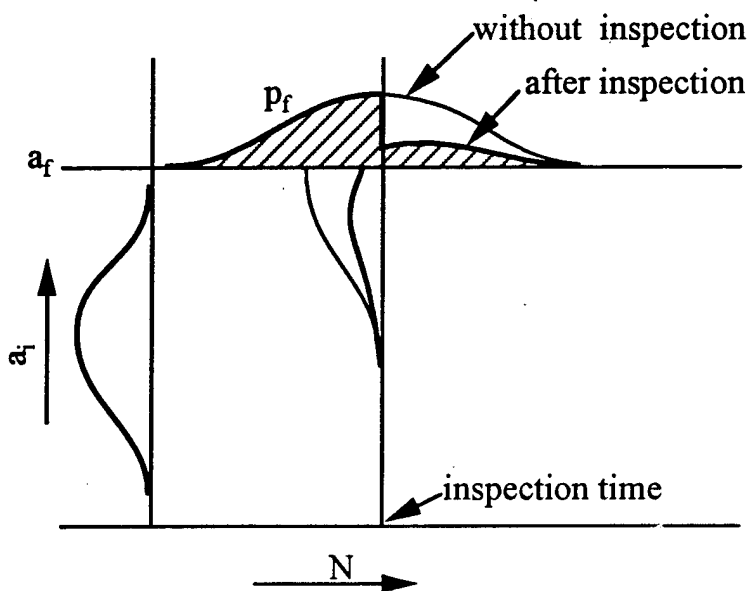
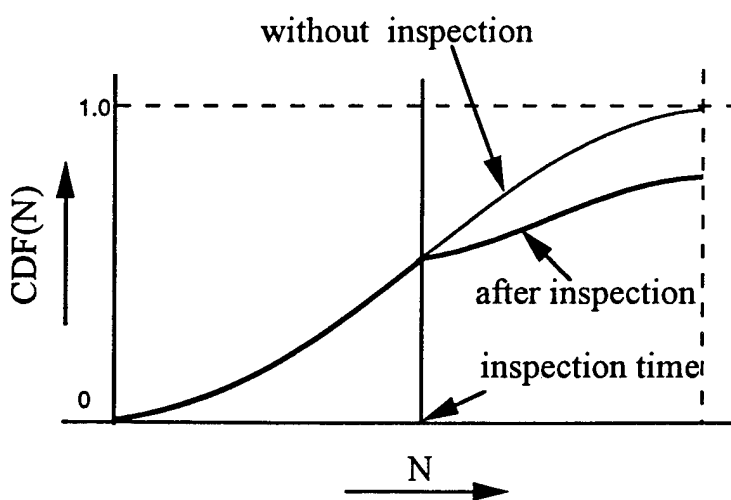


Figure 40 . Change of crack size distribution with the no. of fatigue cycles



**Figure 41 . Shape of failure probability density function (  $p_f$  ) with and without inspection**



**Figure 42 . Change in probability of failure(CDF) curve after inspection**

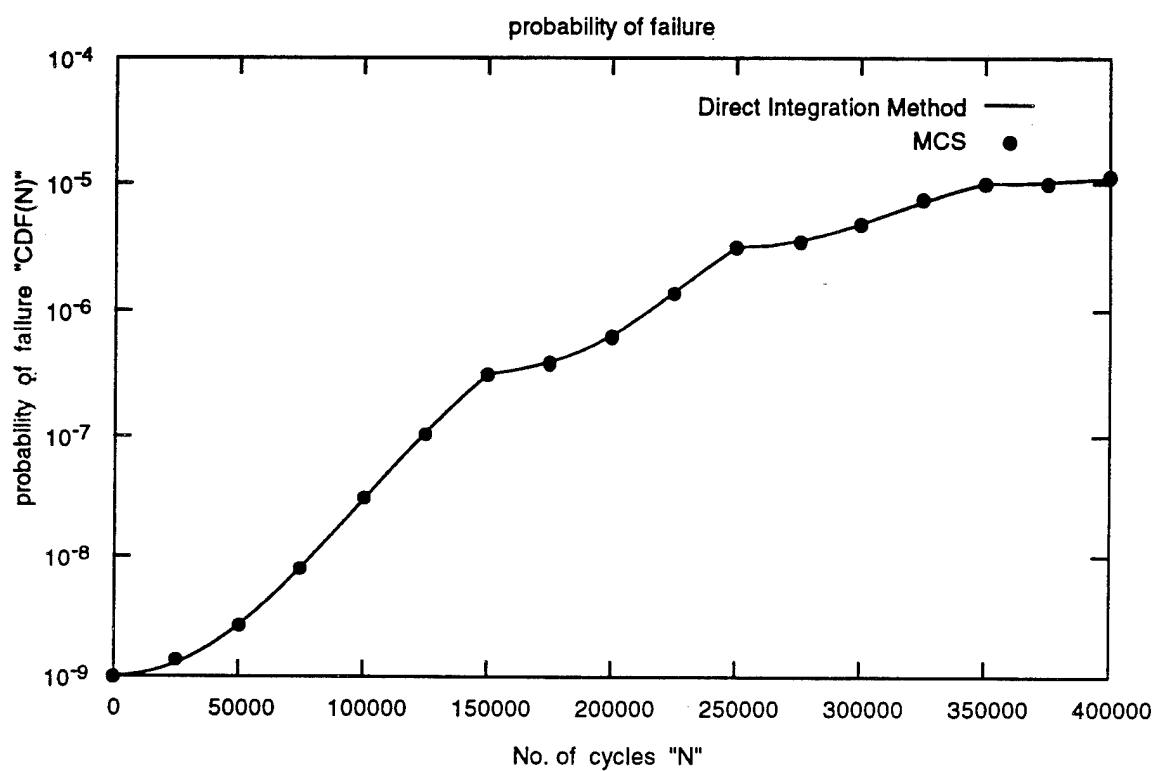


**Figure 43 . CDF versus N for an edge crack in a plate under tension**

## **Plans**

In M-URI year 2, the reliability modeling procedures will be completed and application of the methodology to safety critical components will be begun. In particular the following tasks will be completed:

- Implementation of the direct integration method for 3D fracture problems.
- Complete implementation of the piecewise linear failure surface representation in FORM.
- Investigation of a generalized reliability index for characterizing reliability where there is uncertainty in knowledge of probability distributions for loads, material properties and crack growth relations.
- Selection of safety critical parts (in conjunction with Navy personnel)
- Application of the fatigue reliability methodologies (Direct Integration, FORM, Monte Carlo to safety critical components selected in consultation with Navy personnel).
- A technical report on fatigue reliability methods for condition based maintenance will be completed - 3/31/96.
- Technical Report on application of fatigue reliability methodology to a selected component - 12/31/96.

## *Milestones*

12/31/95	Fatigue reliability methodology for CBM developed
12/31/96	Methodology applied to selected critical components
12/31/97	Software and documentation on methodology prepared for transfer

### 2.3.1 INTEGRATED MICROSENSORS FOR AIRCRAFT FATIGUE AND FAILURE WARNING

Co-investigator: Dennis Polla (University of Minnesota)

#### Overview

The objective of this project is to develop real-time sensing devices and methods to accurately identify conditions leading to the imminent and future failure of critical aircraft components. Two key technologies are brought together: solid-state microsensors and advanced signal processing methods. The microsensors include acoustic emission (AE) sensors for the detection of crack development and unusual wear, microbeam accelerometers for the detection of unwanted excessive mechanical vibrations, and temperature sensors for both signal referencing and identification of excessive heating. Several advanced signal processing methods are used to interpret the amplified signals of the variables being sensed. The signal processing challenge addresses identifying true failure signatures in a real-time and in a noisy environment. A goal of this project is to realize inexpensive silicon chips, or "coupons" which can potentially be distributed over the critical regions of an aircraft. This coupon might contain a variety of microsensors for detection and cross-confirmation of multiple failure signatures. By also integrating analog signal conditioning electronics, A/D converters, digital signal processing circuits, memory, and telemetry, smart microsystems can be formed. The silicon-based coupon concept is represented in Figure 44.

This project therefore addresses the feasibility of applying recent microsensor technologies and signal processing algorithms to 1) make military missions safer, 2) extend the usable lifetime of military platforms, and 3) make routine maintenance more efficient. The following main tasks for this project were accomplished this year:

- Piezoelectric materials were designed and synthesized.
- AE and accelerometer processes were developed.
- AE and accelerometer devices were designed and fabricated.
- Diagnostic AE test chip devices were tested.
- Microcrack physics and AE microsensor calibration has been carried out using nanoindentation.
- AE signal analysis is underway.

##### 2.3.1.1 *Microsensor Development*

This section describes the technical approach taken toward realizing microsensors for aircraft health monitoring, including recent accomplishments and future plans.

#### Accomplishments

Three general areas have been addressed in the first year of this program: a) development of active piezoelectric thin films for microsensors, b) design and fabrication of prototype microsensors, and c) the study of the physics of microcrack initiation and propagation including baseline signal calibration methods.

##### A. PIEZOELECTRIC MATERIALS

Piezoelectric ceramics have desirable characteristics for both microsensor and microactuator applications due to the strong piezoelectric effect commonly observed in these materials. The spontaneous charge induced from mechanical strain in a piezoelectric thin film is easily sensed in a

#### *Direct Sensing, Analysis, and Real-time Diagnosis*

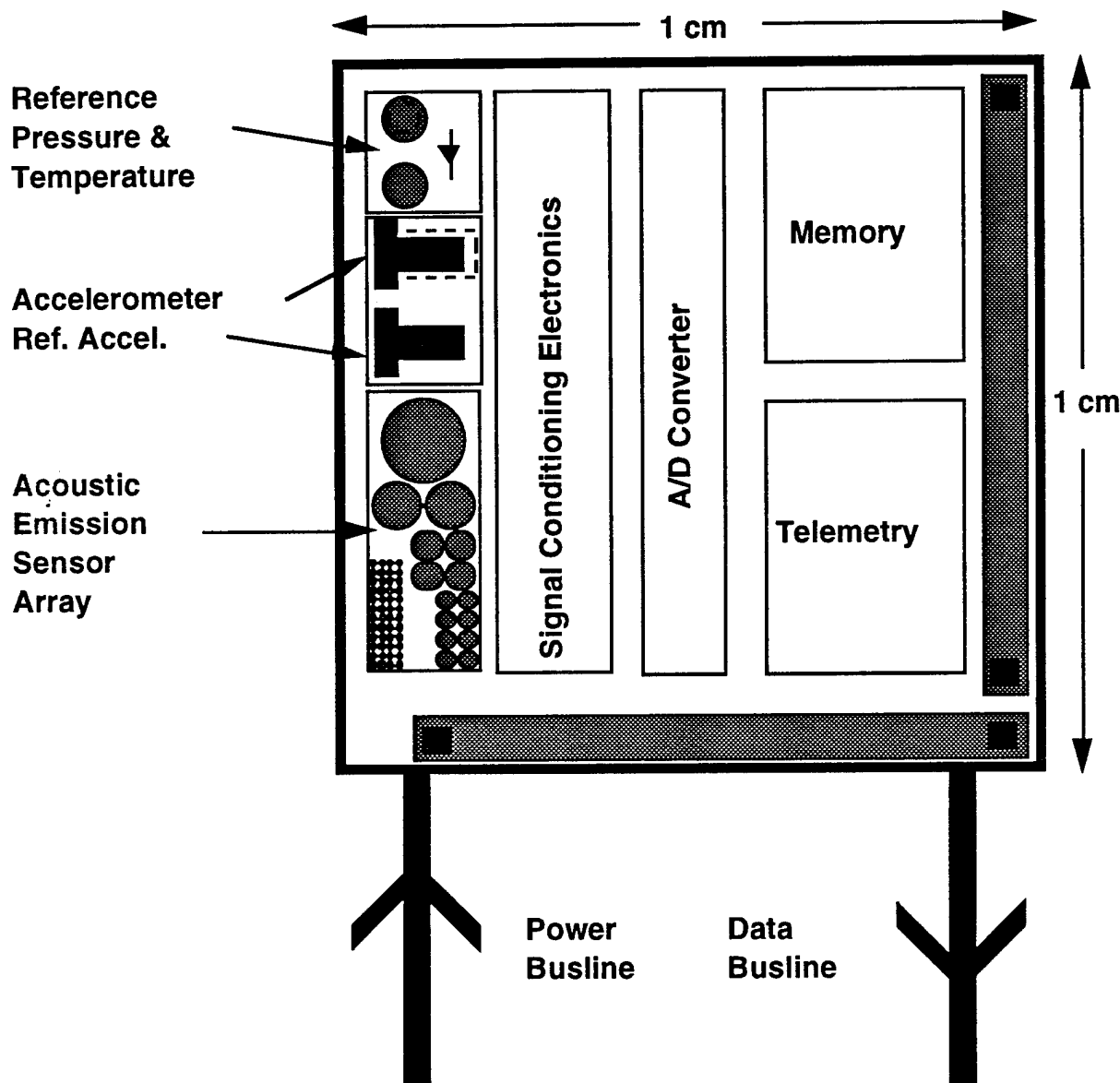


**Figure 44** Concept of an inexpensive, small, and light-weight aircraft condition monitoring coupon. Several microsensors and electronic library cells are used to detect physical signatures associated with incipient failure and record information related to fatigue and wear or critical components.

capacitor structure using a voltage or charge-sensitive amplifier. Furthermore, piezoelectric sensors (and actuators) do not dissipate power in the static mode, and the piezoelectric's excellent dielectric properties result in extremely low electrical noise during operation. Unlike nonferroelectric piezoelectric materials, such as ZnO and AlN, poling allows polycrystalline thin films to be used. Among the many ferroelectric ceramics, materials in the lead lanthanum zirconate titanate, PLZT, family (which includes  $PbTiO_3$  and  $Pb(Zr_xTi_{1-x})O_3$ , PZT) are good candidates as this family contains materials that offer excellent electromechanical, dielectric and pyroelectric properties.[27]

Microelectromechanical systems, or MEMS devices, using piezoelectric ceramic thin films have been the subject of several reports.[28-31] Device designs for electromechanical applications typically include a thin, flexible structural materials covered with the ferroelectric thin film sandwiched between metal electrodes. The composite structure can be fabricated by bulk micromachining in which a silicon membrane is prepared by etching from the back side of the silicon wafer. An alternative technique, surface micromachining [32], involves selective material removal from thin films deposited on the surface, as discussed below. In this project, we have prepared piezoelectric thin films on both flexible membranes and solid silicon surfaces for both vibration and acoustic emission sensing, respectively.

The fabrication of piezoelectric MEMS usually relies on the compatible integration of over fifty individual process modules. Figure 45 shows an abbreviated schematic of the process steps used to fabricate a piezoelectric accelerometer for vibration sensing. In the device design, vibration causes the cantilever to bend, deforming the PZT layer and leading to an induced charge on the electrodes. The fabrication technologies for ferroelectric MEMS include sol-gel processing (or solution deposition) for the ceramic thin film, chemical vapor deposition for sacrificial and structural materials, sputtering for electrodes, photolithography, and selective material etching. In designing a process sequence, consideration is given to ordering of process modules, stress control in MEMS structures, control of impurity diffusion usually set by a so-called thermal budget, thin film deposition methods, etching selectivity, and transistor parameter control. On-chip electronics are typically fabricated first and encapsulated to avoid any possible contamination. Then, MEMS are added in a back-end fabrication process.

Beams and other free standing structures for MEMS are created by depositing a structural material such as silicon nitride onto a sacrificial material that is later removed by etching. This surface micromachining process does not affect the mechanical integrity of the semiconductor substrate and allows the easy incorporation of on-chip electronics.[33] As shown in Figure 45, the sacrificial material is phosphosilicate glass (PSG) which is deposited in a recessed well by low pressure chemical vapor deposition (LPCVD) and then patterned and etched to define the region that will be open in the final structure. PSG has enough thermal stability for the subsequent processing steps and can be etched rapidly with HF. Polysilicon and silicon nitride are common structural material although other materials such as Al are also used. Polysilicon is used in many MEMS devices and has good mechanical properties; however, a high temperature anneal ( $\sim 1050^\circ C$ ) is required to reduce compressive stresses. The high temperature treatment is not always compatible with the on-chip electronics. By contrast, silicon nitride is the material of choice for the MEMS described here, because it can be prepared with low stress (90 - 105 MPa tensile) using LPCVD ( $800^\circ C$ , slightly Si rich conditions) and no annealing is required. The lower electrodes are then deposited on the structural material followed by processing of the ferroelectric coating.

The choice of lower electrode material impacts the performance of the device. Lower electrodes are commonly sputter deposited platinum with thin titanium layer for adhesion to the underlying structure. Silicon diffusion from the structural material can lead to the unwanted formation of platinum silicides, and pyrochlore phase in the ferroelectric layer. To prevent such diffusion, a barrier is incorporated. For MEMS devices, the barrier thickness must be kept to a minimum so that the sensing or actuating response is not compromised.[34] We have found that a very thin layer of titanium dioxide formed in situ during sputtering of titanium prevents both silicide and pyrochlore formation.[35]

The processing of the ferroelectric layer is of central importance to MEMS as this layer provides the piezoelectric properties. In addition to achieving a film with the desired properties, the ferroelectric processing step must be compatible with the entire fabrication sequence. Sol-gel and other solution deposition methods are well suited for MEMS applications, because coatings with reproducible compositions and properties can be prepared at acceptable processing temperatures. In a typical sol-gel process, a solution comprised largely of metal alkoxides is synthesized and deposited by spin coating; the resulting coating is heated to develop a crystalline ceramic layer. Many synthetic routes for solution deposition processing have been proposed. We have mainly used the alkoxide route based on 2-methoxyethanol (2MOE) originally developed by Budd et al.[36] This route provides coatings with consistent microstructure and properties. The main materials synthesis route is described in Figure 46.

Since spin coating is used to prepare the piezoelectric thin films, inherent challenges arise for accommodating MEMS structures with surface topography. To investigate these limitations, we prepared sol-gel PZT coatings (based on the 2MOE route) on substrates with elevated surface features (step height 0.13 - 1  $\mu\text{m}$ ; 45° rise angle). Sol-gel coatings partially planarized the features so that the PZT coatings were thinner on top of the feature as compared with the surrounding substrate surface. After the high temperature (700°C) heating, cracks and delamination developed near the top and bottom of the step when the ratio of coating thickness to step height was less than ~0.35. These defects originated from stresses which are enhanced by the presence of the step and by the thickness nonuniformities. To best accommodate surface features, multilayer deposition was used to build up the coating thickness prior to the higher temperature processing steps. By this method, features up to ~ 0.8  $\mu\text{m}$  high with a rise angle of 45° could be successfully coated. Planar device designs, such as the one shown in Fig. 45, eliminate these problems and are always preferred. For structures that must be raised (e.g., horizontal actuators), shallower rise angles lessen the thickness non uniformity and cracking.

The final processing steps are the deposition of the upper electrode (Pt/Ti), patterning, contact metallization, encapsulation and freeing of the device by selective etching of the sacrificial layer. After Pt/Ti top electrodes are prepared by sputtering, patterning by reactive ion etching (RIE) is carried out using a top-down process which minimizes impurity diffusion into the PZT. Metal contacts are then fabricated and patterned. An encapsulant (e.g., bias sputter deposited silicon nitride, chromium) is then coated over the structure and openings to the PSG layer are prepared. The micromachined structures are released by lateral etching of the PSG in HF, followed by an extended rinse in deionized water and drying. The encapsulant can then be removed if necessary; for example, a blanket dry etch is used to remove sputter deposited silicon nitride.

Figure 47 shows the results of PZT materials synthesis carried out in this program. The x-ray diffraction spectrum shown indicates excellent thin film perovskite crystallinity indicative of a well control materials synthesis route. Other properties important to the microsensor and actuator devices of this program are summarized in Table 3.

**Table 3.** Summary of PZT thin film electrical and mechanical material properties.

Relative dielectric constant	965-1006
Dielectric loss tangent @ 1 KHz	0.02-0.04
Remanent polarization	35 $\mu\text{C}/\text{cm}^2$
Coercive field	54 kV/cm
Resistivity	$> 10^{11} \Omega\text{-cm}$
Dielectric breakdown strength	0.6 - 0.8 MV/cm
Piezoelectric coefficient $d_{33}$	190-220 pC/N
Young's Modulus $E_Y$	$4 \times 10^{11} \text{ N/m}^2$

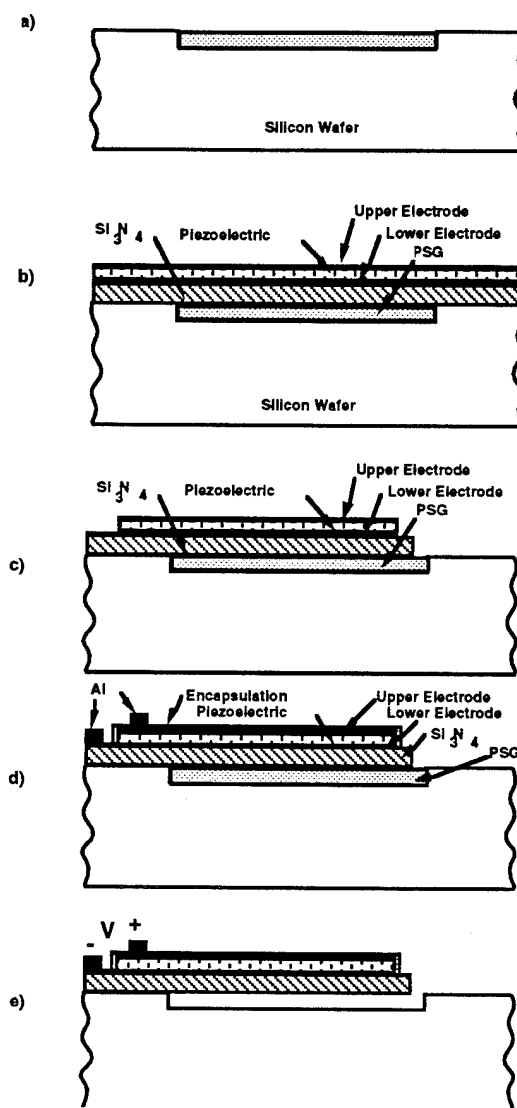


**Figure 45** Abbreviated schematic of process steps used to fabricate an accelerometer showing a cross-section of the device after: (a) deposition and patterning of phosphosilicate glass (PSG) sacrificial material in a recessed well, (b) deposition of silicon nitride structural material, electrodes and PZT piezoelectric layer, (c) patterning of PZT, electrodes and silicon nitride, (d) metallization, deposition of encapsulant and patterning, (e) final etching to remove PSG and free the device.

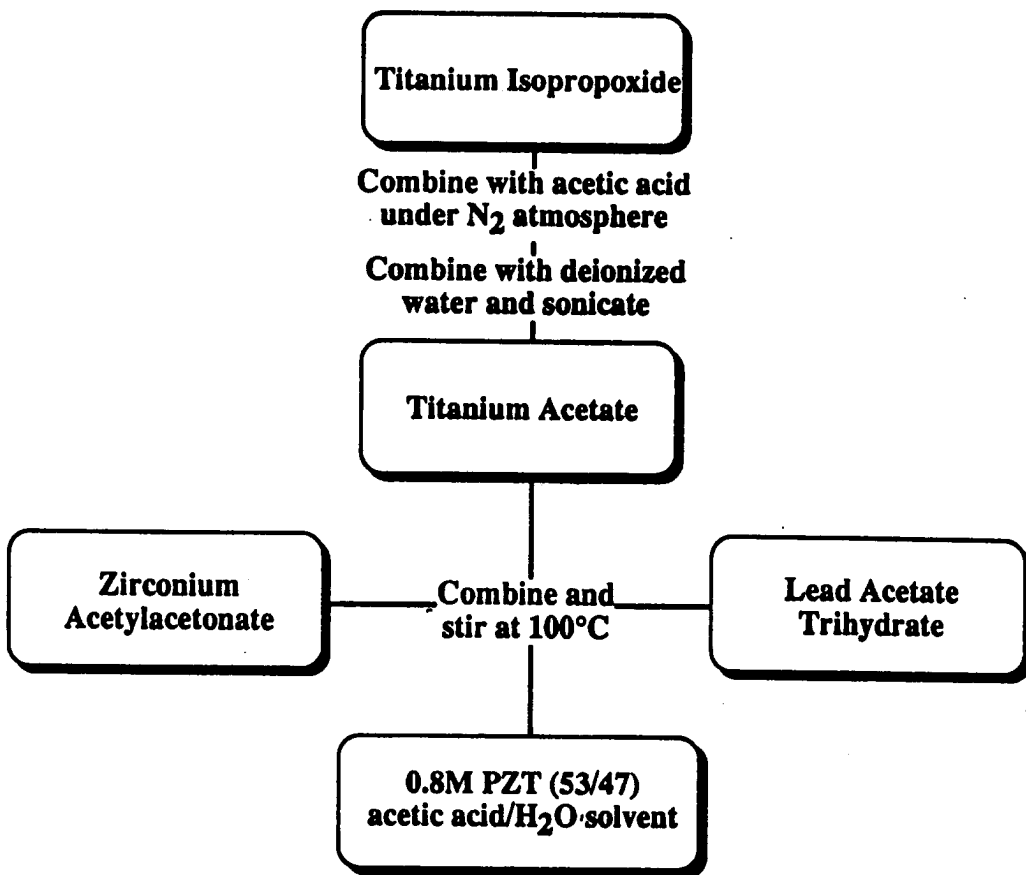


**Figure 46.** Chemical processing route leading to the preparation of piezoelectric thin films for sol-gel dispensing on silicon wafers.

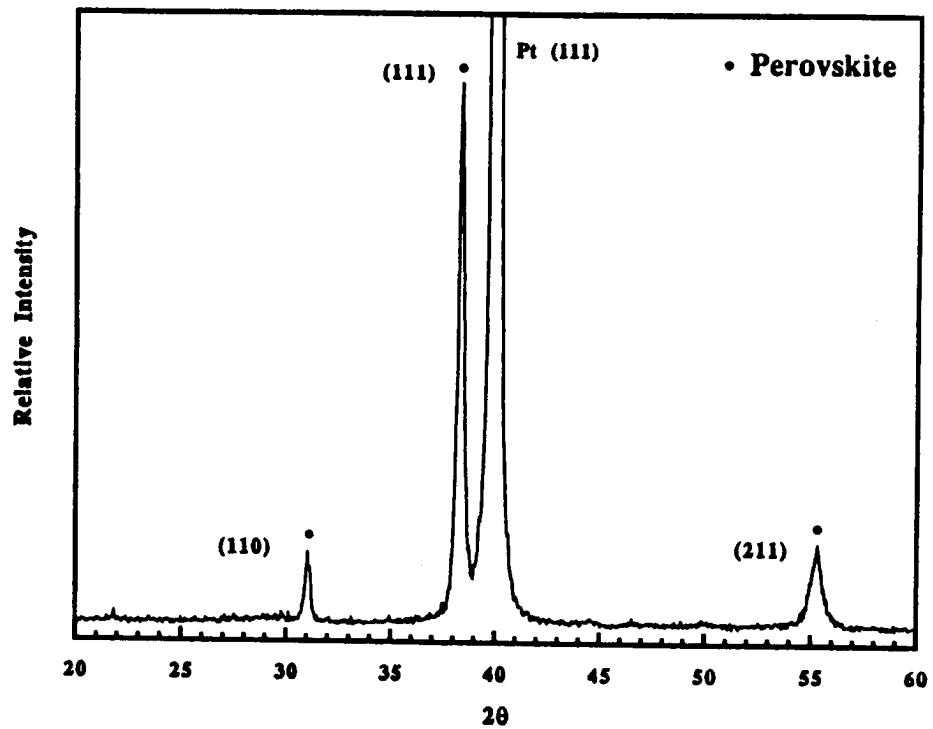


**Figure 47** X-ray diffraction spectrum obtain for a  $0.35\text{ }\mu\text{m}$ -thick PZT thin film on a Pt-coated silicon substrate.

## B. MICROSENSOR DEVELOPMENT

### *Design*

When a piezoelectric crystal is stressed, the natural spacing among constituent atoms is changed altering the net internal dipole moment of the crystal. This change in internal dipole moment is compensated by an induced charge on defined electrode surfaces. By directly reading this charge or converting it to a voltage, an electrical signal is produced in proportion to the stress.

The relationship between electrical and mechanical properties of piezoelectric microsensors and microactuators is governed by the piezoelectric constitutive equations.[27]

$$[S_j] = [s_{ij}][T_j] + [d_{ik}][E_k] \quad (3)$$

$$[D_i] = [\epsilon_{lm}][E_m] + [d_{ln}][T_n] \quad (4)$$

where  $j, n = 1, \dots, 6$ , and  $i, k, l, m = 1, 2, 3$ . Here S is strain, s is the elastic compliance, T is stress, D is the electric displacement, E is electric field,  $\epsilon$  is the dielectric permittivity, and  $d_{ij}$  are the piezoelectric constants, which relate the electric field in direction  $j$  to the deformation in direction  $i$ . These equations express both Hooke's law and Gauss' law for piezoelectric materials, and form the scientific basis for the design of piezoelectric MEMS. Particularly important to MEMS design is a priori knowledge of the important material parameters such as piezoelectric constants, dielectric constants, and compliances (usually expressed as the reciprocal of Young's modulus  $E_Y$ ).

The piezoelectric constitutive equations form the basis of physical microsensors such as that used in the AE sensors and vibration monitoring devices of this project. Table 4 shows a simplified comparison of the induced charge and voltage obtained by piezoelectric voltage and charge readout methods.

### *Acoustic Emission Microsensors*

AE sensors[37] were designed and fabricated for the detection of crack initiation and propagation. The activity in this phase of the program concerned materials development and compatible integration of process modules to realize a silicon-based piezoelectric AE sensor. Figure 48 shows a cross section schematic of a piezoelectric AE microsensor studied in this project.

A diagnostic test chip was fabricated to test the AE microsensor concept presented in Fig. 48. This required the development of several unit process modules including 1) stress-controlled  $\text{Si}_3\text{N}_4$  encapsulation technology which will eventually protect on-chip electronics during integrated AE microsensor fabrication, 2)  $\text{TiO}_2$  buffer layer technology to create stable and reproducible interfaces, and 3) and PZT dry-etch definition techniques compatible with the other materials on the wafer. The PZT AE test chips fabricated were diced and mounted in ceramic packages and wire bonded. An optical photograph of a finished AE microsensor is shown in Figure 49.

AE testing was carried out to confirm sensitivity to acoustic signals. A variety of experiments were carried out to confirm this using discrete AE microsensors and external voltage- and charge-amplifiers. Electrical signals were observed in response to acoustic energy both derived from conventional audio sources and due to simulated cracking events established by mechanical pencil lead breakage experiments.

Several observations were made in the electrical testing experiments. First, electrical interconnections limit the ability of the AE microsensors to perform with optimality. In particular, interconnect capacitance and the relatively large capacitances associated with external pre-amplifiers present signal losses. Second, external wires connected to the AE sensor introduces EMI pick-up which in many cases interferes with the true AE signal. Third, visible light effects influence the output of the piezoelectric material. These problems are largely solvable however. In year 2, we will directly

**Table 4** Voltage and Charge Readout Modes for Piezoelectric Microsensors

Voltage Readout	Charge Readout
<b>Voltage Output (<math>D = 0</math>)</b>	<b>Charge Output (<math>E = 0</math>)</b>
$D = \epsilon E + d T$	$D = \epsilon E + e S$
$E = \frac{V}{t} = - \frac{d}{\epsilon} T$	$D = \frac{Q}{A} = e S$
$\frac{V}{T} = - \frac{d}{\epsilon} t$	$\frac{Q}{S} = e A$
<p>For thin film AE sensor using PZT, <math>d = 3 \times 10^{-10} \text{ m/V}</math>, <math>e = 10 \text{ coul.} \cdot \text{m}^{-2}</math>, <math>\epsilon = 1000 \epsilon_0</math>, <math>t = 1 \text{ micron}</math>, and <math>A = 1 \text{ cm}^2</math> (typical of commercial sensors).</p>	
$\frac{V}{T} = 3 \times 10^{-8} \text{ V} \cdot \text{m}^2 \cdot \text{N}^{-1}$	$\frac{Q}{S} = 0.002 \text{ coul. per unit strain}$
<p>Relative to a reference of <math>T = 1 \text{ microbar} (10 \text{ N/m}^2)</math></p>	
$\frac{V}{T} = -150 \text{ db}$	$\frac{Q}{S} = 2 \times 10^{-15} \text{ coul. (thickness-independent).}$
<p><b>Conclusion:</b> Thin film AE sensors should operate in charge output mode.</p>	

integrate on-chip pre-amplifiers with the AE sensors. EMI pick-up will be minimized by the shortened distance from the AE microsensor to the input pre-amplifier. A metal top cap on the ceramic package also reduces EMI and eliminates the parasitic light effect.

Based on the best experimental testing conditions established, microfabricated AE sensors were tested to confirm responsivity to simulated cracking events. A microsensor package was mounted with a thin epoxy layer directly to a flat surface of a CH-46 pitch shaft housing. A mechanical pencil lead breakage test was used to simulate microcracking. Light banging with a hammer was also used. Figure 50 shows an AE signal (displayed as amplified voltage versus time) detected by a microfabricated sensor under the best conditions of minimizing EMI. The signals measured were approximately 0.25 to 0.5 pC (or 50 to 100  $\mu\text{V}$ ) in peak amplitude without external pre-amplifier gain. Several additional experiments were carried out using external electrical high-pass filtering techniques to eliminate audio signals in the 20 Hz to 20 kHz range as well as varying the location of the signal source with respect to the microsensor location.

The results of these experiments demonstrate 1) functionality of microfabricated AE sensors in detecting high frequency acoustic signals (20 kHz to 1 MHz), 2) the need for integrated AE microsensors with sensor and pre-amplifier located on the same chip or hybrid connected with short wire bonds, and 3) successful signal coupling through the interfaces of the attachment epoxy, ceramic package, and silicon substrate.

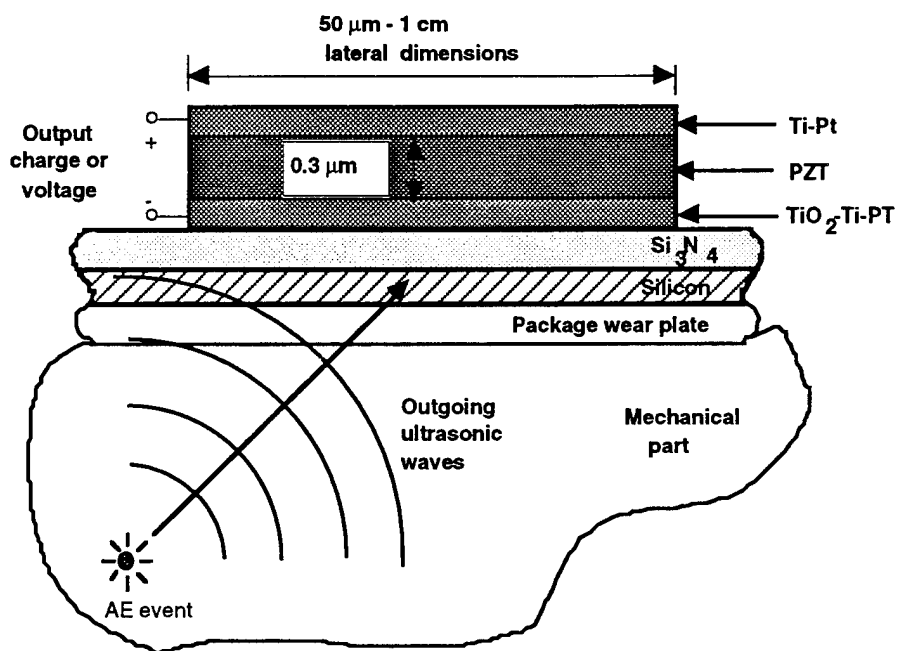


**Figure 48** Acoustic emission microsensor approach showing a piezoelectric thin film acoustically-coupled to an aircraft component.

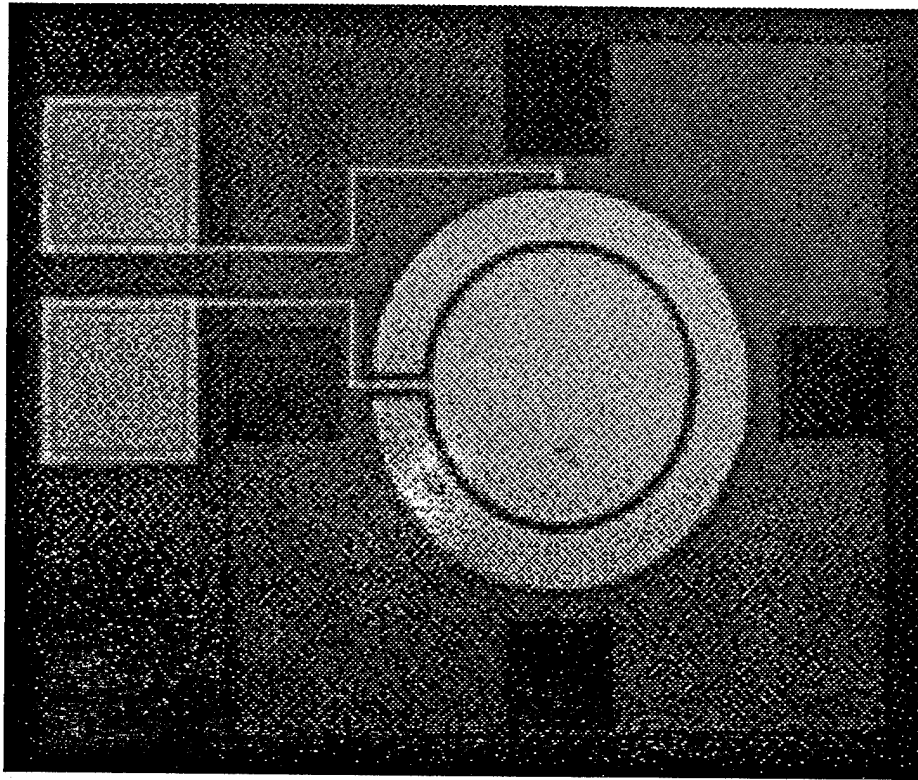


**Figure 49** Optical photograph of an AE piezoelectric microsensor with active area of  $2.0 \times 10^{-3} \text{ cm}^2$ .

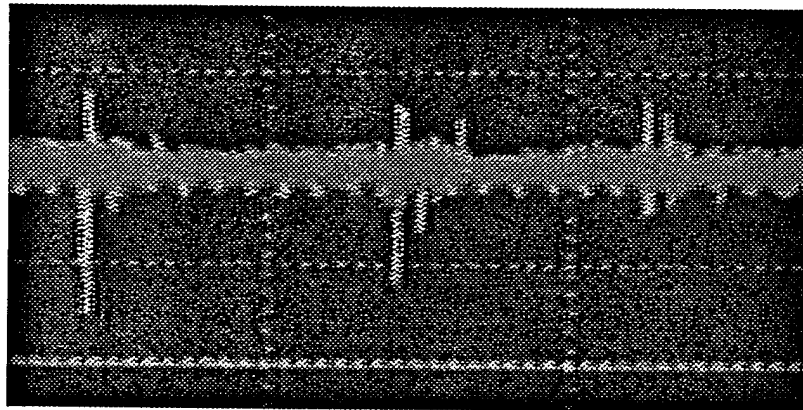


**Figure 50** Voltage responsivity for an AE microsensor to the breakage of a pencil lead. The sensor is located on a helicopter pitch shaft approximately 4 cm from the location of acoustic signal source.

### *Vibration Microsensors*

The real-time detection of extraordinary vibration might provide important information in a failure prediction algorithm for a particular system. Vibration microsensors were fabricated in this program using similar piezoelectric thin film microsensors as those used in the AE microsensor above. A main fabrication difference for the vibration microsensor is the need to have a free-standing cantilever oscillate in response to vibration signals. This requires the use of solid-state micromachining techniques to form a deformable microbeam as shown in Figure 51. The process for making this structure is described in Figure 45.

In the operation of the vibration sensor, inertial movements produce a time-varying stress across the piezoelectric material thereby producing a spontaneous charge. This charge is sensed by an amplifier or converted to a voltage for subsequent signal processing. Figure 52 shows a scanning electron micrograph of a piezoelectric cantilever measuring  $40 \times 200 \mu\text{m}^2$ .

The electrical characterization of this device is underway at the time of this writing. Shaker table testing experiments are scheduled for March 1996. In further refinement of this structure, both real-time vibration monitoring will be used as well as counting of the number of events in which the cantilever undergoes an amplitude excursion above an arbitrary threshold value. By counting the number of these threshold cycles and recording this information during flight, ground-based readout techniques might eventually be applied to determine information on fatigue and remaining useful operating lifetime.

## **C. MICROCRACK MATERIALS PHYSICS AND REFERENCE SIGNAL CALIBRATION**

### *Method*

Detecting fatigue cracking using acoustic emission (AE) in situations which have additional environmental noise will require knowledge of the frequency and pattern of specific events. Once the type of signal that is to be detected is known, the sensor and filtering can be designed to emphasize these events. Therefore, a goal of this project is to generate specific failure events, and then detect and analyze the acoustic emission signals which occur from the failure. Initial testing uses a commercial detector to sense AE events, however, thin film AE microsensors developed during this project will be used to detect events during M-URI year 2.

Physical cracking events are generated using a micromechanical testing device (MMT), which drives a diamond tip into a sample while measuring the load and the penetration depth of the tip into the sample. These types of indentations are commonly referred to as nanoindentation. The MMT has very fine load and depth resolution, and can generate individual physical events, allowing the specific AE signal to be monitored. This is a significant change from previous uses of AE detection, where mostly statistical phenomena regarding count rate and amplitudes of multiple events have been used to identify overall behavior.

The generation of events focuses on several different physical phenomena which will be of interest to this study. First, the delamination of a microsensor from a substrate will be examined. This situation corresponds to many problems in microelectronic circuits and structures, whereupon thin films are deposited in varying layers to produce a specific circuit. When these films are placed under stress or vibration, the possibility exists for the films to delaminate from the substrate and lose contact, thereby failing. Since thin film sensors are to be used for this study, the possibility of sensor failure must be considered. If a portion of the sensor itself fails, an acoustic emission signal will be generated, allowing either the remaining portion of the sensor or another detector to identify what type of failure occurred. This allows the sensors to be replaced if delamination failure occurs. In addition, other physical phenomena related to the sensor which may be of interest are film cracking and substrate cracking. All three types of events can be generated, and will be used to identify events which may effect detector integrity.

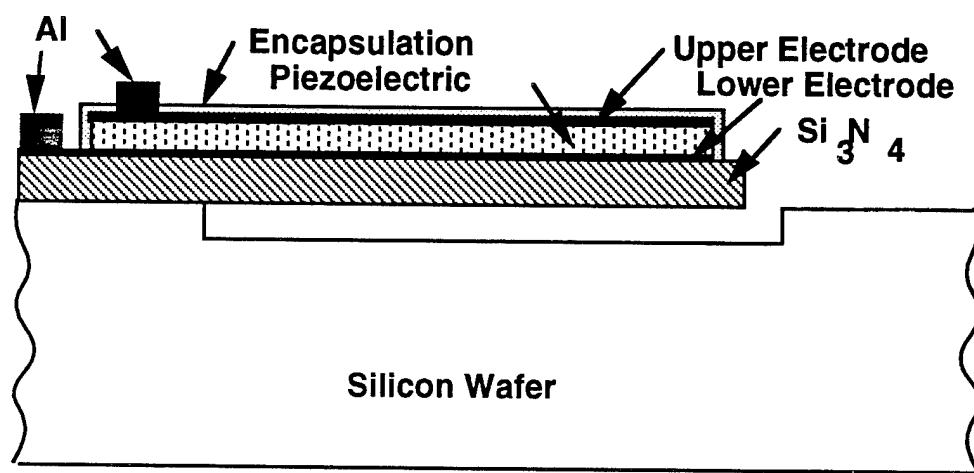
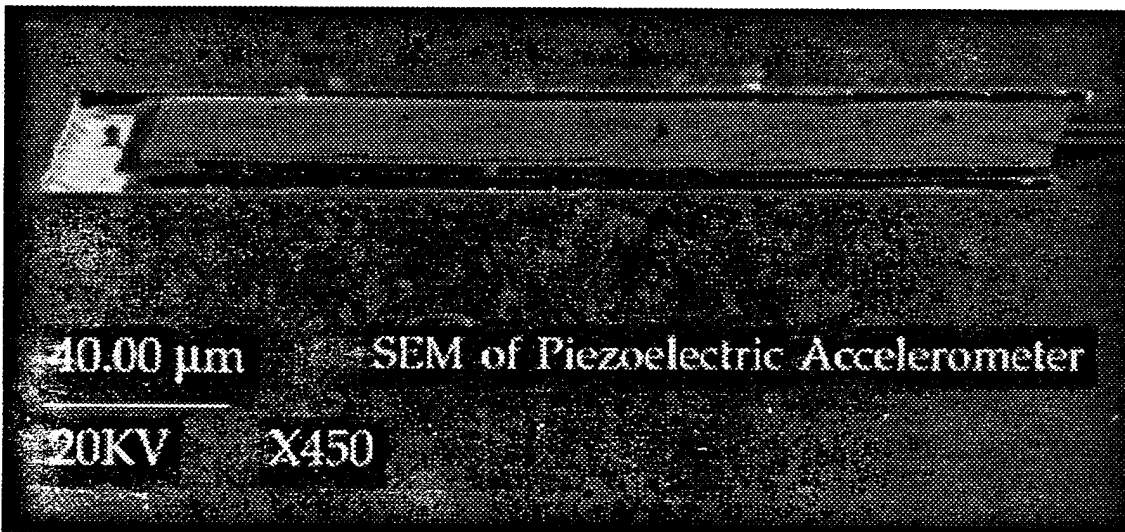
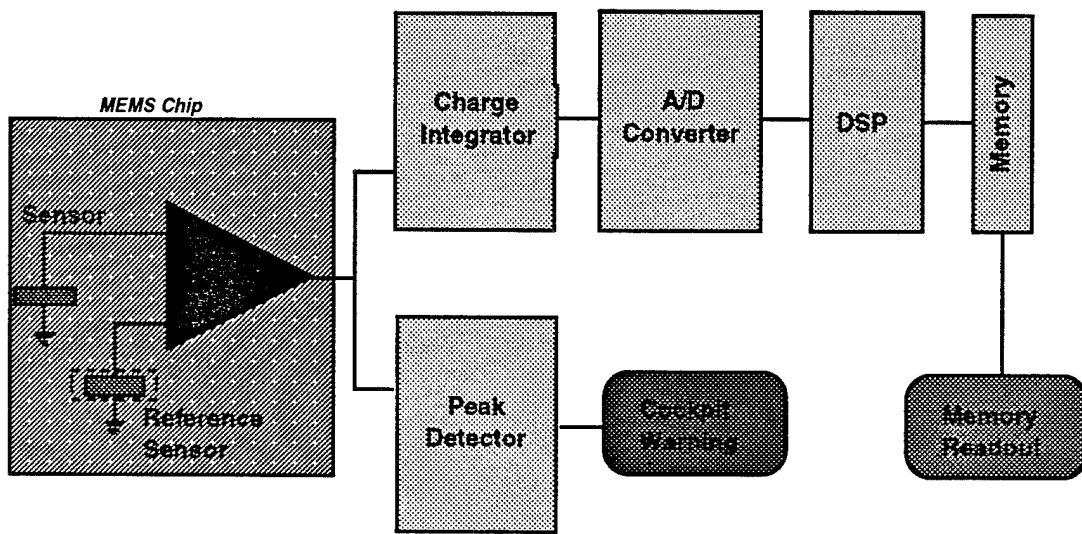


Figure 51 Cross section of a piezoelectric microsensor fabricated on a silicon nitride microbridge.



**Figure 52** Scanning electron micrograph of a cantilever beam piezoelectric vibration monitoring device.



**Figure 53** Vibration monitoring approach for both real-time and maintenance based fatigue cycle monitoring.

The second type of phenomena of interest is the actual events which lead to failure of structural parts. Fatigue cracking, the type of failure which leads to a large portion of parts in aircraft applications, has several components which can cause acoustic signals to be generated. During fatigue, dislocations are generated at a crack tip, and motion of the dislocations during loading cycles advances the crack tip, causing the crack to grow. In addition, a crack path may move inter-granularity leaving behind a tortuous crack path. The sides of the crack will rub together during cyclic loading as the crack opens and closes, causing friction and further acoustic emission. These two behaviors, dislocation generation and friction, may generate different AE signals. Therefore, generating physical phenomena which correspond to these events will provide information to be used for the actual identification of fatigue in structural parts. The understanding of these physical events is important in interpreting the electronic signature detected by a microsensor in-flight.

The last portion of this study will be to compare the sensing capabilities of the thin film piezoelectric microsensors developed during this project to those of commercial AE sensors. Generating individual, well characterized events provides a standard comparison between the microsensors and the commercial sensors. This information can be used to help refine the processing of the microsensors to optimize the signal output.

#### *Instrumentation*

To generate individual physical events, the MMT is used to indent samples of a variety of materials. The testing apparatus is shown in Figure 54. The MMT is run in displacement control in this experiment, so the indenter tip is driven towards the sample at a constant rate. The load and penetration depth are recorded during this indentation, at a recording rate of approximately 10 to 100 points per second. The physical events of interest in this study are usually identified by discontinuities in the load - depth curve. A schematic curve identifying the area of interest is shown in Figure 55. This discontinuity results from the rapid displacement of the tip into the sample, and corresponds to the initiation and growth of a crack along the interface between the film and the substrate. By indenting with the MMT, these events can be generated on a scale where the actual individual crack can be identified using either light or scanning electron microscopy.

The AE signals of interest in this study are collected using a Tektronix 2216 Digital Storage Oscilloscope. The AE sensor is mounted to the sample being indented, as shown in Figure 54, and the output of the sensor is run through an amplifier capable of 40 or 60 dB gain. This amplified signal is then fed into the oscilloscope. The scope is set with a trigger level such that any signal from the AE sensor greater than the noise level of the sensor is recorded using a single burst trigger routine. By varying the length of the record (between 512 points and 128,000 points) and the time step per sample, total record length times between 25.6  $\mu$ s and 16 seconds can be used. For the bulk of this work, sampling rates of 8 to 20 million samples per second for 16,000 samples will be used. Once the AE signal triggers the oscilloscope, the triggered data must be saved and the scope re-armed to collect another event. While presently done manually, this will eventually be controlled by the same computer which drives the MMT. In addition, the output of the sensor can be collected at any time during and indentation by manually triggering the scope. Multiple records can be saved in the oscilloscope memory during one indentation. When the indentation is finished, the data from the scope can be transferred to the MMT computer, and analyzed using any standard graphing program.

Materials tested in this study have been chosen such that the various physical phenomena which are to be examined are represented.  $Ta_2N$  films on sapphire, of varying thickness and with various interlayers, have been shown to delaminate during indentation, with well characterizable load - depth curves. Since the material is still being developed, this allows its use as both indentation characterization and use as a model material for studying the acoustic emission from film delamination. When higher loads are applied to this system, cracking occurs in the film, thereby allowing both film delamination and film cracking to be studied.

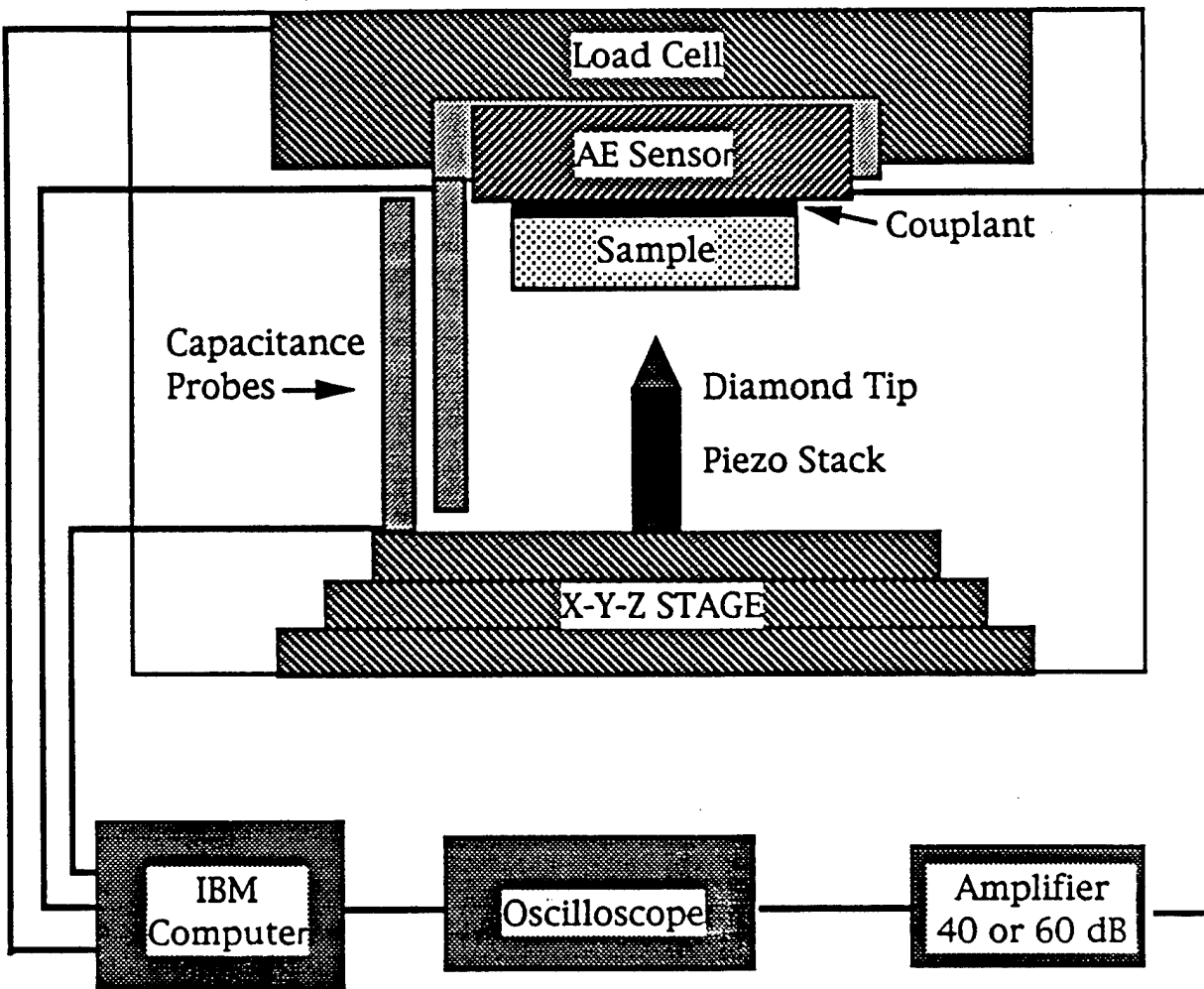


**Figure 54** Experimental setup for monitoring of acoustic emission during nanoindentation.

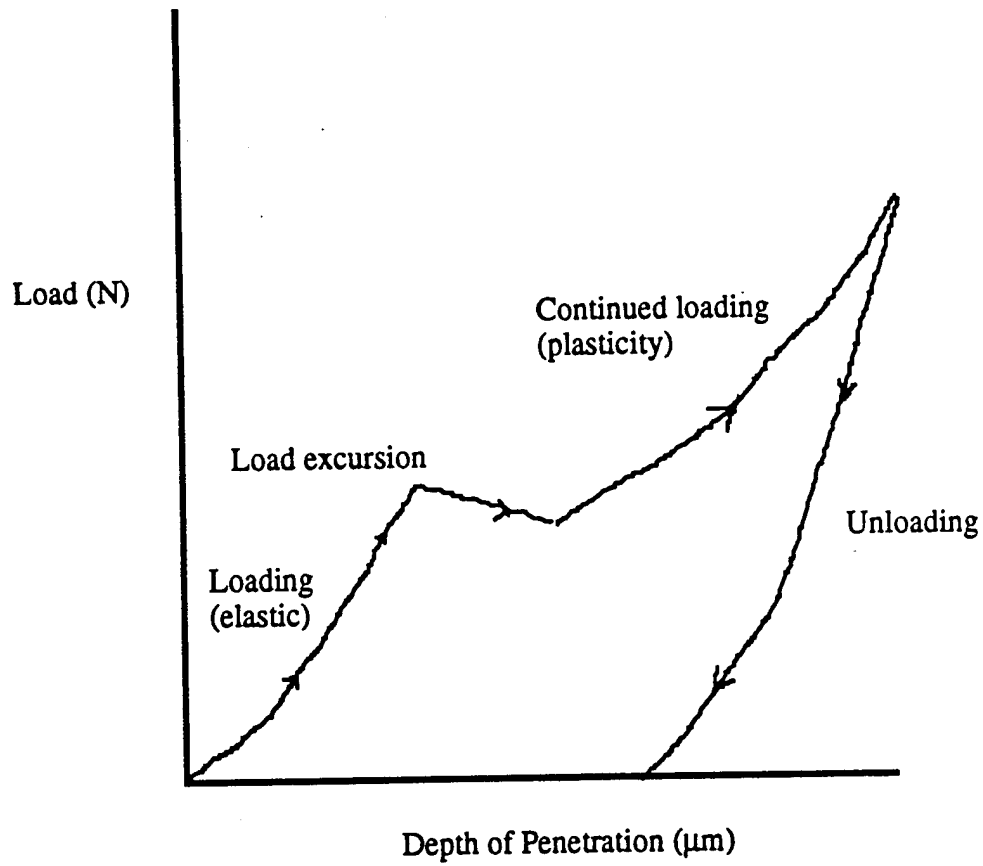


**Figure 55** Nanoindentation sample penetration versus load characteristic.

To test the AE signal from dislocation generation and motion, indentation in single crystals of iron - 3 weight percent silicon (Fe-Si) and of tungsten has been carried out. These materials exhibit elastic loading during the initial indentation, then undergo a physical event which causes a discontinuity in the loading curve. This discontinuity has been linked to the generation and motion of dislocations under the indenter tip. If a sample is indented and the load is removed prior to this discontinuity, there is no residual impression from the indenter. After this discontinuity, there is a residual impression, corresponding to plastic deformation. Therefore, this discontinuity must be connected to the generation and motion of dislocations. By identifying the AE signal from these events, an idea of the signals from a fatigue crack can be gained.

#### *Preliminary Nanoindentation Results ( $Ta_2N$ )*

$Ta_2N$  films on sapphire have been indented using diamond indenter tip in the MMT. Indentations into a film of 500 nm of  $Ta_2N$  on 28 nm of Al on sapphire are shown in Figure 56a, with the corresponding AE data from that indent shown in Figure 56b. The time on the axis of the AE data is just a relative time from the triggering event, and does not correspond to the time of the indentation. Figure 56c, 56d, and 56e are magnified views of the AE signal from each of the three bursts. It is clear that several events occurred during the one loading discontinuity seen from on the load depth curve. Optical microscopy of this indent shows several "lobes" on the delamination, suggesting that not one, but possibly three different interfacial cracks were formed during this load drop. Since the sample is anisotropic and the tip is not perfectly conical, the stress distribution under the tip may be such that the cracks nucleated at separate positions around the tip as the tip moved into the sample during the loading discontinuity. The similarity of the curves in both frequency and rise time of signal is clearly evident.

On the same system, if loading is increased to higher loads, there is the possibility of identifying two loading discontinuities. Figure 57a shows the load - depth data from an indentation into the same film, with Figure 57b showing the AE signals generated during from each indent. The fine structure of the waveforms are almost identical to those shown in Figure 56. Figure 58 is an optical micrograph taken after the indentation, and a second delamination can be seen at the edge of a spalled region. This suggests that the second loading discontinuity is the nucleation and propagation of the second delamination. The AE signals generated from these events are very similar, and with further work should be able to characterize the physical phenomena using the AE signal.

#### *Fe-Si Indentations*

Indentations made into Fe-Si show clear loading discontinuities at low loads using a conical diamond indenter. Figures 59a and 59b show typical load - depth and acoustic emission data from these indents. The samples were coupled to the detector using vacuum grease for ease of removal from the sensor, and therefore the load - depth curves show abnormally large depths due to the low stiffness of the couplant in series with the load cell. The indents clearly show a different pattern in the AE signal than the  $Ta_2N$  films, with a longer rise time and less recovery towards the baseline voltage.

A series of indentations were made on Fe-Si where the load at which the loading discontinuity varied (most likely due to either variations in oxide thickness or surface roughness of the sample). When a material supports a higher load before undergoing plastic deformation, the resulting energy release during the load drop is larger than lower load drops. This results in more plastic deformation, and therefore more dislocation motion and generation. The amplitude of the AE signal was plotted as a function of the load at which a loading discontinuity occurred, and is shown in Figure 60a. The rise time of the signal appears to be relatively independent of the load at which a discontinuity occurs, as shown in Figure 60b. In addition, the rise time of the signal from Fe-Si was about 6  $\mu s$ , as opposed to that of  $Ta_2N$ , which was about 4.4  $\mu s$ . Therefore, it appears to be reasonable to suggest that the magnitude of the AE signal will correspond to the energy expended during the event, whereas the rise time of the signal will be indicative of the type of event.

#### *Direct Sensing, Analysis, and Real-time Diagnosis*

### *Acoustic Emission as an Addition to the MMT*

Adding acoustic emission capability to the MMT allows increased information to be generated during nanoindentation. Conventional nanoindentation uses discontinuities in the loading curves to identify physical events, such as film delaminations. As shown from Figures 56a and 56b, what appears to be a single event from the load - depth data is actually separated into three distinct events using the AE signal. In addition, the length of time the signal is generated may allow post indentation microscopy to identify crack velocities, since the time of an AE signal is active can be used as a boundary of how long the crack was growing. This additional information allows an expanded use of the MMT.

### *Summary of Nanoindentation Studies*

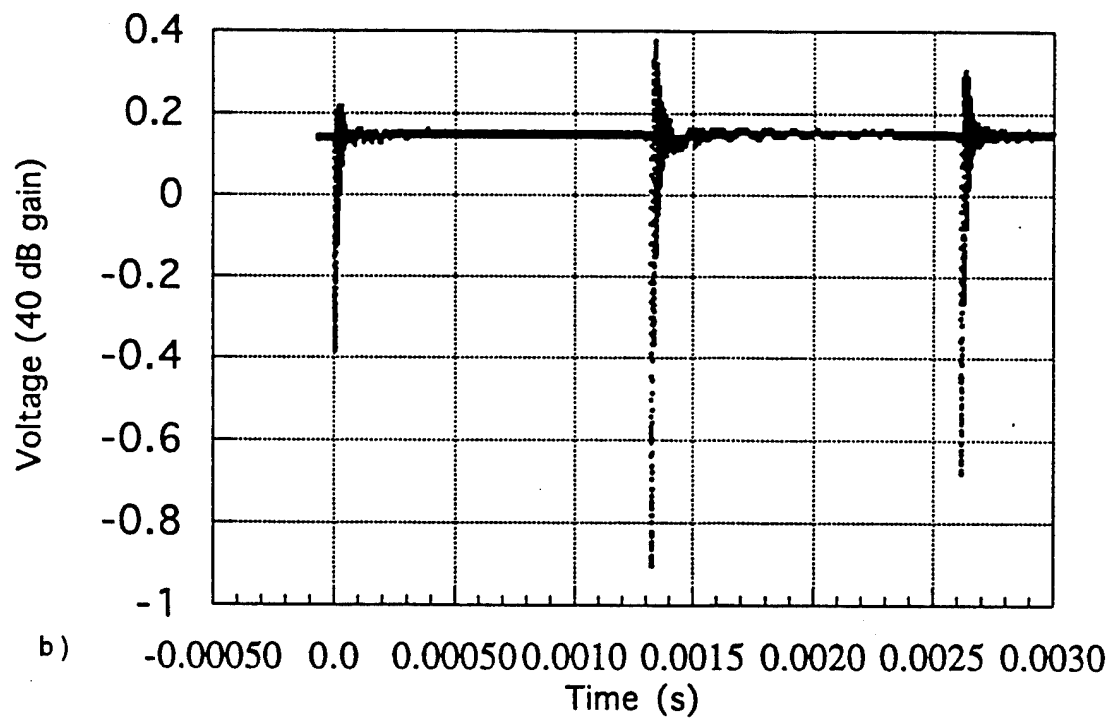
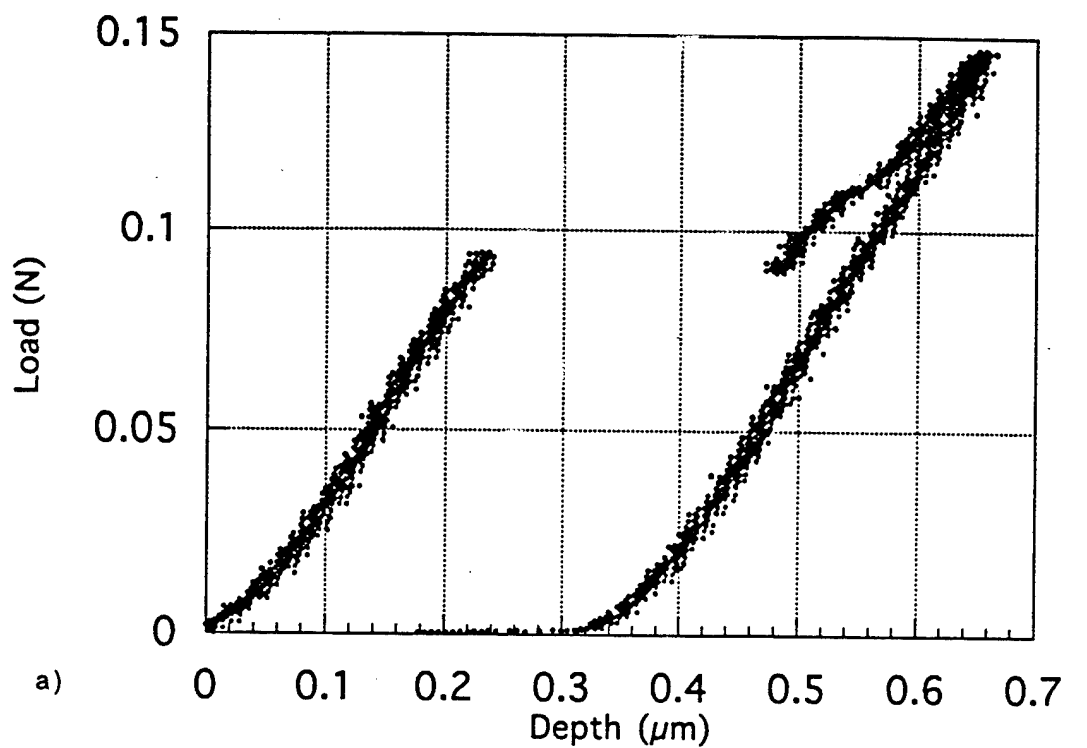
Individual physical events can be generated in a micromechanical testing device during nanoindentation. By varying the system indented, different classes of events can be generated, such as film delamination or dislocation emission. These events are similar to events which may occur in either the failure of a microsensor or a fatigue crack in a structural member.

Acoustic emission during nanoindentations has been used to identify the AE signal which occurs at discontinuities during an indentation. Knowledge of the waveform of the AE signal will allow microsensors to be optimized for amplification and filtering. The rise time of AE signals from a given material appears to be relatively independent to the magnitude of the signal, suggesting that the rise time may be characteristic of the type of event. Ta<sub>2</sub>N films delaminating showed a rise time of 4.4 µs, whereas dislocation emission in Fe-Si had a rise time of about 6 µs. The amplitude of the AE signal can be related to the energy expended during the event which generated the signal, and may be used to estimate the severity of an event.

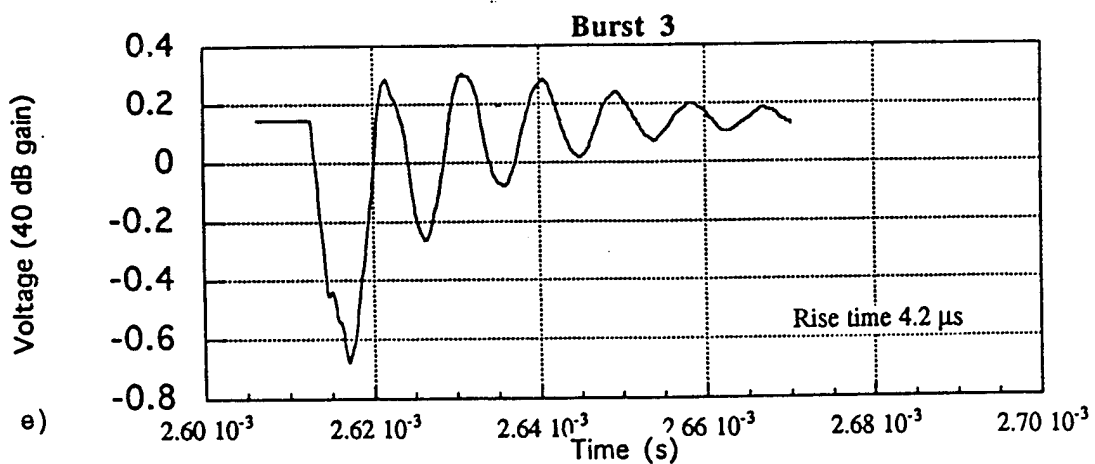
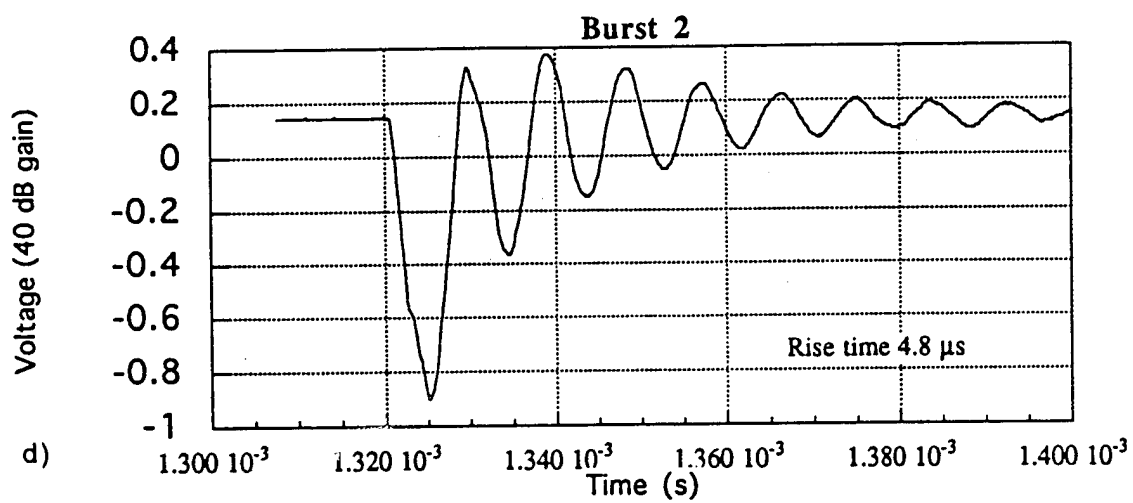
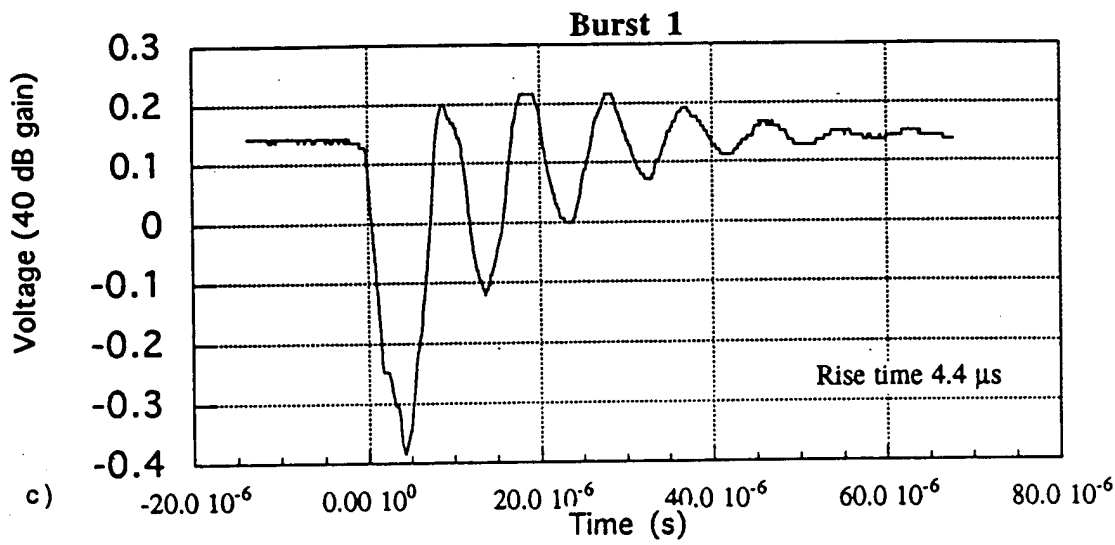
### **Plans**

The following main research activities will take place over year 2 of this program:

- Improve test sensor chips and evaluate diaphragm and cantilever designs
- Fabricate test sensor chips
- Investigate bonding, attachment, and packaging of sensors
- Determine damage at sensor/substrate interface produced by fatigue
- Characterize and model residual stresses in bonded sensor
- Modify chemical composition of PZT layer to improve performance
- Fabricate microsensors with on-chip circuitry
- Investigate frequency response



**Figure 56** a) Nanoindentation sample penetration versus load characteristic for a nitride/Al/sapphire, b) AE signal from indentation shown above, c) Expanded AE burst 1, d) Expanded AE burst 2, e) Expanded AE burst 3.



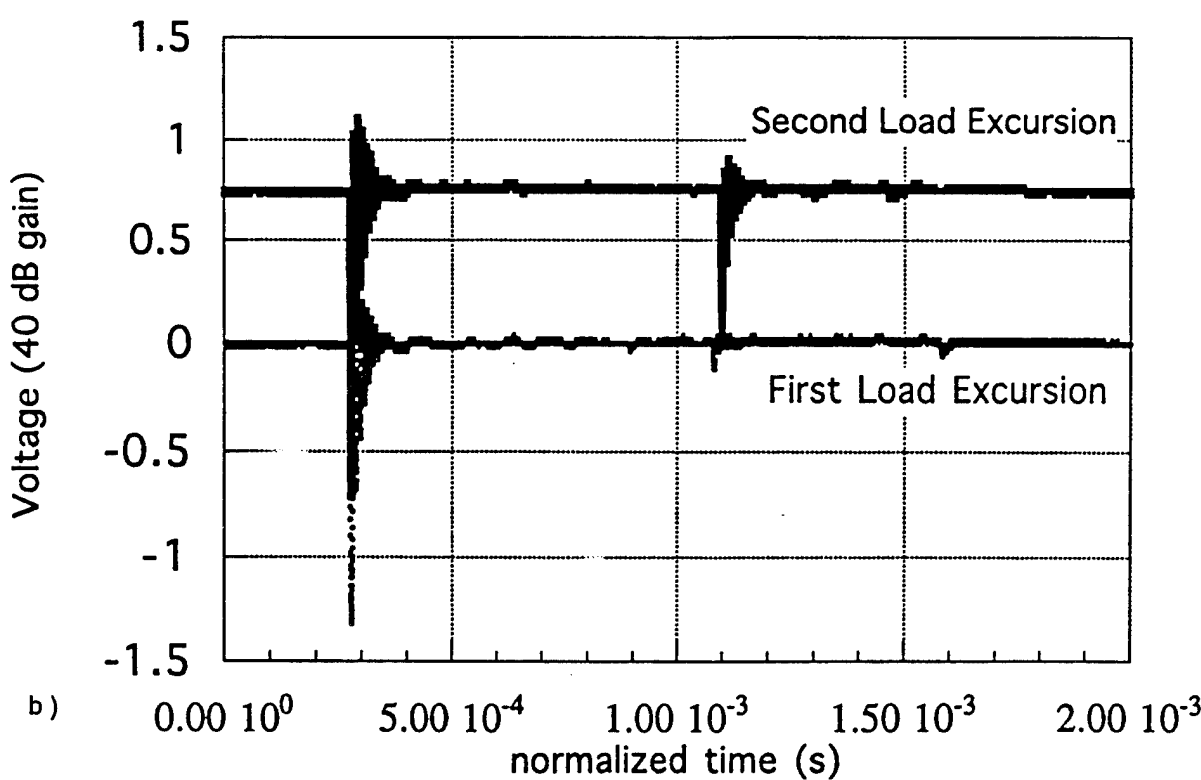
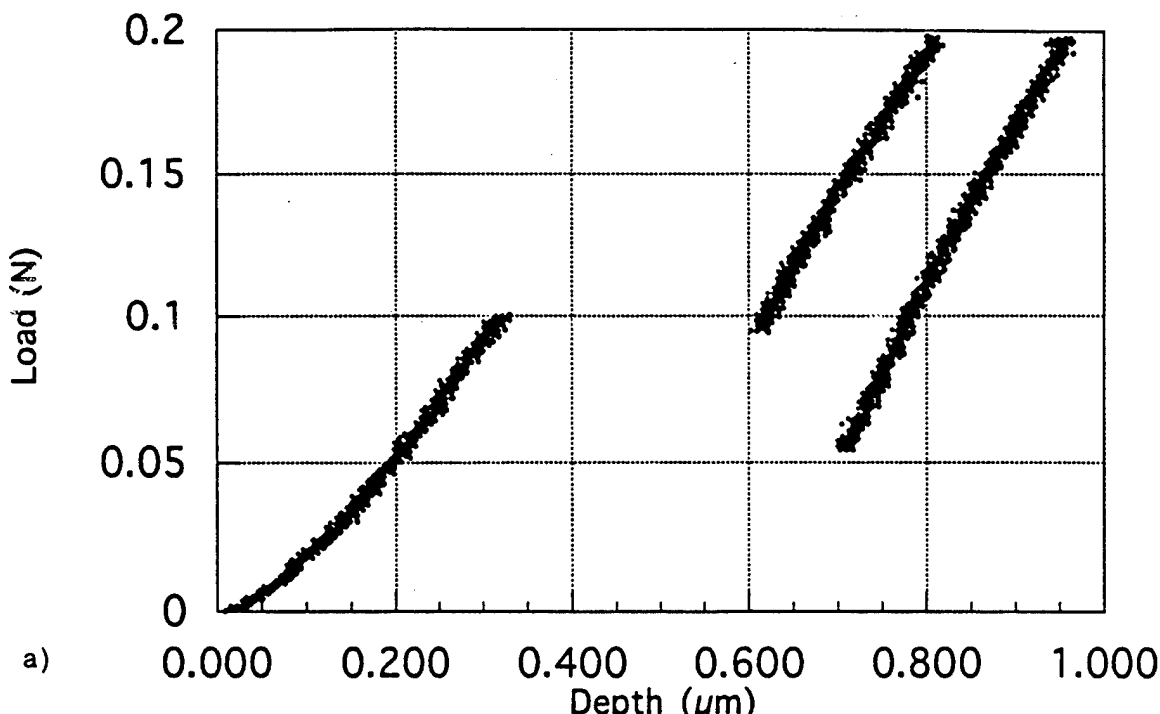


**Figure 57** Nanoindentation into tantalum nitride/Al/sapphire sample with higher loading showing two discontinuities, b) AE signals from both load drops offset for clarity.

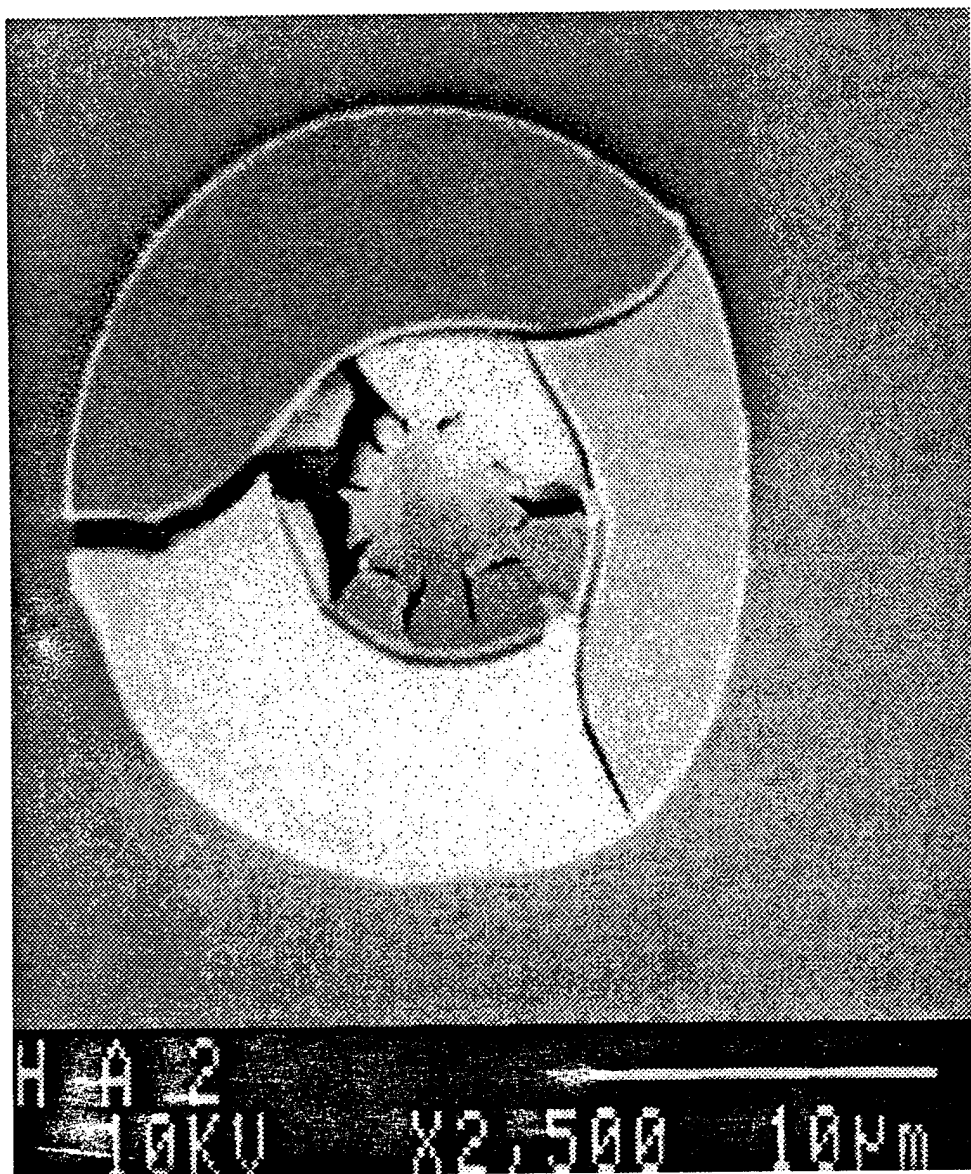


**Figure 58** Scanning electron micrograph of a crack generated using nanoindentation technique.

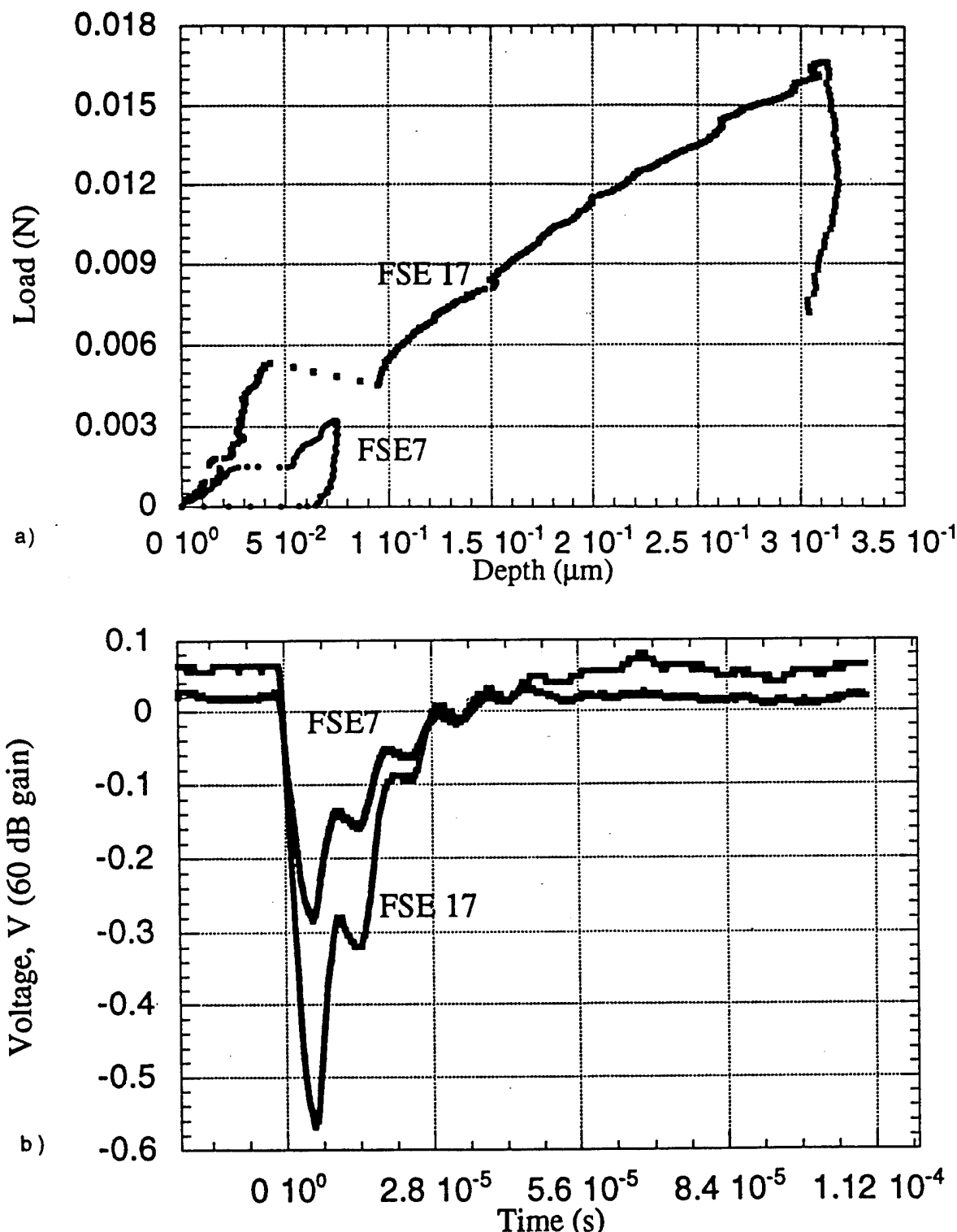


Figure 59 a) Load - depth indentation in - Fe-Si, b) Acoustic emission output obtained from nanoindentation.

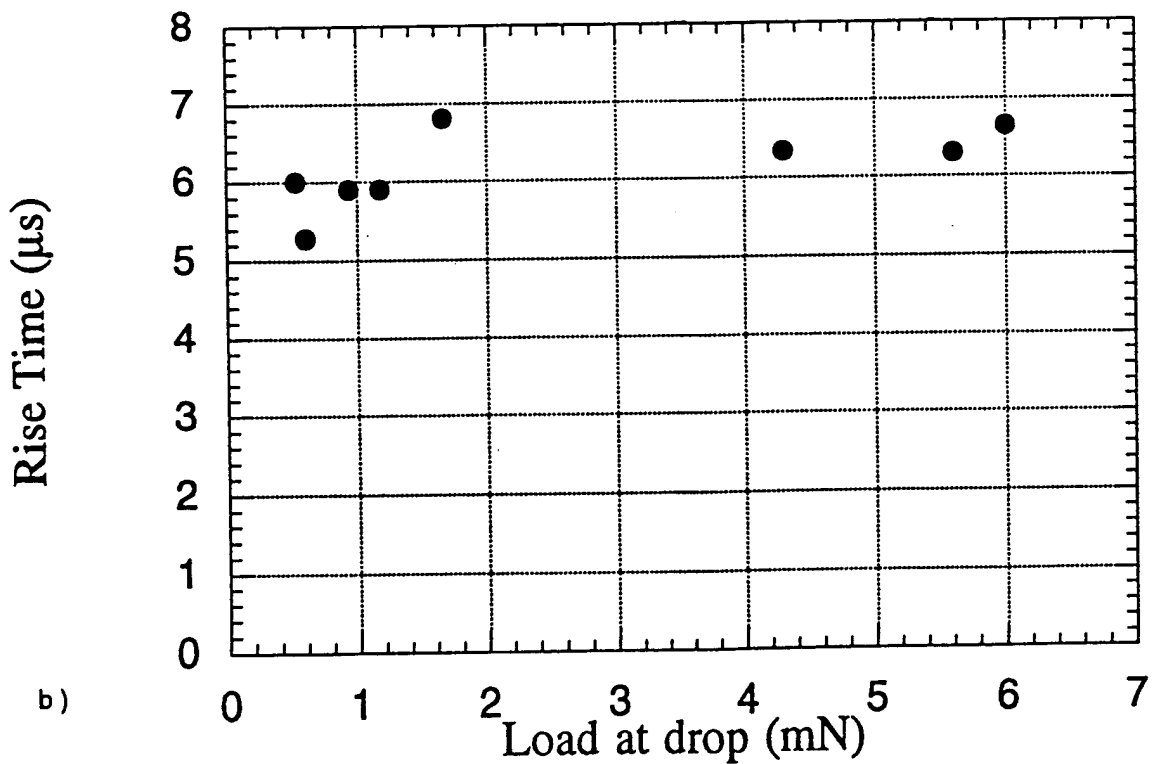
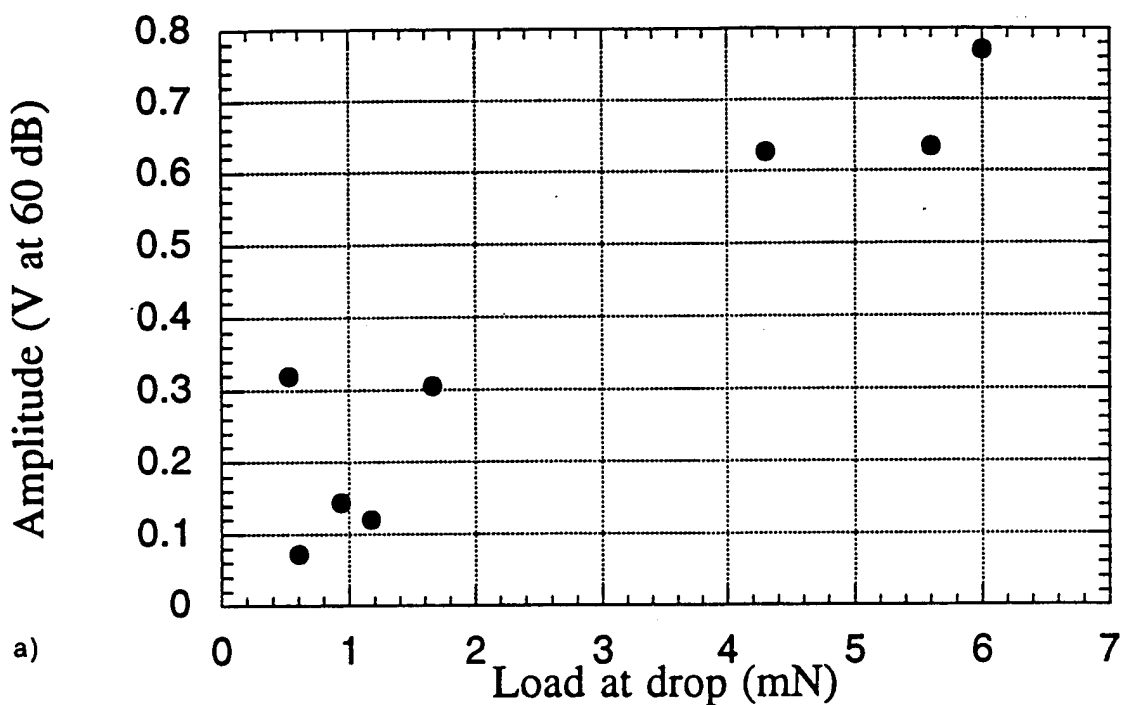


Figure 60 Maximum amplitude as a function of load at first loading discontinuity, and b) Rise time as a function of load at first loading discontinuity.

### **2.3.1.2 *Signal Processing***

*K. Buckley, M. Kaveh, A. Tewfik*

The objective of the signal processing component of this M-URI investigation is the detection and evaluation of helicopter rotor cracks from Acoustic Emission (AE) signals generated during inception of the cracks. Automatic monitoring exploits microcrack AEs, which are propagating acoustic signals created by the formation of microcracks in material. These microcracks are the onset of material fatigue which, if critically located, would result in costly and/or catastrophic failure. Automatic monitoring based on detection and classification of microcrack AEs can provide early warning of impending failure.

AE signals have been studied extensively for the characterization of crack initiation and propagation (e.g. [38-41]). Energy due to a crack source is dissipated in the form of elastic waves which propagate through the material. These waves are damped, broad band, ultrasonic bursts with frequency extent which can be up to several MHz. The principal signal processing challenge is to accomplish AE signal detection and analysis tasks in a very noisy environment where the energy of the received AE signals is orders of magnitude lower than that of received noise signals.

The signal processing approach, as illustrated in Figure 61, is based on monitoring the outputs of AE microsensors located at critical positions on the rotor assembly. The microsensors receive AE signals and provide initial signal conditioning. Output of these sensors are transmitted to an on-board computer for real-time noise reduction and AE signal detection. If an AE signal is detected, the AE sensor outputs are processed further to determine parameters of the AE signals. These parameters are evaluated to determine the AE signal type (i.e. to classify the signal) so that a decision can be made on the appropriate action to be taken.

Noise reduction, detection, parameter estimation and classification all require knowledge of characteristics of the AE and noise signals that are received by the AE microsensors. The better our characterization of the AE signals and noise, the more effectively we can detect and classify the AE signals. Therefore a critical component of this investigation is the acquisition and analysis of real, representative AE and noise signal data.

Considering these signal processing objectives, we have organized this investigation into the following three overlapping and interrelated Phases:

- a) AE and Noise Signal Analysis;
- b) Signal Processing Algorithm Development; and
- c) AE Signal Classification.

Below we report on each of these Phases, reviewing progress to date and outlining the research plan for year two, which includes:

- Continuing the analysis and modeling of AE signals and noise.
- Creating new testing procedures to validate theories and strategies.
- Designing practical, effective data preprocessors and telemetry schemes.
- Developing and evaluating candidate AE detection, localization and classification algorithms.
- Developing and evaluating candidate catastrophic failure prediction algorithms.
- Investigating other relevant failure monitoring scenarios.
- Providing point source standard signals in selected materials from commercial transducers.

#### **A. *AE AND NOISE SIGNAL ANALYSIS***

Signal analysis is required to characterize both AE and noise signals. AE signals for crack initiation and propagation studies have typically been acquired from isolated material specimens in controlled laboratories, where efforts have been made to keep noise levels to a minimum [38-41]. Noise

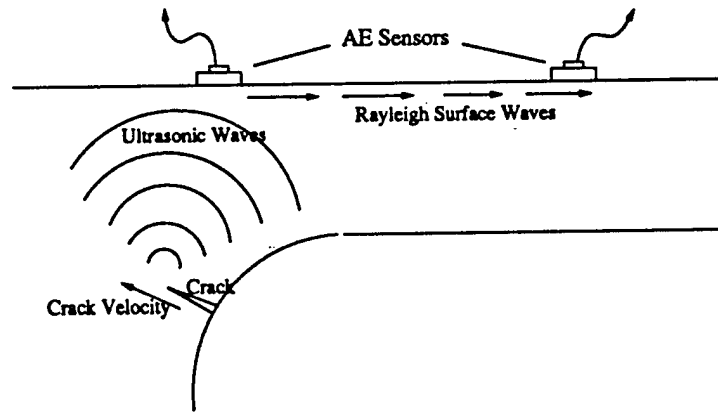
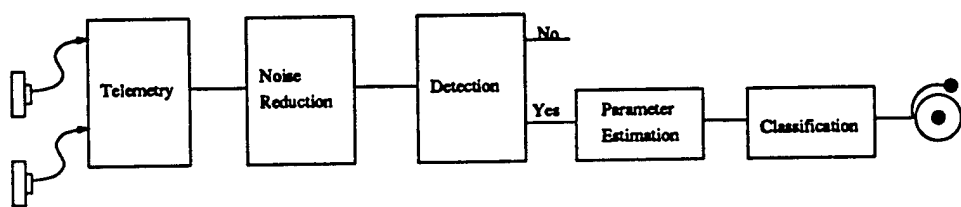


**Figure 61** Illustration of microcrack acoustic emission and associated signal processing block diagram.

generated in machine environments have also been considered in the literature (e.g. [16]). The literature on AE and acoustic machine noise characteristics will be useful in that it provides us with indications of general signal characteristics (i.e. the general band of frequencies of AE signals). However the AE and noise signals we expect to encounter will be very situation dependent. Characteristics of microcrack generated AE signals will be influenced by the material type, size and shape, by crack and sensor locations, and by microsensor response. Air friction noise will be received along with complex mechanical noise components.

Therefore our approach to signal characterization is the acquisition of as much representative AE and noise data as possible, analysis of this data to derive models and identify differentiating characteristics, and interaction with our colleagues and referral to the literature to help guide us in this signal analysis task.

## Accomplishments

The acquisition and analysis of real, representative AE and noise data requires both multidisciplinary collaboration and a signal acquisition and processing facility. In the following sections we describe development and summary of preliminary signal analysis.

### *Collaborations*

Over the first year of this investigation we have worked with the Material Science Department of the University of Minnesota to obtain examples of microcrack generated AE signals. Signals acquired to date are listed in the subsequent sections.

The three universities of the Integrated Diagnostic program are currently interacting with researchers from Georgia Institute of Technology, Honeywell, and Penn State University. Each should be a near future source of AE signals.

### *Facilities*

Signal analysis and algorithm development for this project will take place in the Computing and Acoustic Signal Processing Laboratories of The University of Minnesota, Department of Electrical Engineering, Signal Processing Group. The principal computing facility is a Sun cluster consisting of over 20 SPARCstations supported by numerous X-Terminals. A SPARCstation 5 with a 2 GByte hard drive has been acquired specifically for the computational and data-base storage requirements of this project. A NCD X-Terminal has also been purchased.

For the acquisition of microcrack generated AE signals and noise signals, we have procured a LeCroy 9374L 4-channel oscilloscope with a 1 GHz. bandwidth, 500 MHz sampling rate per channel, 2 MByte memory/channel, and both parallel and serial interface ports. A Pentium-100 workstation and a 486-DX4-100 laptop have been purchased to support this oscilloscope in the field and in our laboratories. We have borrowed two Physical Acoustics A3 sensors and a Physical Acoustics S9220 sensor, and have purchased two each Physical Acoustics S9208 and D9202B AE sensors.

### *Preliminary AE Signal Acquisition*

To date we have obtained a number of microcrack AE signals for each of the following material types: 1) tantalum nitride ( $Ta_2N$ ) on sapphire; 2) iron on silicon (Fe-Si); 3) tungsten; 4) aluminum alloy.

All signals listed above were measured by the MMT nanoindentation using a Physical Acoustic Inc. S9220 AE sensor. The MMT device was used to generate cracks in the 1-st three materials. An Instron servo-hydraulic tester was used for the aluminum alloy. In the following sections, we show representative plots of these signals along with analysis results.

### *Noise Signal Acquisition*

To date we have acquired the following three sets of noise data using the LeCroy oscilloscope:

- 1) two channel motor noise signals using the A3 sensors;
- 2) two channel engine w/ rotor noise using the A3 sensors; and
- 3) single channel engine w/ rotor noise using the S9220 sensor.

Noise data 3) allows us to process and compare AE signals and noise signals observed using the same sensor.

### *Preliminary Signal Analysis*

AE signals from microcracks are damped, broad band, ultrasonic bursts with frequency extent which can be up to several MHz. To evaluate time/frequency characteristics of these signals, we apply Prony's method [43] to each data set we obtain. Below we present representative results and draw preliminary conclusions.

Prony's method models a waveform as a sum of exponentially decaying complex sinusoids of the form  $Ae^{j\omega t} e^{j(2\pi f t + \phi)}$ . The model order, M, is the number of such terms. For real data, these complex sinusoids occur in complex-conjugate pairs, and we obtain (at least) M/2 real terms. As recommended by Kumaresan and Tufts [43], we use the singular value decomposition of the data matrix to estimate M, then eliminate all but the largest M singular values to reduce noise. Also as recommended by Kumaresan and Tufts, we use model order L>M to improve accuracy in the estimates of A,  $\phi$ ,  $\alpha$ , and f. We then use backwards linear prediction to discriminate the L-M noise components from the M signal components.

Appropriate segments of each data set were selected manually, down-sampled by a factor of eight to expedite processing, and adjusted for dc level. Each acoustic emission consisted of N=384 samples after preprocessing. We found that each AE data set was reasonably modeled as a sum of from two to six real-valued, exponentially decaying sinusoids.

Representative results are shown for Tantalum Nitride ( $Ta_2N$ ) on Sapphire, Iron on Silicon (Fe-Si), and Tungsten in Figures 62-64, respectively. In each figure, the original signal is the dotted curve and the Prony fit is the solid curve. The accompanying table indicates the order M of the Prony fit, and lists the amplitude A, phase  $\phi$ , the decay rate  $\alpha$  and the frequency f of each component. The low order Prony models accurately fit the AE signals.

Each damped sinusoidal component of the Prony model is a broad band signal with center frequency given by f, bandwidth determined by  $\alpha$ , and strength given by A. The larger  $\alpha$  is, the broader the bandwidth. Note for example that the microcrack AE signal from the tungsten specimen has a relatively strong signal component centered in frequency at  $f = 78.19$  kHz, with a decay factor  $\alpha = -11,380$  which indicates energy over a broad frequency range.

Our observations from analysis of these AE signals include 1) frequency content depends on material type and specimen size; 2) predominate Prony components can range below 80 kHz in center frequency; 3) predominate Prony components cover a wide range of center frequency; and 4) for a given material type and specimen size, microcrack generated AE signal have consistent phase, frequency and decay rate characteristics (i.e. the AE signals are similar in shape).

To date, we have evaluated the noise signals by estimating their power spectra and by applying Prony's method to fit multiple exponentials to them. We show an example of this below. We have also estimated bifrequency spectra [44] and computed time/frequency distributions [45] after filtering. The purpose of this analysis is to characterize the noise and to search for advantageous domains for separating AE signals from this noise.

Here we consider the two channel engine w/ rotor noise acquired using the A3 sensors. The two channels of data were recorded at a sampling frequency was 20 MHz. The duration of observation was one-twentieth of a second. The time-domain plots of the two channel signals are shown in Figure 65a. Their respective power spectrums are shown in Figure 65b. Note that the y-axis is in log scale. The

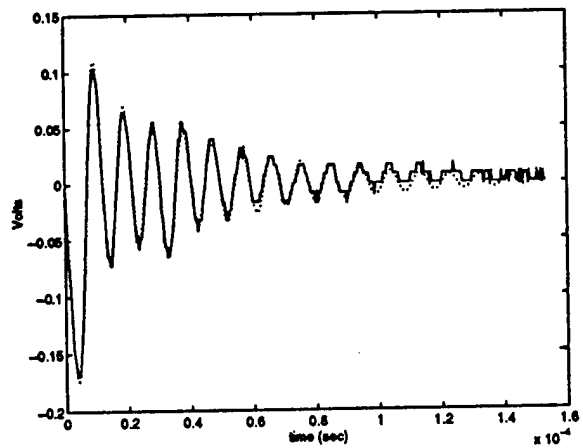
value of the power spectrum at about 105 KHz, which is approximately the dominant component of the Ta<sub>2</sub>N AE signal is of interest. At this point it is difficult to precisely determine the ratio of the contributions of quantization noise and the engine noise at this range of frequencies. It can be seen that the power spectrum flattens out at frequencies greater than about 400 KHz in the case of Channel 2. Hence, this could be taken as the frequency above which the contribution is due to quantization noise only. Also the value of the power spectrum is larger at 105 KHz in the case of Channel 1. Hence, in simulations we have added the AE signal to the Channel 1 data to obtain a more difficult detection scenario.

Figure 66 shows for a block of this noise data the frequencies computed using a Prony fit along a sliding window. Note that frequency components above 80 KHz are identified. This suggests that differentiating lower frequency (e.g. < 75 kHz) AE signal components from engine noise may present a challenge.

## Plans

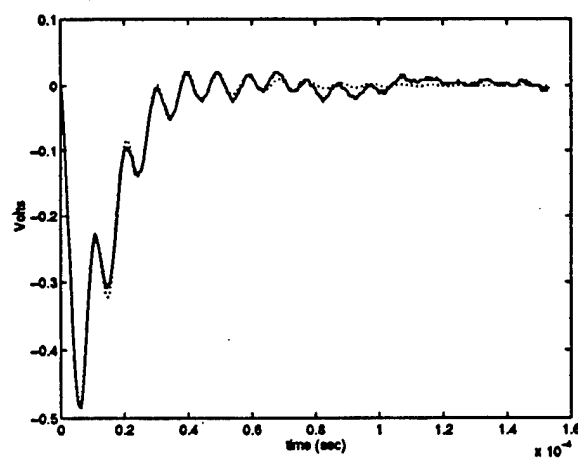
Acquisition and analysis of microcrack generated AE signals and noise signals will continue. Prof. Gerberich will continue to be a principal source of AE signals. Microsensors developed by Profs. Polla and Robbins will soon be available and employed to acquire data. Additional, confirmed sources of microcrack AE signals are: Honeywell, Georgia Institute of Technology and Northwestern University. We plan to acquire data from these sources in the near future.

We will continue to acquire realistic noise data. We are in the process of arranging to capture noise from a helicopter, by recording signals from AE sensors positioned as close as possible to the rotating rotor.



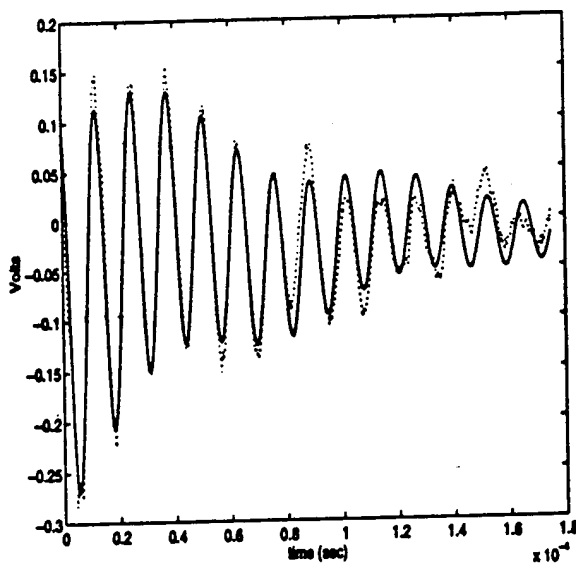
$A$ (V)	$\phi$ (rad)	$\alpha$ (1/sec)	$f$ (Hz)
0.102	0.075	-2.225e+04	1.057e+05
0.099	2.720	-8.116e+04	6.218e+04
0.080	1.938	-7.214e+04	3.923e+04

Figure 62 Tantalum Nitride on sapphire microcrack AE signal: original is the dotted curve, the Prony fit is the solid curve .



$A$ (V)	$\phi$ (rad)	$\alpha$ (1/sec)	$f$ (Hz)
1.502	1.655	-1.136e+05	1.111e+04
0.142	-0.609	-4.084e+04	1.034e+05

**Figure 63** Iron on silicon microcrack AE signal: original is the dotted curve, the Prony fit is the solid curve.



$A$ (V)	$\phi$ (radians)	$\alpha$ (1/sec)	$f$ (Hz)
0.202	0.444	-1.138e+04	7.819e+04
0.041	-3.142	-7.997e+03	0.000e+00
0.048	-3.115	-1.251e+04	1.205e+04

Figure 64 Tungsten microcrack AE signal: original is the dotted curve, the Prony fit is the solid curve.

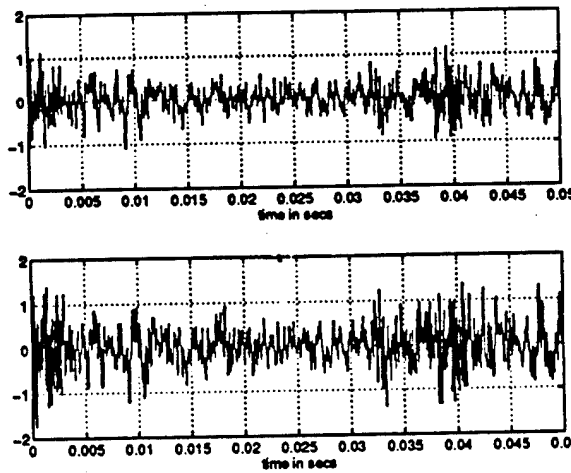


**Figure 65a** Two channel engine with rotor noise acquired with the A3 sensors.

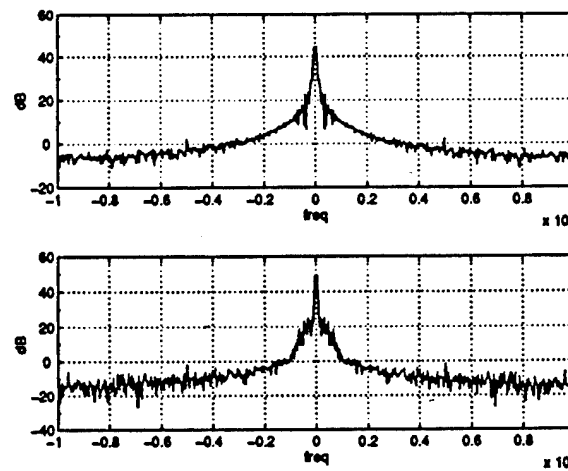


**Figure 65b** Power spectrum estimates for two channel engine with rotor noise acquired with the A3 sensors.

## B. SIGNAL PROCESSING ALGORITHM DEVELOPMENT

As illustrated in Figure 61, noise reduction, detection, parameter estimation and classification signal processing algorithms are required. These need to be designed specifically for helicopter rotor assembly microcrack AE signal processing. Results from a preliminary AE signal processing investigation are reported, followed by an outline of tasks for year 2.

### Accomplishments

In the first year of this investigation, it has been too early for detailed algorithm development. More definitive results from the previous subsection need to be obtained. The purpose of this preliminary investigation has been to develop experience in processing AE signals superimposed on real noise at low SNR.

#### Noise Reduction

In this preliminary study we have considered both high pass filtering and optimum linear prediction filters. The advantage of high pass filtering is that it can effectively and simply remove lower frequency noise. Figure 65b suggests that noise will be predominantly low pass. Care must be taken in the selection of a cut-off frequency or useful AE signal components will be attenuated. One disadvantage of simple high pass filtering is that it does not shape the noise frequency spectrum in the pass band. Optimum detection and parameter estimation methods require knowledge of the shape of the noise power spectrum. A linear prediction approach [46] can be used to suppress low frequency noise while whitening the noise power spectrum.

First, to obtain a suitable order for the linear prediction filter, the SVD of the data matrix of the engine w/ rotor noise (A3 sensor) Channel 1 data was performed. The singular value plot is shown in Figure 67(i). Only the first 8000 data samples out of the total set of 1 Meg samples was used. From the plot the order, P, was chosen to be at 15. Figure 68(i) shows the power spectrum of the output of the LP filter for P=15. It can be seen that the spectrum is not "white" and significant spikes can be seen at approximately 210, 300, and 500 kHz. The LP filtering simulation was repeated using P=80. The power spectrum of the LP filter output is shown in Figure 68(ii). Note that there are now no dominant peaks seen in the power spectrum. Also note the low values of the power spectrum for frequencies lesser than 120 KHz are a result of the attenuation of the dominant periodic noise components by the LP filter.

The large power of the periodic noise components, especially at frequencies lower than 40-60 kHz, contribute to the dominant singular values of the data matrix. These dominant values obscure other relatively smaller terms which become significant when the dominant components are suppressed. This is seen when a model order of P=15 was chosen. From Figure 67(ii) it can be seen that the singular values continue to decay at orders much greater than 15. The decay has not flattened out to the noise floor even at 200. Hence, in practice it might be necessary to use a suitable analog filter to mitigate the influence of these low frequency dominant components. In the above engine noise case a high pass filter with a cut-off of about 40 KHz might be used. This pre-filtering will also significantly reduce the order of the prediction filter required for periodic noise cancellation after sampling.

Finally, the time domain plot of the input and output of the LP filter are shown in Figure 69. Note that there is a significant reduction in the periodic noise interference at the output of the LP filter.

#### AE Signal Detection

Figures 70 and 71 illustrate the potential challenge in detecting microcrack AE signals in noise. Figure 70 is a plot of the superposition of engine noise (A3 sensor) and the Ta<sub>2</sub>N AE signal. The AE signal, which initiates at sample n = 55,000 is not visible. Figure 71 shows the resulting output of an optimum linear prediction filter. Strong low frequency noise components have been attenuated, but the

AE signal is still not observable. Using five other Ta<sub>2</sub>N AE signals to model the signal, and assuming that the noise is white and the data is Gaussian, an optimum detector was designed. This detector first processes the data, effectively focusing the signal energy in time while filtering as much noise as possible. A threshold can then be applied to the result.

Let  $\mathbf{Y}$  be the data vector,  $\mathbf{N}$  the noise vector, and  $\mathbf{S}$  the signal vector. Under the assumptions stated above, we can state the detection hypothesis problem as,

$$\mathbf{H}_0 : \mathbf{Y} = \mathbf{N} \quad \mathbf{H}_1 : \mathbf{Y} = \mathbf{N} + a\mathbf{S}$$

Let  $\mathbf{N}$  be Gaussian with mean  $\mathbf{u}_n$  and correlation matrix  $\mathbf{R}_n$ , and let  $\mathbf{S}$  be Gaussian with mean  $\mathbf{u}_s$  and correlation matrix  $\mathbf{R}_s$ . "a" is the unknown amplitude of the signal vector. No uniformly most powerful (UMP) test exists for the above hypothesis with respect to "a". However, a locally most powerful (LMP) test can be found assuming low SNRs.

The LMP test statistic  $\mathbf{T}_{lo}$  for the above hypothesis after pre-whitening of the additive Gaussian noise is given by,

$$\mathbf{T}_{lo}(\mathbf{Y}) \propto \mathbf{Y}^T \mathbf{R}_s^{-1} \mathbf{Y}$$

where  $\mathbf{Y}$  is the observation vector. This is equivalent to,

$$\mathbf{T}_{lo}(\mathbf{Y}) \propto \sum_{k=1}^r \lambda_k \langle \mathbf{Y}, \mathbf{v}_k \rangle$$

where  $\lambda_k$  is the k-th eigenvalue and  $\mathbf{v}_k$  is the k-th eigenvector of  $\mathbf{R}_s$ . "r" is the rank of  $\mathbf{R}_s$ . The decision statistic  $\mathbf{T}_{lo}$  given in [47] can be implemented with a bank of "r" causal, linear filters in parallel as shown in Figure 72. The impulse response of the k-th channel filter is given by,

$$\mathbf{h}_k(n) = \mathbf{v}_k(N-n)$$

where  $n=1, 2, \dots, N$ .  $N$  is the number of samples in a data block. The output of each channel is squared and the test statistic is obtained by a linear combination (with the corresponding eigenvalues as the weights) of these squared outputs.

The signal plotted in Figure 71 was processed as described above. The resulting test statistic sequence is plotted in Figure 73. It is evident that the test statistic performs quite well in identifying the occurrence of the acoustic emission.

### *Signal Parameter Estimation*

In addition to considering Prony's method of estimating the parameters of an exponential model of the data, we have looked at using Bifrequency and time/frequency distributions of the data to estimate AE signal parameters.

Bifrequency Domain: Let  $x(n)$  be output of the digital noise filter. If  $\mathbf{X}$  is the DFT vector of a block of  $x(n)$ , then the Bifrequency Spectrum (BFS) of the signal is given by the matrix,

$$\mathbf{B}_{xx} = \mathbf{X} \mathbf{X}^H$$

where superscript "H" denotes conjugate transpose. A contour plot of the magnitude of the BFS of a Ta<sub>2</sub>N AE signal is shown in Figure 74(a). We require detection of these peaks when the AE is buried in

noise. The magnitude of the BFS of the output of the LP filter is shown in Figure 74(b). Now, the AE peaks in the bifrequency plane are not visible amidst the high background clutter due to noise.

The variance of the noise components off the main diagonal can be reduced by suitable smoothing. A diagonal smoothing is recommended in [43] to preserve frequency support and to furnish statistically consistent estimates. Figure 74(c) shows the magnitude of the BFS after smoothing the BFS over 16 samples. Note that the AE signal peaks are now clearly visible.

Another method of estimating the AE peak locations in the BFS plane is by using the BFS of the template designed to match the AE signal. This BFS template is convolved with the BFS of the data. The plot of the magnitudes of the diagonal of the smoothed BFS is shown in Figure 74(d). Note that the dominant peak corresponds to the normalized frequency of the AE signal. Its frequency can directly be read off the x-axis of the plot.

**Time-Frequency Domain:** The mesh plot of the Wigner distribution [44] is shown in Figure 75. Due to the low SNR, numerous spurious peaks appear along with the AE peak. These spurious peaks can be reduced by using a suitable smoothing function referred to as the kernel. The resulting distribution belongs to a general class of time-frequency distribution referred to as the Cohen's class [44]. All members of this class of distributions are time and frequency shift invariant, and hence, suitable for our detection problem. However, the optimum smoothing function is dependent on the characteristics of the signal to be detected. The optimum kernel for the case of the signal in additive Gaussian noise is given in [48]. Figure 76 shows the time-frequency plane after optimum smoothing. Note that the AE peak is now distinct.

## Plans

In year two, many of the questions concerning AE and noise signal characteristics will be answered as a result of the Phase I "Acoustic Emission & Noise Signal Analysis" task. These results will be used to develop detection and parameter estimation algorithms for this helicopter rotor microcrack AE signal problem.

For detection, we will consider further the computation of decision statistics. Practical algorithms for real-time implementation are required. We will also develop rules for setting thresholds on the decision statistics to achieve false alarm and probability of detection specifications.

The objective of parameter estimation is to provide information required to classify detected AE signals. Although this is not a real-time processing issue, since estimation is required only when an AE signal is detected, computational cost will be considered. Spectral (e.g. time/frequency, time/scale, bifrequency) and direct (e.g. Prony, maximum likelihood, Bayesian) estimation approaches will be considered.

## C. AE SIGNAL CLASSIFICATION

The objective of this third phase is to process detected signals and the parameters extracted from them, so as to classify the signals. AE signals could be generated for example from plastic deformation, material fracture or sensor degradation. Spurious AE-like signals are also possible. In year two of this investigation, we will collaborate with material scientists to gain an understanding of the differences between various AE signal types. We will then be in a position to classify detected AE signals.

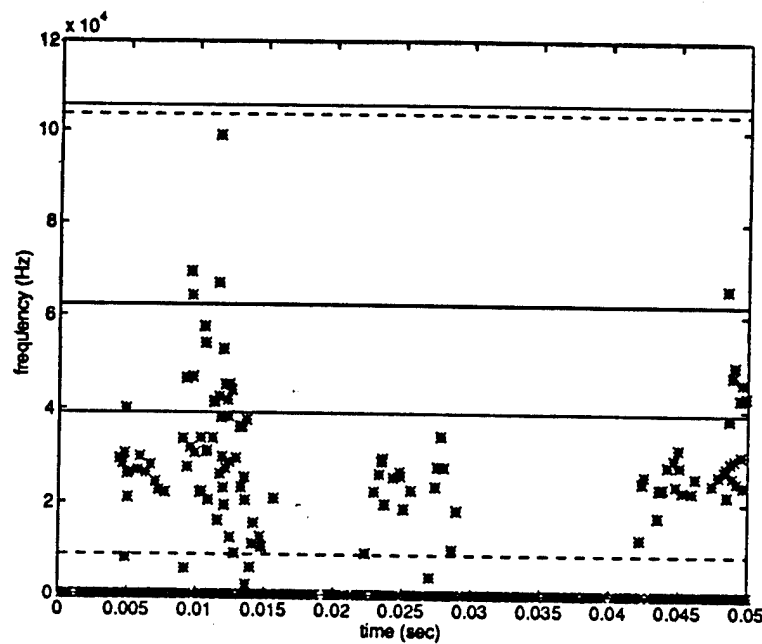


**Figure 66** A principal component frequency vs. time plot for a Prony fit to the engine with rotor noise.

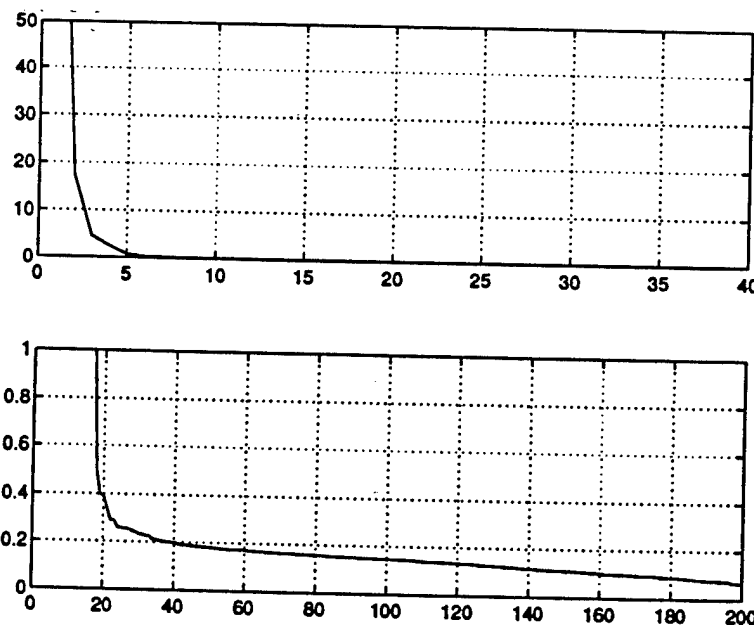


**Figure 67** Singular values of 8000 samples of engine with rotor noise.

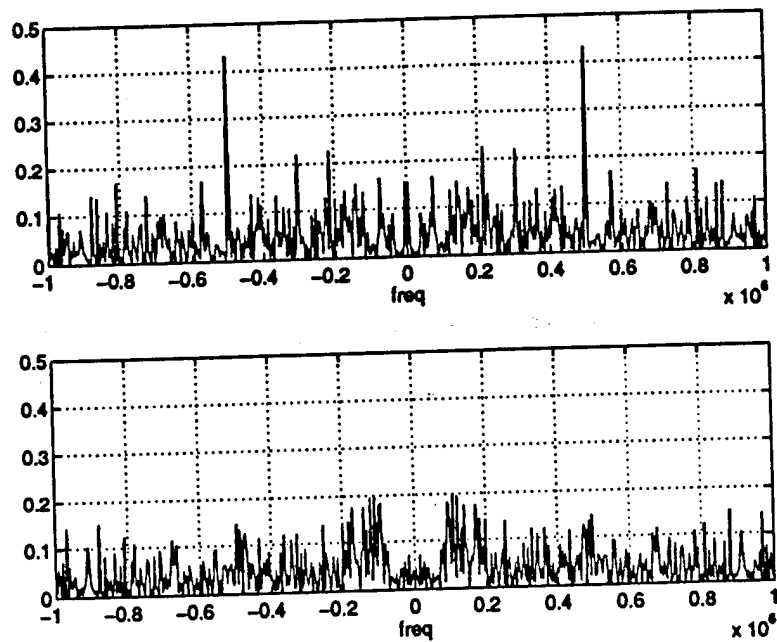


Figure 68 Noise power spectrum at 15-th order LP filter output.

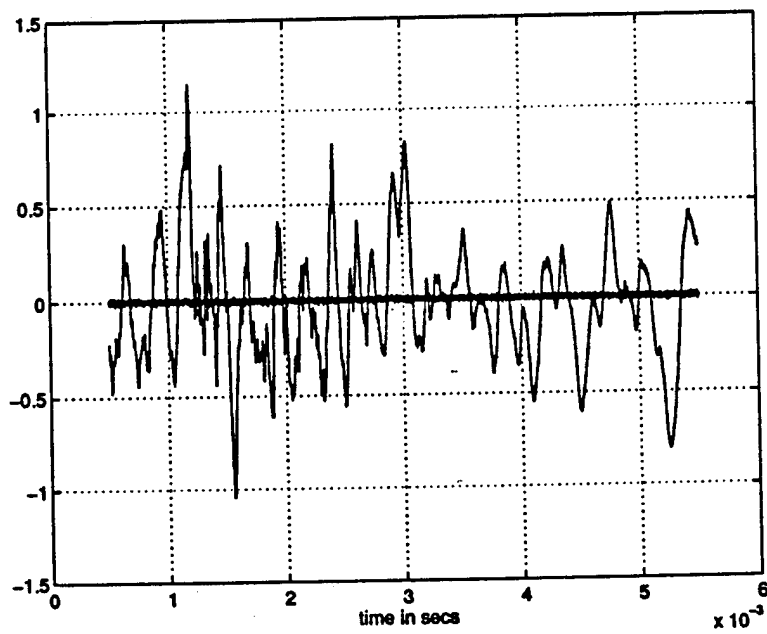
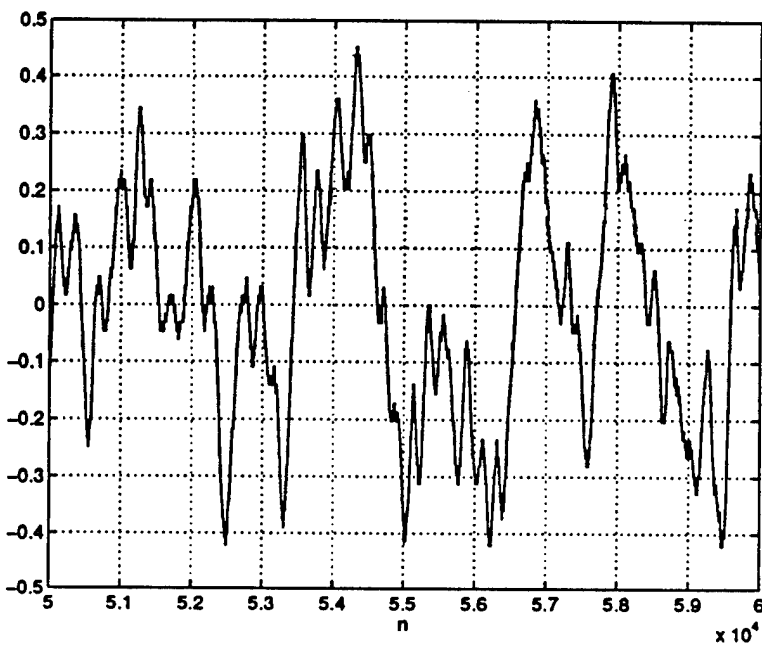
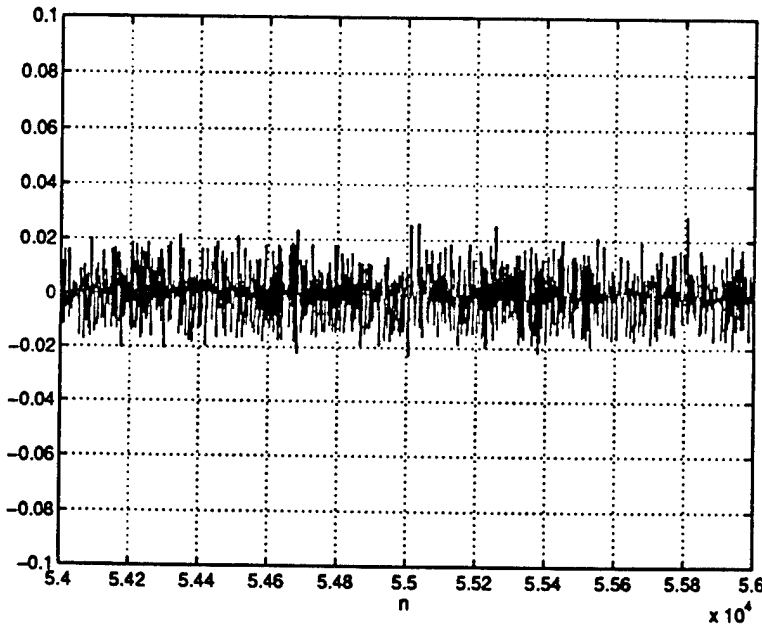


Figure 69 Noise power spectrum at 80-th order LP filter output.



**Figure 70** Tantalum nitride AE signal superimposed on engine with rotor noise. AE signal starts at sample 55,000.



**Figure 71** Linear prediction filter output for Figure 70 signal input.

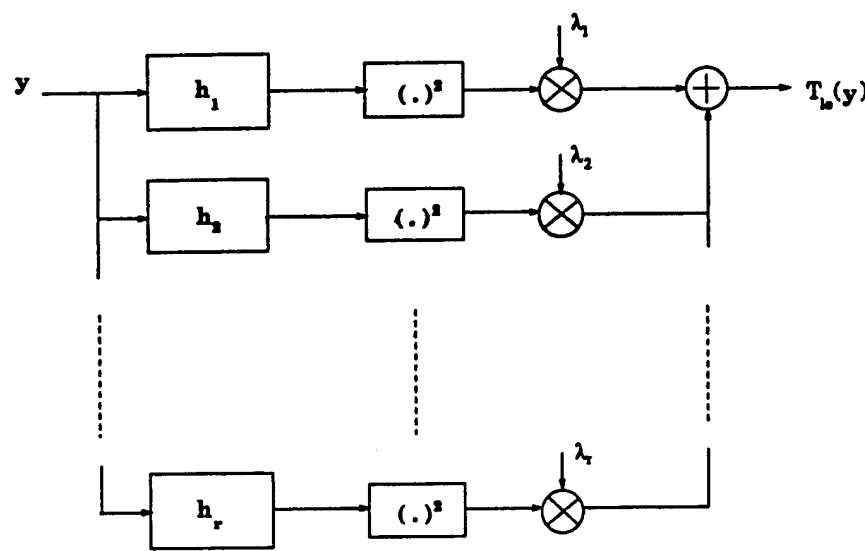


Figure 72 Block diagram of the processor for generating  $-t$ h decision statistic.

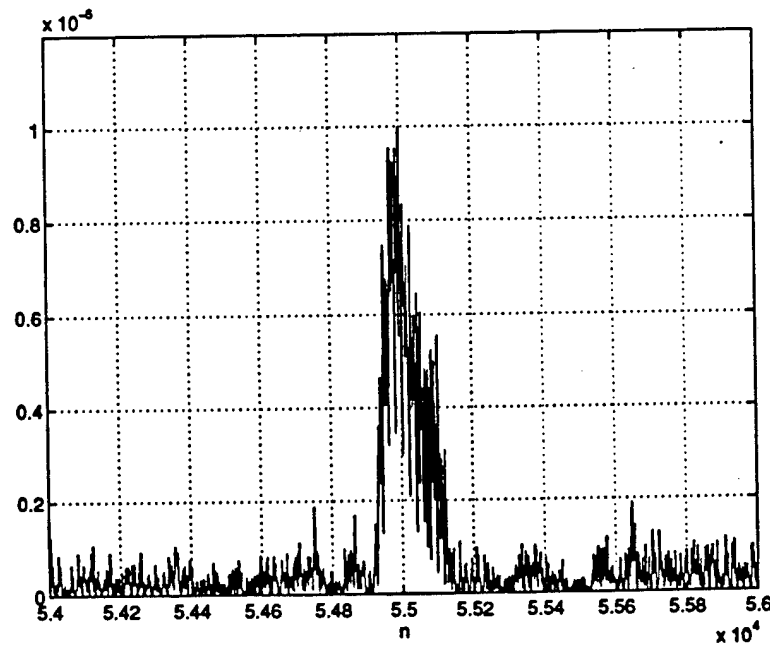
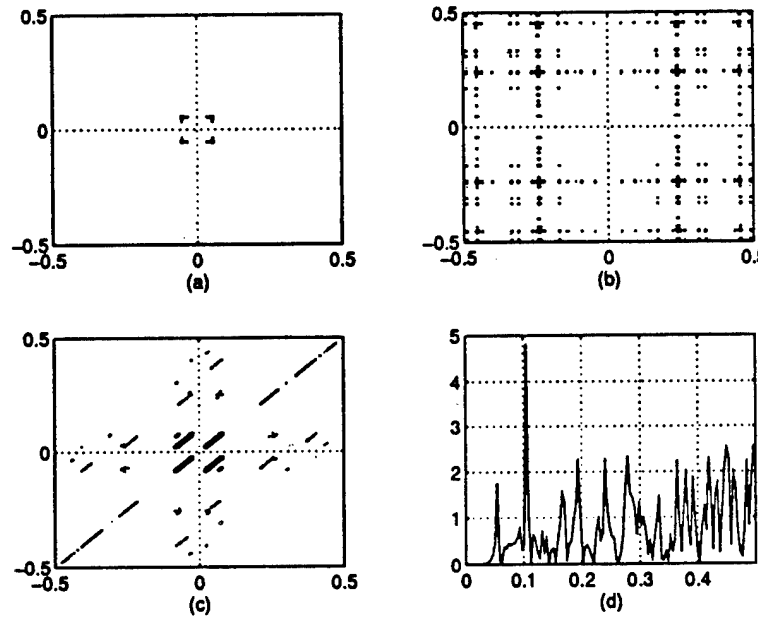
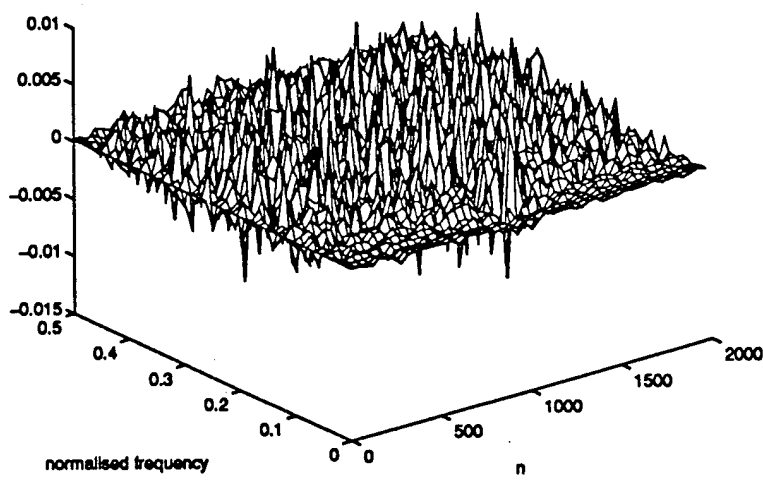


Figure 73 Decision statistic sequence generated by Figure 72 processor with Figure 71 input.



**Figure 74** Bifrequency spectrum magnitude plots: (a) AE signal; (b) AE signal in noise; (c) AE signal in noise - diagonal smoothing; (d) AE signal in noise - template smoothing. (All frequencies normalized to 2 MHz.)



**Figure 75** The magnitude of the Wigner distribution of the AE signal in additive engine with rotor noise after LP filtering.

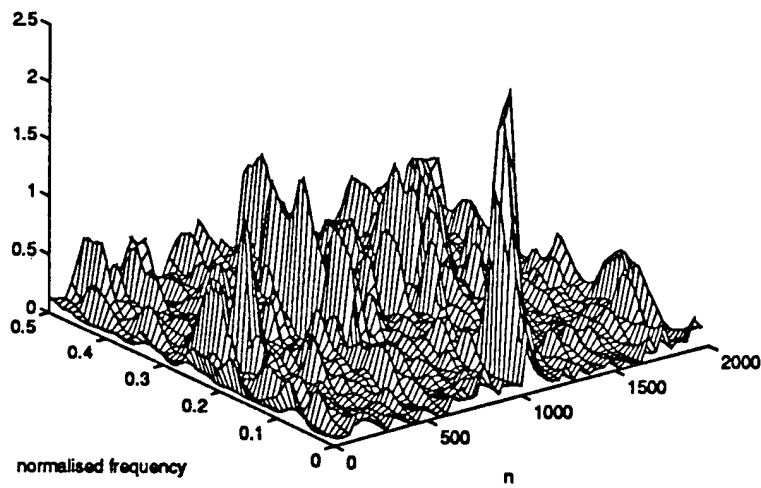


**Figure 76** Time-frequency plot resulting from optimum smoothing.

### 2.3.2 EDDY CURRENT MICROSENSORS FOR INTEGRATED DIAGNOSTICS

Co-investigator: S. Ramalingam (University of Minnesota)

#### Overview

Eddy current nondestructive inspection techniques for flaw detection are well-developed and in wide use. The same basic principles are also used to detect deviations in composition, hardness, transport properties and other properties of conducting materials. The objective of this project of the ONR/M-URI program on Integrated Diagnostics is to adapt and enhance the resolution limit of eddy current inspection techniques for flaw detection in much earlier stages of a component's life when the flaw dimensions are several tens of micrometer in size.

Engineered components of the aviation and defense systems are typically highly stressed. Expected component lives are long. To assure safe operation, stringent inspection and maintenance requirements are imposed. Meeting such requirements is expensive, both in time and personnel, and difficult to sustain over the long product/component lives. To meet the performance, life and reliability requirements of critical components, part design is based on high-cycle fatigue, where flaw nucleation/initiation phase of component life is high. However, in all mechanical systems, fatigue damage accumulates, flaw initiation occurs, and flaw growth ensues. Once a dimensional threshold is exceeded, a transition from the flaw nucleation/initiation phase of part failure to the growth-propagation phase is common.

Flaw growth characteristics in the propagation phase have been studied extensively. It is known that Paris law of the form,  $da/dN = C \Delta k^m$ , relating flaw growth per loading cycle to the range of stress intensity  $\Delta k$  at flaw tip, holds. In nearly all high strength materials,  $m \sim 3$  or more (values between 3.5 and 5 are common). Once transition to propagation stage occurs, residual life, though highly predictable, is comparatively small. Hence, critical components, following flaw detection, may be retired 'for cause' whenever the dimensions of the flaw detected warrant it, since on reaching the critical flaw size, catastrophic failure is virtually certain.

Extended component lives are usually secured by using fracture-resistant materials (high  $K_{IC}$ ) in critical components; periodic inspection to identify prevailing flaws and their largest dimensions, followed by repair; and limiting service loads to safe levels (derating the system). These remedies do not address the fundamental problem: absence of a knowledge-base relating design stresses to the flaw nucleation/initiation phase of a component's life, in order to develop high-reliability critical components.

Mechanics and materials-related projects of the MultiUniversity Center for Integrated Diagnostics seek to address these issues. Damage in and preceding flaw nucleation/initiation can occur within the matrix of the material. However, surface initiated flaws are more common in systems exposed to surface degradation during service (wear, corrosion, surface pitting resulting from cyclic loading in Hertzian contacts, etc.). Slip induced extrusion-intrusion processes due to cyclic (bulk) stressing, and surface-breaking micro-flaws generated in mechanically created surfaces are other most likely sources of micro-flaws which determine the flaw nucleation/initiation life in critical components.

Other projects in the Integrated Diagnostics program address identification of internal damage and flaws. Two parts of the program (this project and the Magnetic-Electrical-Impedance Tomography project, see Section 2.3.3) address the surface, near-surface micro-flaw detection-identification-imaging problem.

#### Goal

A schematic of the eddy current micro-sensor being developed to detect micro-flaws in this research effort of the ONR/M-URI Integrated Diagnostics program is shown in Figure 77. To reduce inspection time, cost and personnel requirements, array sensors are envisaged. To facilitate objective

#### Direct Sensing, Analysis, and Real-time Diagnosis

flaw identification, imaging techniques are to be used for flaw display. The test object is to be scanned with the sensor array in an automated inspection system and results displayed graphically for objective flaw mapping. Resolution limit sought is in the tens of micron range.

## Accomplishments

### Approach

In conventional eddy current inspection, a co-axial excitation/sensing coil assembly is used to interrogate the test object, as shown in Figure 78. Signal detected by the sensing coil is due to excitation coil - sensing coil coupling as well as that due to sensor - test object coupling. Direct coupling contribution is large, and to a large extent, it can be compensated for by using differential measurements [49,50]. Test object coupling varies with stand-off distance, electron transport and magnetic properties of the test object, and flaw distribution (size, shape and orientation) within the test body.

Eddy current inspection is now carried out by measuring changes in reactance of the coil assembly at a fixed stand-off distance, with the unflawed test object as the reference, and accounting for changes in resistivity. Use of normalized impedance plot is common. Highly trained operators, identify and classify the likely flaws. All other factors remaining constant, if now the flaw dimensions are changed slightly, there is a correspondingly smaller perturbation in the observed signal. When, even with a high precision signal measurement, the presence of the changes in flaw dimensions can not be detected, a resolution threshold or limit is reached.

Resolution limit is related to the ratio of test object volume producing the perturbation signal to the total volume interrogated by the coil assembly at a fixed stand off distance. Coil assembly dimensions and interrogation frequency can be altered to reduce the interrogation volume. Doing so greatly reduces the power transferred to the interrogation volume, and the signal sensed from the test object is correspondingly decreased. Nevertheless, it has been demonstrated recently [51] that by using sophisticated measurement techniques (phase-locked loops), micro sensors and micro sensor arrays do exhibit a capacity to resolve fine-scale flaws. To transfer sufficient power to interrogate the test object, a single enveloping excitation coil, spanning all the microsensors, had to be used.

To minimize electronic complexity, an alternate means of enhancing interrogating power transfer is sought in this project. To enhance power transfer, flux focusing techniques have been investigated (based on recent work at NASA-Langley aimed at shielding the sensing coil from the excitation coil).

Computer simulation techniques, summarized in the next section, were used to investigate the utility of flux focusing for non-destructive inspection. For experimental verification of the feasibility of flux focusing, test objects with though-the-thickness and surface-breaking flaws, shown in Figure 79, have been constructed. A test probe assembly with co-axial excitation and sensing coils capable of flux focusing, shown in Figure 80, has also been constructed. Computer simulations were carried with a computational geometry consistent (identical) with the test object and probe dimensions shown in Figures 79 and 80.

### Numerical Simulation

Numerical simulation of eddy current sensing process was carried out using a modified FEM package. The quantities of interest in simulation are: magnetic flux density, magnetic field intensity and induced eddy current densities within the test object and the test coil. Maxwell's equations are used for analysis. The primary unknowns (degree of freedom) determined by FEM analysis are the magnetic potential  $\{A\}$  distributions. Other field quantities sought are derived from the calculated potential distributions. For harmonic analysis (AC excitation), a vector potential formulation is used for both 2-D and 3-D problems.

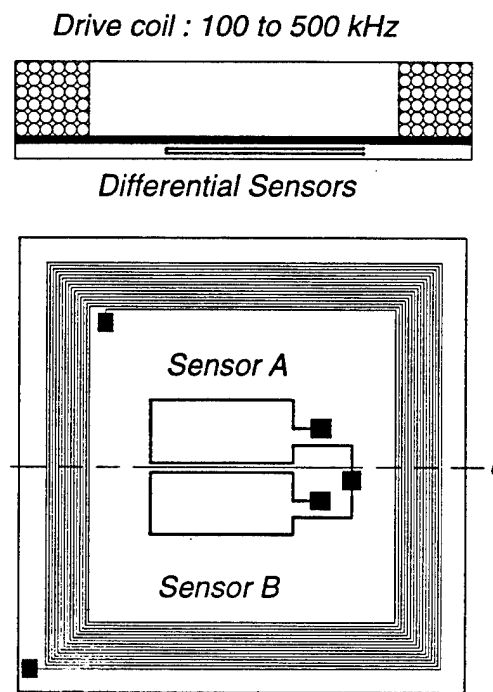


**Figure 77** Single element micro-sensor for eddy current sensing and imaging of micro-flaws

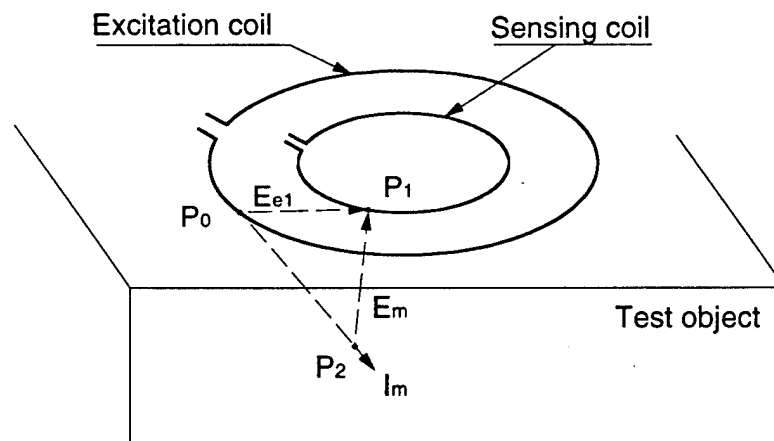
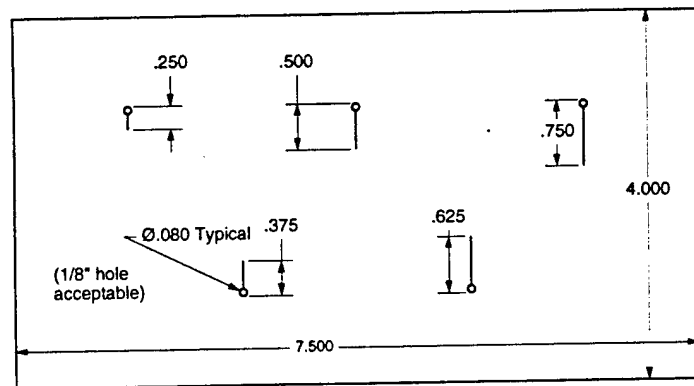
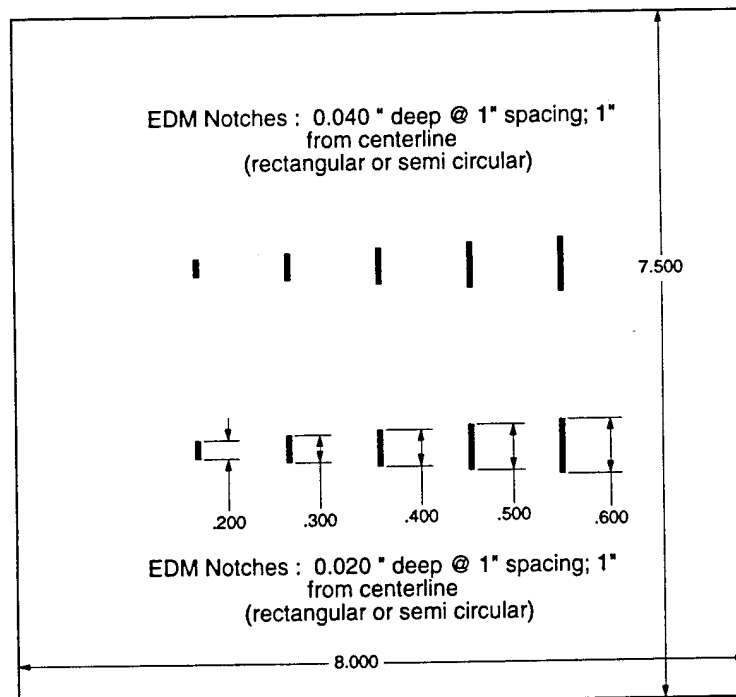


**Figure 78** Schematic of a conventional eddy current sensing system for flaw detection using co-axial excitation and sensing coils



Test sample  
with  
Wirecut EDM slots of varying lengths



Test sample  
with  
through-the-thickness 'artificial defects' of known length

**Figure 79** Test samples built to evaluate the resolution characteristics of experimental eddy current sensors

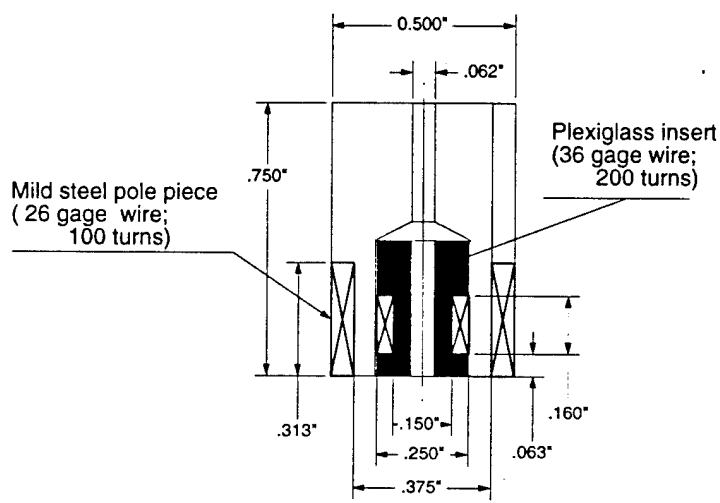


**Figure 80** A flux-focusing eddy current sensor for flaw detection.  
 Identical sensor geometry was used for  
 computer simulation and flaw imaging/mapping by scanning.

The magnetic vector potential method used for harmonic analysis is based on Maxwell's equations given by

$$\nabla \times \{H\} = \{J\} = \{J_s\} + \{J_e\} \quad (5)$$

$$\nabla \times \{E\} = -\left\{ \frac{\partial B}{\partial t} \right\} \quad (6)$$

$$\nabla \cdot \{B\} = 0 \quad (7)$$

where

$\{H\}$	= magnetic field intensity vector	$\{J\}$	= total current density vector
$\{J_s\}$	= applied source current density vector	$\{J_e\}$	= induced eddy current density vector
$\{E\}$	= electric field intensity vector	$\{B\}$	= magnetic flux density vector.

The field equations are supplemented by the constitutive relation which describe the behavior of the electromagnetic material

$$\{B\} = [\mu] \{H\} + \mu_0 \{M_o\} \quad (8)$$

$$\{J\} = [\sigma] \{E\} \quad (9)$$

where  $\{M_o\}$  = remnant intrinsic magnetization vector, zero for saturable material without permanent magnets (magnetic moment)  
 $\mu_0$  = permeability of free space  
 $[\mu]$  = magnetic permeability matrix, in general, a function of  $\{H\}$   
 $[\sigma]$  = electrical conductivity matrix

Solution is obtained by introducing the magnetic vector potential,  $\{A\}$ , which allows the magnetic field  $\{B\}$  and the electric field  $\{E\}$  to be expressed as

$$\{B\} = \nabla \times \{A\} \quad (10)$$

$$\{E\} = -\left\{ \frac{\partial A}{\partial t} \right\} - \nabla V \quad (11)$$

where  $V$  = electric scalar potential.

These satisfy two of the Maxwell's equations, (6) and (7). What remains to be solved is Eq. (5), in conjunction with the constitutive relations, (8) and (9). These equations are subject to the appropriate boundary conditions. Available FEM packages can be modified to solve the problem. Associated details are left out for the sake of brevity.

Once the vector potential distribution  $\{A\}$  has been determined, field quantities of interest are derived. Magnetic flux density is evaluated from vector potential distribution with

$$\{B\} = \nabla \times [N_A] \{A_e\}. \quad (12)$$

Magnetic field intensity is computed from the flux density

$$\{H\} = [\mu]^{-1} \{B\}. \quad (13)$$

Current density due to  $\{A\}$  is calculated with

$$\{J_e\} = -[\sigma] \left\{ \frac{\partial A}{\partial t} \right\} = -[\sigma] \frac{1}{n} \sum_{i=1}^n [N_A]^T \left\{ \frac{\partial A_e}{\partial t} \right\}. \quad (14)$$

The approach used has a sound physical basis [52,53,54].

Axisymmetric models of eddy current sensing system with a driving coil (Figure 80) carrying an AC excitation current at 25 kHz and 100 kHz were used. Quadrilateral solid elements (8 node elements) were used for the harmonic analysis (MKS units). Axisymmetric model of wound-coil sensor consists of driving and sensing coils, aluminum or steel shell (non-ferromagnetic or ferro-magnetic poles for flux focusing), iron core for sensing coil (Figure 80) and the test object. External environment was taken to be air and the test sample geometry (with/without flaws) is shown in Figure 79. Relative permeability and electrical resistivity are defined in the current-conducting regions. A relative permeability of 1.0 was specified for air. For saturable materials, literature relative permeability was used. Problem geometry and the mesh used were generated within the FEM package.

Boundary conditions are specified at the symmetry axis and the far-field boundary of the model. Flux-parallel conditions are used at the symmetry axis to force flux flow parallel to the axis. Far-field zero conditions are used to approximate a far-field boundary by setting the magnetic vector potential there to zero. A macro file to create an element table is needed for eddy current calculations within the test sample and sensing coil. Signal sensed in the sensing coil is calculated from eddy current density generated in it.

#### *Calculated results*

Calculated vector potential distribution in a ferro-magnetic test sample, sensor and the associated near-space are shown in Figures 81 to 85. Vector potential distributions due to an axisymmetric probe with an aluminum shell (non-ferromagnetic pole piece) are shown in Figure 81. Calculated distributions for unflawed (upper left) and flawed test samples are shown. Flaw geometry is taken to be conical and co-axial with the probe. Cone angles used for conical flaws are 90°, 45° and 60°. Cone depth was taken to be 0.080", with a flaw thickness of 0.010" (250 micron wide flaws). AC excitation at 25 kHz was assumed for this simulation. Calculated eddy current density distributions, for each geometry shown in Figure 81 are shown at corresponding locations of Figure 82.

Calculated vector potential distribution with a high permeability (ferromagnetic) pole piece replacing the aluminum shell (non-ferromagnetic pole piece) in the probe are shown in Figure 83. Results obtained with 25 kHz excitation is supplemented with those obtained at 100 kHz (Figure 84). Calculated eddy current density distributions, 25 kHz AC excitation, are shown in Figure 85.

Calculated results show that a ten-fold improvement in power transfer is feasible by flux focusing and that flux focusing can be effected both at low (25 kHz) and moderate (100 kHz) interrogation frequencies. Changes in magnitude and spatial location of peak eddy current densities with flaw geometry, and the associated changes in induced current density in the sensing coil observed, indicate that the approaches being pursued have a sound physical foundation.

The results also indicate that the probe resolution limit, with flux focusing, will be determined by the pole piece/excitation coil dimensions; the microsensor approach of this project is sound; and that an order of magnitude improvement in interrogation power transfer is feasible by flux focusing. (No attempt is made at quantitative comparisons here since the approximate, far field zero boundary conditions used to reduce computational complexity and time, introduce numerical errors. Error bounds have, however, been determined by calculating multi-turn, solinoidal coil fields. On a relative basis results presented are sound and valid).

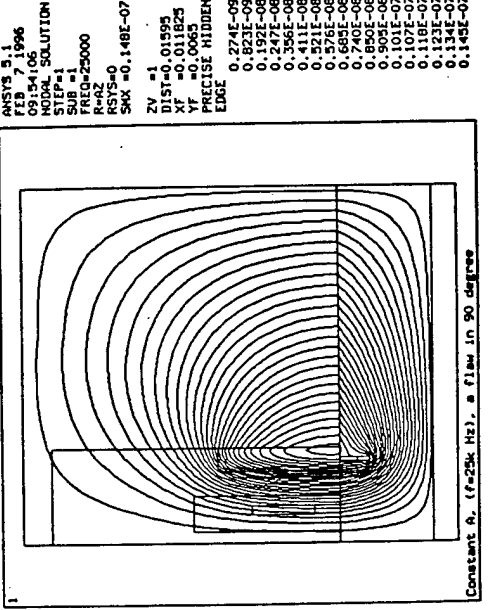
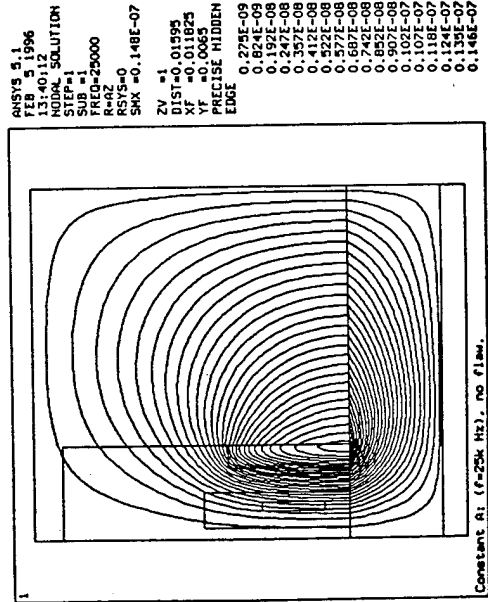


**Figure 81** Calculated vector potential distribution in a ferro-magnetic test sample, sensor, and the associated near space. Axisymmetric model with an aluminum (non-ferromagnetic) pole piece. Sensor dimensions per Figure 80; Unflawed (upper left) and flawed test samples; flaw geometry - conical (90, 45, and 60 degree cones) flaws, 0.080" deep and 0.10" wide, co-axial with the sensor; AC excitation 25kHz.

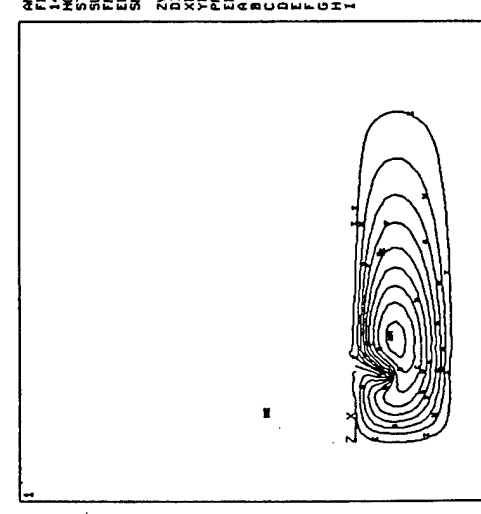
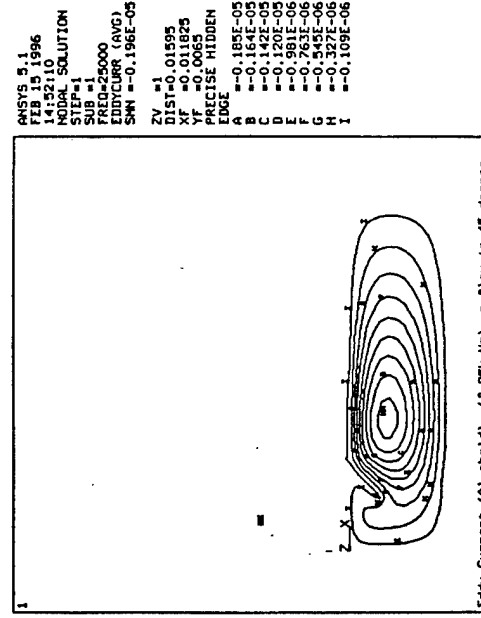
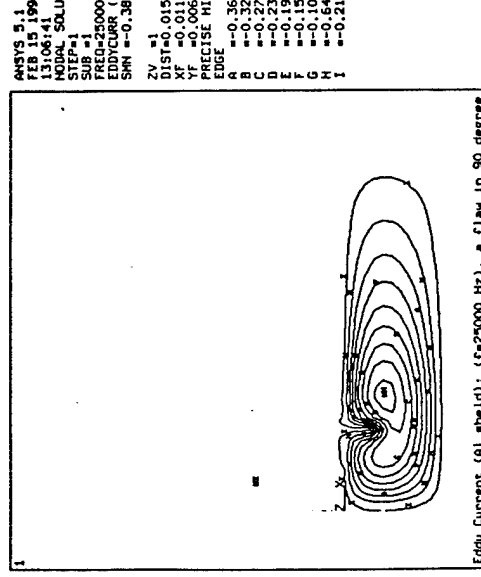
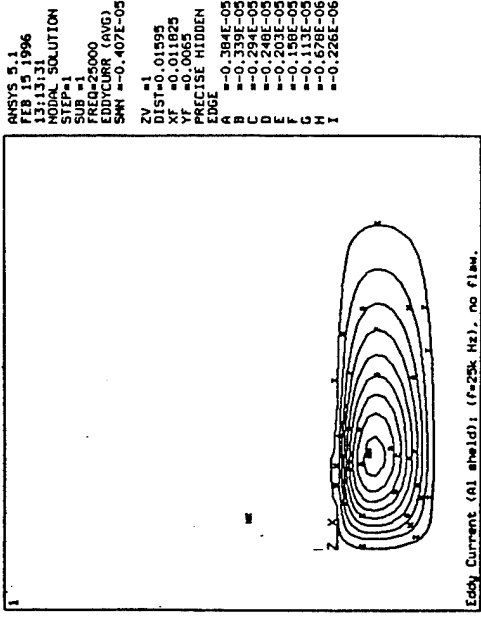


**Figure 82** Calculated eddy current density distribution in a ferro-magnetic test sample, sensor, and the associated near space. Axisymmetric model with an aluminum (non-ferromagnetic) pole piece. Sensor dimensions per Figure 80; Unflawed (upper left) and flawed test samples; flaw geometry - conical (90, 45, and 60 degree cones) flaws, 0.080" deep x 0.10" wide, co-axial with the sensor, AC excitation at indicated frequencies.

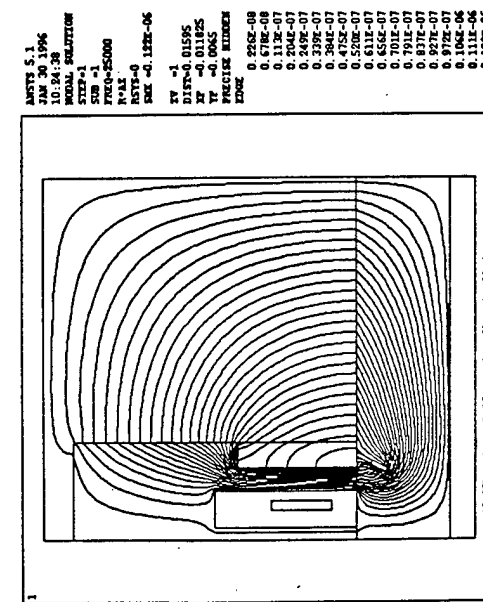
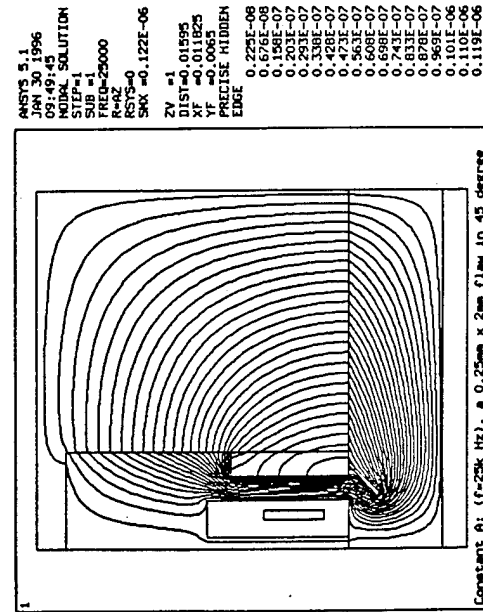
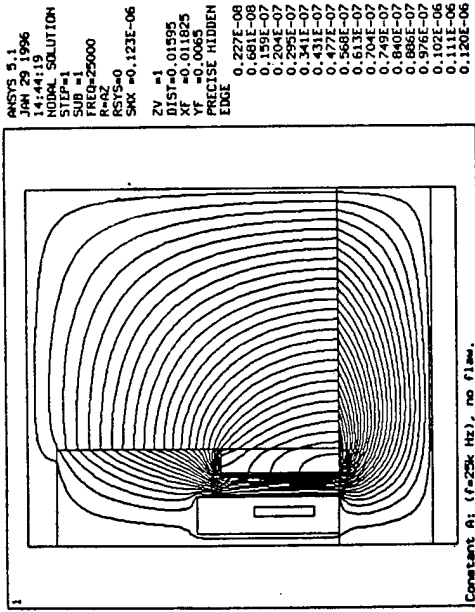


**Figure 83** Calculated vector potential distribution in a ferro-magnetic test sample, sensor, and the associated near-space. Axisymmetric model with a high permeability (ferromagnetic) pole piece. Sensor dimensions per Figure 80; Unflawed (upper left) and flawed test samples; flaw geometry - conical (45 and 60 degree cones) flaws, 0.080" deep and 0.10" wide, co-axial with the sensor; AC excitation at 25 kHz. Compare the numerical values obtained by flux focusing with those shown in Figure 81.

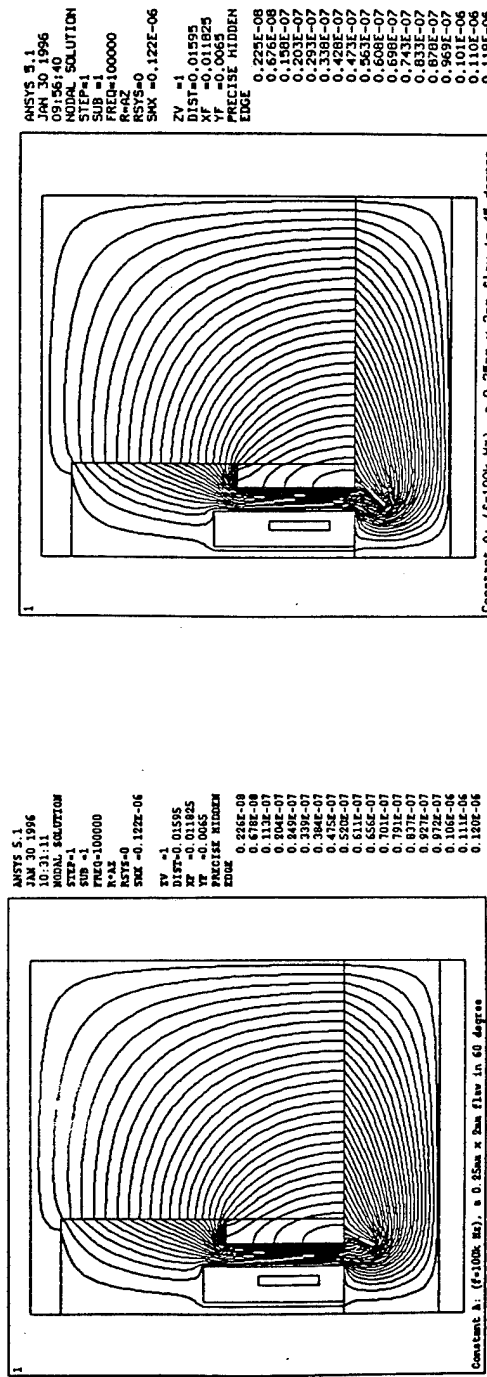
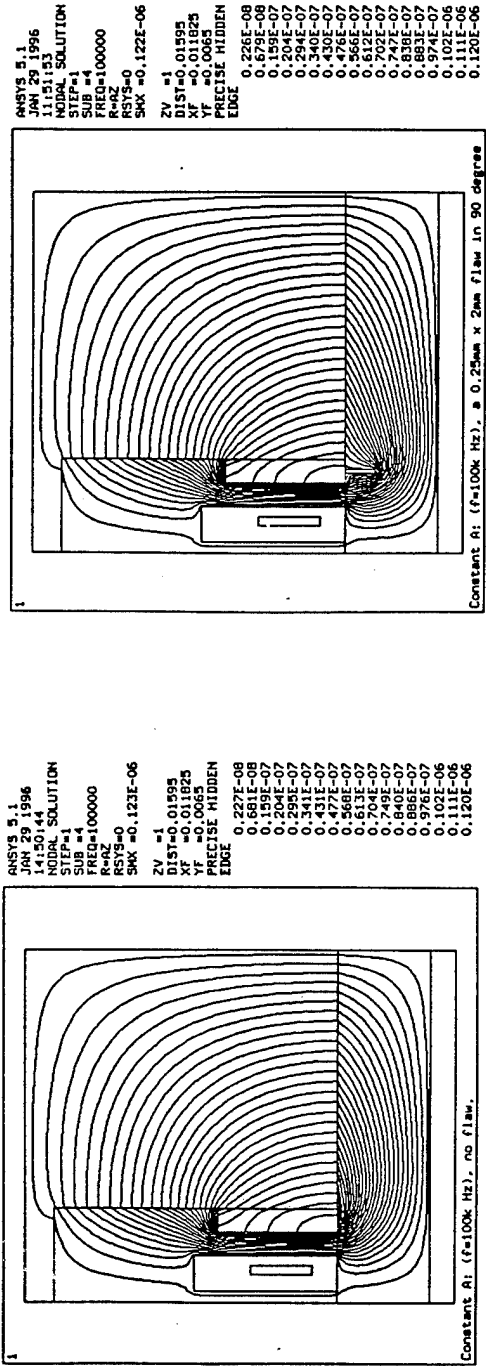


**Figure 84** Calculated vector potential distribution in a ferro-magnetic test sample, sensor, and the associated near-space. Axisymmetric model with a high permeability (ferromagnetic) pole piece. Sensor dimensions per Figure 80; Unflawed (upper left) and flawed test samples; flaw geometry - conical (90, 45, and 60 degree cones) flaws, 0.080" deep and 0.10" wide, co-axial with the sensor; AC excitation at 100 kHz. Compare the numerical values obtained by flux focusing with those shown in Figure 81.

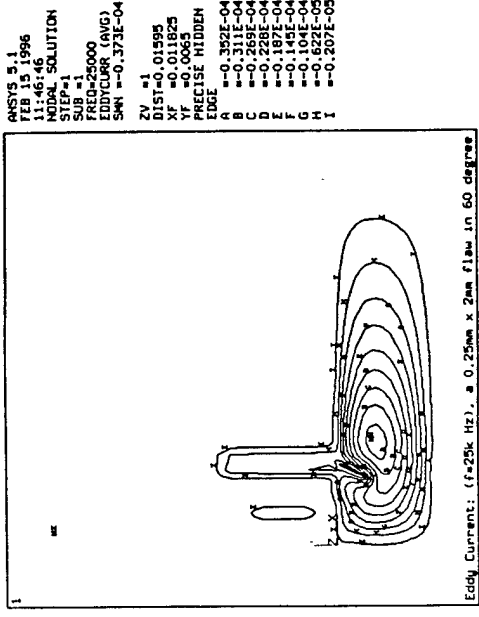
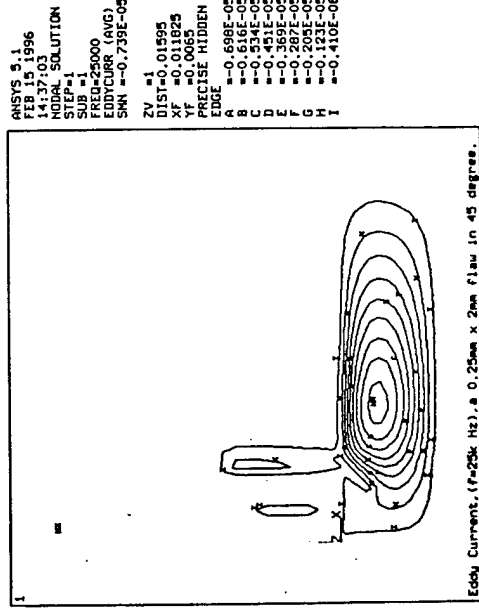
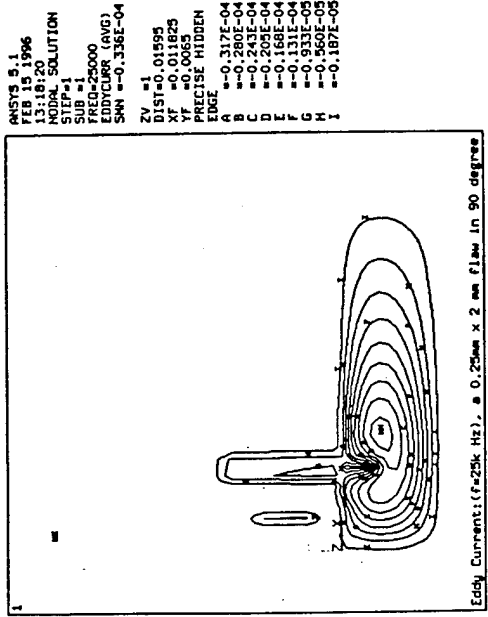
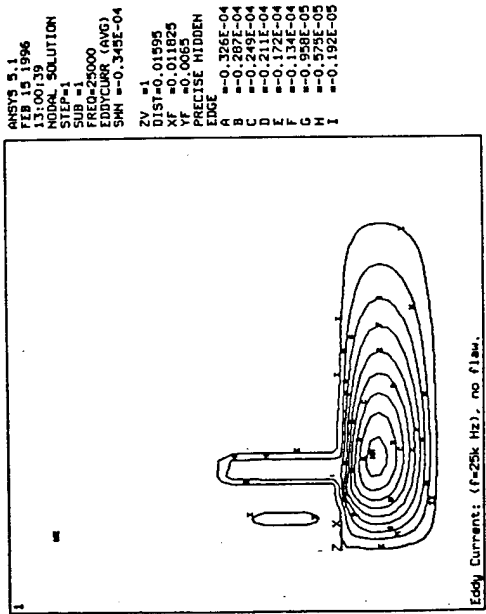


**Figure 85** Calculated eddy current density distribution in a ferro-magnetic test sample, sensor, and the associated near-space. Axisymmetric model with a high permeability (ferromagnetic) pole piece. Sensor dimensions per Figure 80; Unflawed (upper left) and flawed test samples; flaw geometry - conical (90, 45, and 60 degree cones) flaws, 0.080" deep x 0.10" wide, co-axial with the sensor; AC excitation at indicated frequencies. Compare the numerical values obtained by flux focusing with those shown in Figure 82. An order of magnitude increase in eddy current density is obtained by flux focusing.

### *Experimental Evaluation of Flux Focusing*

To experimentally test the soundness of the approaches being pursued and the numerical calculations carried out, a variable speed, motor-driven x-y table was assembled and an eddy current probe was constructed with the same excitation coil, sensor coil and pole piece dimensions as those shown in Figure 80. Test samples shown in Figure 79 were scanned at a stand off distance  $\sim 0.005"$ . The as-acquired sensor signals at 12 kHz were RMS-to-DC converted (Gain = 1). Scanned signals, obtained every 0.020" along and transverse to the scanning direction, were used to image a flawed samples containing a 1/4" (6.25 mm) drilled hole and a test sample containing a 0.008" wide slot (terminating at a 0.080" drilled hole).

Flaw map constructed by scanning the through-the-thickness flaw (drilled hole, 1/4" in diameter) in a steel plate, with the flux-focusing sensor (of Figure 80), is shown in Figure 86(a). As suggested by the numerical simulations, edge detection dominates due to flux focusing, raising the apparent flaw size. Efficient power transfer for interrogation is attested to by signal acquisition requiring no gain. Flaw map constructed by scanning a through-the-thickness flaw (0.008" slot, 1/2" in length terminating at a drilled hole, 0.080" in diameter, Figure 79) in a steel plate is shown in Figure 86(b). Again, edge detection dominates, raising the apparent flaw size, as in the previous case.

To verify that the spatial resolution can be improved by reducing the flux focusing pole piece dimensions, a smaller probe with a 1/8" diameter pole piece was constructed and used to scan the same test samples as those used to generated the flaw maps shown in Figure 86. Results, shown in Figure 87, confirm that improved spatial resolution is feasible by scale reduction (miniaturizing the probe).

### *Microsensors*

Scale reduction for miniaturizing the probe requires sensor construction based on thin film deposition, photo-lithography, wet etching, lead bonding and packaging. These are established micro fabrication technologies. An RF generator, in this co-PI's laboratory, was used in conjunction with the resources of the Micro Technology Laboratory at the University of Minnesota (co-PI Dr. Dennis Polla is the Director of MTL, see Section 2.3.1) to develop device-making processes. Single-element and micro sensor arrays have been fabricated on 2" Silicon wafers using the mask shown in Figure 88.

Even with 10  $\mu\text{m}$  technology, design requirements dictate a device, 4.5 mm square in size. At project initiation, device fabrication based on PC Board technology was envisaged. Since the state-of-the-art, minimum PC board metal line thickness is 0.004" (100  $\mu\text{m}$ ) for surface mounts, implementation of PC board technology was not pursued and device implementation proceeded directly to photo-lithography and sensor construction on silicon substrates.

Numerical and experimental work carried out in the first year indicate that flux focusing with a pole piece can greatly enhance interrogation power transfer and simplify signal conditioning and/or amplification complexity. Micro-sensor fabrication now requires a 3-metal process with 5 masks. Because the fabrication technology is a batch process, this is not a technology barrier. Principal barrier in shrinking device dimensions is the coil geometry (co-axial; multi-turn coils).

### **Plans**

With no increase in the number of metal layers, an improved process for coil construction not entailing spatial penalties, can be achieved by device implementation in a plane normal to the plane of fabrication. Plan and section view for a 3-mask micro sensor, which allows single element and array sensors of this form, is shown in Figure 89. It is expected that the second year program will focus on transverse eddy current micro sensors, following evaluation of planar eddy current micro sensors fabricated with the mask shown in Figure 88.

Following numerical simulations to verify design concepts, 3-mask micro sensors fabricated on Silicon will be evaluated with the focusing pole piece shown in Figure 90. This is considered to be an

### ***Direct Sensing, Analysis, and Real-time Diagnosis***

essential step before committing to several additional masks to implement 5 - 7 layer, transverse eddy current, micro sensors.

With modest design modifications, a simultaneous effort will be pursued to build dipole and quadrupole micro-sensors based on transverse coil geometry to support the Magnetic-Electrical-Impedance Tomography project underway at Georgia Tech (see Section 2.3.3, co-PI's Scott and Vachtsevanos).

Microflaw identification and mapping are based on eddy current density (this effort) or magnetic field anomalies (collaborative project, see Section 2.3.3) arising from disturbances due to presence of surface-breaking and near-surface flaws in test objects. Substantial and major progress has been made in recent years in understanding magneto resistance (MR) principles and in the design of MR devices. Thin, multi-layer films have also been found to display Giant Magneto Resistance (GMR) effects. Fields as small as 50 G can yield change in resistance DR of ~ 0.2 to 0.7% in GMR-based sensors [55,56]

Device implementation based on GMR and the thoroughly understood Wheatstone bridges can greatly simplify micro flaw identification tasks relevant to flaw detection in the flaw nucleation or initiation phases of a component's life. A microsensor based on GMR, again implementing flux focusing (flux concentration), is shown in Figure 91. It is anticipated that part of the M-URI year 2 effort will focus on evaluating the feasibility of GMR microsensors and microsensor arrays.

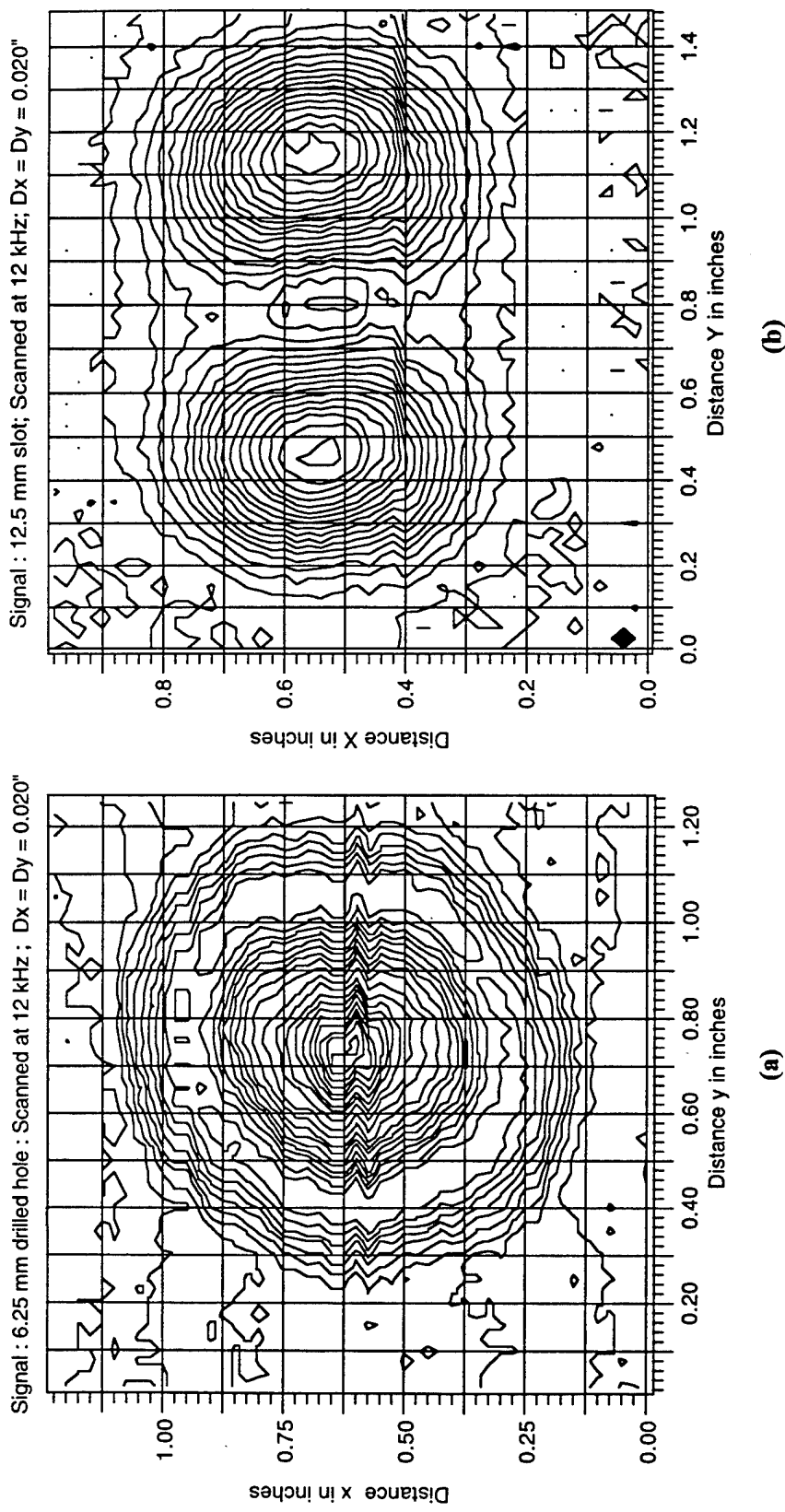
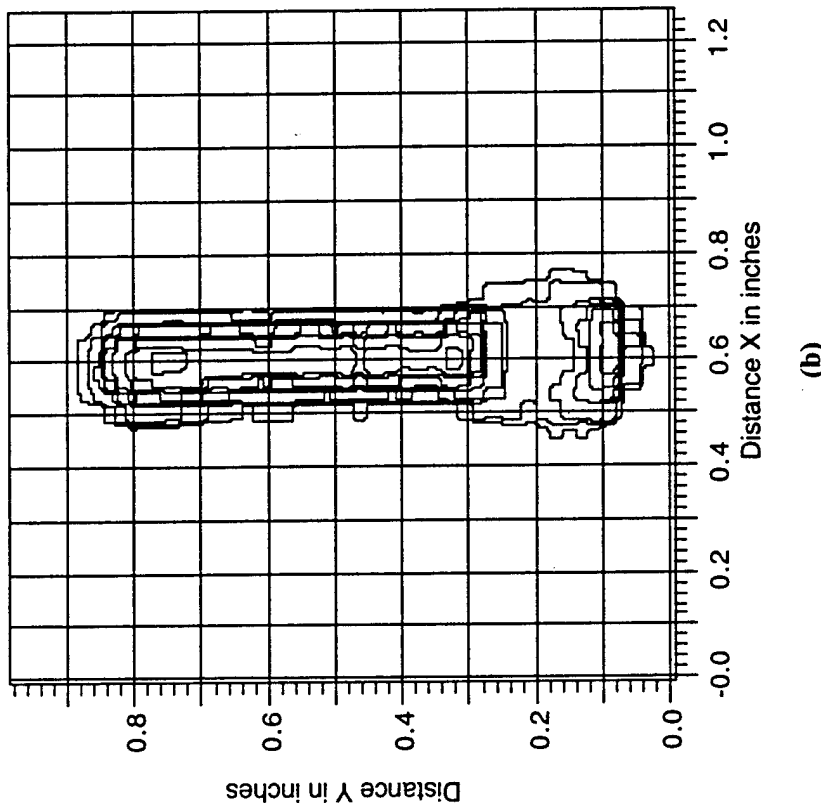


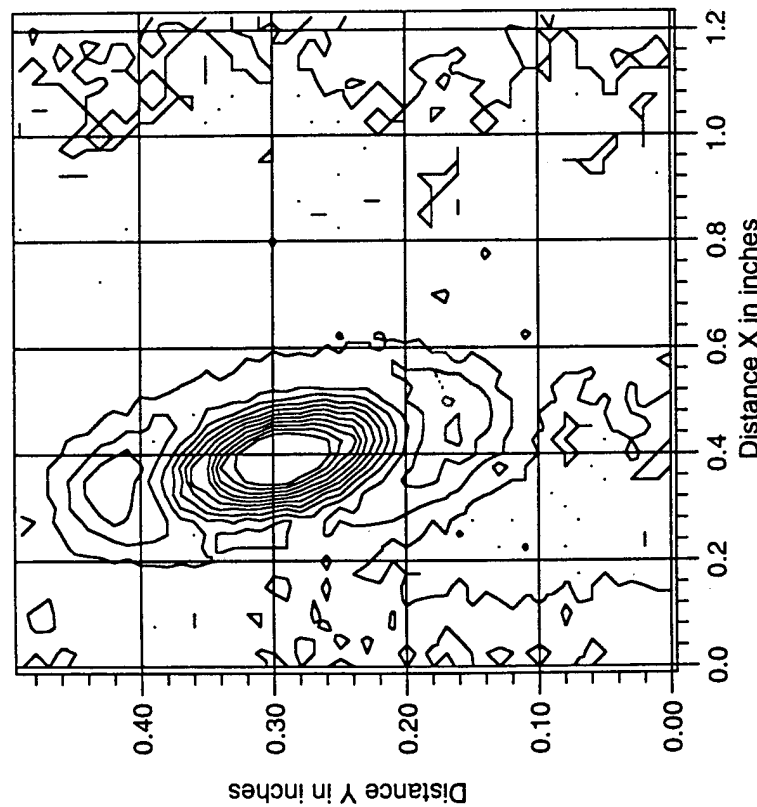
**Figure 86 (a)** Flaw map constructed by scanning a through-the-thickness flaw (drilled hole, 0.250" in diameter) in a steel plate with the flux-focusing sensor of Figure 80. Edge detection dominates, raising the apparent flaw size.

**Figure 86 (b)** Flaw map constructed by scanning a through-the-thickness flaw (drilled hole, 0.080" in diameter, connected to a 0.008" slot, 1/2" in length, as shown in Figure 79) in a steel plate with the flux-focusing sensor of Figure 80. Edge detection dominates, raising the apparent flaw size.



(b)

**Figure 87 (b)** Flaw map constructed by scanning a through-the-thickness flaw (drilled hole, 1/8" in diameter, connected to a 0.008" slot, 1/2" in length, as shown in Figure 79) in a steel plate with the flux-focusing sensor having a 0.125" dia. pole piece diameter. Edge detection still dominates, but spatial resolution is enhanced. (Shape distortion due to scale differences.)



(a)

**Figure 87 (a)** Flaw map constructed by scanning a through-the-thickness flaw (drilled hole, 0.080" in diameter, connected to a 0.008" slot, 1/2" in length, as shown in Figure 79) in a steel plate with the flux-focusing sensor having a 0.125" dia. pole piece diameter. Edge detection still dominates, but spatial resolution is enhanced. (Shape distortion is the same as that for Fig. 86 (b), rotated by 90 degrees.)

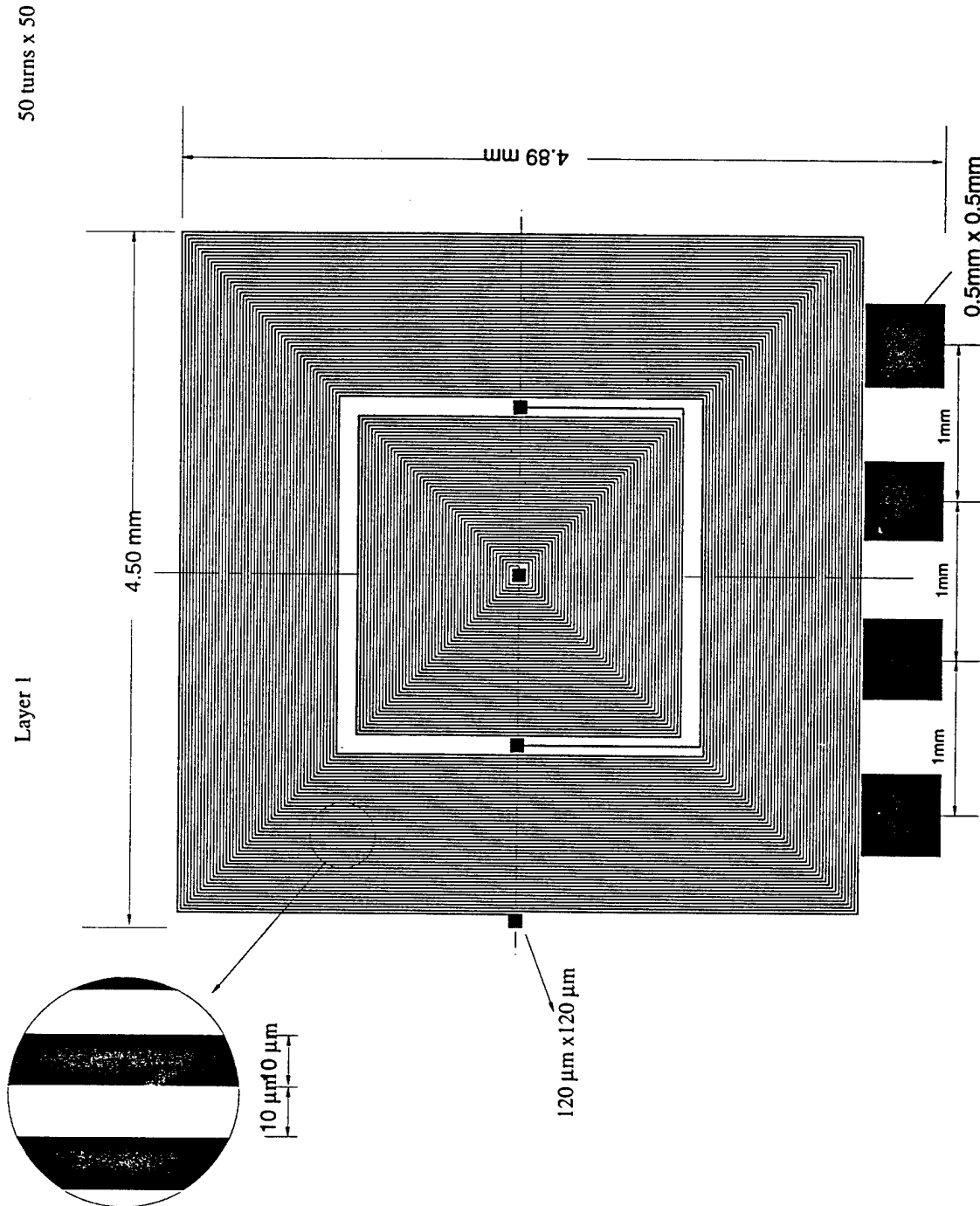
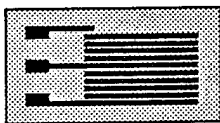
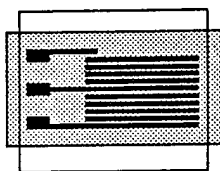


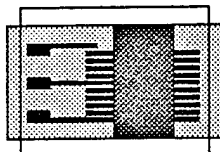
Figure 88 Mask geometry used for fabrication of single element and multi-element microsensor arrays



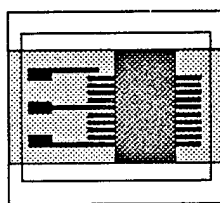
Deposit metal film and pattern



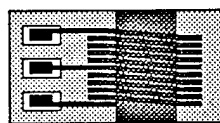
Cover with PSG/Alumina



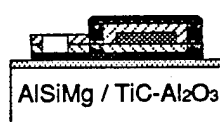
Pattern and deposit flux concentrators



Cover with PSG/Alumina



Pattern and deposit metal film



Section : 3 mask, 5 layer device

**Figure 89** Schematic illustration of redesigned, eddy current micro-sensor arrays, embodying flux focusing principles. A 3-mask device of the sensing coil is shown. Array sensors are to be implemented with co-axial excitation coils (5 or more masks).

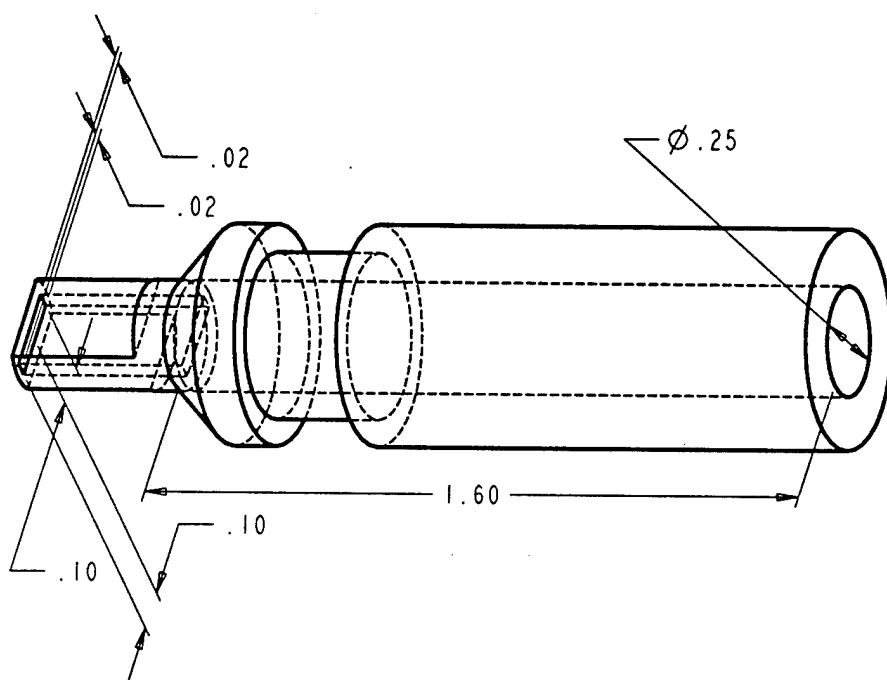


**Figure 90** Schematic of the excitation coil pole piece for first evaluation of the 3-mask, flux focusing, single-element eddy current micro-sensor.

## GMR Micro-sensor for Eddy Current Sensing

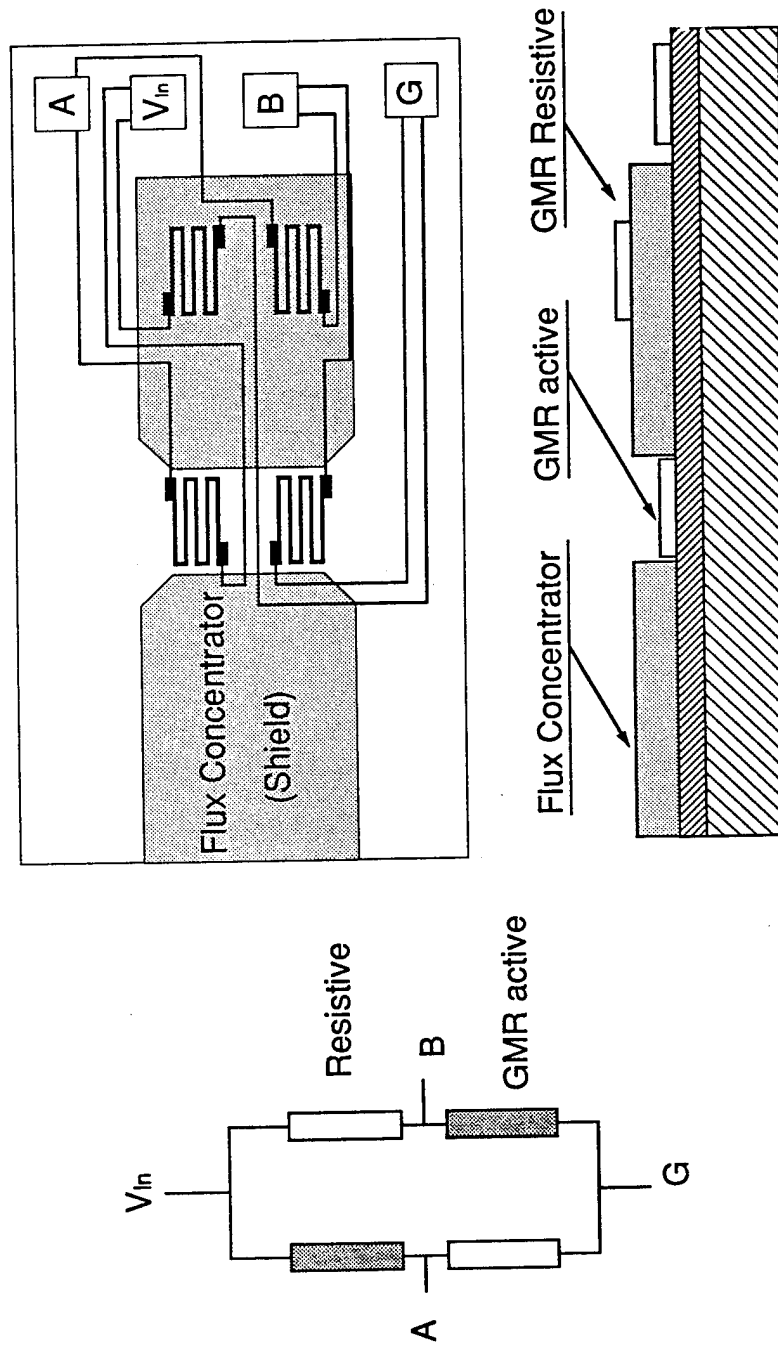


**Figure 91** Schematic illustration of a flux focusing micro-sensor based on GMR (Giant Magneto Resistance). Signal conditioning and amplifying are both greatly simplified with sensor designs relying on Wheatstone bridges.

### 2.3.3 MAGNETIC-ELECTRICAL-IMPEDANCE TOMOGRAPHY

Co-investigators: Waymond Scott, Jr. and George Vachtsevanos (Georgia Tech)

#### Overview

The objective of this research is to develop a new technique for noninvasively probing a piecewise homogenous body for small internal flaws on the order of 50  $\mu\text{m}$  in size. The technique is a hybrid of two existing techniques - eddy current testing and electrical impedance tomography. In this technique, current is injected into the device under test with electrodes placed on the surface. The injected current flows between the electrodes along the surface of the device under test. Figure 92 is a diagram illustrating the current flowing between two electrodes on a device under test with and without a flaw. When a flaw is not present, the current flows smoothly between the electrodes; however, when a flaw is present, the current changes abruptly near the flaw. The abrupt change in the current will result in a distinctive signature in the magnetic field. A focusing magnetic probe is used to detect the magnetic signature of the flaw. Thus, by scanning the surface of the device under test with the focusing magnetic probe, one can locate a flaw by detecting the magnetic signature of the flaw. Since the depth at which the currents will penetrate into the device under test decreases with increasing frequency, one can also ascertain information about the depth of the flaw by adjusting the frequency of the injected currents.

#### Accomplishments

The first year of this project has been very productive; all of the goals have been met. The two-dimensional experimental test bed has been designed and constructed, a two-dimensional computer model has been partially developed, a new type of focusing probe has been developed, and we have demonstrated that we can detect flaws with the proposed technique.

#### Experimental Test Bed

Figure 93 is a schematic diagram of the experimental test bed designed and constructed for this project. The test bed is being used to demonstrate the viability of the new measurement technique and to evaluate the effectiveness of the focusing heads. The test bed consists of a HP3577a automatic network analyzer, a power amplifier, a matching transformer, a current probe, a differential low-noise amplifier, a focusing probe, and a device under test. The network analyzer is used to generate and analyze the signals for the test bed. Since the amplitude of the signal generated by the network analyzer is insufficient to adequately test and evaluate the system, the power amplifier is used to amplify the signal. Since the impedance of the device under test is much less than the output impedance of the power amplifier, the matching transformer is used to change the impedance level of the signal. The maximum amplitude of the current output by the matching transformer is approximately 45 A. The amplitude of this current is monitored using a current probe that is connected to the reference channel of the network analyzer. When this current is sent through the device under test, it will generate a magnetic field. The distribution of the magnetic fields will depend on the distribution of the currents in the device under test. The focusing probe is used to measure the magnetic fields and is designed to selectively respond to the magnetic signature of a flaw in the device under test. The output of the focusing probe is amplified by a differential, low-noise amplifier and is then input into a signal channel of the network analyzer. The network analyzer displays the magnitude and phase of the ratio of the signal channel to the reference channel. The magnitude of this response is the strongest when the probe is placed over a flaw. Thus, by scanning the probe over the device under test one could discern the location of a flaw by monitoring the response.

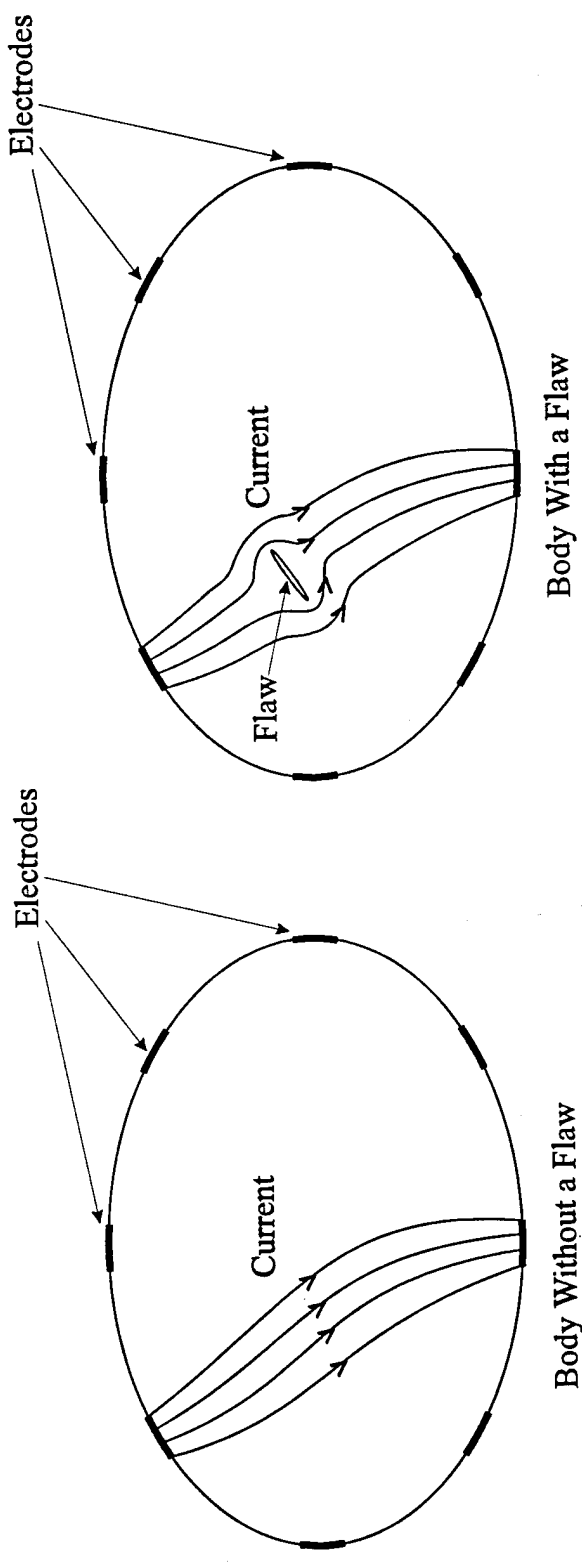


**Figure 92** Diagram illustrating the current flowing between two electrodes on a device under test with and without a flaw.

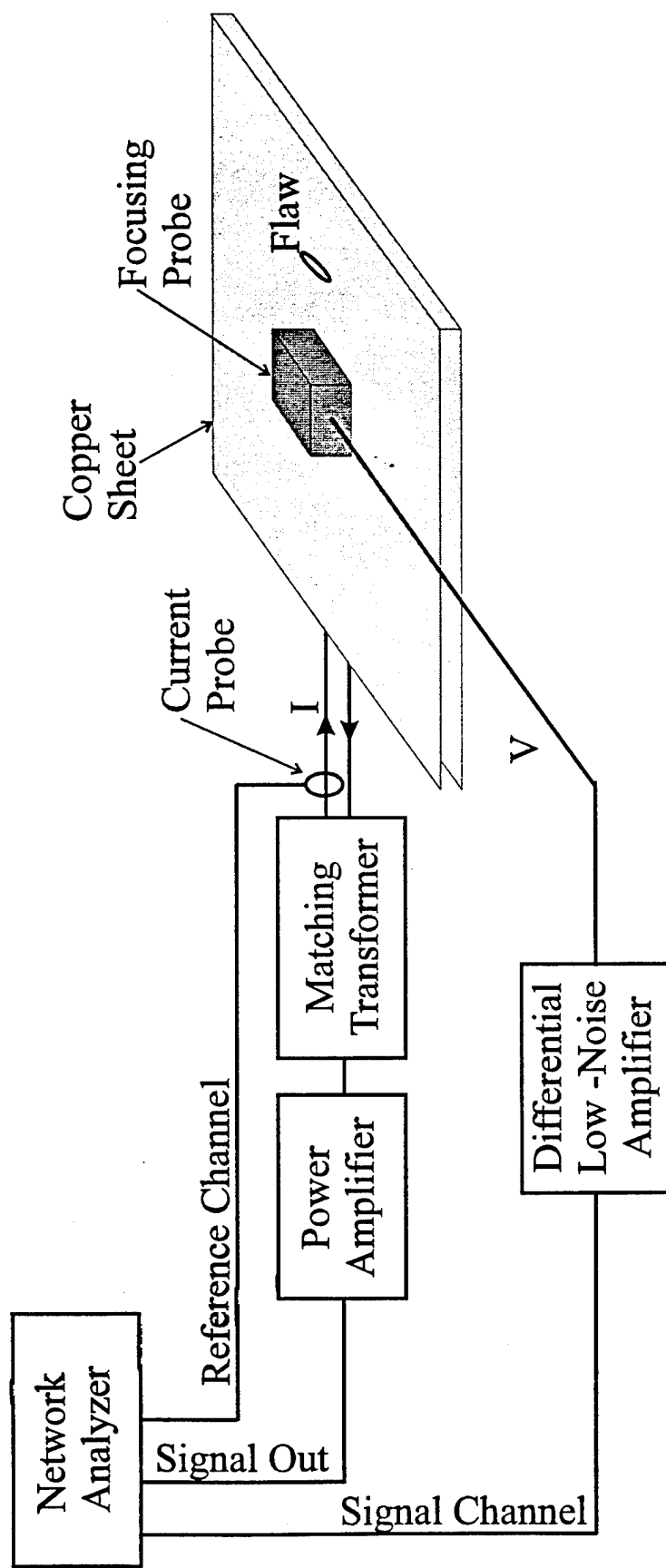


Figure 93 . Schematic diagram of the experimental test bed.

For the initial tests, the device under test consists of a two sided, copper clad, circuit board with flaws machined into the copper cladding. The circuit board is approximately 28 cm wide, 40 cm long and 1.6 mm thick. The copper cladding is approximately 0.07 mm thick. The circuit board is connected as shown in Figure 93. The current is injected at one end of the copper cladding on the top of the circuit board and collected at the same end on the copper cladding on the bottom. The current flows from the top to the bottom cladding by ways of a current shunt soldered on to the opposite end. For the initial testing, this geometry was chosen to make the flaws easier to detect. The magnetic fields generated by currents on the top and bottom claddings approximately cancel, making it easier to detect the magnetic fields generated by a flaw in one of the sheets. The device under test will be generalized to a more practical geometry in second year.

#### *Two-Dimensional Numerical Model*

A two-dimensional numerical model has been developed. The model consists of three parts: a current model, a magnetic field model, and a probe model. The current model uses the finite element method to compute the potentials in the device under test and then takes the gradient of the potential to compute the currents. Higher-order elements are used in the finite element method to improve the accuracy. The magnetic field model calculates the magnetic field from the currents using the Biot-Savart law. At this time, the probes have not been incorporated into the model.

#### *Focusing Probes*

The focusing probes are the heart of the flaw detection technique. A perfect focusing probe would respond strongly to the magnetic signature of the flaw and would not respond at all to extraneous magnetic fields. Unfortunately, it is not possible to build a perfect probe. In the proposal, monopole, dipole, and quadrapole magnetic sensing coils were proposed as focusing probes. A more effective type of focusing was discovered in the initial research of the technique. The probe uses magnetic materials to help focus the field in a manner very much like that in the head of a tape recorder or computer disk. Two versions of the probe have been fabricated, and both versions have produced very promising results.

Sketches of both probes are in Figure 94. The probes will be referred to as C and D type as indicated in Figure 94. The probes are made of a ferrite material: Amidon material number 77. The magnetic coils are wrapped around the portion of the core opposite the slit, and the slit portion of the core is placed next to the device under test. Initial testing has been performed on the probes in two configurations: a single probe which behaves similarly to a magnetic dipole and a differential pair of probes which behave similarly to a magnetic quadrapole. The differential pair of probes are aligned so that the axes of the probes are along the same line and are located 1 cm apart. The differential pair of D type probes has performed best in the initial testing. Its response to the magnetic signature of a flaw is the strongest relative to its response to the extraneous magnetic fields.

Figure 95 is a graph of the magnitude of the response on the differential pair of D type probes as a function of frequency for five different cases. In the first three cases, the probe is place directly above flaws in the device under test: a slit of length 2.54 mm, a slit of length 0.64 mm, and a circular hole with a diameter of 0.34 mm. In the fourth case, the probe is placed at five different locations above the device under test away from the flaws. In the fifth case the probe is placed several meters from the device under test. In all of the cases the magnitude of the response is seen to be approximately proportional to the frequency, just as one would expect. The deviations from a linear response at the higher frequencies are due to capacitive coupling between the heads and the device under test. The magnitude of the response is seen to be stronger when the probe is placed above a flaw than when it is placed away from a flaw, and the magnitude of the response is seen to be stronger for the larger flaws. Note that the magnitude of the response is approximately 40 dB stronger when the probe is placed above the 2.54 mm as compared to an unflawed portion of the device under test.

To demonstrate that the proposed technique can be used to detect flaws, measurements were made in which the probe was scanned across the device under test in which flaws of known size were

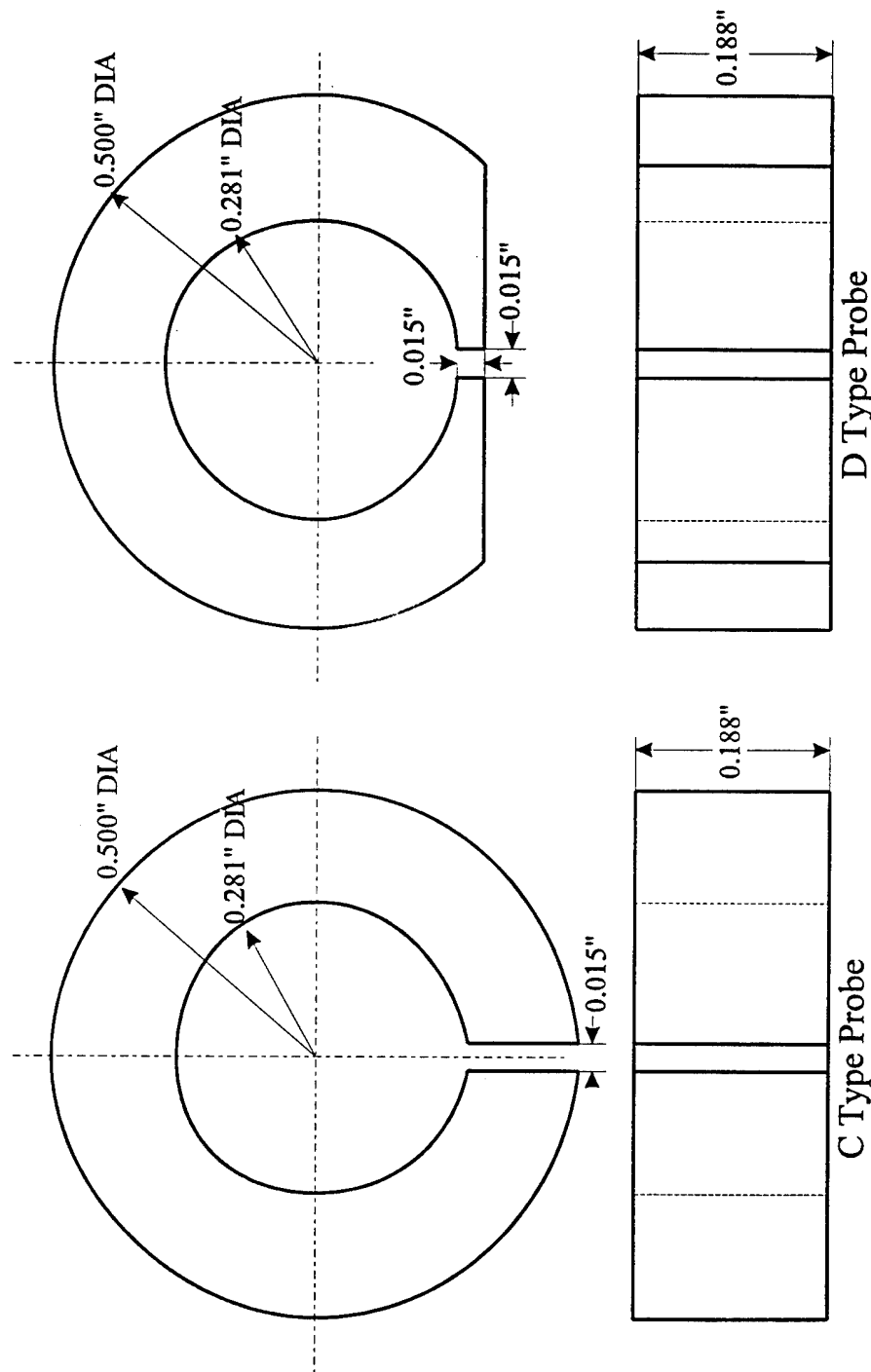


Figure 94 . Drawings of the C and D type focusing probes that have been constructed.

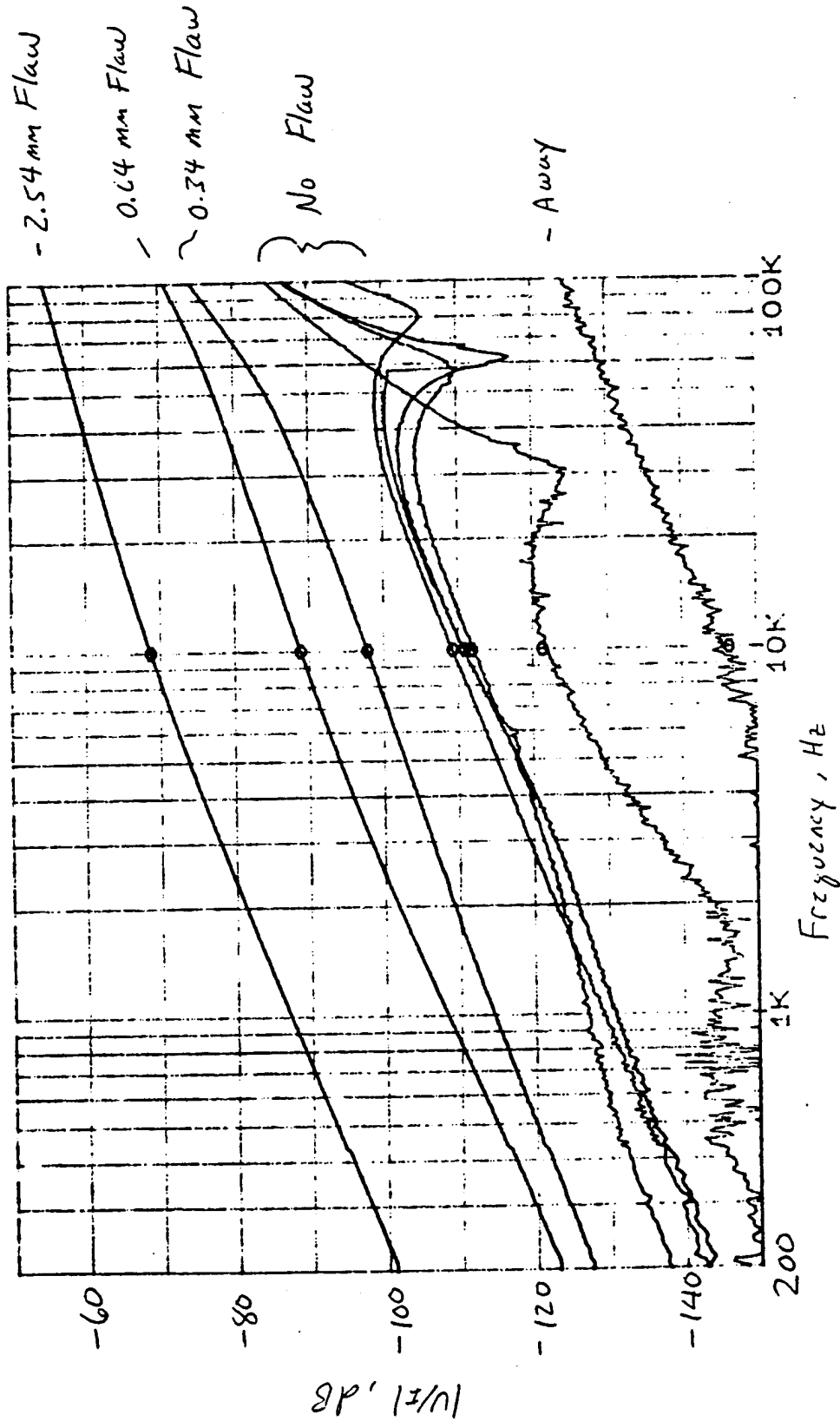


Figure 95 . Response of the differential pair of D type probes as a function of frequency for 5 cases.

machined. The differential pair of D-type probes was used in these measurements. The method in which the scanning was performed is indicated in Figure 96. The probe was scanned across the device under test in the  $x$  direction. The scans were made with the probe placed in two positions: position A in which one of the probes passes directly over the flaw and position B in which the other probe passes directly over the flaw.

The magnitude and phase of the response of the probe are graphed in Figures 97 and 98 as a function of position for both scans A and B at a frequency of 1 kHz. Figure 97 is for the 2.54 mm flaw and Figure 98 is for the 0.34 mm flaw. It can be seen in Figure 97 that the strongest response by far is at  $x = 15$  cm when the probe is directly above the 2.54 mm flaw, and that the second strongest response is at  $x \approx 1$  and 29 cm when the probe is over the edges of the device under test. The response when the probe is over the flaw is seen to be approximately 20 dB stronger than the second strongest response at the edge of the device under test. Clearly, one can locate the 2.54 mm flaw from these measured data. It can be seen in Figure 98 that the strongest response is at  $x \approx 1$  and 29 cm when the probe is over the edges of the device under test, and that the response is weaker at  $x = 15$  cm when the probe is over the 0.34 mm flaw. Clearly, one cannot locate the 0.34 mm flaw without further processing of these data.

From Figures 97 and 98, the responses from scans A and B are seen to be very similar except for the phase at  $x = 15$  cm when the probe is directly over the flaws, where the phases of the responses are seen to differ by approximately 180 degrees. The phase of the responses at  $x = 15$  cm are expected to differ by 180 degrees because the probes are connected in a differential configuration. Thus, differencing the responses of Scans A and B was tried to improve the performance of the technique. Graphs of the difference of scans A and B are shown in Figures 99 and 100 for the 2.54 mm flaw and the 0.34 mm flaw, respectively. The response due to the extraneous fields is seen to be reduced in both cases; the reduction is the greatest at the edges of the device under test. The strongest response for both flaws is now seen to be at  $x = 15$  cm. In Figure 99, the response when the probe is over the 2.54 mm flaw is seen to be approximately 40 dB stronger than the next strongest response. In Figure 100, the response when the probe is over the 0.34 mm flaw is seen to be approximately 10 dB stronger than the next strongest response. Clearly, one can locate both flaws using these data. More dramatic improvements could be obtained by improving the probes or by using more sophisticated signal processing.

#### *Equipment for Experimental Test Bed*

Several items needed in the experimental test bed were not commercially available and were designed and constructed as part of this project.

Power Amplifier: The amplifier is based on an APEX PA45 operational amplifier. The maximum power output of the amplifier is 50 W into a  $10\ \Omega$  load, and the 3 dB full power bandwidth is 100 kHz.

Matching Transformer: The transformer is wound on a toroidal ferrite core. The core is made of Phillips 3C85 ferrite material and has an outer diameter of 7.4 cm, an inner diameter of 3.9 cm, and a height of 3.8 cm. The transformer has a single primary winding with 45 turns of solid 18 gauge wire and four secondary windings each with 2 turns of 18 gauge stranded wire. The four secondary windings are distributed around the core and connected in parallel. The separate secondary windings and the stranded wire are used to improve the high frequency response of the transformer. The high-frequency response of the transformer is dependent on the parasitic distributed capacitance and inductance of the windings. The high-frequency rolloff of the transformer is approximately 30 kHz. The low-frequency response of the transformer is dependent on the cross sectional area of the core, the saturation magnetic flux density in the core, the number of turns on the windings, and the voltage across the windings. The low frequency rolloff of the transformer is approximately  $f=5I$  where  $f$  is the frequency in Hz and  $I$  is the output current of the transformer in amperes.

Current Probe: The probe consists of a 100 to 1 transformer wound on a toroidal core and a  $1\ \Omega$  sampling resistor.

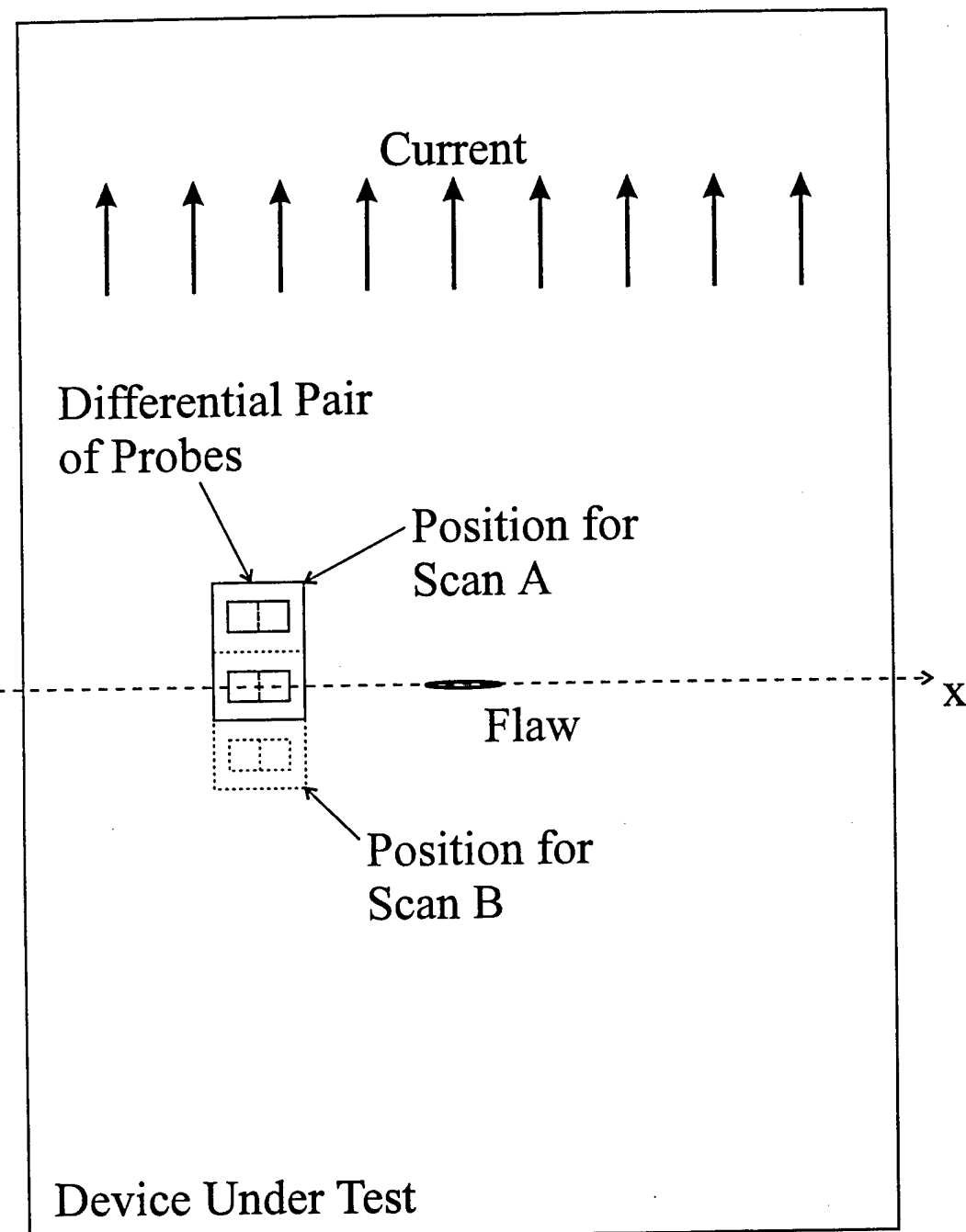


**Figure 96 .** Diagram indicating the geometry used to scan the probe across the device under test.

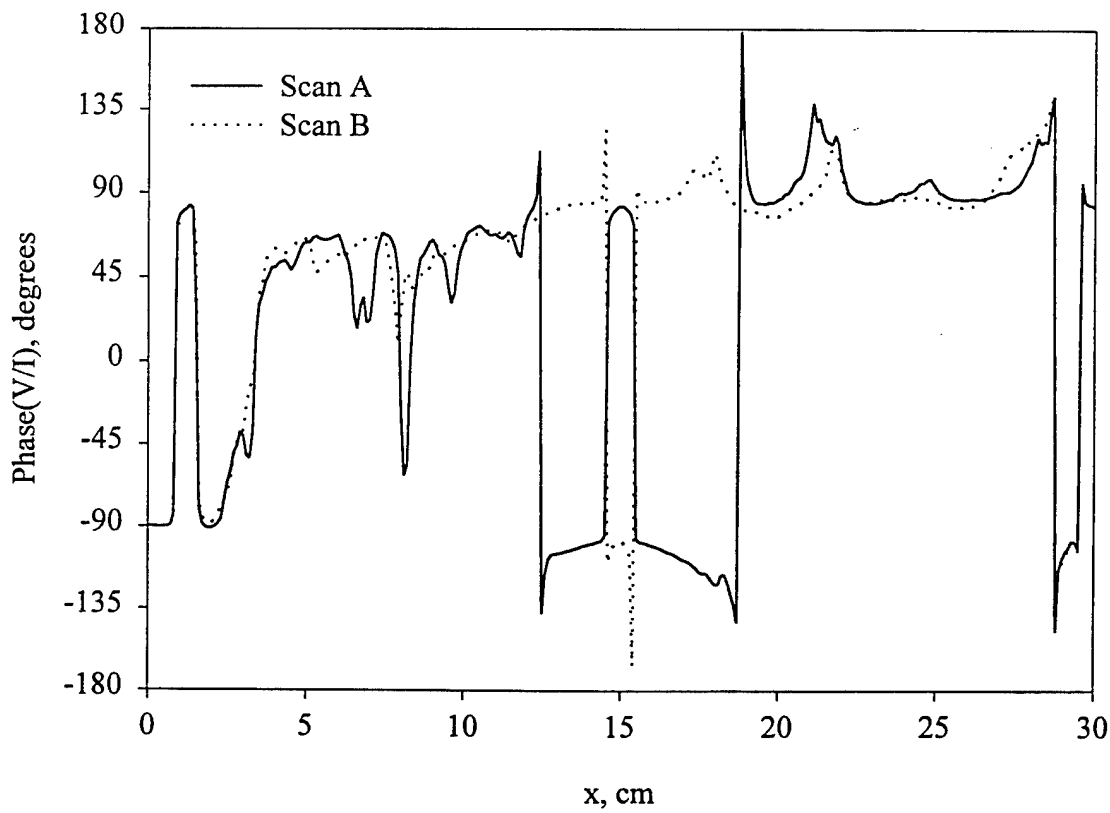
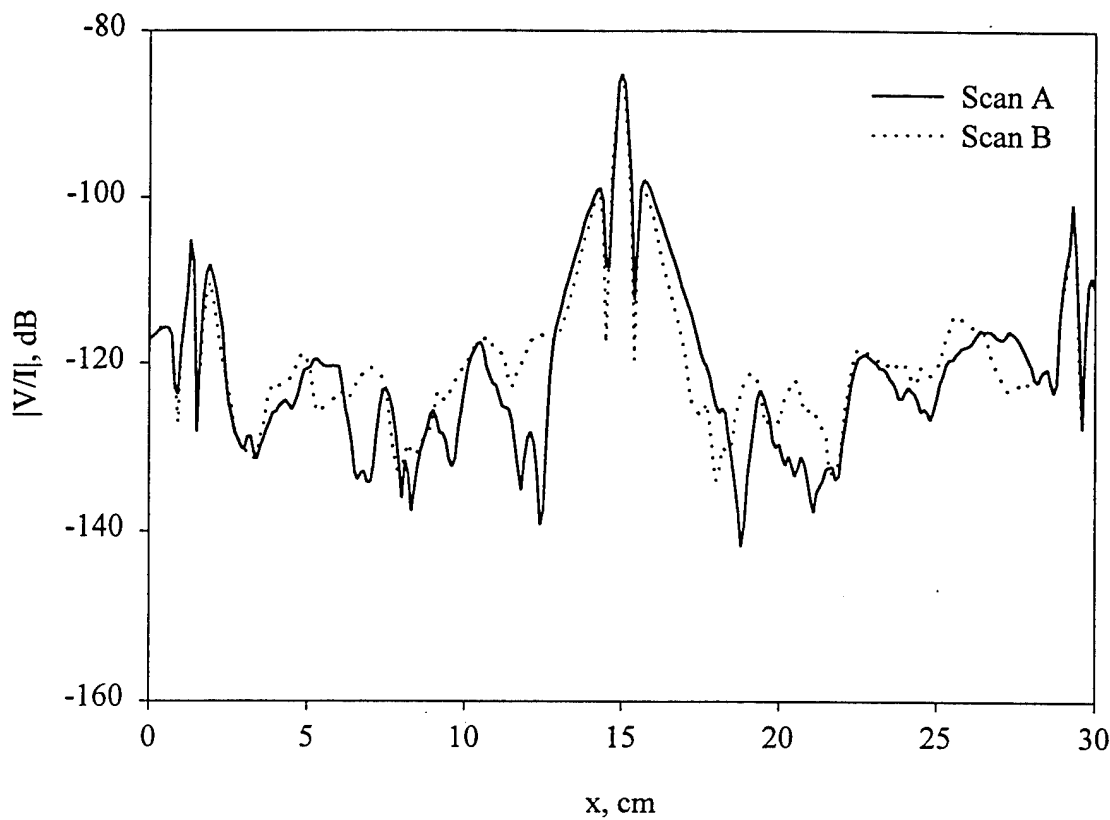


**Figure 97** Magnitude and phase of the response of the D-type probe as a function of position for scans A and B when the flaw is a 2.54 mm slit and  $f = 1$  kHz.

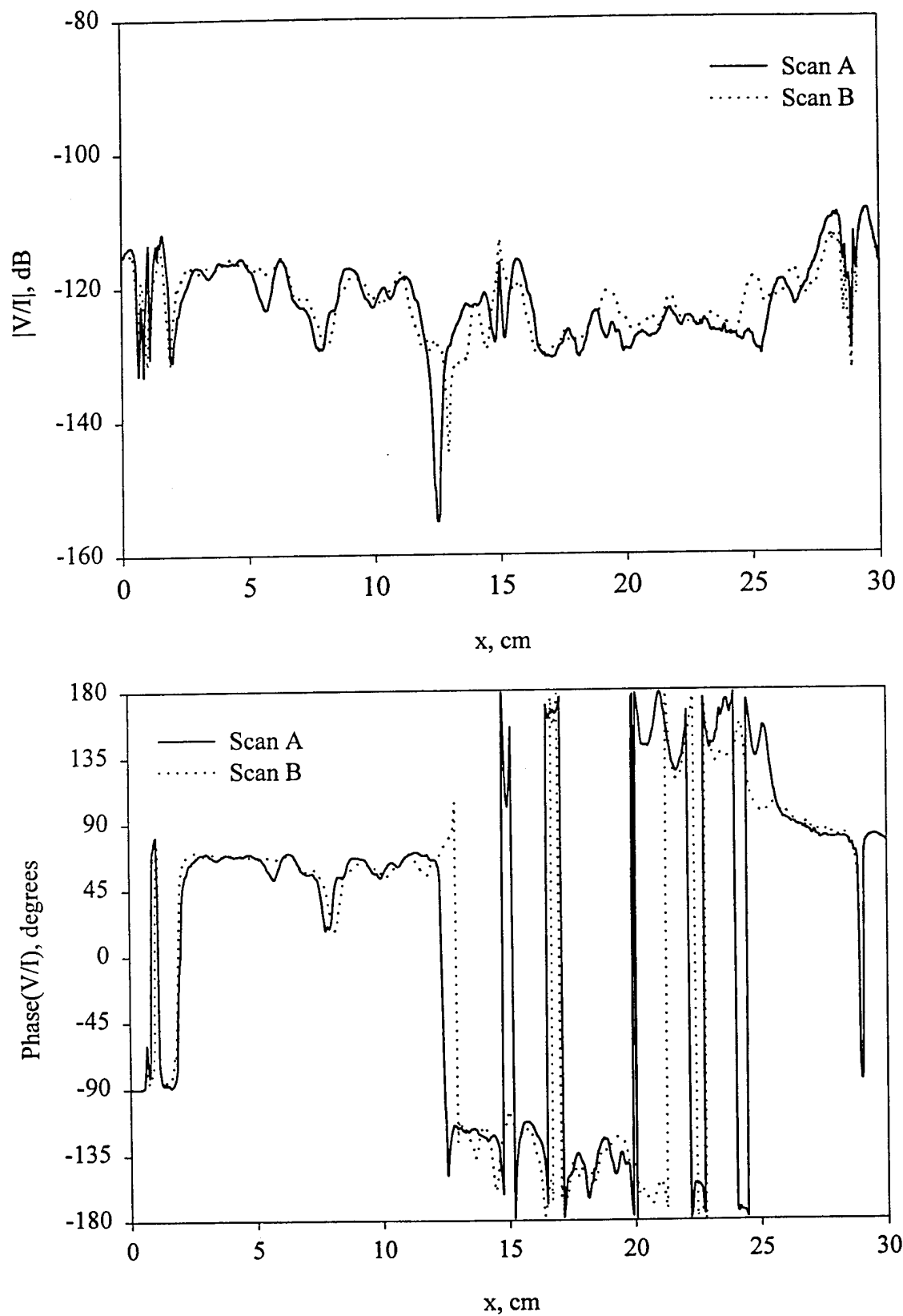


**Figure 98 .** Magnitude and phase of the response of the D-type probe as a function of position for scans A and B when the flaw is a 0.34 mm diameter hole and  $f = 1$  kHz.

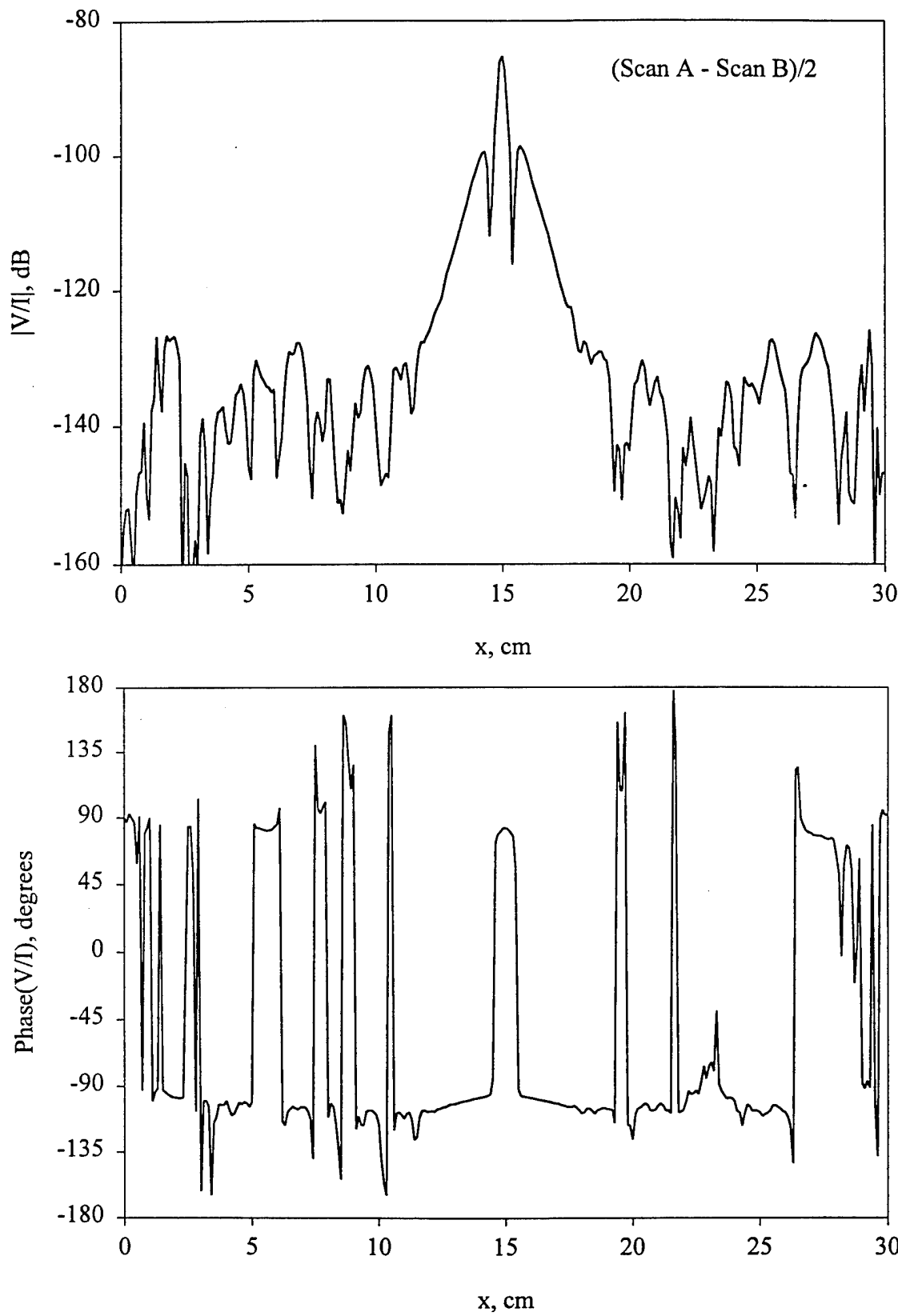


**Figure 99** Magnitude and phase of the difference between the responses for Scans A and B as a function of frequency for the D-type probe when the flaw is a 2.54 mm slit and  $f = 1$  kHz.

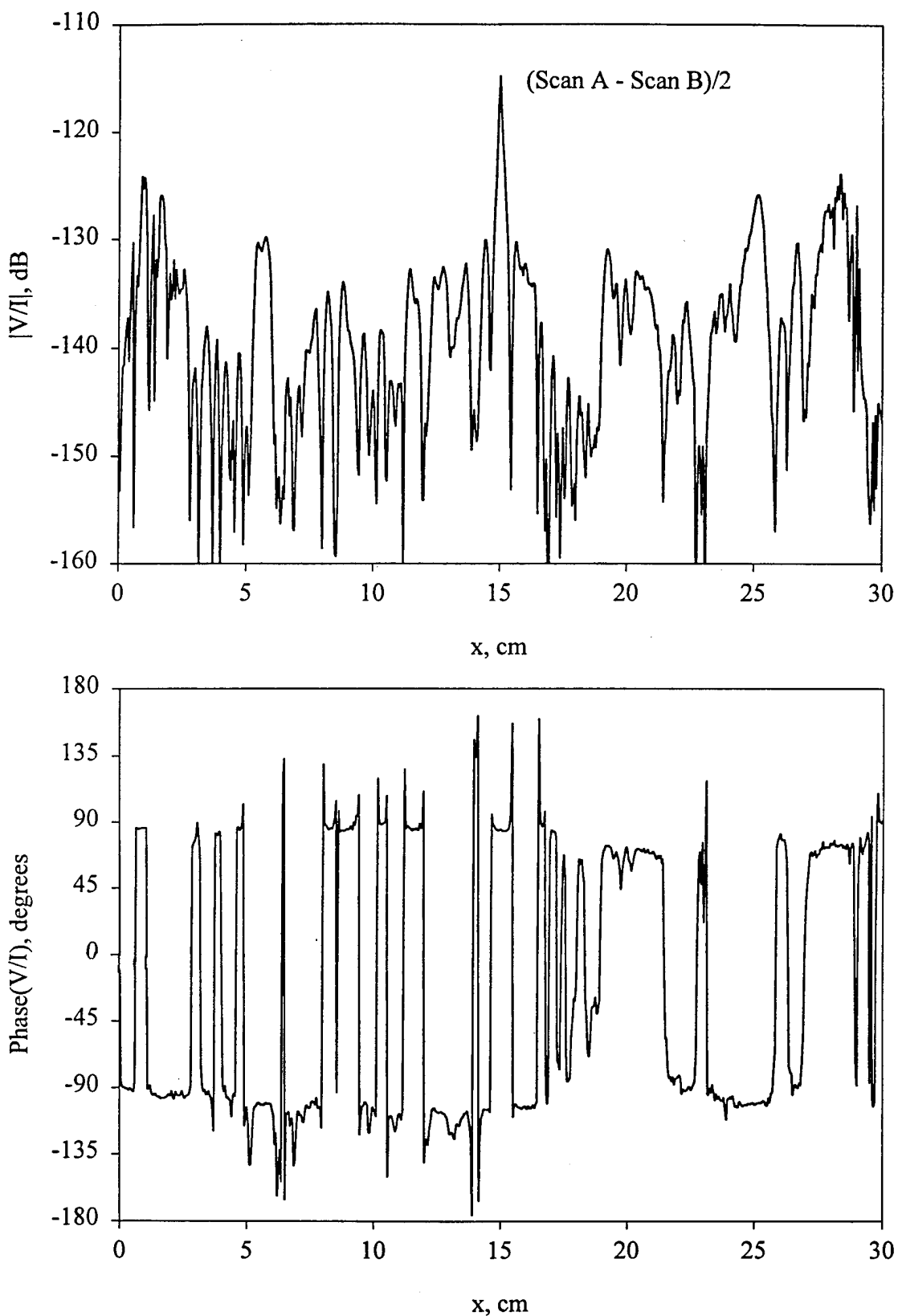


**Figure 100** Magnitude and phase of the difference between the responses for Scans A and B as a function of position for the D-type probe when the flaw is a 0.34 mm diameter hole and  $f = 1$  kHz.

Differential Low-Noise Amplifier: The amplifier is used to amplify the signal picked up by the focusing head. This signal consists of a wanted differential signal and an unwanted common mode signal. The wanted differential signal is due to the magnetic fields sensed by the focusing probes, and the unwanted common mode signal is due to capacitive coupling between the focusing head and the device under test. The differential amplifier will amplify the wanted differential signal while rejecting the unwanted common mode signal. The amplifier has a gain of 100, a 3 dB bandwidth of 900 kHz, an equivalent input noise voltage of  $10 \text{ nV}/\sqrt{\text{Hz}}$ , and a common mode rejection ratio of 80 dB.

## Plans

1. Improve the focusing probes. We want to increase their sensitivity to the magnetic signature of the flaw while simultaneously decreasing their sensitivity to extraneous magnetic fields. We are particularly interested in decreasing their sensitivity to the extraneous fields generated by the edges of the device under test. Both the shape and the configuration of the focusing probes will be investigated to try to improve their performance. As part of this effort, we will investigate the miniature probes being developed by Professor Ramalingam at the University of Minnesota (see Section 2.3.2).
2. Create a better set of flaws to test the system.
3. Incorporate the ferrite loaded probes into the numerical model.
4. Investigate the use of the proposed technique with geometries of practical interest including three-dimensional objects.
5. Future plans include modeling and developing identification routines for defect characterization.

### 2.3.4 ACOUSTIC EMISSION MODELING FOR INTEGRATED DIAGNOSTICS

Co-investigator: Isaac M. Daniel (Northwestern)

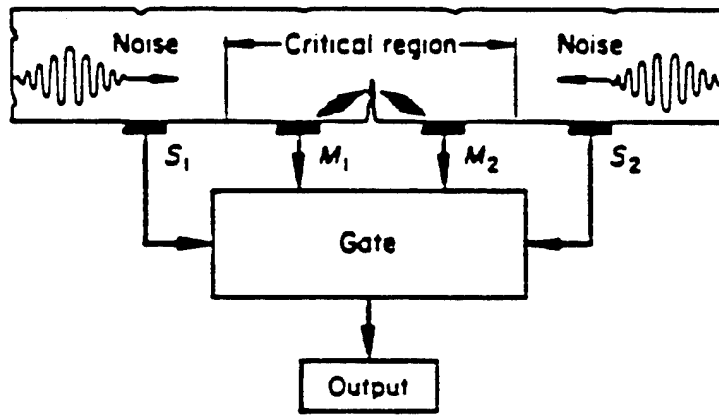
#### Overview

The objective of this project is to investigate and develop/adapt acoustic emission methods for flaw detection and characterization and for failure prediction of flight vehicle components. A literature survey was initiated on applications of acoustic emission relevant to modes of failure in critical helicopter components. Materials of interest identified are 4340 steel and 13-8 PH stainless steel. Acoustic emission techniques were screened/evaluated using available instrumentation and materials. Considerable effort was directed at signal/noise discrimination. Unnotched and notched specimens were tested under monotonic and fatigue tensile loading. Results from fatigue tests of notched specimens show a characteristic acoustic emission output over the lifetime of the specimen, consisting of three stages. The first stage, comprising approximately the first 15% of the lifetime, is characterized by high but decreasing rate of acoustic emission; the second stage, extending up to approximately 80% of the lifetime, is characterized by a low (minimum) and constant acoustic emission rate; and the third stage, comprising the last 20% of the lifetime, is characterized by increasing acoustic emission rate up to failure. The rate of acoustic emission output in the second stage can be described by a power law in terms of the stress intensity factor range, analogous to the Paris law relating crack extension rate and stress intensity factor range.

Acoustic emission (AE) consists of high frequency stress waves generated by the rapid release of energy due to fracture, plastic deformation, wear or interfacial friction [57]. Acoustic emission monitoring is a very sensitive method with a wide dynamic range and can be used as a diagnostic means of continuous assessment of the mechanical condition of flight vehicle components. Key factors in the successful application of the method are the selection or design of appropriate sensors for each case, installation of sensors, means of transduction, and physical interpretation of output. This problem is a challenging one in view of the severe constraints encountered in flight vehicle components in service. Acoustic emission can provide a wealth of information and has a great potential for monitoring the onset and growth of certain types of flaws, such as crack initiation and propagation, and friction between crack surfaces under fatigue conditions. Acoustic emission real time monitoring is a very promising method for assessing the mechanical condition of vehicle components.

Acoustic emission transducers are usually piezoelectric ceramic transducers with a wide frequency range between 50 kHz and 10 MHz. Criteria for selecting the optimum frequency band for a specific case include the frequency content of the acoustic emission generated by the flaw and that of the background noise. The latter is usually of lower frequency in the range of 10-100 kHz. In applications to composite specimens under fatigue loading, the writer found that the AE output was not affected by the testing machine noise [58]. Discrimination between signal and noise is of paramount importance. The background noise can be hydraulic, electrical or mechanical. Methods of noise suppression that have been used to date include high-pass frequency filtering, floating signal threshold and spatial filtering such as guard sensor array. The principle of the latter is illustrated in Figure 101. An array of sensors is used consisting of two master sensors ( $M_1$  and  $M_2$ ) located near the expected source of acoustic emission and two slave or guard sensors ( $S_1$  and  $S_2$ ) on either side of the master sensors. When a noise signal originating outside the critical region arrives at this array, one of the slave sensors intercepts the signal and closes the gate, which is normally open. Thus, when the master sensors sense this noise, there is no output.

Acoustic emission methods can be applied to metallic components and specimens subjected to monotonic tensile loading or to fatigue loading with varying loading parameters (stress ratio  $R$ ). In



$S_1, S_2$  – Slave/guard sensors

$M_1, M_2$  – Master sensors

**Figure 101** Example of Spatial Filtering for Noise Suppression

general, acoustic emission can be used to monitor crack initiation and propagation and to locate the source of the emission (damage).

The AE output is a very complex waveform. Many characteristics such as amplitude, frequency content, duration, rise time, energy, rate or cumulative number of counts can be used to obtain correlations with the physics of the problem. Many studies have been conducted dealing with correlations of AE output and fracture mechanics and fatigue damage parameters. Under monotonic loading AE can detect yielding as illustrated in Figure 102 for 7075-T6 aluminum [59]. The dashed curve in the figure is a fit of Gilman's equation for mobile dislocation density. According to this equation the AE rate is expressed as

$$\dot{\eta} = A \varepsilon_p \exp(-B \varepsilon_p) \quad (15)$$

where  $\varepsilon_p$  = plastic strain; and A, B = constants.

Similar results were obtained by Berkovits and Fang [60] for Incoloy 901 (Figure 103). The cumulative number of AE counts was expressed as

$$\eta = \eta_{\max} \left\{ 1 - \exp \left[ -\frac{1}{2} \left( \frac{\varepsilon - \varepsilon_0}{d} \right)^2 \right] \right\} \quad (16)$$

where  $\eta_{\max}$  = sum of counts at  $\sigma_{\max}$ ,  $\varepsilon_0$  = threshold strain necessary to initiate AE, and d= scale constant.

Under monotonic loading it has also been demonstrated [59] that the cumulative AE output from a notched specimen is directly related to the stress intensity factor regardless of the location and type of notch (Figure 104). It was found that in the case of 7075-T6 aluminum the cumulative AE output  $\eta$  was related to the stress intensity factor K by a power law of the form

$$\eta = A K^n \quad (17)$$

where A, n = constants. In this case it was found that  $n = 5.4$ .

For a pure mode I loading it is known that  $K = B a^{1/2}$ , where a= crack length and B=constant. Then, the AE output  $\eta$  can be related directly to crack length by a relationship of the form

$$\eta = C a^{n/2} = C a^{2.7}. \quad (18)$$

Acoustic emission is very useful for detecting crack initiation and propagation under fatigue loading [61]. A correlation has been found between acoustic emission and stress intensity factor range under fatigue conditions. The number of ringdown counts (positive crossings of a selected threshold) can be related to fatigue damage. Peak amplitudes can be directly related to peak crack velocities. Other mechanical characteristics, such as crack propagation, threshold value of stress intensity factor,  $K_{th}$ , and crack closure, have also been related to AE. The AE rate can be related to the range of the stress intensity factor as

$$\frac{d\eta}{dN} = A (\Delta K)^n \quad (19)$$

where A, n = constants, and N = number of fatigue cycles.

This relationship is similar to the Paris law relating crack extension rate and stress intensity factor range

$$\frac{da}{dN} = C (\Delta K)^m. \quad (20)$$

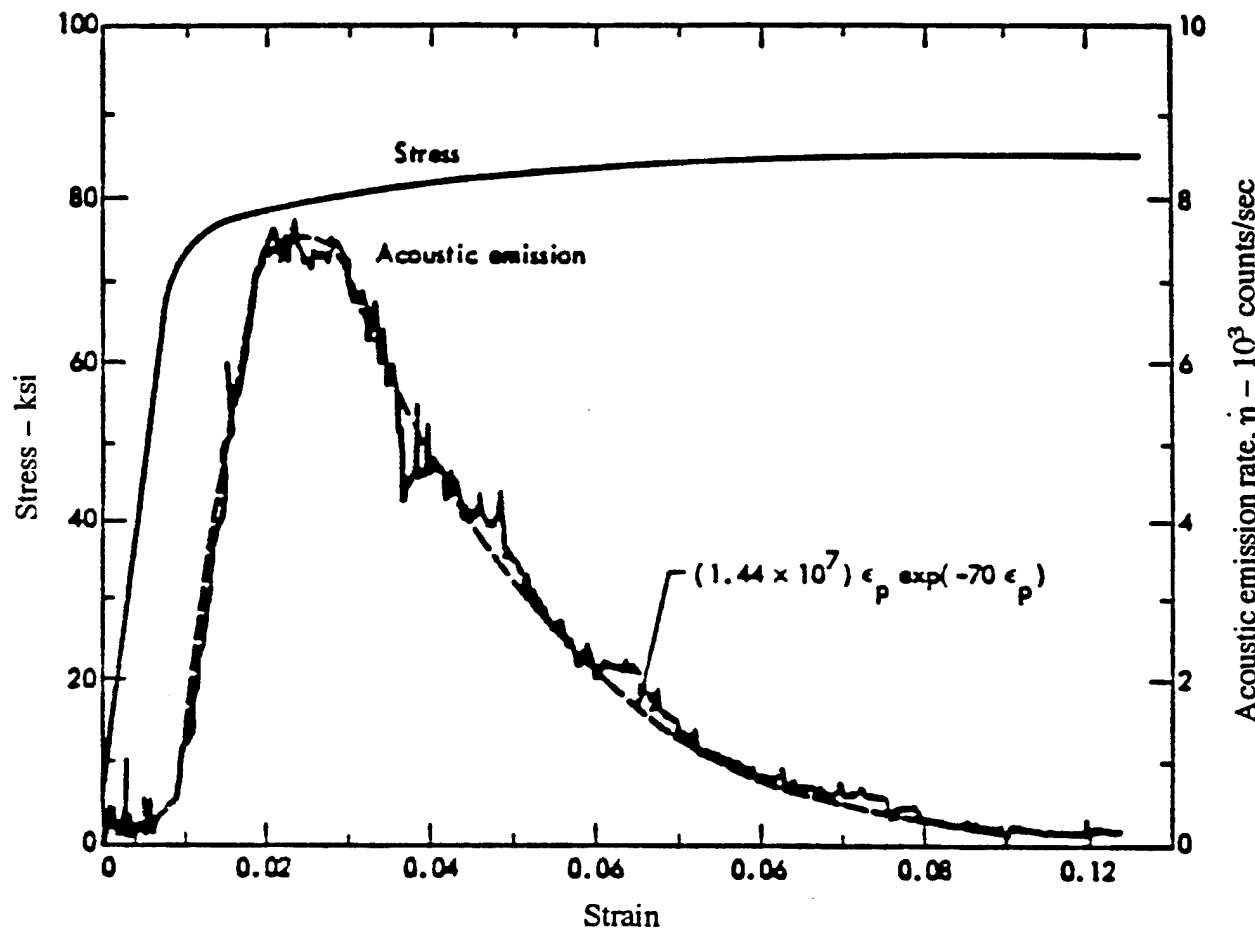


**Figure 102** Acoustic Emission and Stress vs. Strain for a 7075-T6 Aluminum Specimen under Monotonic Tension (Dashed curve is a fit of Gilman's equation for mobile dislocation density)

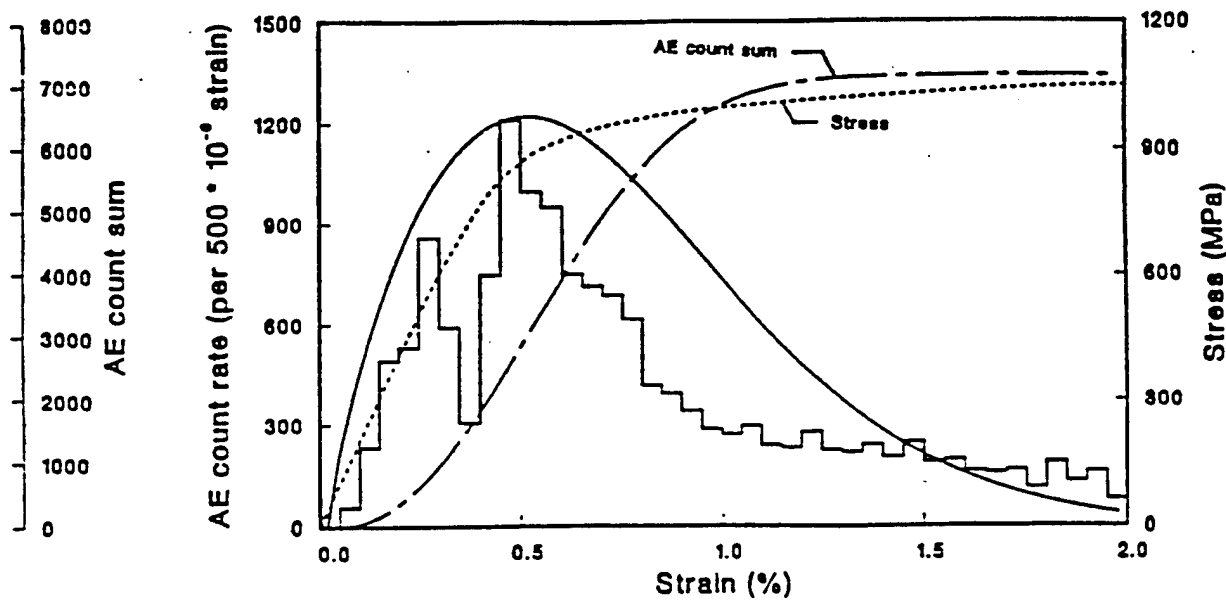


Figure 103 AE Output and Stress vs. Strain for Incoloy 901 under Monotonic Tension

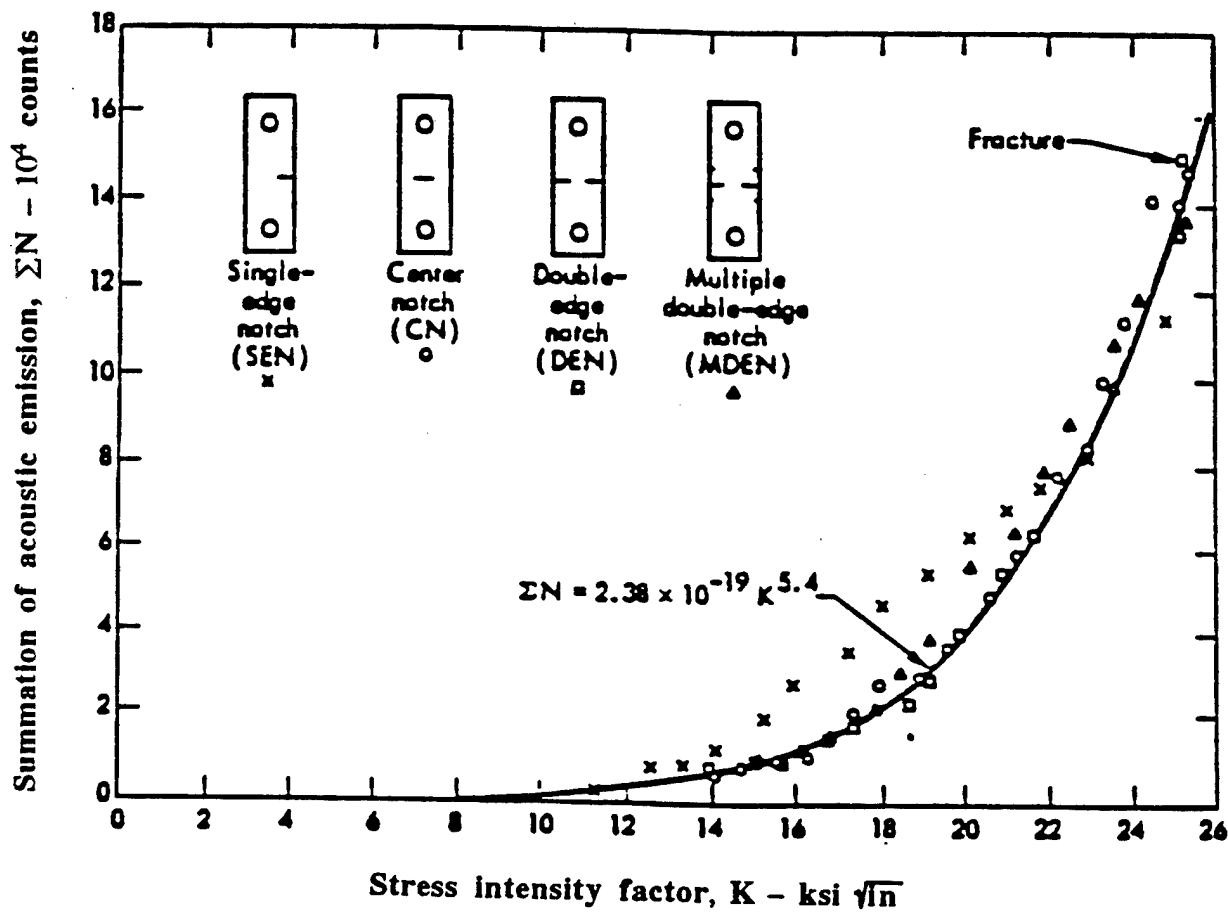


Figure 104 Cumulative Number of AE Counts vs. Stress Intensity Factor for Notched Specimens

The relationship between exponents  $m$  and  $n$  above depends on the failure mechanisms producing acoustic emission, i.e., on the energy released during crack extension and the deformation and fracture within the plastic zone [62-64]. It also depends on other factors, such as the loading ratio ( $R = \sigma_{\min}/\sigma_{\max}$ ) [64]. In general it can be expected that

$$m \leq n \leq m + 2 \quad (21)$$

Berkovits and Fang have proposed relationships between cumulative number of AE counts and number of cycles for high cycle fatigue [65]. They distinguished three stages in damage development. Stage I corresponding to dislocation dynamics and first cycle softening or hardening is described by the relationship

$$\eta_I = \eta_{I/4} + \lambda(\Delta\sigma)^\alpha N^\beta, \quad \beta < 1 \quad (22)$$

with  $\lambda, \alpha, \beta$  constants. Stage II corresponding to crack nucleation and initiation is described by

$$\eta_{II} = \lambda(\Delta\sigma)^\alpha N^\beta, \quad \beta = 1 \quad (23)$$

Stage III corresponding to crack propagation is described by

$$\eta_{III} = \lambda(\Delta\sigma)^\alpha N^\beta, \quad \beta > 1 \quad (24)$$

In many cases, the complexity and variety of the applications make it difficult to obtain explicit correlations between AE features and mechanical damage. In such cases it is more expeditious to use neural network pattern recognition techniques [66]. The network, for example, would consist of an input layer of AE amplitude data, a hidden layer to accommodate failure mechanism mapping, and an output layer for ultimate strength or fatigue life prediction. This would require training programs for each critical component containing known degrees of damage.

## Accomplishments

Vehicle platform (e.g., H46 helicopter) and machinery components are of interest. To date, the H46 helicopter rotor hub, tie bar, and connecting link have been identified for use as a reference for the ultimate application of methods developed. The materials of interest have been identified as 4340 steel, 13-8 precipitation hardened stainless steel, Titanium alloy, and Aluminum (7075-T73). Two plates of the first two materials, received at Georgia Tech from the Cherry Point Naval Depot, will be sent to Northwestern University for this study.

Two types of specimens have been selected as shown in Figures 105 and 106, a single edge-notch specimen and the standard ASTM compact tension specimen.

Various AE techniques and sensors were screened by preliminary testing of notched and unnotched specimens under monotonic tensile loading. As anticipated, the background noise was identified as the single most crucial problem to address.

An instrumentation upgrade was initiated. Two different systems, emphasizing two fundamentally different approaches, were evaluated. One system (MISTRAS 2001, Physical Acoustics Corp.) is fully digital, multichannel and performs simultaneous real-time extraction of AE features and recording of waveforms. It provides software selectable filters and is well suited for detecting multiple site or dispersed damage. It uses primarily resonance high sensitivity transducers. It is also well suited for the neural network pattern recognition approach. The other system evaluated (Digital Wave) is based on waveform analysis for a dominant source (crack) in a mathematically well defined body. It has high fidelity and accurate source location capability. It uses primarily broad band transducers which have lower sensitivity. The system is primarily suited for detection and characterization of a localized

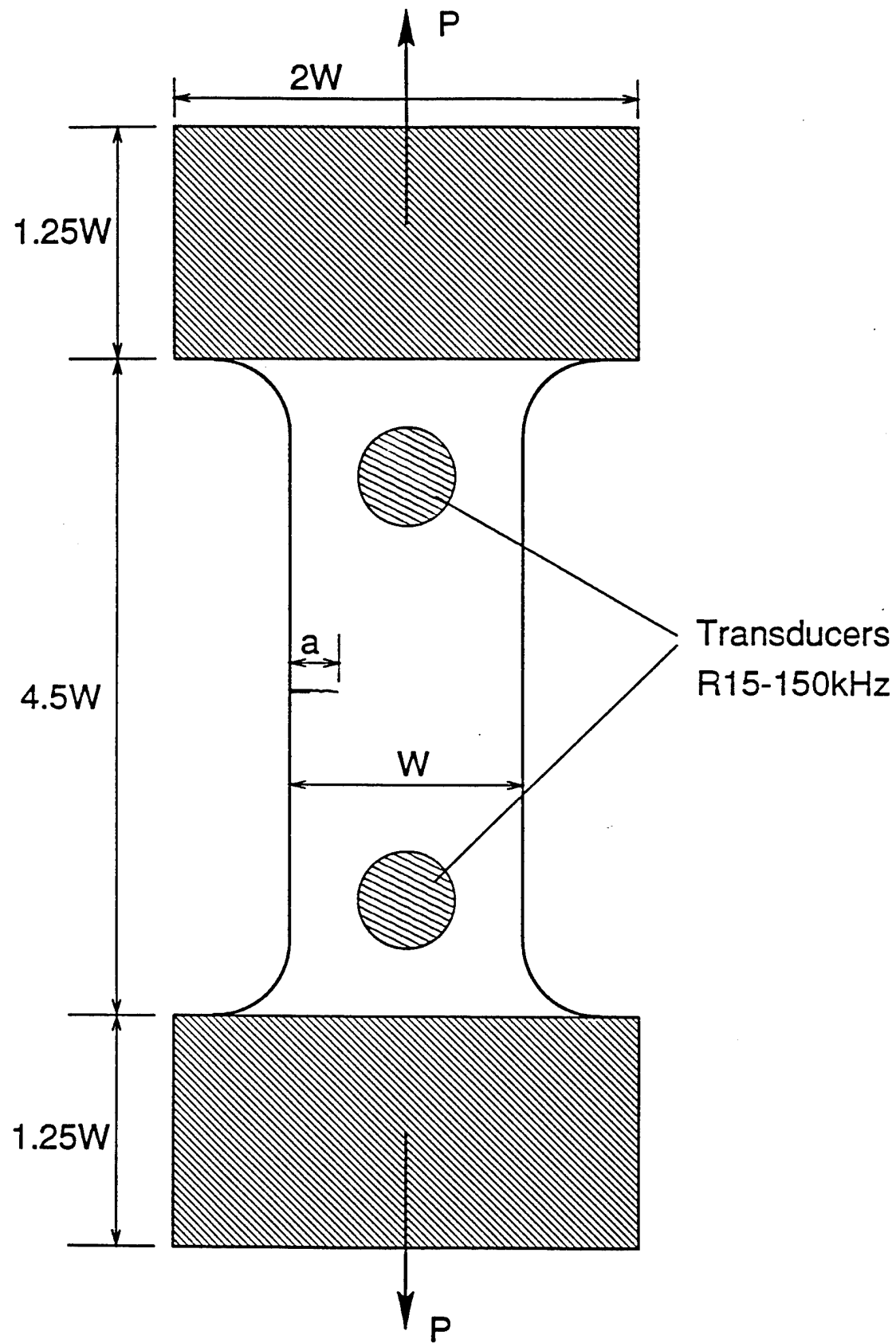
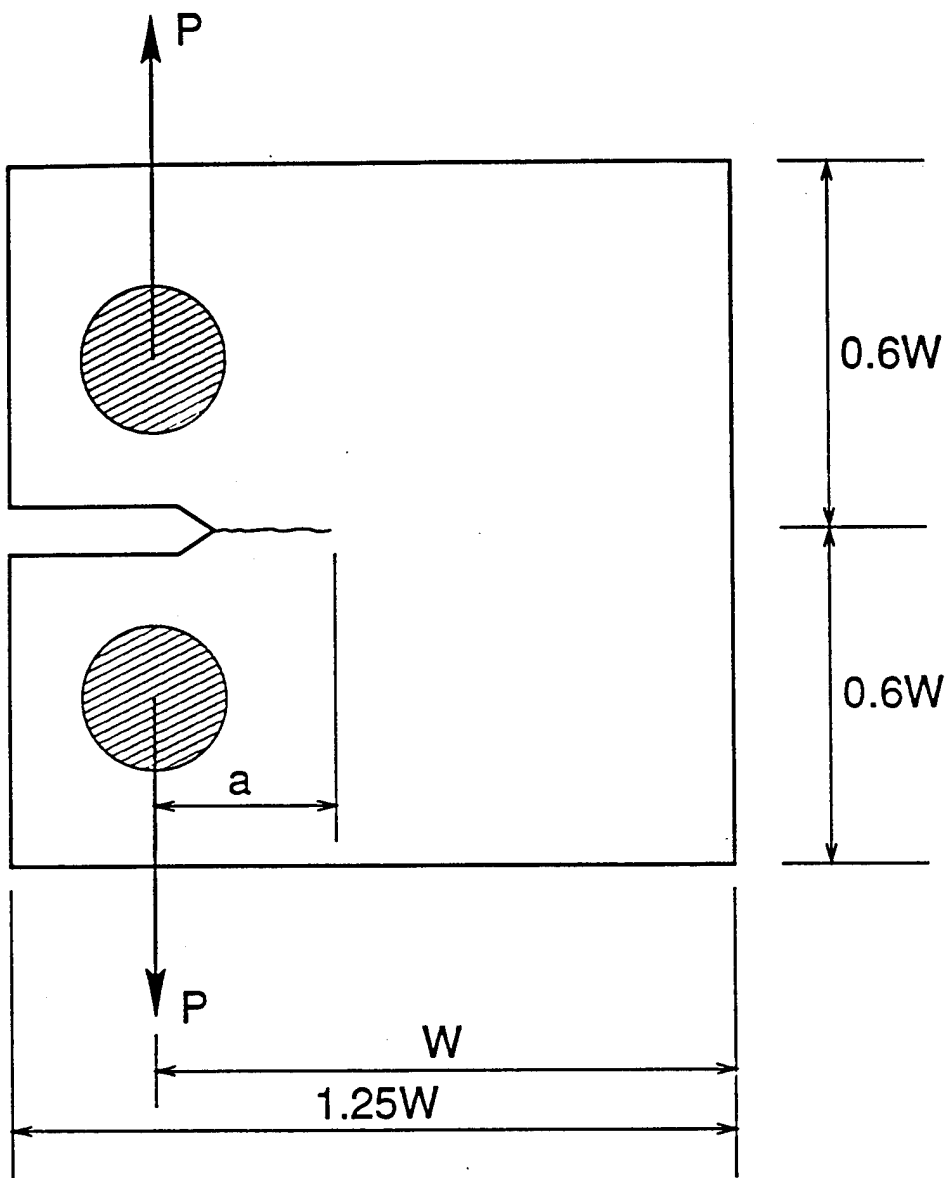


**Figure 105** Edge-notch Tensile Fatigue Specimen



$$\text{Thickness: } B = \frac{W}{2}$$

Figure 106    Compact Tension Specimen (ASTM 399)

dominant source (large crack). An order was placed for the first system (MISTRAS) which was considered a natural and more powerful extension of our existing system (LOCAN-AT).

Preliminary tests were conducted on notched and unnotched 2024-T3 aluminum specimens under monotonic tensile loading. A 150 kHz resonance sensor (R15) was used with the existing instrumentation (LOCAN-AT, Physical Acoustics). It was found that AE output due to yielding, especially localized yielding, is too low to be detected and discerned from background noise.

Fatigue tests were initiated on the same material using the single edge-notch specimen of Figure 105. The specimen was 5.08 cm (2.0 in.) wide and 3.17 mm (0.125 in.) thick. A notch 1.27 mm (0.05 in.) wide and 4.35 mm (0.171 in.) long was machined on one edge. Low amplitude cyclic preloading was applied in some cases to initiate a fatigue crack at the root of the notch. This preloading with maximum stress of  $\sigma_{max} = 69$  MPa (10 ksi), a stress ratio  $R = 0.1$  and a frequency of 3 Hz was applied until a fatigue crack was initiated. A typical initial fatigue crack was 0.76 mm (0.03 in.) long and 0.38 mm (0.015 in.) wide. Two 150 kHz transducers were mounted on the specimen at equal distance from the crack on either side of it. A 45 dB threshold was used to suppress lower amplitude background noise. Furthermore, because of the equal distances from the source, only signals arriving at the transducers at the same time were recognized as signals from the source.

A low cycle fatigue test with a stress ratio of  $R = 0.1$  and  $\sigma_{max}=172$  MPa (25 ksi) was conducted at a frequency of 0.5 Hz. This particular specimen failed at  $N_f = 2,671$  cycles. The cumulative AE output in terms of events or hits was plotted versus normalized cycles in Figure 107. The curve consists of three characteristic parts corresponding to three stages of crack propagation. The first stage, which covers approximately 15% of the lifetime, is characterized by high but decreasing AE rate; the second stage, extending up to approximately 80% of the lifetime, is characterized by a low (minimum) and constant AE rate; and the third stage, comprising the last 20% of the lifetime, is characterized by increasing AE rate up to failure. The AE output was also plotted in terms of cumulative counts and in terms of energy, but the shape of these curves was very similar to that of Figure 107.

Given a specimen or component of unknown condition or prior history, it is not possible to determine the stage of damage on the basis of cumulative AE events. However, in view of the characteristic features of the curve of Figure 107, it may be possible to ascertain the state of damage and estimate the remaining life on the basis of the second derivative of AE output.

Thus, the initial stage can be identified when

$$\frac{d^2\eta}{dN^2} < 0$$

The specimen would be in Stage II if

$$\frac{d^2\eta}{dN^2} = 0 \quad \text{or} \quad \frac{d\eta}{dN} = \text{constant}$$

although it would not be possible to pinpoint the location within this stage.

When  $\frac{d^2\eta}{dN^2} > 0$ , then it could be said that the specimen is in the last 20% of its lifetime.

Concurrently with the AE measurements, the crack extension was monitored by optical means and plotted versus normalized lifetime in Figure 108 along with the cumulative number of AE hits. It can be seen that for the first 80% of the lifetime, corresponding to Stage II, crack extension varies nearly linearly with normalized life, thereafter it increases at an increasing rate like the AE output.

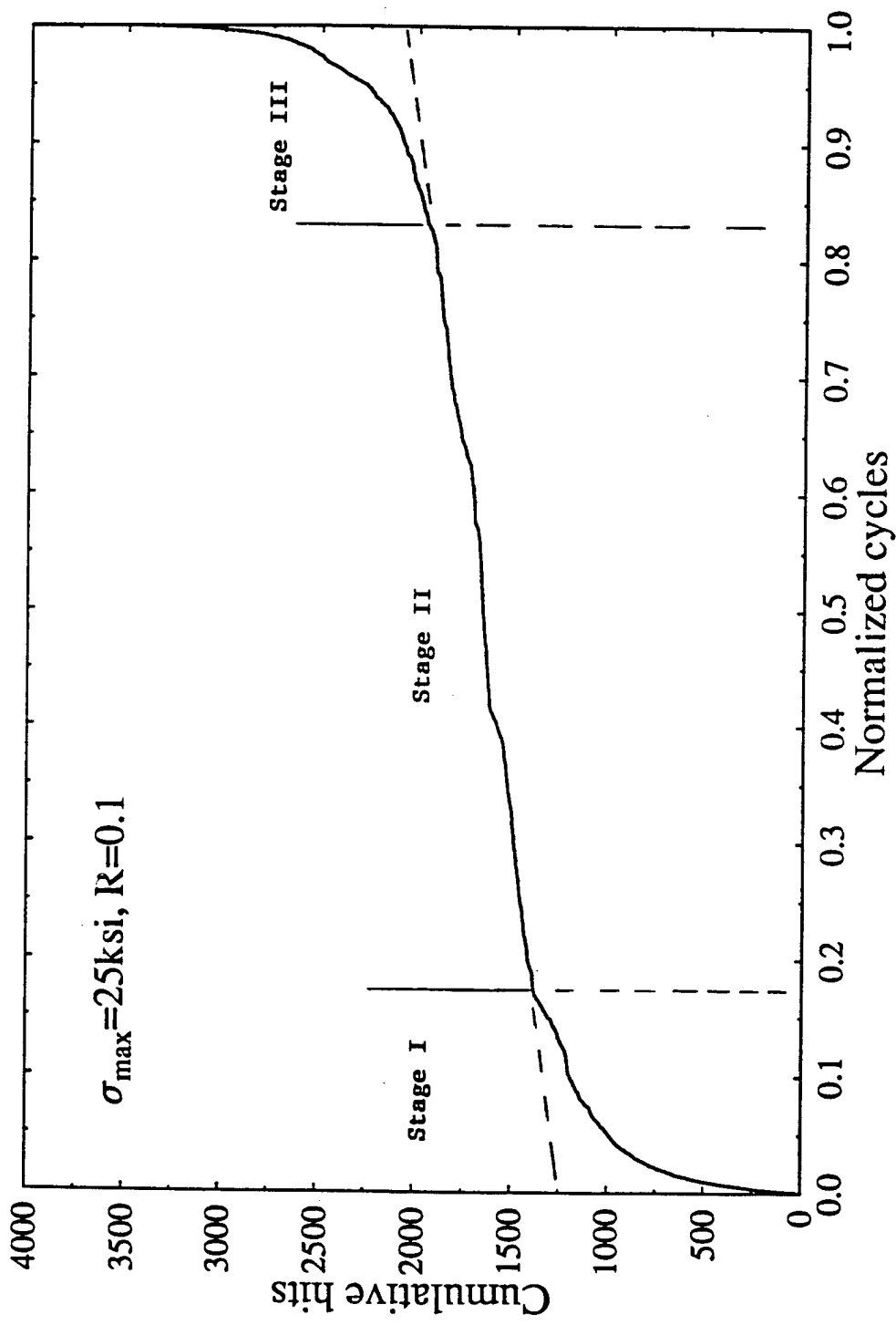


Figure 107 Stages of Fatigue Life and Characteristic AE Output

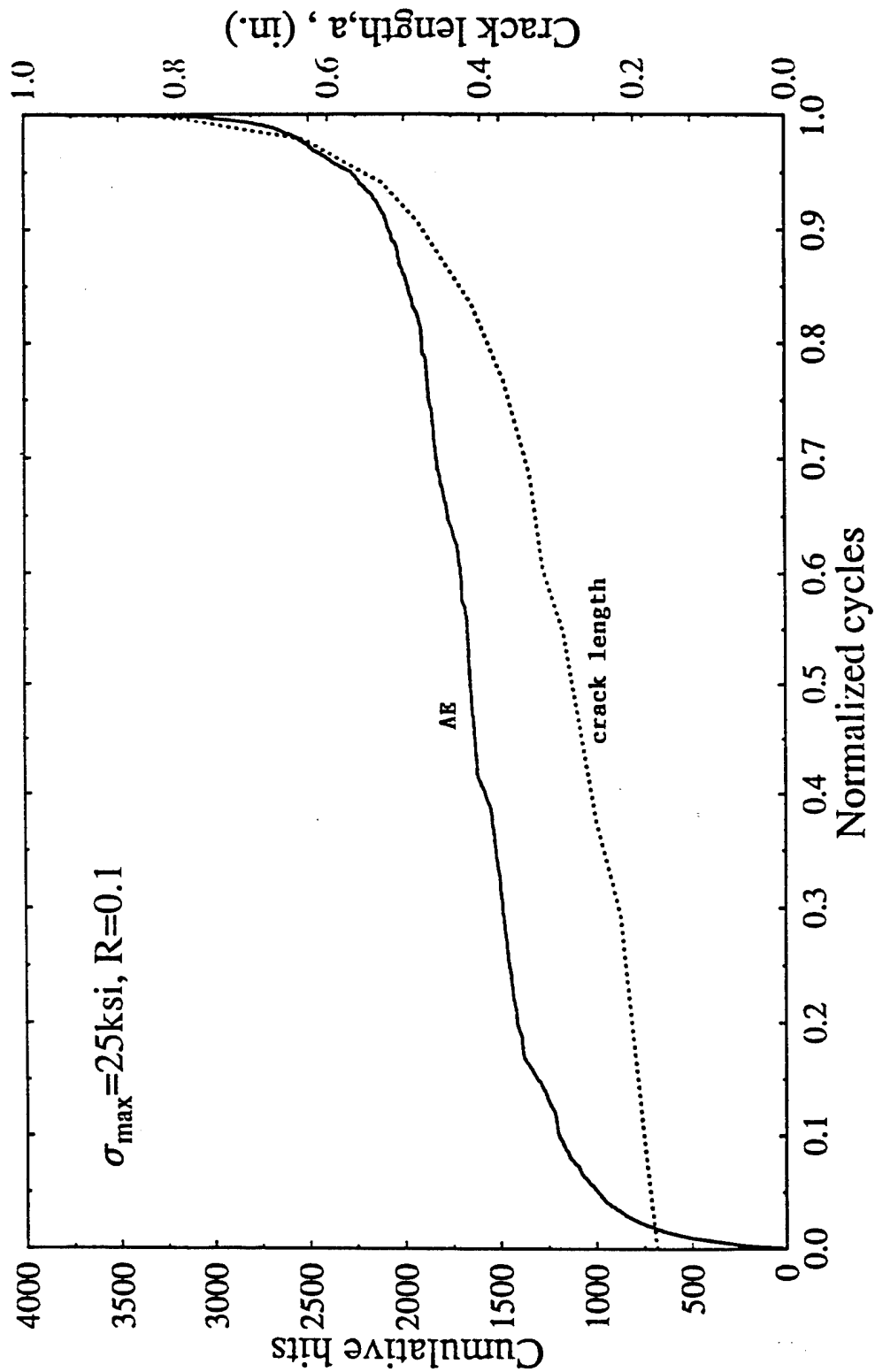


Figure 108 Acoustic Emission Events and Crack Extension vs. Normalized Fatigue Cycles (2024-T3 Aluminum)

The crack extension rate was plotted versus stress intensity factor range in Figure 109. Following the initial stage of crack extension, the crack extension rate follows a Paris law relationship to the stress intensity factor range as

$$\frac{da}{dN} = A (\Delta K)^m \quad (25)$$

with  $m = 3.95$ .

The rate of AE counts follows a similar relationship as shown in Figure 110,

$$\frac{dn}{dN} = C (\Delta K)^n \quad (26)$$

with  $n = 5.82$

According to the previous discussion [64], since  $n \geq m+2$ , most of the AE output is due to yielding and fracture within the plastic zone near the crack tip. Similar results have been found [67] before for 1% C steel and 7075-T651 aluminum (Figure 111).

Histograms of the AE events as a function of stress level within the cycle, i.e., loading phase, are shown in Figures 112, 113 and 114 for Stages I, II and III, respectively. These histograms represent the total number of AE events at a given stress level for all the cycles of the respective stage. It can be seen that in Stage I most of the events (hits) occur near the peak of the stress cycle (Fig. 112). In Stage II the situation seems to be reversed with most hits occurring at the low end of the cycle (Fig. 113). In Stage III a shift in phase distribution of the events occurs toward slightly higher loads (Fig. 114). The gradual shifting of phase distribution is illustrated in Figure 115, along with the constant amplitude cyclic stress. Similar plots are shown in Figure 116 and 117, where the increasing amplitude in stress intensity factor and net stress are illustrated. The above characteristic shifts in phase distribution of the AE output, if they prove to be consistent, could be very helpful in identifying the damage state and "age" of a specimen or part.

## Plans

The plans for the second year of this M-URI effort consist of the following tasks:

1. Instrumentation: The new instrumentation on order (MISTRAS) will be set up.
2. Materials: New materials including 4340 steel and 13-8 PH stainless steel will be obtained and tested using both edge-notch and compact tension specimens.
3. AE Master Curve: The existence of master curves will be explored for normalized AE output as a function of normalized fatigue life. Fatigue tests will be conducted at various stress levels but with a constant stress ratio.
4. Effects of Stress Amplitude and Stress Ratio: The effects of stress amplitude and stress ratio on AE output will be investigated by conducting fatigue tests with stress amplitudes around the yield region as shown in Figure 118.
5. Threshold Stress Intensity Factor: The threshold stress intensity factor,  $K_{th}$ , will be determined.

Tests will be conducted at a constant stress amplitude and different stress ratios until the point of crack initiation is detected by a peak in the AE output. At that point the initial (threshold) crack length  $a_{th}$  will be measured under the microscope and used in the following relation

$$K_{th} = Y(a_{th}) \Delta\sigma \sqrt{a_{th}}$$

where  $Y(a_{th})$  = finite width correction.

6. Crack Closure: Acoustic emission is very sensitive to frictional noise, therefore, it is an excellent tool for determining the crack-face rubbing during the portion of the cycle when the crack or part of it closes. After crack closure it takes a certain stress to open the crack. This crack opening stress,  $\sigma_{op}$ , during cyclic loading will be determined from the AE output and the corresponding  $K_{op}$  will be determined. Then, the effective stress intensity factor range

$$\Delta K_{eff} = K_{max} - K_{op}$$

is used in the modified Paris-Erdogan relation  $\frac{da}{dN} = C \Delta K_{eff}^m$ .

7. Damage Modeling

A damage accumulation model leading to life prediction will be sought based on AE parameters.

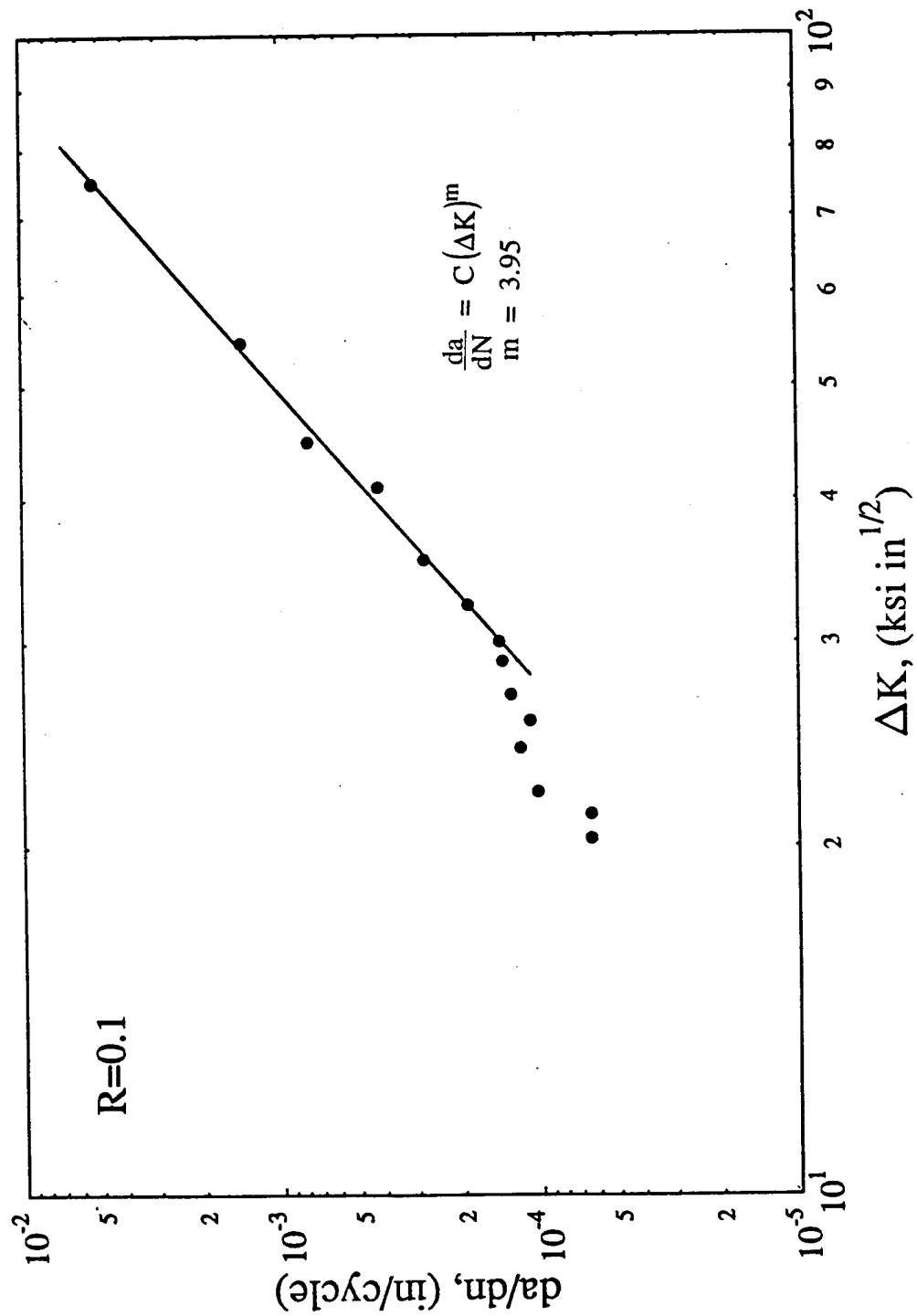


Figure 109 Crack Extension Rate as a Function of Stress Intensity Range

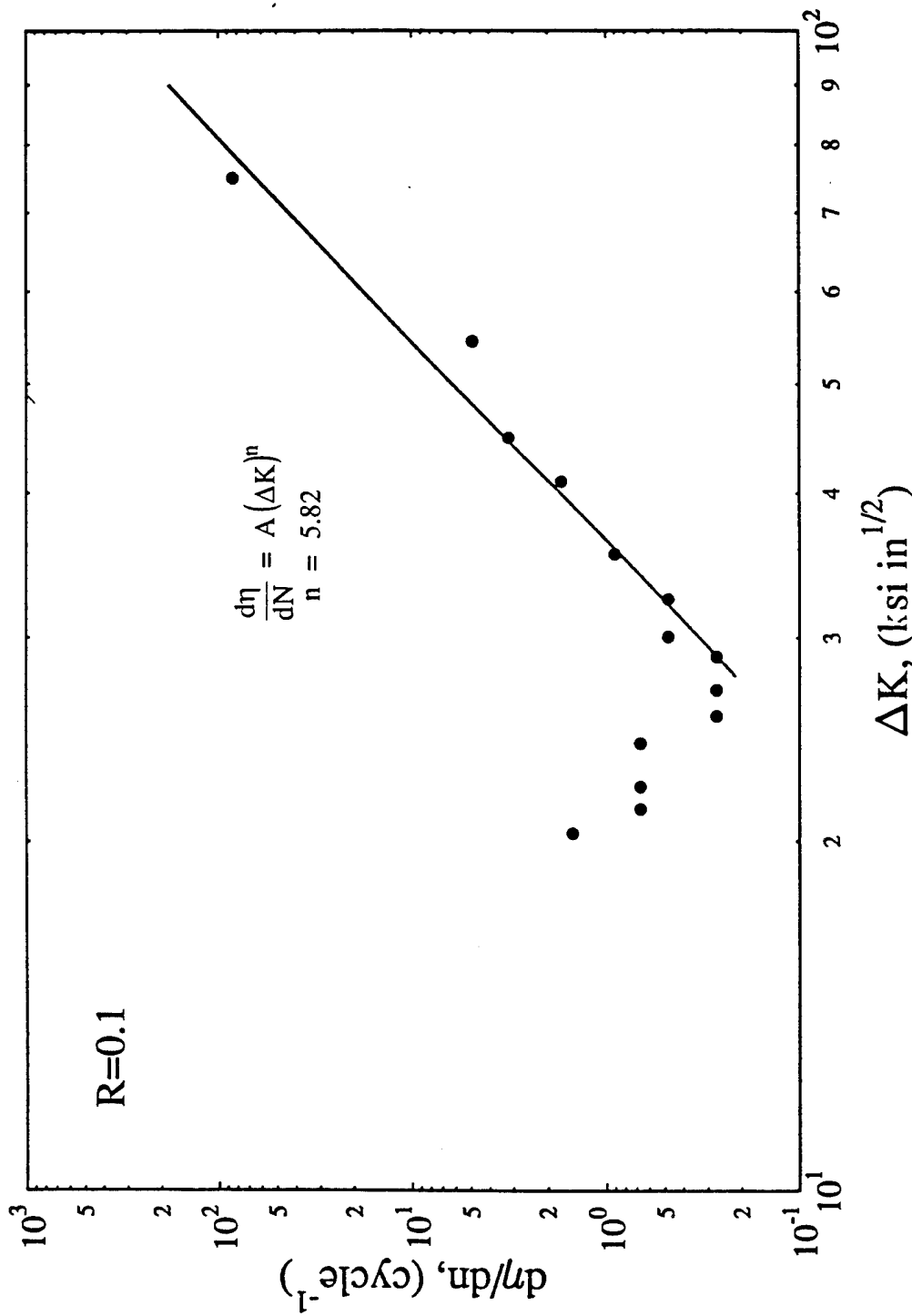
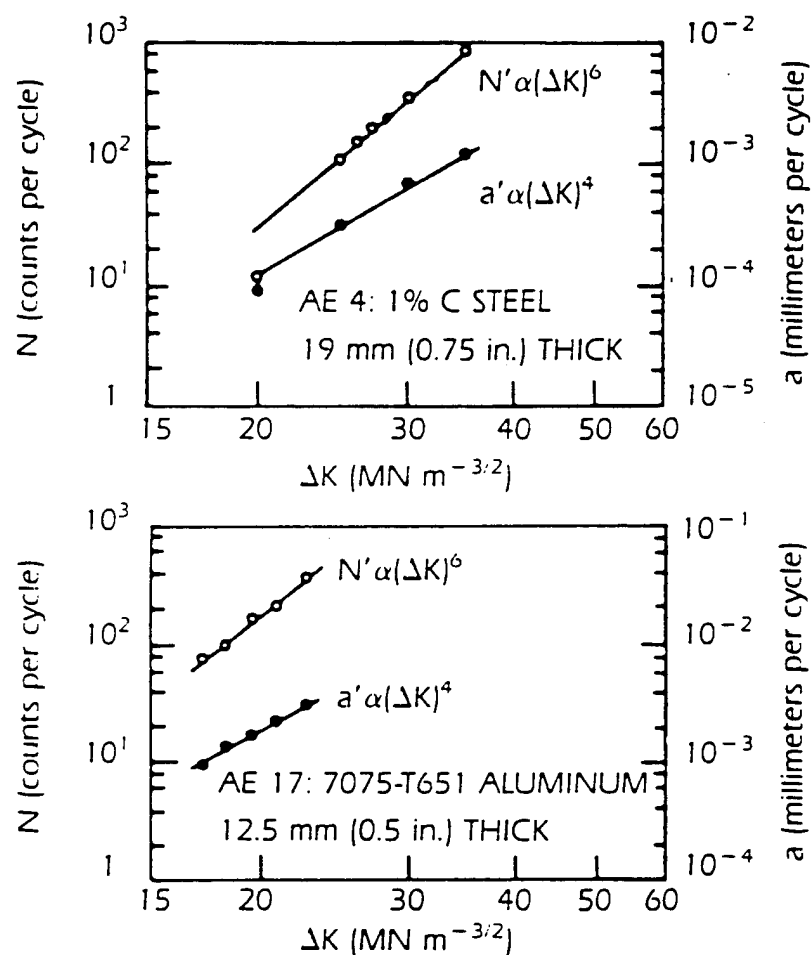


Figure 110 Rate of Acoustic Emission Counts as a Function of Stress Intensity Range



**Figure 111** Crack Extension Rate and AE Count Rate vs. Stress Intensity Factor Range for Two Materials

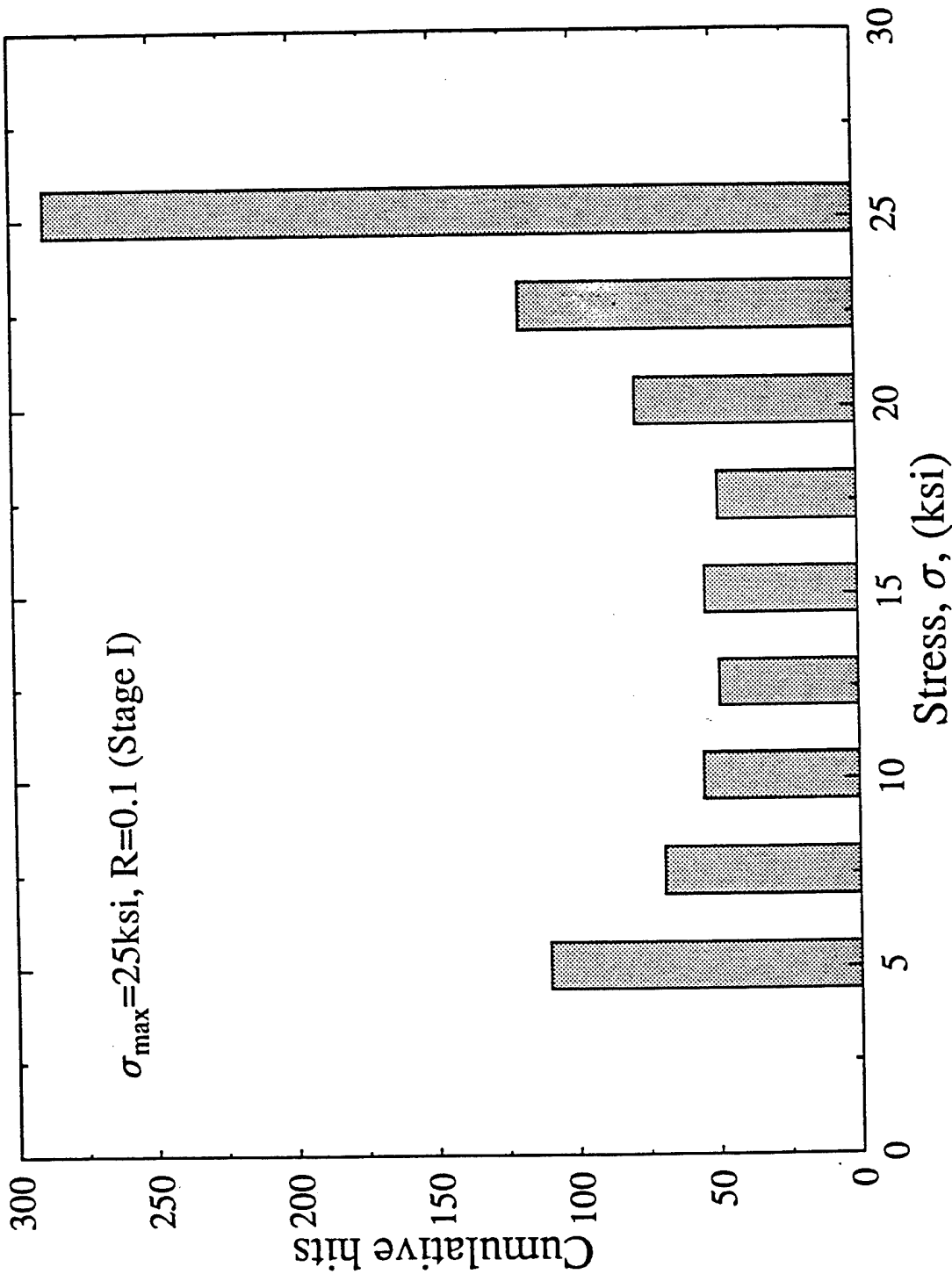


Figure 112 Histogram of AE Events as a Function of Stress

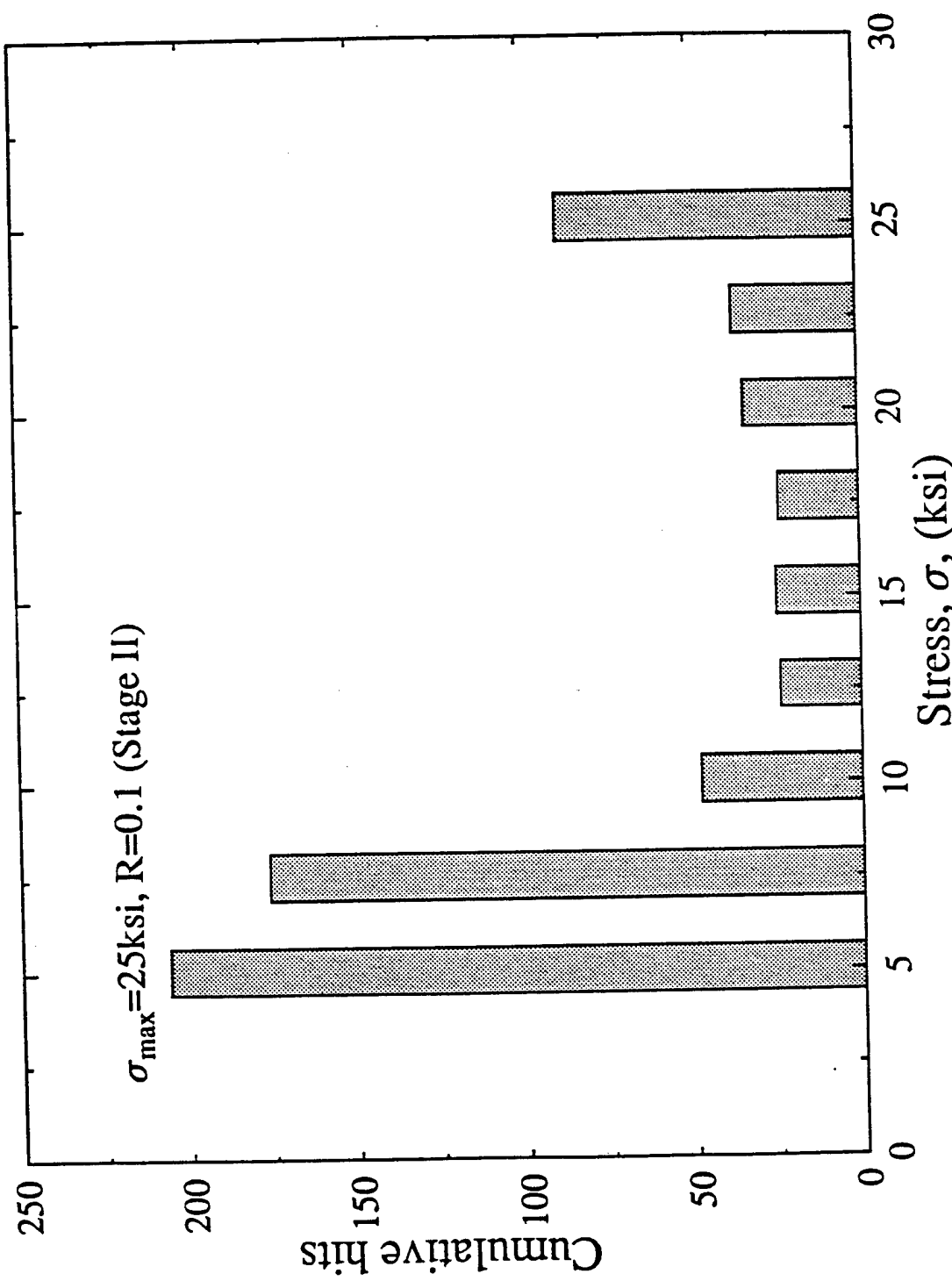


Figure 113 Histogram of AE Events as a Function of Stress

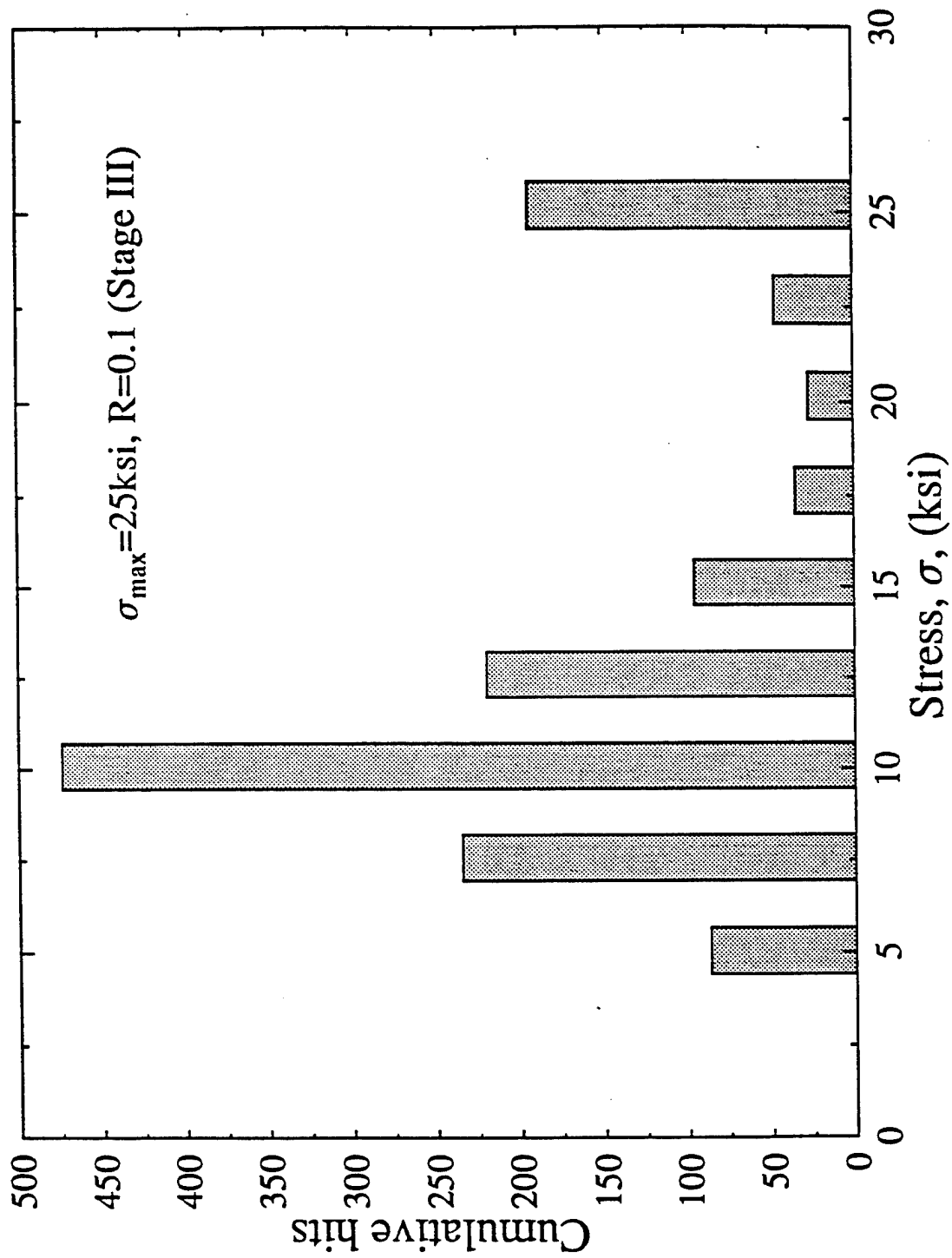
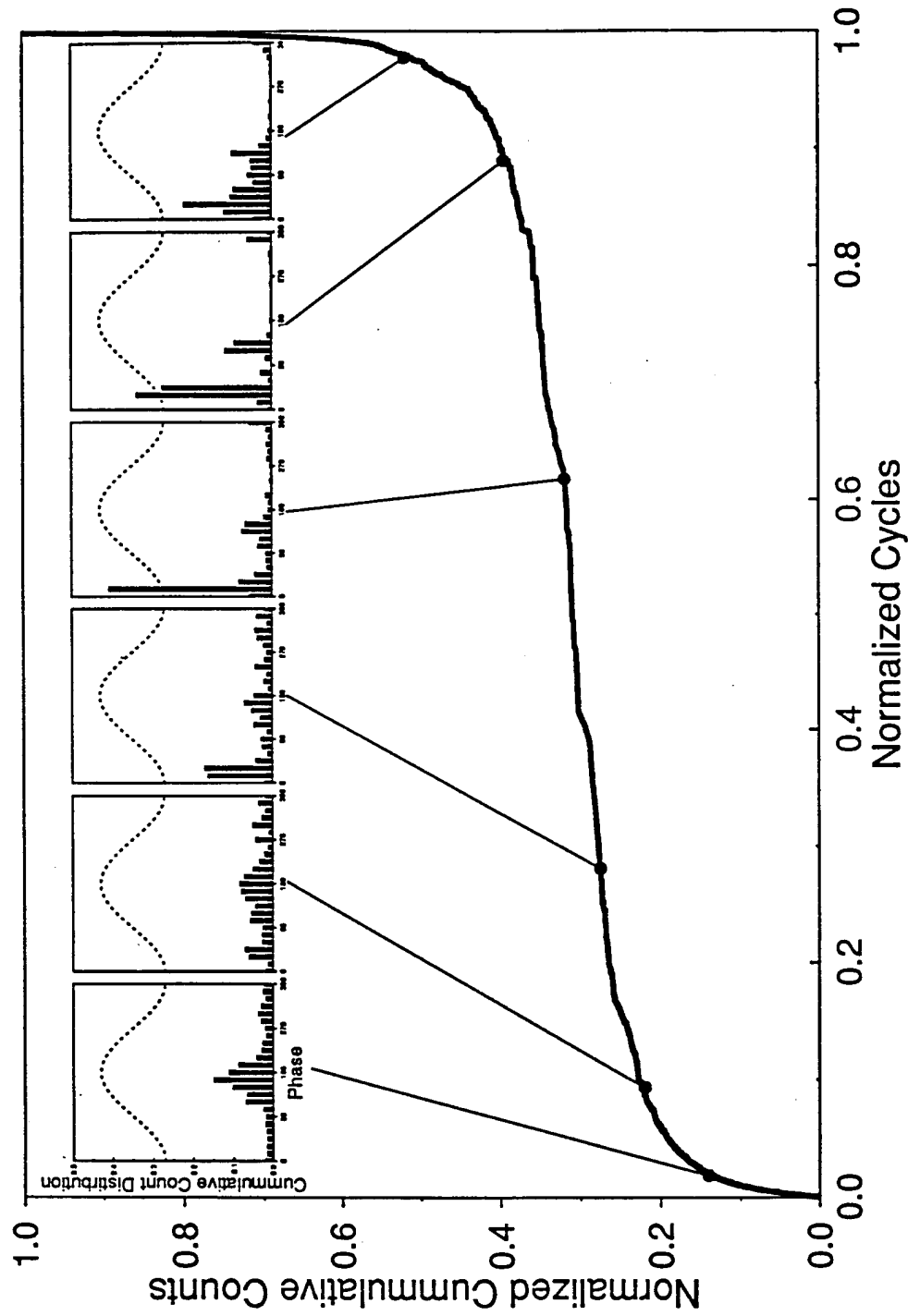
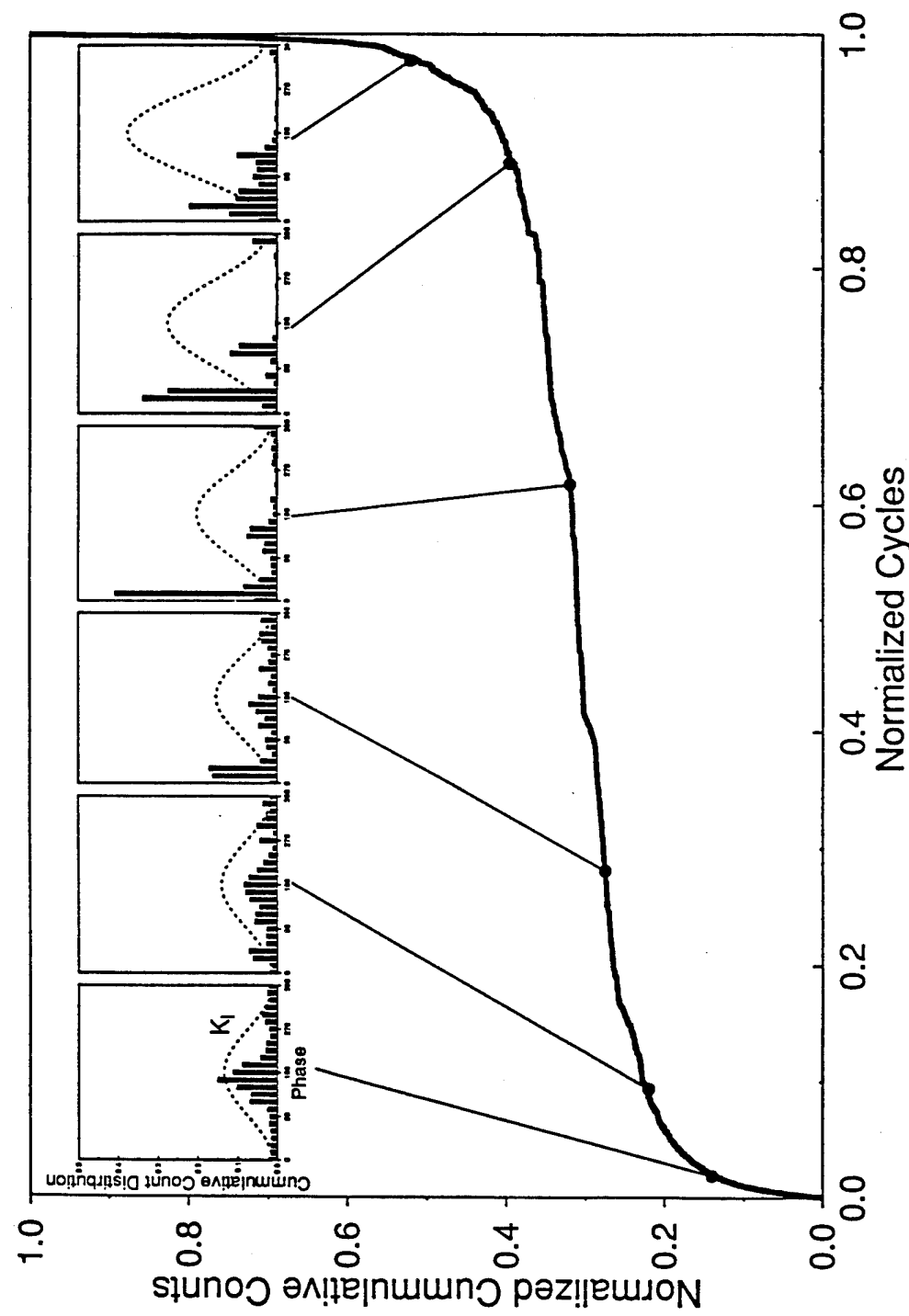


Figure 114 Histogram of AE Events as a Function of Stress



**Figure 115** Development of Phase Distributions of Cumulative Counts for a Low Cycle Fatigue Test of an Aluminum Plate



**Figure 116** Development of Phase Distributions of Cumulative Counts for a Low Cycle Fatigue Test of an Aluminum Plate

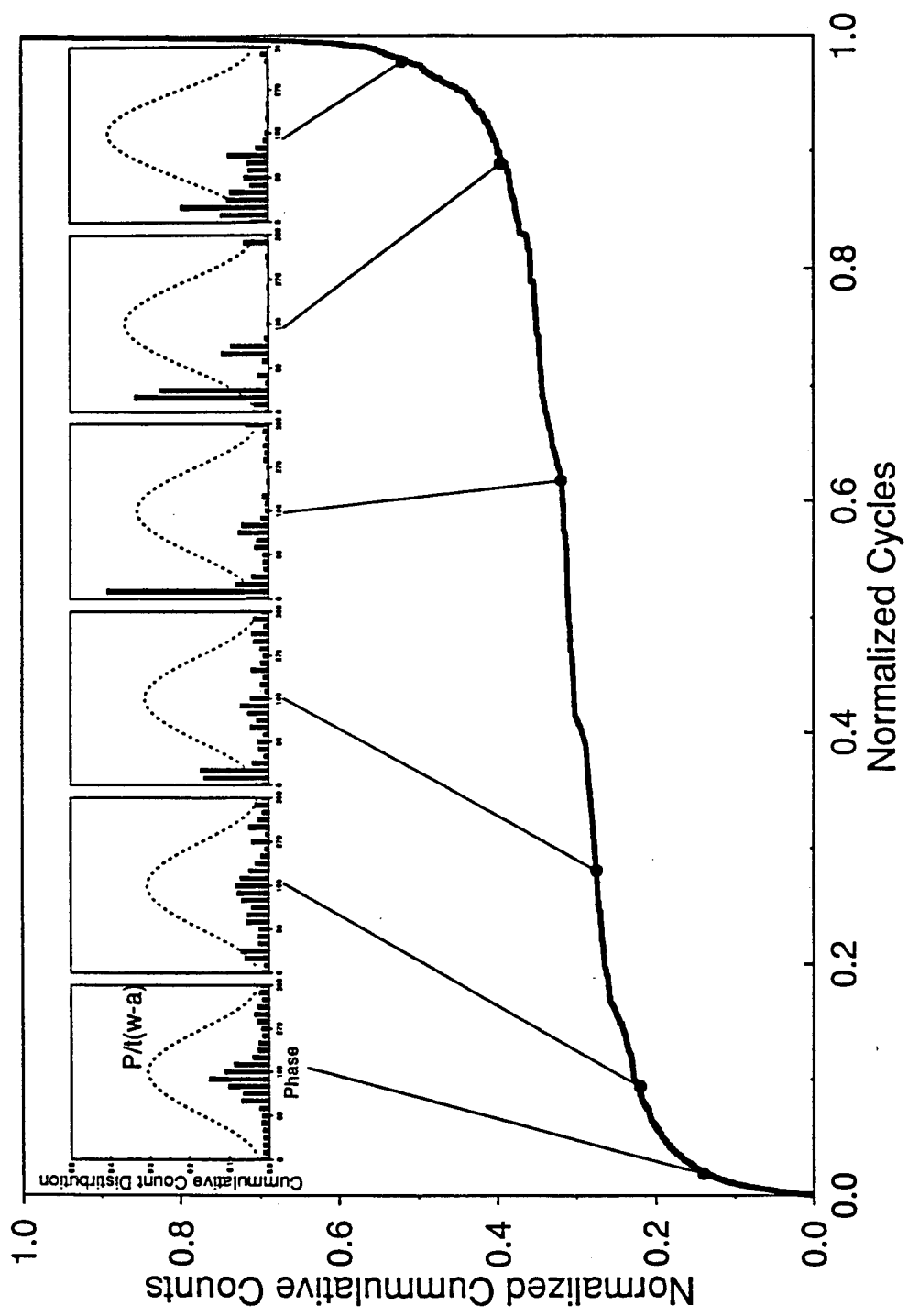
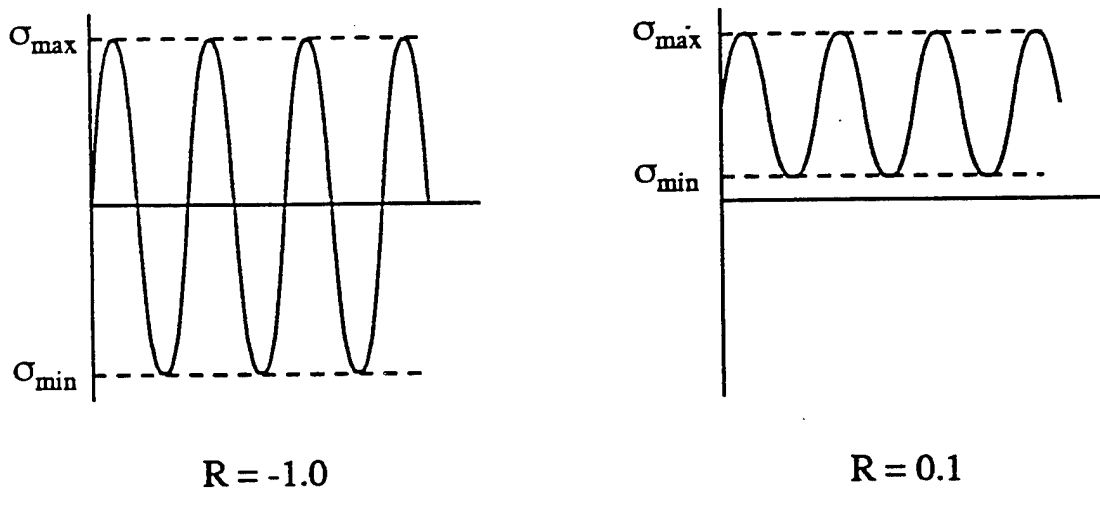
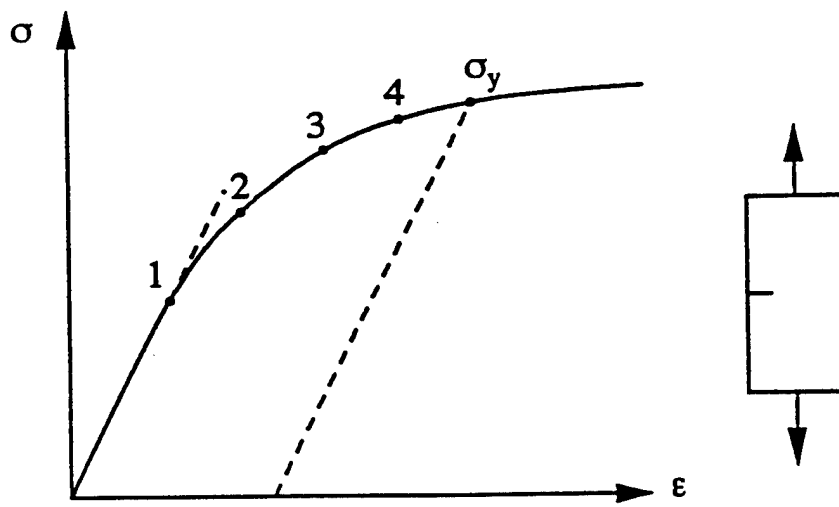


Figure 117 Development of Phase Distributions of Cumulative Counts for a Low Cycle Fatigue Test of an Aluminum Plate



**Figure 118** Fatigue Testing for Investigation of Effects of Stress Amplitude and Stress Ratio (Maximum stresses correspond to points 1, 2, 3, 4 of the stress-strain curve)

### **2.3.5 MONITORING OF SUB OR HIGHER HARMONIC OSCILLATIONS IN ROTATING MACHINE ELEMENTS**

Co-investigator: Itzhak Green (Georgia Tech)

#### **Overview**

**T**riboelements, e.g., gears seals, rolling-elements and sliding bearings, exhibit higher harmonic oscillations (HHO) when on the verge of failure due to degradation. The objective of this research is to identify and investigate the various sources of HHO in a mechanical face seal system and offer solutions to avoid a catastrophic failure.

#### **Approach**

An experimental test rig was built to study the dynamic response of a flexibly mounted rotor (FMR) mechanical face seal. This particular rig is being used to study harmonic oscillations because they have been detected under various operating conditions. The mechanical face seal was designed to operate in a noncontacting mode, but the detected HHO indicated the existence of contact between the rotor and stator. It is this contact that leads to damage, and hence must be avoided. The seal system operates under the balance of an opening force and closing force. The opening force is provided by pressurized water. A closing force is provided by pressurized air. At this stage of the project, provisions for the adjustment of the closing force on the rotor exists; however, this force is not controlled automatically. It is preset manually (this is consistent with all existing seal designs where this force is inherently fixed). A detection, recognition, and classification system of HHO, based on eddy-current proximity probes and acoustic transducers, is being constructed. Since the clearance between the rotor and stator depends upon the balance between the closing and opening forces, an adaptive control scheme for the closing force is to be incorporated in the system, in order to prevent seal contact by reducing and eliminating the presence of HHO.

#### **Accomplishments**

Research activity for M-URI year 1 focused on the following activities:

1. Reactivating the test rig and making it operational - (completed).
2. Reproducing higher harmonic oscillation (HHO) - (in progress).
3. Assembling data acquisition system (DAS) (eddy-current proximity probes and A/D DAS board) interfaced with personal computer - (completed).
4. Designing an adaptive control strategy. Acquire an adaptive controller (pneumatic, hydraulic, or stepper motor). Write closed loop (feedback) control programs. Test strategy and program on test rig - (in progress).

The main effort during this reporting period was devoted to reactivating the test rig. Currently, the research effort is moving to control strategy, algorithm and design (i.e., integrating the controller design with signal analysis).

#### **Test Rig Description**

The photograph of the noncontacting flexibly mounted rotor (FMR) mechanical face seal test rig is shown in Figure 119. The schematic of the test rig is shown in Figure 120. The rotor is flexibly mounted on the shaft by means of an elastomeric Nitrile (Buna N) O-ring, to allow it to track the stator misalignment. A sealing dam is formed between the faces of the stator and the carbon graphite ring that is attached to the rotor. Separation of the two faces is achieved by utilizing the hydrostatic effect that prevails in a converging gap between the flat-face carbon graphite ring and the coned-face stator. The closing force is varied by supplying air pressure to the rotor chamber through holes in the shaft and

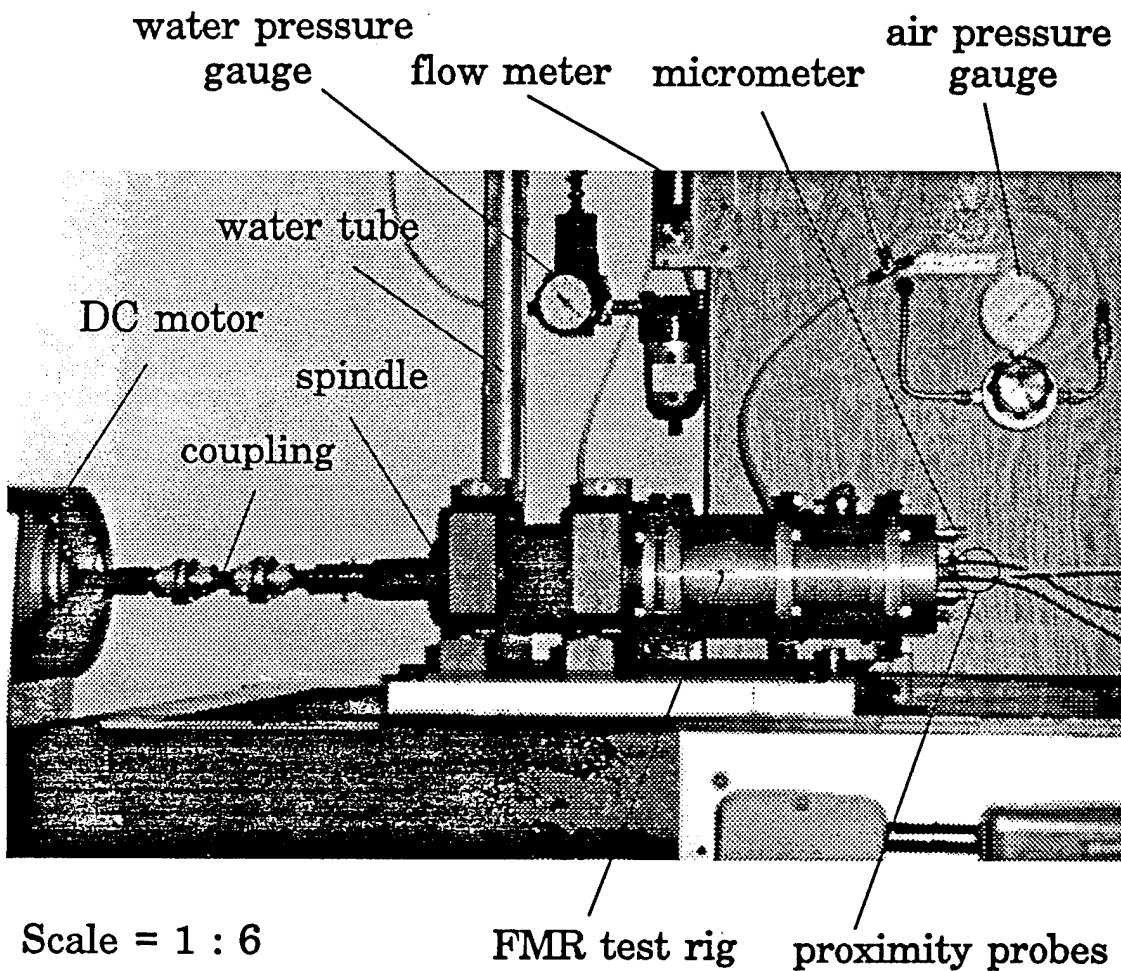


Figure 119 Photograph of FMR Mechanical Face Seal Test Rig

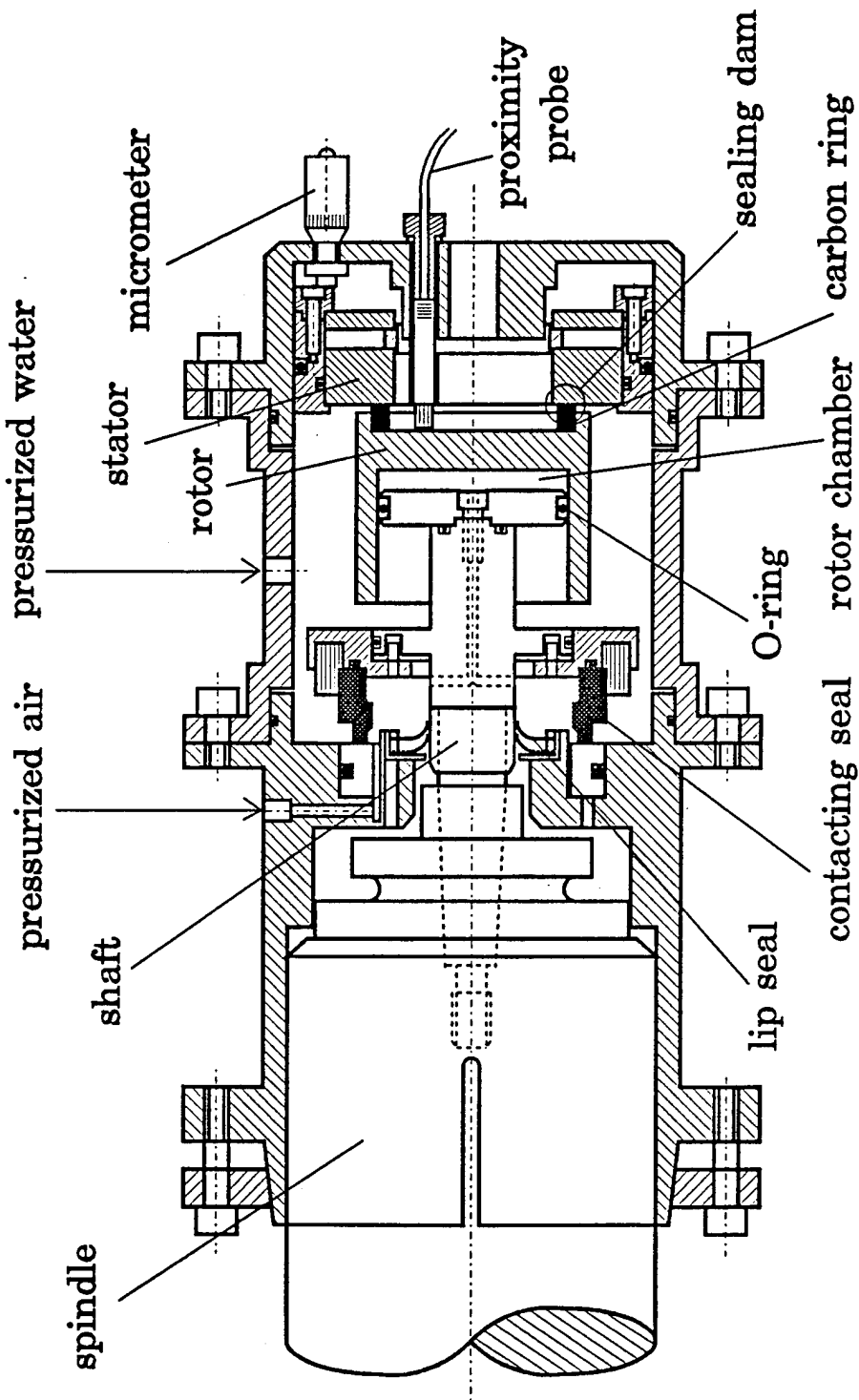


Figure 120 Noncontacting FMR mechanical face seal test rig

housing. The shaft is screwed into a precision spindle which is driven by a motor mounted on a separate structure through a wafer spring coupling. The coupling isolates vibration from the motor and also allows some misalignment between the spindle and the motor. The motor speed is controlled by a speed controller. The stator misalignment is adjusted by three micrometers. The dynamic behavior of the rotor is detected by three eddy-current proximity probes whose signals are sampled by a data acquisition system. Leakage is measured by a flow meter placed on the supply line of pressurized water.

#### *Test Rig Operation*

The pressurized air and water system connections are shown in Figure 121. Air from the main air source goes to two lines: one is connected to the air pressure gauge, which controls the air pressure at the rotor chamber. In this way the film thickness at the sealing dam can be controlled at any given water pressure. The other line is connected to a filter and to the water pressure gauge. The water gauge controls the water pressure to the water tube. The filter is used to remove any moisture or oils from the supply air.

The operation procedure for the test rig is the following:

1. With zero water gauge pressure and sufficient air gauge pressure, open the water tube plug slightly and open the water supply valve and supply the water to water tube.
2. Close the water tube plug and water supply valve for pressurizing the test rig.
3. Set the water pressure level and drop the air gauge pressure. When there is some small amount of leakage through the seal, run the motor.
4. Control the air gauge until a desired (pre-designed) leakage is obtained from the flow meter.
5. Take the experimental data using data acquisition system.

#### *Higher Harmonic Oscillation Reproduction*

In the test rig, the rotor was expected to have a sinusoidal response at shaft speed due to a sinusoidal forcing function in the form of initial rotor misalignment. However, preliminary experimental results obtained from the test rig showed that the FMR seal was vulnerable to higher harmonic oscillations, where superimposed signals of integer multiples of the shaft speed were observed. Such oscillations in mechanical face seals may indicate imminent failure. Therefore, it is extremely important to understand the cause of HHO and offer a remedy to prevent it.

Tests under the conditions that produced HHO are being reconstructed to allow its study. These conditions are: one O-ring support, shaft speed of 30 Hz, a stator coning angle of 7.2 mrad, water pressure of 0.2068 MPa, and a mean seal clearance of 3.75  $\mu\text{m}$ .

Tests under various operating conditions will be conducted in order to study the various anticipated results that can be obtained from the operation of the FMR mechanical face seal test rig.

#### *Signal Detection System Description*

The rotor dynamic response is detected by three Bentley Nevada's 7200 Series 5mm Proximity Transducer Systems (eddy-current proximity probes) which can measure instantaneous (DC and AC) distances between the probes and the observed target. They give voltage results proportionally to the distance between the probes and the target. The results of three eddy-current proximity probes can be used to determine the rotor dynamic responses and to analyze the HHO. Other signal detection systems will be added to the test rig as needed.

#### *Data Acquisition System Description*

The output of the three eddy-current proximity probes is acquired by Model DAS16F Analog/Digital I/O Interface Boards from OMEGA. Because the output of each proximity probe can reach as high as 24V and DAS16F A/D board can not accept an input higher than 10V, the output is routed through a voltage divider to step it down. From there, the signal passes through a low pass filter

#### *Direct Sensing, Analysis, and Real-time Diagnosis*

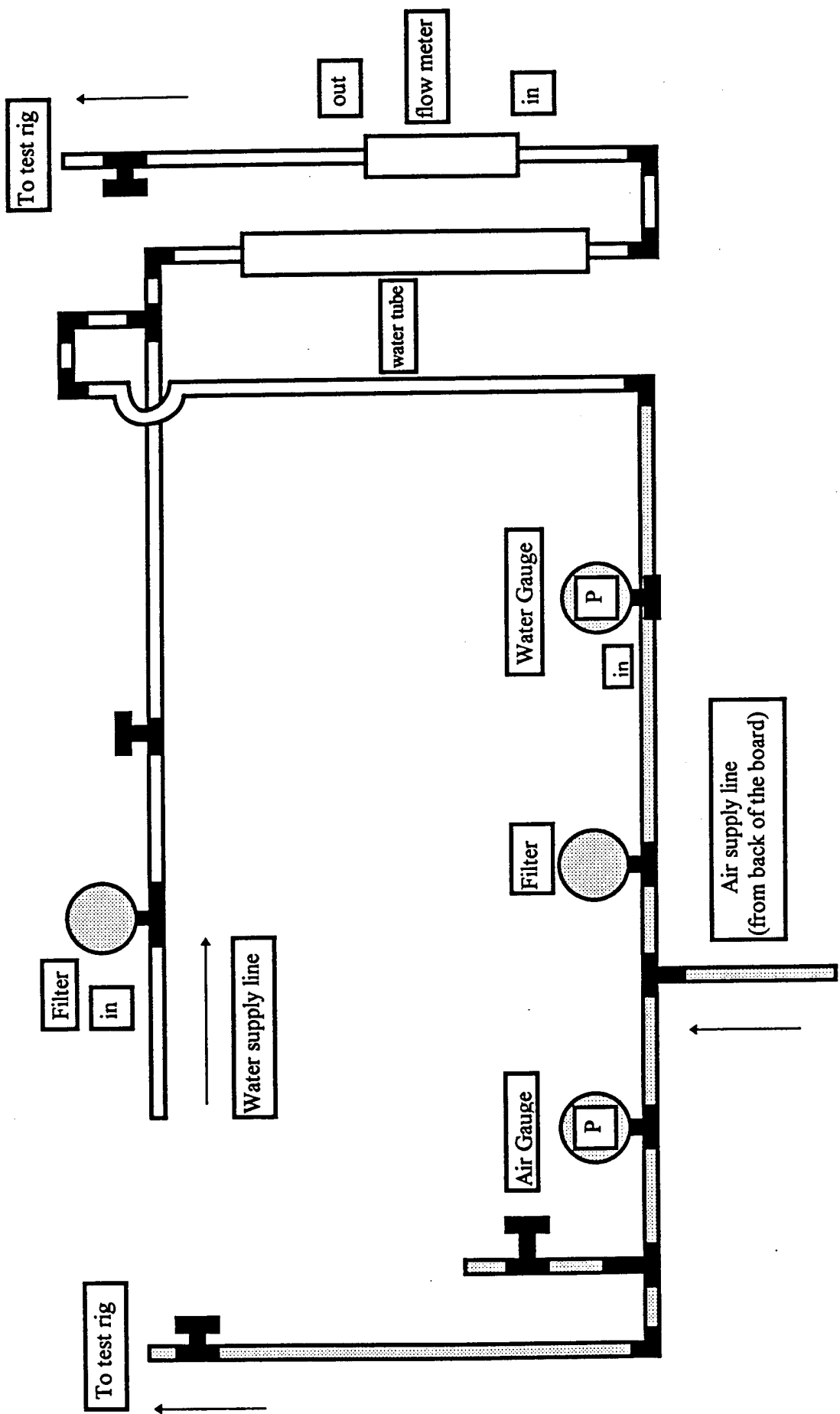


Figure 121 Pressurized Air and Water Connections

which has a cut-off frequency of 1000 Hz. This is used to eliminate high frequency noise. The proximity probes are powered by a DC voltage supply which provides a +24V source. The low pass filters are powered by a +12V power supply.

#### *DAS16F Analog/Digital Interface Board Recalibration*

Periodic recalibration of DAS16F is recommended to retain full accuracy. The recommended recalibration interval for laboratory conditions is 6 months to 1 year. The board was calibrated in the range of -10V ~ +10V input signal, resulting in a maximum error of 0.8%.

#### *Signal Analysis*

A signal analysis program has been developed to analyze the data acquired from the DAS16F board. The program can give the power spectrum density of the signal which is a criterion for deciding whether sub or higher harmonic oscillation has occurred. The program can also give the rotor dynamic response and the rotor reference plane.

The dynamic response of the rotor has been obtained through the DAS16F Board without the stator, pressurized water and air. The data then has been analyzed using the signal analysis program. The results show that both the signals obtained are correct and that the program developed works well.

Further signal analysis will be performed using Matlab Signal Processing Toolbox and other advanced signal processing software (such as DSP) and hardware.

#### *Control Strategy*

The closed-loop (feedback) control strategy was chosen for the test rig. Feedback or closed-loop control corrects for disturbances by measuring their effect on the system output and then calculates a correcting action that counteracts the disturbances and maintains the desired output. Feedback of a fraction of the output signal to the input occurs to allow a comparison between the actual process condition and the desired condition. The difference between these two signals (the error) is fed into the control plan that uses this information to alter the output signal to the required value.

#### *Control Design and Implementation*

The test rig system dynamics model, sensor and actuator system models, and control system dynamics model will be analyzed and designed using MATLAB, SIMULINK, Real-Time Workshop and other Matlab Toolboxes, products of MATH WORKS Inc.

Real time control will be implemented using MATH WORKS's software and dSPACE's hardware and software system. The above mentioned combination is very efficient in rapid prototyping. Rapid prototyping can be defined as a process for automatic implementation of a block diagram on real-time hardware. It offers fast design iterations, including real-time testing that enables designs to be completed significantly faster than with traditional design methods.

#### **Plans**

1. Complete analysis of rub and impact kinetics (dynamics) - (projected AASERT student).
2. Verify experimentally dynamics analysis - (projected AASERT student).
3. Opening force vs. closing force strategies - (projected AASERT student).
4. Establish frequency patterns for various HHOs.
5. Construct a detection system for recognition and differentiation of HHO.
6. Integrate adaptive controller and strategy with A/D-D/A DAS and apply to test rig.
7. Design modification in the test rig for the incorporation of above.
8. Perform exhaustive experimentation with and adaptive control system.

The main research effort to be conducted is shown schematically in Figure 122.

#### *Direct Sensing, Analysis, and Real-time Diagnosis*

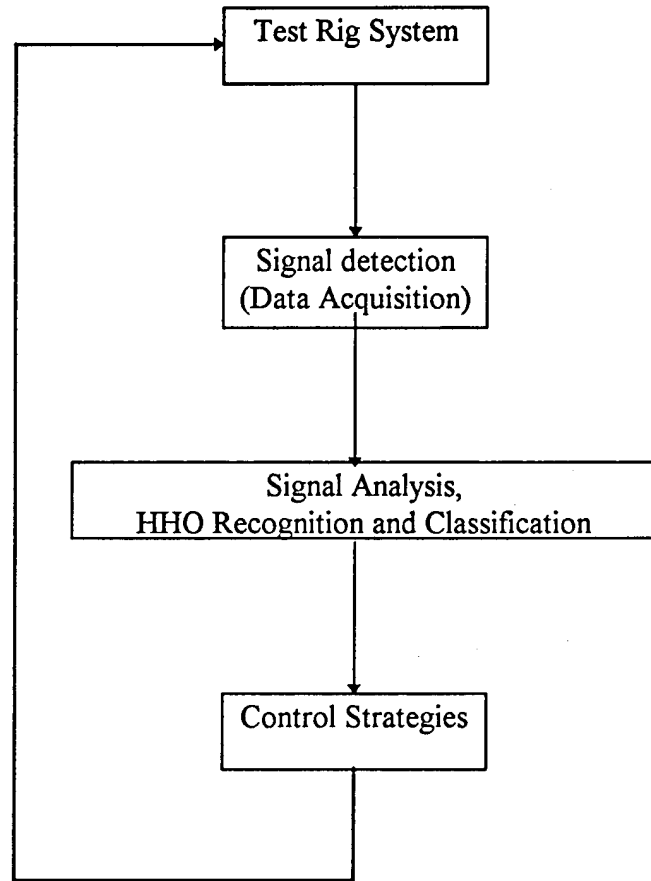


**Figure 122** Schematic of HHO Research Effort

### **2.3.6 DYNAMIC METROLOGY AS A WEAR DIAGNOSTIC**

Co-investigators: Steven Liang, Thomas Kurfess, Steven Danyluk (Georgia Tech)

#### **Overview**

Utilizing sensors that are available and up-to-date, this project targets the development and implementation of real-time and in-line methods for bearing wear and failure detection. The ultimate objective of the project is to develop a small self-contained processing package that can be attached to an array of sensors used to monitor bearing health for an operating machine or vehicle platform, e.g., rotary-winged aircraft. To accomplish this, a number of sensors will be employed, including contact potential difference probes (CPD), eddy current, accelerometer, and acoustic emission sensors. These individual sensors will be calibrated and integrated into a single diagnostic package. By using a multiple sensor approach, it is anticipated that a number of wear and failure modes will be detected in real-time. Furthermore, the use of multiple sensors will improve the confidence interval associated with bearing condition estimation.

The following progress has been made with respect to the administrative organization and technical tasks associated with diagnosing wear through dynamic metrology. Two students have been hired, and prior works on accelerometer, acoustic emission, eddy current and contact potential difference sensors have been integrated into this M-URI project. The monitoring and real-time sensor (AE eddy current and accelerometer) signal processing has been accomplished on prototype shafts; the signal characteristics for wear and defect monitoring have been identified for individual sensors. A benchtop rotating shaft (alpha) system has been built and retrofitted with an electrical field contact potential difference (CPD) sensor.

The second year plan calls for the construction of a rotating shaft (beta) system, miniaturization of the sensors through MEMS technology, integration of sensor signals, and increase in the sensitivity of sensors for defect and wear detection in bearings. The following paragraphs expand on the items listed above.

#### **Accomplishments**

##### *Administrative Progress*

The early part of this first year was used to recruit and hire two graduate students from the Woodruff School of Mechanical Engineering. Jason Shiroishi, an MS candidate, and Yawei Li, a Ph.D. candidate, have been hired to work on this project. These students have completed a literature review, assembled and constructed a bearing demonstration system, and evaluated and exercised a data acquisition system for multi-sensor detection. They are currently organizing a dedicated laboratory and facilities for this project.

Prior sensor work has been integrated into this project. Acoustic emission, eddy current and accelerometer sensors developed under other programs have been modified for wear monitoring under dynamic conditions. A contact potential difference (CPD) probe, developed under the auspices of other ONR funds, has been integrated into this project. The test stand and data acquisition system developed under that program have been modified and calibration of the CPD probe versus wear sensitivity has been completed.

A number of discussions have been held with industry that have resulted in offers of support from The Timken Company and the Torrington Company. Site visits have been made to these two companies. Their support will be in the form of providing expertise in developing appropriate bearing test facilities as well as procedures. Furthermore, they have offered to supply this research team with

healthy, worn, as well as damaged bearings, and they have offered their facilities in Canton, Ohio, for implementing the concepts developed in this research.

#### *Technical Progress*

Four major items are noteworthy as to technical progress.

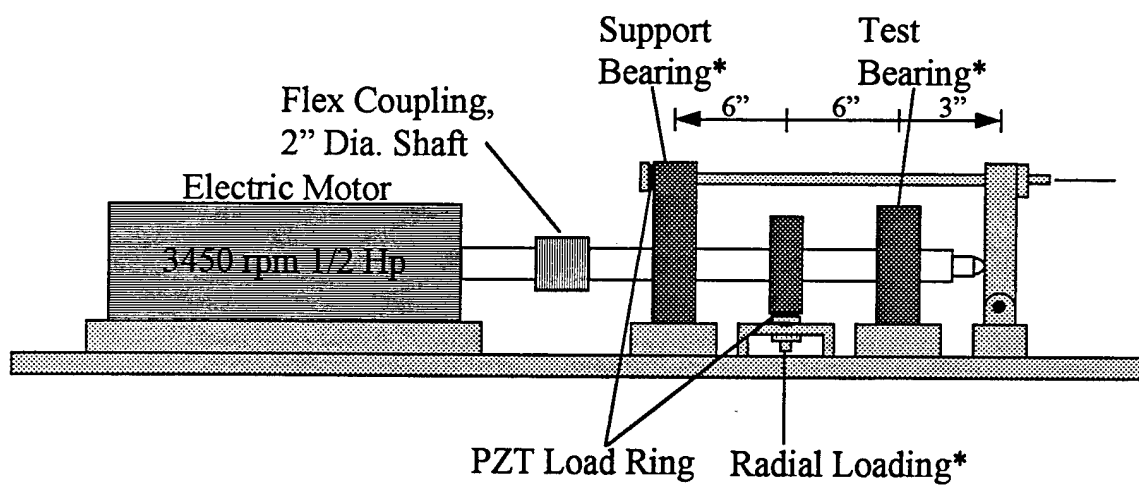
1. An extensive review of the literature has been conducted in order to document prior work on probe type, signal analysis, and sensitivity for wear and surface defect detection. Table 5 shows a summary of the literature review including the sensitivity of each probe. It should be noted that the wear and defect sensitivity depends on physical parameters of the probe, environmental conditions of the tests, and analysis techniques. Given this variability, little work has been done in real-time, in-site analysis of multiple sensors. This is the subject of this task.
2. Since this project targets high speed mechanical components, and there are a plethora of such elements available to study, we have chosen to target bearings for our initial studies. This choice is based on the fact that bearings are critical components in a number of applications, and their failure can be catastrophic for a wide variety of systems including aircraft. Extensive discussions have taken place with our industrial contacts (Timken and Torrington) on the wear modes and failures of bearings and Table 6 presents a summary of this prior knowledge. As can be seen in this table, the degradation of bearings can be grouped into localized deformation and defects, and uniform wear and degradation. This project addresses multiple defects and an integrated approach to signal processing so that both local and 'distributed' wear can be detected on-line, in-site, and in real-time.
3. Test stands from other projects have been used to test signal analysis concepts, sensor positions on bearings and sensitivity to defect/wear detection. For example, accelerometer and acoustic emission probes have been positioned on an end mill to test for sensitivity of dents, and the sensitivity versus dent size has been determined. In another case, the CPD probe has been used to determine its sensitivity for wear monitoring. Using the results of this experience, a beta test stand has been designed, and construction is underway. Figure 123 shows a schematic diagram of the beta test stand. Acoustic emission, eddy current, accelerometers and CPD sensors will be used to monitor the uniform wear and localized damage in a prototype bearing assembly.
4. A new type of wear/defect sensor under development in another ONR sponsored project, will also be used in this study. The contact potential difference probe (CPD) measures differences in work functions between surfaces. The signal strength of this probe is also related to the spacing between the probe and the surface under study so that signals can be related to either uniform wear or localized wear if the probe is in proximity of a defect. Figure 124 shows a schematic of the probe and an example of the sensitivity to spacing between the probe and a reference surface. This figure shows a signal output (volts) versus spacing between a flat plate probe and a rotating shaft. The rotational frequency was 10, 15, 20 and 25 Hz. The wear sensitivity for this particular probe is approximately 0.2mm. It is estimated that the sensitivity can be increased by a factor of 100 and the construction of high sensitivity probes has been initiated.

**Table 5** Literature Summary of Sensor Type/Sensitivity for Wear and Defect Monitoring

Researcher	Sensor Type	Bearing Type	Defect Type	Defect Location, Size	RPM	Loading	Notes
Alfredson & Matthew A	B&K 4333 Accel.	Ball	Lub. Contam. Small Groove-- Flats on Rollers Overloading Lub. Drain	Outer Race	Up to 2865	Up to 15 kN	Only RMS and Shock pulse were reliable. Others had limited use for broad detection. Bandpass was also tried, but failed.
Alfredson & Matthew B	B&K 4333 Accel.	Ball	Lub. Contam. Small Groove-- Flats on Rollers Overloading Lub. Drain	Outer Race	Up to 2865	Up to 15 kN	Recommended not relying on one method, i.e. earliest detection is based on method/defect type.
Campbell	PCB 308B15 Accel.	Needle	Rockwell Tester C Scale Indention	Outer Race, 50,55,60 (RWC) preloads	984	85lb	MFRMS Performed best overall.
Carney & Mann	Sound Pressure Mic.	Ball		Outer Race, Inner Race, Ball			Sound Pressure measurements are unreliable.
Daadi bin & Wong		Ball, Roller		Outer Race, Inner Race, Rolling Elem.		Radial	Spectral Analysis was carried out on LPF 500 Hz signal (defect frequency).
Hawman & Galinaitis	AE B&K 4393 Accel.	Roller	Scratches 0.010" wide were detected	.006" wide x .0002" deep to 0.2" wide x .050" deep	5700	Axial-2400lbf	AE provided more information related to defect size and location
Kim	Eddy Current	Ball	Artificial Spalling	Outer Race Inner Race	2450	Radial & thrust, 700-900 lbf	100% Detection was found with Eddy signal.
Li & Ma	PCB 303A02 Accel.	Tapered Roller			870	Radial & thrust	All of Ma's work is related to the many of the same materials/conditions
Li & Wu	PCB 303A02 Accel.	Tapered Roller	Dents	Outer Race Roller 0.06" dia 0.06" dia 0.005" depth		Thrust	
Ma & Li	PCB 303A02 Accel.	Tapered Roller	Dents	Outer Race Roller 0.06" dia 0.005" depth	1804, 2032	Thrust	
Martin & Hormarvar	PCB 307A Accel.	Ball	Artificial Defects	Inner Race Outer Race Ball	1000-3000	Radial 0-827N	
Martin & Thorpe Pandit, Joshi & Paul	Accel. Simulation	Roller	EDM	Inner Race Outer Race Roller	2000		Defect signal emulated those from Li & Ma 1992
Tandon	Accel.	Ball	EDM Identification began from 75-250µm diameters	Inner Race Outer Race 100µm deep	1500	Radial 50kg	
Tandon & Nakra	B&K 3519 Sound Intensity	Ball	EDM Identification began around 200µm diameters	Inner Race, Outer Race 50-500µm dia 50-150µm deep 150-500µm dia	100-1500	Radial 20-100kg	Radial Noise was higher than that found axially

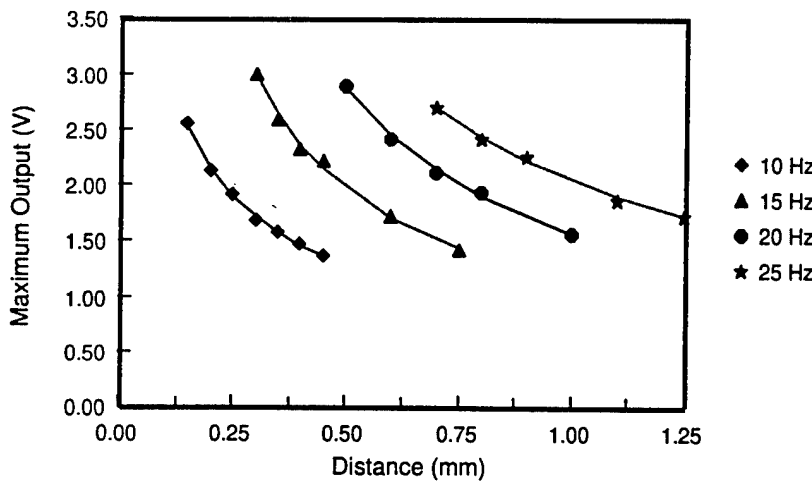
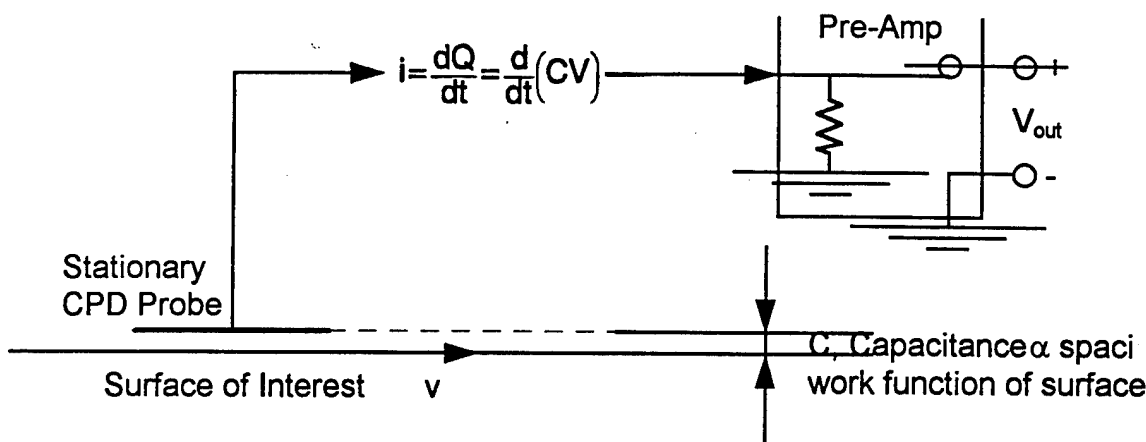
Acceleration	AE	Eddy Current	CPD	Bearing Failure Mode
		✓	✓	Adhesive Wear
	✓	✓	✓	Corrosive Wear
✓	✓	✓		Debris Denting
✓				Inclusion Spalling
✓	✓			Point Surface Fatigue
✓	✓		✓	Stress Concentration Fatigue
	✓		✓	Peeling

Table 6 The Primary Failure Modes of Bearings



\*Tapered Roller Bearing

Figure 123 Schematic Diagram of the  $\beta$ -Test Stand



**Figure 124** Schematic diagram and Sensitivity Measurements for the Contact Potential Difference Probe. The maximum output (voltage of the probe depends on the spacing between the probe and the reference surface, and the linear velocity ( $v$ ) of the surface. These data were obtained for a shaft rotating at 10, 15, 20 and 25 Hz.

## **Plans**

During the second year of this project, the following milestones will be accomplished.

1. Fabrication and structural analysis of beta test stand will be completed. It is anticipated that the beta stand will be operational by May 1996; at which time, calibrated sensors will be integrated into the system.
2. Calibration of four sensors to determine dents and uniform wear will be completed. This procedure will be carried out by testing individual sensors at various dented bearings. It is anticipated that initial sensor calibration will be completed November 1996 for initial integration into the beta test stand. At the completion of this stage, the sensitivity of various sensors to various bearing failure modes will be established.
3. Development of multiple signal processing techniques using the sensors mounted on the beta test stand will be completed. This step involves the development of the time series, eigenvalues, long and short term entropy decomposition, and frequency decoloring methodology, followed by coding simulation, and data testing. This will be conducted during the Winter of 1997. At the completion of this stage, the signal processing and analysis system will be realized for various sensors at different bearing damage conditions. This component of the research will support enhancement of the beta system as well as the sensor calibration, and it provides a prerequisite for the final stage of sensor integration.
4. A visit to the Cherry Point Naval Depot in North Carolina will be done to discuss physical operations of helicopters and to acquire geometric information as to how diagnostic packages may be integrated into flight operational aircraft.
5. A visit to the University of Minnesota will be made to coordinate fabrication of microscale sensor packages (see Section 2.3.1.1). The objective is to integrate some of these sensors into the proposed diagnostic package, and to investigate the possibility of having the Minnesota group fabricate a micro-scale CPD probe.

## 2.4 REFERENCES

### Section 2.1.3 Flaw Detection and Characterization

- [1] Yang et al., 1993, *Ultrasonics*, Vol. 31, No. 6, pp. 387-394.
- [2] Bruinsma and Vogel, 1988, *Applied Optics*, Vol. 27, No. 22, pp. 4690-4695.

### Section 2.2.1 Structural Fatigue Investigation

- [3] McDowell, D.L. and Berard, J.-Y., 1990, "A J-Based Approach to Biaxial Low-Cycle Fatigue of Shear Damaged Materials," in *Fatigue Under Biaxial and Multiaxial Loading*, ESIS10, K. Kussmaul, D. McDiarmid and D. Socie, Eds., Mechanical Engineering Publications, London, pp. 413-431.
- [4] McDowell, D.L. and Berard, J.-Y., 1992, "A J-Based Approach to Biaxial Fatigue," *Fatigue Fract. Engng. Mater. Struct.*, Vol. 15, No. 8, pp. 719-741.
- [5] Miller, K.J., 1993, "The Two Thresholds of Fatigue Behaviour," *Fatigue Fract. Engng. Mater. Struct.*, Vol. 16, No. 9, pp. 931-939.
- [6] Miller, K.J., 1993, "Materials Science Perspective of Metal Fatigue Resistance," *Mater. Sci. Techn.*, Vol. 9, pp. 453-462.
- [7] Tanaka, K., 1987, "Short-Crack Fracture Mechanics in Fatigue Conditions," in *Current Research on Fatigue Cracks*, T. Tanaka, M. Jono and K. Komai, Eds., Current Japanese Materials Research, Vol. 1, Elsevier, pp. 93-117.
- [8] Hoshida, T., Miyahara, M. and Inoue, T., 1988, "Elastic-Plastic Behavior of Short Fatigue Cracks in Smooth Specimens," in *Basic Questions in Fatigue: Volume I*, ASTM STP 924, J.T. Fong and R.J. Fields, Eds., Philadelphia, pp. 312-322.
- [9] Chan, K., Lankford, J. and Davidson, D., 1986, "A Comparison of Crack-Tip Field Parameters for Large and Small Fatigue Cracks," *ASME J. Engng. Mater. Techn.*, Vol. 108, pp. 206-213.
- [10] Berard, J.-Y., McDowell, D.L. and Antolovich, S.D., 1993, "Damage Observations of a Low-Carbon Steel Under Tension-Torsion Low-Cycle Fatigue," in *Advances in Multiaxial Fatigue*, ASTM STP 1191, D.L. McDowell and R. Ellis, Eds., ASTM, Philadelphia, pp. 326-344.
- [11] Ogata, T., Nitta, A. and Blass, J.J., 1993, "Propagation Behavior of Small Cracks in 304 Stainless Steel Under Biaxial Low-Cycle Fatigue at Elevated Temperature," in *Advances in Multiaxial Fatigue*, ASTM STP 1191, D.L. McDowell and R. Ellis, Eds., ASTM, Philadelphia, pp. 313-325.
- [12] Nisitani, H., 1987, "Behavior of Small Cracks in Fatigue and Relating Phenomena," in *Current Research on Fatigue Cracks*, T. Tanaka, M. Jono and K. Komai, Eds., Current Japanese Materials Research, Vol. 1, Elsevier, pp. 1-26.
- [13] Manson, S.S. and Halford, G.R., 1986, "Re-examination of Cumulative Fatigue Damage Analysis - An Engineering Perspective," *Engng. Fract. Mech.*, Vol. 25, Nos. 5-6, pp. 539-571.
- [14] Chaboche, J.L. and Lesne, P.M., 1988, "A Non-Linear Continuous Fatigue Damage Model," *Fatigue Fract. Engng. Mater. Struct.*, Vol. 11, No. 1, pp. 1-17.
- [15] Socie, D.F., 1993, "Critical Plane Approaches for Multiaxial Fatigue Damage Assessment," in *Advances in Multiaxial Fatigue*, ASTM STP 1191, D.L. McDowell and R. Ellis, Eds., ASTM, Philadelphia, pp. 7-36.
- [16] Socie, D., 1987, "Multiaxial Fatigue Damage Models," *ASME J. Engng. Mater. Techn.* 109, pp. 293-298.
- [17] Robillard, M. and Cailletaud, G., 1991, "Directionally Defined Damage in Multiaxial Low-Cycle Fatigue: Experimental Evidence and Tentative Modeling," in *Fatigue Under Biaxial and Multiaxial Loading*, ESIS10, K. Kussmaul, D. McDiarmid and D. Socie, Eds., Mechanical Engineering Publications, London, pp. 103-130.
- [18] Weiss, J. and Pineau, A., 1993, "Continuous and Sequential Multiaxial Low-Cycle Fatigue Damage in 316 Stainless Steel," in *Advances in Multiaxial Fatigue*, ASTM STP 1191, D.L. McDowell and R. Ellis, Eds., ASTM, Philadelphia, pp. 183-203.
- [19] Dafalias, Y.F., 1993, "Planar Double-Slip Micromechanical Model for Polycrystal Plasticity," *J. Engineering Mechanics*, Vol 119, No. 6.
- [20] Rashid, M., 1992, "Texture Evolution and Plastic Response of Two Dimensional Polycrystals," *J. Mech. Phys. Solids*, Vol. 40, No. 5, pp. 1009-1029.

- [21] Cailletaud, G., 1992, "A Micromechanical Approach to Inelastic Behavior of Metals," *Int. J. Plasticity*, Vol. **8**, pp. 55-73.
- [22] Newman, J.C., Jr., 1994, A review of modeling small-crack behavior and fatigue-life predictions for aluminum alloys. *Fatigue Fract. Engng. Mater. Struct.* **17**, No. 4, pp. 429-439.

### **Section 2.2.2 Failure Prediction Methodology using FORM**

- [23] Bowen J., et al., "Critical Equipment Failures and Maintenance Issues," Subgroup Report, *Proc. Workshop on Condition Based Maintenance*, Office of Naval Research and Georgia Institute of Technology, Atlantic Beach, NC, November 15-17, 1993.
- [24] Glaeser, B. A. and Wedeven, L. D., "Failure Models," Subgroup Report, *Proc. Workshop on Condition Based Maintenance*, Office of Naval Research and Georgia Institute of Technology, Atlantic Beach, NC, November 15-17, 1993.
- [25] Harkness, H. H., Belytschko, T. B., and Liu, W. K., 1992, "Finite Element Analysis of Fatigue Life," *Nucl. Engng Des.*, Vol. **133**, pp. 209-224.
- [26] Harkness, H., Fleming, M., Moran, B. and Belytschko, T. B., "Fatigue Reliability Method with In-Service Inspections," *Proc. FAA/NASA International Symposium on Advanced Structural Integrity Methods for Durability and Damage Tolerance*, Hampton, VA, May 4-6, 1994.

### **Section 2.3.1 Integrated Microsensors for Aircraft Fatigue and Failure Warning**

- [27] Jaffe, B., W. R. Cook and H. Jaffe, 1971, *Piezoelectric Ceramics*, R. A. N. Publishers, Marietta, OH.
- [28] Polla, D. L., R. M. White, and R. S. Muller, 1986, "Integrated Multi-Sensor Chip," *IEEE Electron Dev. Lett.*, EDL-7, pp. 254-256. Reprinted in *Microsensors*, 1990, R. S. Muller, R. T. Howe, S. D. Senturia, R. L. Smith, and R. M. White, eds. IEEE Press, New York.
- [29] Tamagawa, T., D. L. Polla, and C.-C. Hsueh, 1990, "Lead Zirconate Titanate (PZT) Thin Films in Surface-Micromachined Sensor Structures," *IEEE International Electron Devices Meeting*, San Francisco, CA.
- [30] Hsueh, C.-C. , T. Tamagawa, C. Ye, A. Helgeson, and D. L. Polla, 1993, "Sol-gel Derived Ferroelectric Thin Films in Silicon Micromachining," *Integrated Ferroelectrics* **3**, p. 21.
- [31] Muralt, P., M. Kohli, T. Maeder, A. Kholkin, K . Brooks, N. Setter, and R. Luthier, 1995, *Sensors and Actuators A* **48**, p. 157.
- [32] Howe, R. T., 1988, "Surface Micromachining for Microsensors and Microactuators," *J. Vac. Sci. and Technol.* **B6**, pp. 1809-1813.
- [33] Polla, D. L., H. Yoon, T. Tamagawa, and K. Voros, 1989, "Integration of Surface-Micromachined Zinc Oxide Sensors in n-Well CMOS Technology," *IEEE International Electron Devices Meeting*, Washington, DC.
- [34] Glumac, D. E., T. G. Cooney, L. F. Francis, W. P. Robbins, in *Ferroelectric Thin Films IV*, edited by B. A. Tuttle, S. B. Desu, R. Ramesh and T. Shiosaki (*Mater. Res. Soc. Symp. Proc.* **360**, Pittsburgh, 1994) p. 407.
- [35] Cooney, T. G., D. E. Glumac, W. P. Robbins, L. F. Francis, in *Ferroelectric Thin Films IV*, edited by B. A. Tuttle, S. B. Desu, R. Ramesh and T. Shiosaki (*Mater. Res. Soc. Symp. Proc.* **360**, Pittsburgh, 1994) p. 401.
- [36] Budd, K. D., S. K. Dey, D. A. Payne, 1985, *Br. Ceram. Proc.* **36**, p. 107.
- [37] Schiller, P., D. L. Polla, and M. Ghezzo, "Surface-Micromachined Piezoelectric Pressure Sensors," *IEEE Solid-State Sensors and Actuators Workshop*, Hilton Head, S.C., June 1990.
- [38] Scruby, C., 1987, "An introduction to acoustic emission," *J. Phys. E: Sci. Instrum.*, Vol. **20**, pp. 946-953.
- [39] Jacobs, L., 1991, "Characterization of acoustic emission signals from mode I crack," *Journal of Engineering Mechanics*, Vol. **117**, No. 8, pp. 1878-1889.
- [40] Barna, B., J. Johnson and R. Allemeier, 1988, "Determination of acoustic-emission sites using digital non destructive-evaluation workstation," *Exp. Mech.*, pp. 210-213.
- [41] Mitrakovic, D., I. Grabec and S. Sedmak, 1985, "Simulation of AE signals and signal analysis systems," *Ultrasonics*, Vol. **23**, pp. 227-232.
- [42] Isermann, R., 1993, "Fault diagnosis of machines via parameter estimation and knowledge processing - tutorial paper," *Automatica*, Vol. **29**, pp. 815-835.

- [43] Kumaresan, R. and D. W. Tufts, 1982, "Estimating the Parameters of Exponentially Damped Sinusoids and Pole-Zero Modeling in Noise," *IEEE Trans. Acoust., Speech, Signal Processing*, vol. ASSP-30, no. 6, pp. 833--840.
- [44] Gerr, N. and J. Allen, 1994, "The generalized spectrum and spectral coherence of a harmonizable time series," *Digital Signal Proc.*, Vol. 4, pp. 222-238.
- [45] Cohen, L., 1989, "Time-frequency distributions - a review," *Proc. of the IEEE*, Vol. 77, No. 7, pp. 941-981.
- [46] Haykin, S., 1996, *Adaptive Filter Theory*, 3rd Ed, Prentice-Hall.
- [47] Helstrom, C., 1995, *Elements of Signal Detection and Estimation*, Prentice-Hall.
- [48] Sayeed, A. and D. Jones, 1994, "Optimal quadratic detection using bilinear time-frequency and time-scale representations," *Proc. International Sym. on Time-Freq. and Time-Scale Analysis*, pp. 365-368.

#### **Section 2.3.2 Eddy Current Microsensors for Integrated Diagnostics**

- [49] Libby, Hugo L., 1971, *Introduction to Electromagnetic Nondestructive Testing Methods*, Wiley-Interscience, New York.
- [50] Blitz, Jack, 1991, *Electrical and Magnetic Methods of Nondestructive Testing*, Adam Hilger, Bristol.
- [51] Uesaka, M., Nakanishi, T., Miya, K., Komatsu, H., Aoki, K., and Kasai, K., 1995, *IEEE Transactions on Magnetics*, **31**, pp. 870 - 876.
- [52] Dodd, Caius V., 1967, *Solutions to Electromagnetic Induction Problems*, Doctoral Dissertation, University of Tennessee, Knoxville, Tenn.
- [53] Palanisamy, Ramasamy, 1980, Doctoral Dissertation, Colorado State University, Fort Collins, Colo.
- [54] Ida, Nathan, 1983, *Three-dimensional Finite Element Modeling of Electromagnetic Nondestructive Testing Phenomena*, Fort Collins, Colo.
- [55] Ranmuthu, K. T. M., Pohm, A. V., Daughton, J. M., and Comstock, C. S., 1993, *IEEE Transactions on Magnetics*, **29**, pp.2593 - 2595.
- [56] Daughton, J. M., and Chen, Y. J., 1993, "GMR Materials for Low Field Applications," *IEEE Transactions on Magnetics*, **29**, pp. 2705 - 2710.

#### **Section 2.3.4 Acoustic Emission Modeling for Integrated Diagnostics**

- [57] Liptai, R. G., D. O. Harris, R. B. Engle and C. A. Tatro, 1971, "Acoustic Emission Techniques in Material Research," *Inter. Journal of Nondestructive Testing*, Vol. 3, pp. 215-275.
- [58] Daniel, I. M. and T. Liber, 1979, "Nondestructive Evaluation Techniques for Composite Materials," *Proc. of the 12th Symposium on Nondestr. Testing*, W. W. Bradshaw, ed., Southwest Research Institute, San Antonio, TX, pp. 226-244.
- [59] Dunegan, H. L. and D. O. Harris, 1969, "Acoustic Emission - A New Nondestructive Testing Tool," *Ultrasonics*, Vol. 7, No. 3, p. 160.
- [60] Fang, D. and A. Berkovits, 1993, "Fatigue Damage Mechanisms on the Basis of Acoustic Emission Measurements," *Novel Exper. Techniques in Fracture Mechanics*, ed. by A. Shukla, AMD Vol. 176, ASME, pp. 213-235.
- [61] *Acoustic Emission Testing in Nondestructive Testing Handbook*, 1987, Vol. 5, ed. by R. K. Miller and P. McIntire, Second Ed., American Soc. for Nondestructive Testing, Columbus, OH.
- [62] Morton, H. L., R. M. Harrington and J. G. Bjeletich, 1973, "Acoustic Emissions of Fatigue Crack Growth," *Engineering Fracture Mechanics*, Vol. 5, No. 3, p. 691.
- [63] Lindley, T. C., I. G. Palmer and C. E. Richards, 1978, *Materials Science and Engineering*, Vol. 32, p. 1.
- [64] Hamel, F., J. P. Bailon and M. N. Bassim, 1981, "Acoustic Emission Mechanisms during High Cycle Fatigue," *Engineering Fracture Mechanics*, Vol. 14, p. 853.
- [65] Berkovits, A. and D. Fang, "An Empirical Design Model for Fatigue Damage on the Basis of Acoustic Emission Measurements," 17th ICAF Symposium, Stockholm, June 1993.
- [66] Hill, E. V. K., P. L. Israel and G. L. Knotts, 1993, "Neural Network Prediction of Aluminum-Lithium Weld Strengths from Acoustic Emission Amplitude Data," *Materials Evaluation*, Vol. 51, No. 9, pp. 1040-45.
- [67] Sinclair, A. C., D. C. Connors and C. L. Formby, 1977, *Materials Science and Engineering*, Vol. 28, p. 263.

### 3. TECHNOLOGY TRANSFER ACHIEVEMENTS

---

The pivotal objective of the Integrated Diagnostics program is to accommodate academia's need to explore and discover, and industry's need to develop and improve. To expedite the transfer of the knowledge obtained from academic research, information has been disseminated through a variety of means, including publications, monthly updates, meeting presentations, and the educational process.

#### 3.1 Publications

Faculty and students have been encouraged to publish their findings in such archival materials as publications, meeting transactions, and books. Current abstracting and computer search activities make such resources quite valuable to the world at large. Manuscripts from Integrated Diagnostic activity, submitted and/or published during this reporting period, are listed below with their respective abstracts.

##### Refereed Journal (3)

1. McDowell, D. L., "An Engineering Model for Propagation of Small Cracks in Fatigue," *Engrg. Fract. Mech.*, submitted May 1995.

Microstructurally and even mechanically small cracks have been shown to consistently exhibit higher crack growth rates than predicted using standard threshold and Paris growth law concepts based on linear elastic fracture mechanics (LEFM) applied to mechanically long cracks. Here, the viewpoint is adopted that multiple microstructure interactions and closure effects may simultaneously influence the propagation of small cracks; moreover, driving force parameters based on self-similar crack growth arguments of elastic-plastic fracture mechanics (EPFM) for mechanically long cracks, such as the cyclic J-integral or crack tip opening displacement, may apply in principle, but not rigorously, as the driving force for small cracks. As an engineering approach, a recent extension of the multiaxial microcrack propagation model first proposed by McDowell and Berard for the growth of microstructurally small and mechanically small fatigue cracks in multiaxial fatigue is considered. Integrated between initial and final crack lengths, the model is fully consistent with standard strain-life laws of fatigue crack initiation mechanics under various states of stress. The existence of a fatigue limit (nonpropagating crack limit) is neglected in this work. It is shown for uniaxial loading of both 1045 steel and Inconel 718 that the model is able to describe, to first order, the anomalous high propagation rates of small cracks and convergence with long crack  $da/dN - \Delta K$  data as the crack transitions from small to mechanically long scales. It is shown that the model essentially reflects a closure transient in the context of a cyclic J-integral approach, similar to the EPFM plasticity-induced closure modeling concepts of Newman, and McClung et al. for small cracks in fatigue. However the present model implicitly reflects multiple forms of crack tip shielding effects, not just plasticity-induced closure. Finally, the model is shown to provide realistic treatment of cumulative damage in two level loading sequences as reflected by comparison with the damage curve approach of Manson and Halford.

2. McDowell, D. L. and Bennett, V. P., "A Microcrack Growth Law for Multiaxial Fatigue," *Fatigue Fract. Engrg.*, revised January 1996.

Critical plane approaches have gained increasing support based on correlation of experimentally observed fatigue lives and microcrack orientations under predominantly low cycle fatigue (LCF) conditions for various stress states. In this paper, an engineering model is further developed for microcrack propagation consistent with critical plane concepts for correlation of both LCF and high cycle fatigue (HCF) behavior, including multiple regimes of small crack growth. The critical plane microcrack approach of McDowell and Berard serves as a starting point to incorporate multiple regimes of crack nucleation, shear growth under the influence of microstructural barriers, and

transition to linear crack length-dependent growth related to elastic-plastic fracture mechanics (EPFM) concepts. Microcrack iso-length data from uniaxial and torsional fatigue tests of 1045 steel and Inconel 718 are examined and correlated by introducing a transition crack length that governs the shift from nonlinear to linear crack length dependence of  $da/dN$ . This transition is related to the shift from strong microstructural influence to weak influence on the propagation of microcracks. Simple forms are introduced for both the transition crack length and the crack length-dependence of crack growth rate within the microcrack propagation framework introduced previously by McDowell and Berard, and are employed to fit the 1045 steel and IN 718 microcrack iso-length data, assuming pre-existing sub-grain size cracks. The nonlinear evolution of crack length with normalized cycles is then predicted over a range of stress amplitudes in uniaxial and torsional fatigue. The microcrack growth law is shown to have potential to correlate microcrack propagation behavior as well as damage accumulation for HCF-LCF loading sequences and sequences of applied stress states.

3. McDowell, D. L., "Basic Issues in the Mechanics of High-Cycle Fatigue," *Int. J. Fract.*, submitted January 1996.

Extension of damage tolerance concepts to lower length scales and small cracks relies critically on deeper understanding of (a) small crack behavior including interactions with microstructure, (b) heterogeneity and anisotropy of cyclic slip processes associated with the orientation distribution with grains, and (c) development of reliable small crack monitoring techniques. The basic technology is not yet sufficiently advanced in any of these areas to implement damage tolerant design for high-cycle fatigue (HCF). The lack of consistency of existing crack initiation and fracture mechanics approaches for HCF leads to significant reservations concerning application of existing technology to damage tolerant design of aircraft turbine engines, for example. The intent of this paper is to discuss key areas in which further research is required to enhance the accuracy of HCF life prediction. Predominant concern will rest with polycrystalline metals, and most of the issues pertain to wide classes of alloys.

#### Nonrefereed Publications (3)

1. Buckley, K., Venkatesan, G., West, D., and Kaveh, M., "Detection and Characterization of Cracks for Failure Monitoring and Diagnostics," *Proc. ICASSP96*, (Atlanta: ICASSP), submitted Jan. 1996.

An early indicator of the onset of material failure due to fatigue and/or stress is the appearance of microcracks. Generation of these cracks creates propagating acoustic signals in the material, termed Acoustic Emissions (AE). This paper presents results from an ongoing investigation into the detection and characterization of microcracks using AE signals measured in the presence of strong correlated interference and white noise.

2. Cowan, R. S. and Winer, W. O., "Recent Developments in Health Appraisal and Life Extension of Mechanical Systems," *Proc. Korea-USA Tribology Symp.*, (Seoul: KSTLE), 1995, pp. 17-24.

Learning from the failure of mechanical systems is a necessity, given it is the understanding of how and why things fail that generates effective redesign. This subsequently enables the technology that surrounds us to become more reliable, safer, and more economical by extending component life and minimizing the wasteful decisions made to replace systems that are either sound for operation or could be easily repaired. Considerations for cost-effective decision making, so as to promote healthy machinery, equipment, and structures, are discussed in terms of learning from failure analysis, improving via reliability engineering, and achieving longevity through integrated diagnostics.

3. Qu, J., Berthelot, Y., and Li, Z., "Dispersion of Guided Circumferential Waves in a Circular Annulus," *Proc. QNDE*, (Seattle: QNDE), submitted 1995.

Fatigue cracks have been found to initiate and grow in the radial direction in many of the annulus shaped components of aging helicopters, e.g., rotor hub, pitch shaft. Detection of such cracks relies mainly on visual inspection. Conventional ultrasonic imaging techniques can be used, but are impractical for real-time diagnosis. It is proposed that guided ultrasonic waves that propagate in the circumferential direction be used for detecting radial fatigue cracks in annulus components. For this purpose, the propagation of guided circumferential waves must be understood. This paper investigates the dispersion relations for waves that propagate in the circumferential direction of a circular annulus.

### Books, or sections thereof (2)

1. McDowell, D. L., "Multiaxial Fatigue Strength," *ASM Handbook, Fatigue and Fracture*, Vol. 19, (Materials Park: ASM), submitted 1995.
2. Saxena, A. and Muhlstein, C. L., "Fatigue Crack Growth Testing and Applications," *ASM Handbook, Fatigue and Fracture*, Vol. 19, (Materials Park: ASM), submitted 1995.

### Miscellaneous

#### *Monthly Progress Updates:*

To keep the Integrated Diagnostic community (e.g., ONR Scientific Officer, M-URI Team Members) up-to-date and informed about the ongoing activities of the program, status reports from the program's researchers have been collected, edited, and distributed as a monthly progress report.

#### *Informational Brochure:*

Intended for those interested in knowing more about the MultiUniversity Center for Integrated Diagnostics (e.g., potential collaborators, prospective students), a brochure, based on the theme "a safe tomorrow through innovation today" was developed. It describes the ONR M-URI goals, the research being conducted, and the educational opportunities available in Integrated Diagnostic disciplines.

#### *Information Highway:*

To ensure a wide dissemination of Integrated Diagnostic information, electronic reporting is to be utilized. To achieve this goal, a World-Wide-Web Homepage is presently under construction. Access can be achieved using the address <http://www.me.gatech.edu/Diagnostics/>.

## 3.2 Presentations

The process of technology transfer not only involves the recording of information, but also assisting in the understanding of that information and promoting its implications; hence, Integrated Diagnostic activity has been presented at a number of venues during this reporting period as listed below.

1. "Integrated Diagnostics M-URI Kickoff Meeting," Georgia Institute of Technology, Atlanta, GA, April 13, 1995.
2. "Integrated Diagnostics M-URI Annual Review," Office of Naval Research, Arlington, VA, February 12, 1996.
3. Cowan, R. S., "MultiUniversity Center for Integrated Diagnostics," 49th Mtg. Soc. Machinery Failure Prevention Technology, Virginia Beach, VA, April 1995.
4. Cowan, R. S., "Recent Developments in Health Appraisal and Life Extension of Mechanical Systems," 1995 Korea-USA Tribology Symposium, Seoul, Korea, October 1995.
5. Cowan, R. S. and Winer, W. O., "Health and Safety Improvement through Tribological Failure Analysis and Prediction," Technische Akademie Esslingen 10th Intl. Tribology Colloquium, Stuttgart/Ostfildern, Germany, January 1996.
6. Polla, D. L. and Francis, L. F., "Microelectromechanical Systems (MEMS) based on Electroceramic Thin Films," 7th USA-Japan Seminar on Dielectric and Piezoelectric Ceramics, Tsukuba, Japan, November 1995.
7. Qu, J. and Davis, J., "Effects of Interface on Fiber Structure in a Single Fiber Composite Specimen," ASME Summer Meeting, Los Angeles, CA, June 28-30, 1995.
8. Qu, J., "Dispersion of Circumferential Guided Waves in a Circular Annulus," 22nd Annual Review of Progress in QNDE, Seattle, WA, August 1995.

### **3.3 Education**

A primary mode of technology transfer is through students, who, trained in an aspect of integrated diagnostics, may subsequently apply such knowledge upon entry in an engineering profession. Post-doctoral, graduate, and undergraduate students have taken an active role in the research activities pursued during this reporting period. They are identified in Appendix A.

#### *Graduate Education*

Graduate education leading to M.S. and Ph.D. degrees is a major emphasis of the Integrated Diagnostics program. Twenty-four (24) research assistantships have been awarded to date, of which 12 are at Georgia Tech, 3 are at Northwestern University, and 9 are at the University of Minnesota.

#### *Undergraduate Education*

The Integrated Diagnostics program has granted five internships at Georgia Tech and one at the University of Minnesota, providing part-time employment during the junior/senior college year. This unique opportunity to collaborate with faculty and graduate students provides these individuals with valuable experience and incentives as they seek future employment or continue their studies through graduate education.

### **3.4 Partnerships**

Faculty and staff associated with the MultiUniversity Center for Integrated Diagnostics have initiated ties with various academic, industrial, and government organizations. Such partnerships have occurred to assure that the research being sponsored is conducted in an effective manner, and is of continued relevance to potential developers. Collaborations that have resulted during this reporting period are noted below with respect to the agency involved and the purpose intended.

- *Autonomous Scout Rotorcraft Testbed, Atlanta, GA* - Sponsored by the Department of Defense and the Georgia Tech School of Aerospace Engineering, this pilot project addresses the development of an autonomous unmanned vertical take-off and landing (VTOL) vehicle for surveillance missions. The rotorcraft is available for use in evaluating Integrated Diagnostic research developments (e.g., materials, sensors, processing methods) prior to their application on actual vehicle platforms.
- *Cherry Point Naval Depot, Atlantic Beach, NC* - This facility performs inspection and maintenance routines on an assortment of US defense assemblies including engines, carrier components, and aircraft. Information has been provided with respect to many areas, including the location and identification of critical components and failures, service environments, and material/design needs.
- *Honeywell, Inc., Minneapolis, MN* - A participant of the Air Vehicle Diagnostics System (AVDS) program through the development of a Rotor Acoustic Monitoring System (RAMS), the Honeywell Technology Center has provided the Center with pertinent information with respect to component failure, load-history, and sensor access for the H46 rotorhead assembly.
- *Rotorcraft Industry Technology Association (RITA)* - An arm of the National Rotorcraft Technology Center (NRTC), Georgia Tech is an active participant in this organization, intended to maintain awareness and provide assistance with identifying and expediting the development of dual-use pre-competitive rotorcraft technologies.
- *Torrington Co., Norcross, GA* - Dedicated to the development of various mechanical systems, this organization has provided expertise with respect to rolling-element bearings and test methods.

## APPENDIX A. Program Participants

---

### PRINCIPAL INVESTIGATOR (1)

Ward O. Winer

Georgia Tech

Mechanical Engineering

### Co-PI's (20)

Jan D. Achenbach  
Scott Bair  
Yves Berthelot  
Isaac Daniel  
Itzhak Green  
Laurence Jacobs  
Jacek Jarzynski  
W. Steven Johnson  
Thomas Kurfess  
Steven Liang  
David L. McDowell  
Brian Moran  
Richard Neu  
Dennis Polla  
Jianmin Qu  
S. Ramalingam  
Richard Salant  
Ashok Saxena  
Waymond Scott  
G.Vachtsevanos

Northwestern  
Georgia Tech  
Georgia Tech  
Northwestern  
Georgia Tech  
U. of Minnesota  
Georgia Tech  
U. of Minnesota  
Georgia Tech  
Georgia Tech  
Georgia Tech  
Georgia Tech

Quality Engineering  
Mechanical Engineering  
Mechanical Engineering  
Mechanical & Civil Engineering  
Mechanical Engineering  
Civil & Environmental Engineering  
Mechanical Engineering  
Materials Science & Engineering  
Mechanical Engineering  
Mechanical Engineering  
Mechanical Engineering  
Civil Engineering  
Mechanical Engineering  
Electrical Engineering  
Mechanical Engineering  
Mechanical Engineering  
Mechanical Engineering  
Materials Science & Engineering  
Electrical Engineering  
Electrical Engineering

### SUPPORT FACULTY (11)

Kevin Buckley  
Steven Danyluk  
Arthur Erdman  
Lorraine Francis  
William Gerberich  
Mostafa Kaveh  
Susan Mantell  
William Robbins  
Charles Stancil  
J. S. Steckenrider  
Ahmed Tewfik

#### *Collaborating with:*

Polla  
Kurfess/Liang  
Polla  
Polla  
Polla  
Polla  
Polla  
Polla  
Winer  
Achenbach  
Polla  
U. of Minnesota  
Georgia Tech  
U. of Minnesota  
Georgia Tech Research Institute  
Northwestern  
U. of Minnesota

## Program Participants

### POST-DOCTORAL RESEARCHERS (6)

D. Bruttomesso (12/95-1/96)  
 H. J. Chun  
 Li Li  
 Guoli Liu  
 Chr. Sifniotopoulos  
 Shayne Zurn

<i>Sponsor:</i>	
Bair	Georgia Tech
Daniel	Northwestern
Polla	U. of Minnesota
Qu/Jacobs	Georgia Tech
Daniel	Northwestern
Polla	U. of Minnesota

### GRADUATE STUDENTS (24)

William Anderson  
 David Bahr  
 Valerie Bennett  
 Tom Cooney  
 Richard S. Cowan  
 Anne Gao  
 Brian Gardner  
 David Harris  
 Hyeon-Sang Kim  
 Yawei Li  
 Zongbao Li  
 J. J. Luo  
 David Markus  
 Akshay Patel  
 David Rink (6/95-12/95)  
 Jason Shiroishi  
 Christine Valle  
 Gopal Venkatesan  
 Dennis West  
 Jianhua Xue  
 Fan Yang  
 Lanshi Zheng  
 Min Zou  
 Ali Zulfiqar

<i>Advisor:</i>	
Salant	Georgia Tech
Polla	U. of Minnesota
McDowell	Georgia Tech
Polla	U. of Minnesota
Winer	Georgia Tech
Polla	U. of Minnesota
Qu	Georgia Tech
Scott/Vachtsevanos	Georgia Tech
Polla	U. of Minnesota
Liang	Georgia Tech
Berthelot	Georgia Tech
Daniel	Northwestern
Polla	U. of Minnesota
Neu	Georgia Tech
Daniel	Northwestern
Kurfess	Georgia Tech
Jacobs/Qu	Georgia Tech
Buckley/Kaveh	U. of Minnesota
Tewfik	U. of Minnesota
Ramalingam	U. of Minnesota
Saxena/Johnson	Georgia Tech
Ramalingam	U. of Minnesota
Green	Georgia Tech
Moran	Northwestern

### UNDERGRADUATE STUDENTS (6)

R. W. Cowan (4/95-12/95)  
 Richard Hamm  
 Jennifer Hsieh  
 Dan Scott (6/95-1/96)  
 Josh Warren (6/95-7/95)  
 Alice Zhang (5/95-12/95)

<i>Advisor:</i>	
Green	Georgia Tech
Johnson	Georgia Tech
Jacobs	Georgia Tech
Neu	Georgia Tech
Green	Georgia Tech
Polla	U. of Minnesota